STATISTICAL AND ANALYTICAL INNOVATIONS FOR HIGH-RESOLUTION PALEOCLIMATE RECONSTRUCTIONS USING CORALS AND BIVALVES

Hunter Passman Hughes

A dissertation submitted to the faculty at the University of North Carolina at Chapel Hill in partial fulfillment of the requirements for the degree of Doctor of Philosophy in the Earth, Marine and Environmental Sciences (Geological Sciences) in the College of Arts and Sciences.

Chapel Hill
2025

Approved by:

Donna Surge

Gavin Foster

Jonathan Lees

Richard Smith

Diane Thompson

ABSTRACT

Hunter Passman Hughes: Statistical and Analytical Innovations
for High-Resolution Paleoclimate Reconstructions Using Corals and Bivalves
(Under the direction of Donna Surge)

High-resolution marine archives (e.g., corals and bivalves) offer critical insight into past climate variability. However, many potential archives are either inaccessible given due to slow growth rates, or limited in interpretability due to non-climate-related variability in their skeletal geochemistry. This dissertation seeks to advance both analytical and statistical techniques to improve the fidelity, resolution, and reproducibility of paleoclimate reconstructions from two key high-resolution marine archives: the high latitude bivalve *Astarte borealis* and tropical *Porites* corals.

Chapter 2 explores the use of secondary ion mass spectrometry (SIMS) to generate ultra-high-resolution δ^{18}O records from *A. borealis* collected in the southern Baltic Sea. These records are used to assess the sensitivity of shell δ^{18}O values to local and regional environmental variability, demonstrating strong correlations with salinity, temperature, and large-scale climate modes such as the North Atlantic Oscillation. The results establish *A. borealis* as a viable high-latitude proxy archive capable of recording hydroclimatic variability over seasonal to decadal scales.

Chapter 3 introduces a novel analytical pipeline for converting two-dimensional LA-ICP-MS maps from *Porites astreoides* into one-dimensional time series, enabling high-resolution reconstructions of sea surface temperature (SST) and seawater pH. This chapter also presents the Scleractinian Multivariate Isotope and Trace Element (SMITE) method, a multivariate calibration framework that leverages geochemical covariance to improve reconstruction skill. SMITE is shown to outperform traditional univariate methods in terms of accuracy, robustness to noise, and reproducibility across synthetic experiments and short coral datasets.

Chapter 4 evaluates the performance and reproducibility of SMITE, Sr/Ca, and Li/Mg temperature estimates using 15 coral records from the Great Barrier Reef and 2 records from the Galápagos Archipelago. Synthetic climate field reconstructions reveal tradeoffs between statistical performance and signal recoverability, with SMITE providing more reproducible calibrations at the expense of variance suppression.

Together, these chapters demonstrate a flexible and scalable approach for enhancing both analytical access and statistical rigor in high-resolution marine paleoclimatology. By extending proxy coverage into high-latitude environments and establishing a multivariate statistical framework for tropical coral reconstructions, this work lays the foundation for next-generation paleoclimate proxy networks and climate data assimilation efforts.

To my family... those who have come, those who have gone, and those who have always been here. I could not have done any of this without you.

ACKNOWLEDGEMENTS

It is with a deep and heartfelt sense of gratitude that I write these words, to thank everyone who made this body of work possible. No amount of words could sufficiently express what the last five years have meant to me. However, since there are (finally) no guidelines for how to write this section, I will let the pen fly loose from my hand, so to speak.

To begin, I would like to thank my advisor, Dr. Donna Surge. Your unwavering confidence in my abilities from the outset was a constant source of stability and comfort in a uniquely trying time. You encouraged me to pursue every opportunity to broaden my perspective, as both a scientist and a human being. Even as my interests stretched beyond both of our collective expertise, you guided my curiosity with steady and pragmatic reasoning. I cannot thank you enough for such a formative doctoral journey, and I hope to pay it forward for future generations.

Next, I would like to thank each committee member in the order that they joined my committee.

To Dr. Diane Thompson, thank you for welcoming me into your lab and home, and for constantly reminding me that I have something truly valuable to contribute to this field. With you, I engaged in some of the richest technical discussions of my doctoral experience. Thank you for always challenging my decisions with a keen intellect and a genuine sense of curiosity and scientific discovery. I hope that water bottle is still serving you well.

To Dr. Jonathan Lees, thank you for teaching me the mystical arts of inverse theory, and for nurturing my curiosity and passion for statistical modeling. Your faith in my abilities helped me find equilibrium, even as I had learned to run before I could walk. I am only slightly sorry for regularly taking advantage of your open-door policy, since it often led to valuable feedback and advice that I will carry with me throughout my career.

To Dr. Gavin Foster, thank you for recognizing my potential from our first meeting. You constantly supplied me with new exciting data to work with, and the time I spent across the Big Pond was one of the most enriching experiences of my doctoral journey. Of course, this in no small part due to the profound sense of hospitality and intellectual curiosity that you have cultivated amongst the B-team. Also, thank you for recognizing my eclectic book collection that my wife had carefully curated to be just barely visible in my Zoom background.

To Dr. Richard Smith, although we met somewhat later in my doctoral journey, I have much to thank you for with respect to introducing me to the proper rigors of multivariate statistics. You truly helped me gain a quantitative grasp of the methods I was implementing, which nourished my conceptual curiosity when I naively believed I was reaching an imminent plateau. I will always appreciate your enduring support, both through academia and through our shared love of theater.

Next, I would like to thank the suite of coauthors and collaborators who have made each of these chapters possible. Ian Orland, Michael Zettler, and David Moss; your expertise, constructive feedback, palpable investment, and collective trust in my abilities helped me find my voice amidst novel ground. Chris Standish, your towering talent as an analytical geochemist is second only to your patience and kindness as a human being. Duo Chan, the *piece de resistance* of this dissertation would not have been possible without your guidance. I would also like to thank the incredibly capable geochemists who manage the Geochemistry labs at the University of Southampton, National Oceanography Centre, namely Andy Milton, Heather Goring-Harford, and Matthew Beverly-Smith.

To the staff at the Earth, Marine and Environmental Sciences Department at UNC Chapel Hill who keep its heart beating, I cannot thank you enough for the logistical support you provided me with throughout my doctoral experience. From coordinating funding and social events to putting out (metaphorical) fires spread by my own negligence, your hard work kept me on a steady course towards finishing this final body of work.

I would also like to thank the funding agencies that made this work possible. This research was supported by grants from the National Science Foundation awarded to my advisor and collaborators, funding from the Federal Maritime and Hydrographic Agency awarded to my collaborator Dr. Michael Zettler, as well as funding from the European Research Council and the British Ocean Sediment Core Research Facility awarded to my committee member, Dr. Gavin Foster. Additional support came from the Geological Society of America Graduate Student Research Fund, The Scientific Research Honor Society Sigma Xi, the Preston Jones and Mary Elizabeth Frances Dean Martin Fellowship Fund, and the William R. Kenan Jr. Fellowship. I am sincerely grateful for the financial support that enabled both the analytical work and the international collaborations central to this dissertation. A special thanks goes to the Royster Society of Fellows, and all who make this wonderful community thrive. You honored and enriched my graduate experience in countless ways, and I hope to stay connected with you for many years to come.

To my former mentors throughout my many years becoming an Earth scientist: Dr. Ken Rasmussen, Dr. Hali Kilbourne, and Dr. Johan Schijf. Thank you for sharing with me your love of the natural world, your passion for research and teaching, and for continuously shaping me into the best scientist I could be. Your unrelenting faith in me emboldened me when I was plagued by doubt or despair. Everything I have done here, and everything I will continue to do, was possible because of you.

I would like to give special thanks to all of the students I have taught throughout the years. As deeply entrenched as one can get in their dissertation research, your curiosity and zeal kept me grounded; not only in the fundamentals of Earth Science (which brought me here to begin with), but in one of the most important reasons why I love the fertile ground for growth that is academia. On this same note, I would like to thank Dr. Megan Plenge. My experience as your learning assistant and collaborator is only a small example of how you embody the pinnacle of teaching in higher education.

To the broader community of paleoclimatologists, particularly my peers navigating their early careers, I count it as one of the greatest honors of my life to work amidst such clever, hard-working, and good-natured people. You remind me constantly that none of this is done in a vacuum; that together, we reach further than we ever could have in isolation.

To my close friends who saw me through this journey, both within and outside of the sciences. Your presence and support, both direct and indirect, helped get me through the hardest parts of graduate school in more ways than you could possibly know. I want to send particular thanks to my groomsman, lab mate, "son", fellow wing connoisseur, statistical consultant, and much-welcome distraction during the marathon that is the dissertation, Garrett Braniecki. I hope our laughter and themed music continues to echo through the halls of the department long after we are gone.

To my family, through the wonderful mixture of love, support, critiques, challenges, laughter, tears, and shared experiences, I have never felt alone in this endeavor. From the bottom of my heart, thank you.

And finally, to my wife, Marissa. Words would only diminish how much your love and companionship has meant to me over these many years. You may never go diving on a coral reef with me (it's okay, you don't have to). You may not always know what I am mumbling about when we are 'talking' about my research. But as our lives move forward together, know that you are the life and breath of everything I do.

TABLE OF CONTENTS

LIST OF TABLES

LIST OF FIGURES

LIST OF ABBREVIATIONS

B/Ca	Boron to Calcium Ratio
BATS	Bermuda Atlantic Time-series Study
CFR	Climate Field Reconstruction
ENSO	El Niño Southern Oscillation
EOF	Empirical Orthogonal Function
ESR	Effective Signal Recoverability
IOD	Indian Ocean Dipole
LA-ICP-MS	Laser Ablation Inductively Coupled Plasma Mass Spectrometry
LOWESS	Locally Weighted Scatterplot Smoothing
Li/Ca	Lithium to Calcium Ratio
Li/Mg	Lithium to Magnesium Ratio
Mg/Ca	Magnesium to Calcium Ratio
NAO	North Atlantic Oscillation
ORA-20C	Ocean Reanalysis of the 20th Century
pH_{sw}	Seawater pH
RMSE	Root Mean Square Error
SEP	Standard Error of Prediction
SIMS	Secondary Ion Mass Spectrometry
SMITE	Scleractinian Multivariate Isotope and Trace Element
Sr/Ca	Strontium to Calcium Ratio
SST	Sea Surface Temperature
TE/Ca	Trace Element to Calcium Ratio
U/Ca	Uranium to Calcium Ratio
$x_{\dagger}$	SMITE Model Loading Score
δ^{11}B	Boron-11 Isotope Ratio
δ^{18}O	Oxygen-18 Isotope Ratio

CHAPTER 1

Introduction

1.1 Past is Prologue: The Necessity of Paleoclimatology

Anthropogenic climate change is projected to accelerate through the 21st century, resulting in a wide range of environmental hazards with increased frequency and magnitude (Cook et al., 2020; Donat et al., 2013; Douville et al., 2021; O'Gorman, 2015). Agriculture, water resources, military and civilian infrastructure, and even disease prevalence are all inexorably linked to how the climate will change in the coming decades (Ficklin et al., 2022; Lafferty, 2009; Manolis et al., 2024). Thus, accurate and precise projections of future climate are paramount for mitigating the detrimental effects of climate change, as well as informing adaptation strategies and planning for present and future crises (VijayaVenkataRaman et al., 2012).

Although climate change is a global phenomenon, the ocean plays an outsized role in shaping its trajectory. The ocean covers more than 70% of the Earth's surface, acting as a vast reservoir of heat and greenhouse gasses that buffers against the relatively rapid changes of the atmosphere (Schmitt, 2018). Not only does the surface ocean respond to atmospheric changes, but also actively drives many of the climate patterns that govern weather extremes, water availability, and long-term climate variability around the globe (Wang, 2019). Thus, climate variables like sea surface temperature (SST), salinity, and seawater pH (pH_{sw}) are considered essential variables linked to the occurrence and magnitude of extreme events such as heat waves, anoxia, and hurricanes (Chan, 2021; Garcia-Soto et al., 2021; Trenberth and Fasullo, 2012).

To determine their accuracy and utility, climate models require rigorous testing against historic climate change in a process often referred to as 'hindcasting' (Hausfather et al., 2020). This process generally involves the models being initialized with the best available estimates of the climate conditions at the onset of the industrial era. The model-predicted variables are then compared against observational data to assess model skill and determine whether the simulated physics behave realistically. However, the effectiveness of this validation process is limited by the quality and duration of the observational record. Although humans have monitored aspects of climate for millennia, systematic measurements of key variables like SST only began in the mid-19th century (Freeman et al., 2017; Kennedy et al., 2011). These efforts have proven invaluable, and as the observational network has expanded over the

past 175 years, so too has our understanding of climate variability across multiple timescales (de Boisséson et al., 2018; Huang et al., 2017).

However, the instrumental record is limited for a number of reasons. First, while 175 years is sufficient to characterize interannual to decadal modes of climate variability, such as the El Niño Southern Oscillation (ENSO) or the Pacific Decadal Oscillation (PDO), it is challenging to resolve multidecadal variability like the Atlantic Multidecadal Oscillation (AMO) (Delworth and Mann, 2000). As a result, centennial-scale and longer modes of climate variability remain beyond the domain of the instrumental record, limiting our confidence in how these modes interact with and modulate shorter-term variability (Jones et al., 2009; Mann et al., 2009). Furthermore, the beginning of the instrumental record coincides with the onset of the industrial revolution, the driving mechanism behind anthropogenic climate change. Without data from before this period, we cannot fully assess how major climate modes may have evolved in response to rising greenhouse gas concentrations (Steiger et al., 2018; Tierney et al., 2020).

Furthermore, the instrumental record is spatially limited up until the beginning of the satellite era in the late 1970s (Kennedy, 2014). Prior to this, most ocean-based observations were based on shipboard measurements, primarily from commercial vessels operating for purposes unrelated to climate research (e.g., navigation Davis et al., 2019; Kennedy et al., 2011). Shipping routes have historically been concentrated in the North Atlantic and, to a lesser extent, the North Pacific (Kennedy, 2014), leaving vast regions like the Southern Hemisphere and the tropics chronically undersampled before the satellite era (Davis et al., 2019). The combination of these temporal and spatial limitations hampers our ability to characters long-term climate variability across time and to resolve even shorter-term variability, like ENSO, across space (Steiger and Smerdon, 2017). For example, different types of ENSO events, such as the Eastern Pacific versus Central Pacific El Niño, have distinct global teleconnection patterns (Alizadeh, 2024; Ashok et al., 2007). Accurately identify when specific types of ENSO events occurred is essential for understanding their impacts propagate globally.

Furthermore, the uncertainty of the instrumental records is often understated. Because nearly all major SST products are based on the International Comprehensive Ocean-Atmosphere Data Set (ICOADS), they inherit shared structural uncertainties that remain largely unquantified (Cowtan and Way, 2014; Davis et al., 2019; Kennedy et al., 2011; Kent et al., 2017). The magnitude of these structural uncertainties is not trivial, as differences in data processing and correction choices can obscure the timing and detection of internationally-agreed upon warming thresholds such as 1.5°C or 2.0°C (Schurer et al., 2017).

Given these limitations, independent archives of the climate are essential for constraining historic climate variability and improving confidence in model-based projections of future climate change (Tierney et al., 2020). To address the spatial and temporal gaps in the instrumental record, paleoclimate archives (e.g., corals and bivalves) are invaluable tools for estimating essential ocean climate variables like SST, salinity, and pH_{sw} in the absence of direct observations (Jones et al., 2009; Surge and Schöne, 2015; Thompson, 2021). These natural archives preserve

environmental information as variability in the physical, chemical, or biological properties of a particular archive, often in the geologic record. Since this record is vast, and contains material as old as the Earth itself, paleoclimate archives are rich stores of information that are akin to windows into Earth's climatic history (Masson-Delmotte et al., 2013; Tierney et al., 2020).

1.2 High-resolution Marine Biogenic Archives

1.2.1 Background

Historically, most paleoceanographic archives have been derived from sediment cores, as the deep ocean provides a uniquely stable environment where material accumulates and is preserved over millions of years (Lisiecki and Raymo, 2005). However, these records are typically low in temporal resolution, often yielding only one data point every few thousand years (Kucera, 2007). As such, they are best suited for documenting long-term, large-scale shifts in Earth's climate system, such as Quaternary glacial–interglacial cycles or the gradual cooling of the Cenozoic era (Lisiecki and Raymo, 2005; Mudelsee et al., 2014).

In contrast to sediment cores, high-resolution marine archives are typically derived from the shells or skeletons of surface-dwelling marine organisms, most often in the form of biogenic carbonate (Jones et al., 2009). Many of these organisms produce accretionary hard parts that preserve subannual to annual environmental signals, making them invaluable for reconstructing short-term climate events and interannual variability associated with phenomena such as ENSO and the North Atlantic Oscillation (NAO).

Among these archives, scleractinian corals and bivalves are two of the most widely used, largely because both groups form annual growth increments that allow for precise chronological control (Ansell, 1968; Barnes, 1970; Surge and Schöne, 2015; Thompson, 2021). Scleractinian corals are colonial marine invertebrates that secrete calcium carbonate skeletons, forming rigid structures that anchor them within typically shallow, sunlit tropical waters (Veron, 2000). Bivalves, by contrast, are soft-bodied invertebrates that produce a hinged shell for protection. They occupy a wide range of marine environments, from tropical coral reefs to cold polar regions (Gosling, 2008).

1.2.2 Geochemical Climate Proxies in Corals and Bivalves

High-resolution paleoclimatology using corals and bivalves typically involves measuring the geochemistry (e.g., isotopes and elemental ratios) of their skeletal growth via mass spectrometry. This process is usually done by collecting material along the major growth axis of the organism. The spatial coordinates of skeletal growth are mapped to time (i.e., timestamped) using a transfer function that is at least partially anchored in the annual growth increments deposited by the organism. Thus geochemical variations can be directly correlated with the environmental variables of interest.

The foundational principles behind this approach were first established in the mid-twentieth century with Urey (1947), who theorized that the fractionation of oxygen isotopes during carbonate formation was temperature-dependent. This claim was validated by Epstein et al. (1951), who demonstrated a quantitative relationship between temperature and the oxygen isotope composition of carbonate ($\delta^{18}O_c$) using mollusk shells. Emiliani (1955) was the first to use the temperature dependence of $\delta^{18}O_c$ to make direct inferences of Earth's temperature history, reconstructing the last 300,000 years using planktic foraminifera from deep-sea cores. Since these seminal works, paleotemperature reconstruction using $\delta^{18}O_c$ were extended to other marine archives, including the high-resolution records available from bivalves (Beu, 1974; Strauch, 1968) and corals (Shackleton and Matthews, 1977; Weber and Woodhead, 1972).

While it was understood at the onset of $\delta^{18}O$-based paleothermometry that $\delta^{18}O_c$ covaries with both temperature and seawater $\delta^{18}O$, the latter was often assumed relatively constant within an acceptable margin of error. Over time, however, the limitations of this assumption became increasingly apparently, especially in coastal and tropical environments where seawater $\delta^{18}O$ can vary significantly due to evaporation, precipitation, freshwater runoff, and advection (LeGrande and Schmidt, 2006; Rohling, 2013). Today, $\delta^{18}O$ systematics in natural systems remains a highly active area of research, with $\delta^{18}O_c$ now being utilized more commonly used as a proxy for seawater $\delta^{18}O$ and, by correlation, sea surface salinity (Fairbanks et al., 1992; LeGrande and Schmidt, 2006; Thompson et al., 2011).

As questions about the variability of seawater $\delta^{18}O$ grew more prominent, researchers began seeking alternative proxies that could estimate paleotemperature more directly. One such approach involved measuring the ratio of certain trace elements to calcium (TE/Ca) in biogenic carbonates, such as Mg/Ca in bivalves (Klein et al., 1996) and Sr/Ca in corals (Smith et al., 1979). These TE/Ca ratios were found to correlate with temperature in controlled experiments and field studies, offering a promising geochemical tool that, in theory, was not confounded by substantial changes in seawater isotopic composition. This optimism was further supported by the assumption that many trace elements in seawater behaved conservatively, or at least varied slowly over geologic timescales, making them seemingly stable baselines for temperature reconstructions (Dittmar, 1884; Forchhammer and Sabine, 1865; Horibe et al., 1974).

While certain trace element ratios in corals (e.g., Sr/Ca) and bivalves (e.g., Mg/Ca) indeed show temperature sensitivity, it is now well established that they can also exhibit considerable variability unrelated to seawater temperature. Broadly, these non-climate-related sources of variability fall into two categories. The first I term "local environmental effects", which involve direct changes to seawater chemistry that are not related to the climate parameters of interest. These local environmental effects typically directly impact the TE/Ca of seawater, such as vertical gradients in seawater Sr/Ca ratios associated with the biogenic production of celestite (Alibert et al., 2003; Bernstein et al., 1987, 1992; de Villiers et al., 1994; de Villiers, 1999). Other factors may include terrestrially-sourced groundwater or runoff, each of which possess distinct TE/Ca ratios from seawater (Basu et al., 2001; Brennan et al., 2014;

Khare et al., 2021, 2023; Khaska et al., 2013; Lubarsky et al., 2018; Macdonald and Crook, 2010; Stalker et al., 2009; Surge and Lohmann, 2002), or variations in the local seawater carbonate chemistry associated with the balance between photosynthesis and calcification (Muehllehner et al., 2016; Schneider et al., 2009).

The second non-climate-related source of variability involves kinetic or metabolic effects propagated by biological controls on trace element incorporation into the shell of the marine organism (Weiner and Dove, 2003). Given that these controls differ greatly between corals and bivalves, I explore this topic in greater detail in the following section. Interestingly, it is now common practice to use different isotopic ratios or TE/Ca ratios to track non-climate-related variability in pursuit of answering research questions of a chemical or biological nature. For instance, boron systematics (Zeebe and Wolf-Gladrow, 2001) have been employed to probe the carbonate chemistry of both corals (McCulloch et al., 2017) and bivalves (Alvarez Caraveo et al., 2024). These studies carry important implications for human welfare, spanning conservation, fisheries management, and biomedical applications (Allemand et al., 2004; Weiner and Dove, 2003; Huang and Zhang, 2022).

1.2.3 Benefits and Limitations of Corals and Bivalves as Paleoclimate Archives

Scleractinian Corals

Despite many similarities as high resolution paleoclimate archives, corals and bivalves are distinct tools with often non-overlapping applications when it comes to paleoclimatic inferences. Beginning with shallow-water scleractinian (or reef-forming) corals (henceforth simply referred to as 'corals'), these are typically used to infer tropical climate variability within the last few centuries (e.g., DeLong et al., 2013). Due to their relatively low tolerance for annual temperature variability, corals are confined to the shallow tropical oceans (Veron, 2000). This ecological constraint makes them useful indicators of past sea level, as subaerial coral terraces or fossil coral deposits can signal that a location was once submerged beneath a shallow tropical sea (Woodroffe and Webster, 2014).

Corals are also remarkably long lived, as a single colony can grow continuously for decades to centuries (Corrège, 2006; Sadler et al., 2014). During that time, changes in the density and porosity of the coral skeleton create distinct annual growth increments that can be precisely dated at high resolution (Barnes and Lough, 1993; Knutson et al., 1972). Corals are among the fastest marine calcifiers on the planet, in large part due to a symbiotic relationship with a dinoflagellate algae referred to as zooxanthellae that provides up to 90% of their energy requirements (Falkowski et al., 1984; Muscatine and Porter, 1977; Service, 2024a). This causes them to grow quickly at regular intervals: tens of millimeters per year for the slow growing massive corals, and upwards of 100 mm per year for the faster branching corals (Service, 2024b; Pratchett et al., 2015). Logistically, this makes their annual growth increments easily discerned, age modeled, and sampled for geochemical analysis (DeLong et al., 2016; Schrag, 1999).

Corals are also distributed across key regions of the tropical oceans that serve as centers of activity for major modes of interannual to interdecadal climate variability, such as ENSO and the AMO (Cobb et al., 2003; Hetzinger et al., 2008). As a result, individual geochemical variables in corals often covary strongly with interannual forcing (Cole and Fairbanks, 1990; Felis et al., 2000; Jose and Michael JR, 1994; Sayani et al., 2021), or multiple variables can together track the composite variability associated with specific climate modes (Bolton et al., 2014; Kilbourne et al., 2004b; Krawczyk et al., 2020; Linsley et al., 2004).

However, because corals are restricted to tropical ocean environments, coral-based paleoclimate records are primarily informative of tropical ocean dynamics (Kleypas et al., 1999; Veron, 2000). While this is valuable given the central role of the tropics in global climate variability, it limits the spatial coverage of high-resolution paleoclimate information to a relatively narrow latitudinal band, with only occasional exceptions extending into the subtropics (e.g., DeLong et al., 2011; Felis et al., 2000).

Additionally, corals are a keystone species for a valuable ecosystem that provides tens of billions of dollars to the global economy (Cesar et al., 2003; Spalding et al., 2017). Unfortunately, coral reefs are increasingly threatened by a combination of global and local stressors associated with anthropogenic climate change (Baumann et al., 2019; Cornwall et al., 2021; Hughes et al., 2018; McCulloch et al., 2017; van Dam et al., 2011). Sampling a coral colony for paleoclimate reconstruction typically involves extracting a small-diameter core ($\sim$5 cm) along the major growth axis (e.g., Barnes and Lough, 1993; DeLong et al., 2016). When conducted carefully, this method minimizes structural damage and often allows the colony to recover over time with limited long-term effects (Hubbard, 2011). However, even minimally invasive procedures can cause physiological stress and may increase the colony's vulnerability to disease or mortality, particularly in already compromised reef systems (Hawkins and Roberts, 1993; Raymundo et al., 2018; van de Water et al., 2015). As such, coral sampling must be undertaken judiciously and sparingly.

Furthermore, coral-based paleoclimate reconstructions are a costly and laborious endeavour, from gaining permits for sample collection, to coring and transportation of the material to a geochemical laboratory, to subsequent microsampling and analysis. These constraints limit the number of replicates that can be collected within a single reef system, reducing the statistical power of site-specific reconstructions and complicating efforts to distinguish localized environmental signals from colony-specific variability.

One of the most persistent challenges in coral-based paleoclimate reconstructions is the high degree of uncertainty in the regression coefficients between a particular coral geochemical proxy and the environmental variable of interest. These regression coefficients can vary significantly between adjacent colonies, taxa, regions, nutrient concetrations, different sections of the same core, regression techniques, and even between laboratories using similar analytical setups (Cahyarini et al., 2008; Corrège, 2006; Fowell et al., 2016; Hathorne et al., 2013; Ross et al., 2019; Standish et al., 2024; Stewart et al., 2020; Walter et al., 2023; Xu et al., 2015). A commonly cited cause for these

discrepancies is the presence of so-called "vital effects", a broad term encompassing both kinetic effects (e.g., those related to calcification rate and growth dynamics) and metabolic effects (e.g., biological regulation of the carbonate chemistry of the calcifying fluid). These physiological controls, exerted by the coral holobiont, modulate trace element and isotope incorporation into the aragonitic skeleton and can result in disequilibrium between the composition of the calcifying fluid and that of ambient seawater (Alpert et al., 2016; Clarke et al., 2017, 2019; Grove et al., 2013; Hetzinger et al., 2016; Hirabayashi et al., 2013; Kuffner et al., 2012; D'Olivo and McCulloch, 2017; Sinclair et al., 2006; Reed et al., 2021).

The resultant disequilibrium from these metabolic and kinetic effects between the coral calcifying fluid and the surrounding seawater is a well-acknowledged problem in the field, and significant effort has gone into improving reproducibility of coral geochemical proxies (Allison and Finch, 2009; DeLong et al., 2013, 2016; Sayani et al., 2019; Stephans et al., 2004; Stewart et al., 2020). In addition to improved sampling strategies and careful core selection, another complementary approach involves using multiple proxies to better constrain common variability, or multiproxy calibration (DeCarlo et al., 2016; Gaetani et al., 2011; Hathorne et al., 2013; D'Olivo et al., 2018; Saenger and Wang, 2014; Sinclair, 2015). While multiproxy methods are not without their own challenges, this remains an active area of research that has produced significant progress in coral-based paleoclimate studies. However, the considerable uncertainty in regression parameters continues to limit the precision and interpretability of fossil coral records, especially when applied to paleoclimate reconstructions beyond the modern calibration period.

Bivalves

As paleoclimate archives, bivalves span a wide variety of applications, from short snapshots of seasonal amplitude using *Mercenaria mercenaria* (Braniecki et al., 2024; Crippa et al., 2016) to long, seasonally resolved records from *Arctica islandica* (Reynolds et al., 2022; Schöne, 2013; Wanamaker et al., 2012). However, due to its unusual biology, photosymbiosis, and high growth rates, *Tridacna gigas* provides ultra-high resolution records more akin to scleractinian corals than most other bivalves (Elliot et al., 2009). Accordingly, this section focuses on the broader benefits and challenges of using bivalves as paleoclimate archives, excluding *T. gigas*.

Bivalves have demonstrated remarkable evolutionary success, adapting to a wide range of marine and freshwater environments across the globe (Moss et al., 2016; Harte, 2001). While not all species are suitable for paleoclimate applications, many are (Arnold et al., 1998; Cargnelli et al., 1999; Gillikin et al., 2006; Schöne and Gillikin, 2013; Surge and Schöne, 2015), making climate records derived from bivalves accessible from coastal regions worldwide. Additionally, many bivalve species also produce annual growth increments that enable the development of precisely dateable chronologies (Ansell, 1968; Fritz, 2001). Unlike corals, which exhibit banding due to differences in skeletal density and porosity, bivalves typically form growth increments through seasonal variations in organic matter deposition, with slower growth during particular seasons (Fritz, 2001). Species that commonly exhibit clear growth

increments also tend to be fast-growing (e.g., *Arctica islandica*, *Margaritifera margaritifera*), which facilitates sampling and improves temporal resolution (Surge and Schöne, 2015).

Bivalves often constitute a significant portion of local marine biomass (Gosling, 2008; Moss et al., 2016). As a result, sites targeted for paleoclimate reconstruction are typically rich in potential specimens. This makes replication of climate signals highly feasible, allowing multiple samples to be analyzed without significant ethical or logistical concerns. Bivalves also benefit from a demonstrable tendency to precipitate shell carbonate very-close to equilibrium with ambient seawater, particularly for oxygen isotopes, though some trace elements still show species- or growth-related effects (Mook and Vogel, 1968). Thus, the same transfer function that relates shell geochemistry to the climate signal of interest can be used across many specimens with reliable accuracy (e.g., Grossman and Ku, 1986; Dettman et al., 1999; Braniecki et al., 2024).

Bivalves are also relatively resistant to diagenetic alteration. While the oldest high-resolution coral-based paleoclimate records date back to the Quaternary (Kilbourne et al., 2004a), bivalve-based records have been successfully extended to the Carboniferous (Brand, 1982; Ivany and Runnegar, 2010; Beard et al., 2015; Jimenez et al., 2019).

However, only a few bivalve species are extremely long-lived and grow continuously for long periods of time (e.g.,*A. islandica*). Most bivalves live for decades at a time (e.g., *Mercenaria* spp., *Spisula* spp., *Chione* spp., *Crassostrea virginica*), but the majority of their growth occurs early in ontogeny. Consequently, usable samples are often limited to material formed closest to the hinge plate, which generally represents just the first few years of growth (Jones and Quitmyer, 1996; Quitmyer et al., 1997; Wang et al., 2011). Beyond this, growth rates slow and increments become increasingly difficult to resolve. While crossdating techniques can overcome this limitation by developing "master" chronologies, they are currently feasible only for the longest-lived species like *A. islandica* (Butler et al., 2010; Schöne, 2013).

Furthermore, ontogenetic (i.e., age-related) effects also present challenges. These effects unfold gradually over time and manifest in shrinking growth increment widths, reducing the number of subannual samples that can be collected in older parts of the shell. This may lead to subtle distortions in climate interpretations, such as an apparent dampening of seasonal amplitude or low-frequency variability (Elliot et al., 2003; Goodwin et al., 2003). In some cases, ontogenetic effects include growth cessations, where shell formation halts under environmental stressors like extreme temperatures or limited food availability (Ansell, 1968; Jones and Quitmyer, 1996; Fritz, 2001). Such cessations may obscure seasonal maxima and minima (Braniecki et al., 2024), and are often difficult to detect, posing further complications for paleoclimatic interpretations (Hughes et al., 2023).

1.3 Dissertation Structure and Contributions

In this dissertation, I implement novel analytical and statistical techniques to improve paleoclimatic information interpretations from two archives specifically: *Astarte borealis*, a small bivalve specimen from the Baltic Sea; and scleractinian corals of the *Porites* genus from Bermuda, the Galapagos Archipelago, and across the Great Barrier Reef.

The analytical advances center on the use of secondary ion mass spectrometry (SIMS; Chapter 2) and laser ablation inductively coupled plasma mass spectrometry (LA-ICP-MS; Chapter 3) to measure trace element-to-calcium (TE/Ca) and isotope ratios at ultra-high spatial resolution. These tools allow for sampling bivalves and corals that are too small to sample at subannual resolution using conventional methods. The statistical advances involve the development of a multivariate calibration framework that exploits the covariance SST and seawater pH across multiple geochemical proxies in coral skeletons (Chapters 3 and 4). This method creates a flexible framework to yield more reproducible regression coefficients while also yielding highly accurate and precise reconstructions.

To quantify uncertainty in our final analyses, I implement a robust block-bootstrap cross-validation scheme (Chapter 4) to derive confidence intervals for all downstream metrics, including model parameters and fitted values. This approach is particularly well suited for small, autocorrelated datasets with non-normal error structures (Ólafsdóttir and Mudelsee, 2014). Chapter 5 concludes the dissertation by summarizing the findings of Chapters 2–4 and contextualizing them within the broader landscape of high-resolution paleoclimatology.

Together, this body of work enhances both the spatial resolution and interpretive reliability of paleoclimate reconstructions derived from *A. borealis* and *Porites* spp., while also establishing a transferable framework for disentangling complex environmental signals across diverse oceanographic settings.

BIBLIOGRAPHY

C. Alibert, L. Kinsley, S. J. Fallon, M. T. McCulloch, R. Berkelmans, and F. McAllister. Source of trace element variability in great barrier reef corals affected by the burdekin flood plumes. *Geochim. Cosmochim. Acta*, 67:231–246, 2003. ISSN 0016-7037. doi: 10.1016/S0016-7037(02)01055-4.

O. Alizadeh. A review of enso teleconnections at present and under future global warming. *WIREs Clim. Change*, 15 (1):e861, 2024. ISSN 1757-7780. doi: 10.1002/wcc.861.

D. Allemand, C. Ferrier-Pagès, P. Furla, F. Houlbrèque, S. Puverel, S. Reynaud, Tambutté, S. Tambutté, and D. Zoccola. Biomineralisation in reef-building corals: from molecular mechanisms to environmental control. *C. R. Palevol*, 3:453–467, 2004. doi: 10.1016/j.crpv.2004.07.011.

N. Allison and A. A. Finch. Reproducibility of minor and trace element determinations in porites coral skeletons by secondary ion mass spectrometry. *Geochem. Geophys. Geosyst.*, 10(4), 2009. ISSN 1525-2027. doi: 10.1029/2008GC002239.

A. E. Alpert, A. L. Cohen, D. W. Oppo, T. M. DeCarlo, J. M. Gove, and C. W. Young. Comparison of equatorial pacific sea surface temperature variability and trends with sr/ca records from multiple corals. *Paleoceanography*, 31:252–265, 2016. doi: 10.1002/2015PA002897.

B. Alvarez Caraveo, M. Guillermic, A. Downey-Wall, L. P. Cameron, J. N. Sutton, J. A. Higgins, J. B. Ries, K. Lotterhos, and R. A. Eagle. Magnesium (mg/ca, 26mg), boron (b/ca, 11b), and calcium ([ca2+]) geochemistry of arctica islandica and crassostrea virginica extrapallial fluid and shell under ocean acidification. *EGUsphere*, 2024: 1–44, 2024. doi: 10.5194/egusphere-2024-1957.

A. D. Ansell. The rate of growth of the hard clam mercenaria mercenaria) throughout the geographical range. *ICES J. Mar. Sci.*, 31(3):364–409, 1968. ISSN 1054-3139. doi: 10.1093/icesjms/31.3.364.

W. S. Arnold, T. M. Bert, I. R. Quitmyer, and D. S. Jones. Contemporaneous deposition of annual growth bands in mercenaria mercenaria (linnaeus), mercenaria campechiensis (gmelin), and their natural hybrid forms. *J. Exp. Mar. Biol. Ecol.*, 223(1):93–109, 1998. ISSN 0022-0981. doi: 10.1016/S0022-0981(97)00152-4.

K. Ashok, S. K. Behera, S. A. Rao, H. Weng, and T. Yamagata. El niño modoki and its possible teleconnection. *J. Geophys. Res-Oceans*, 112(C11), 2007. ISSN 0148-0227. doi: 10.1029/2006JC003798.

D. J. Barnes. Coral skeletons: an explanation of their growth and structure. *Science*, 170:1305–1308, 1970. doi: 10.1126/science.170.3964.1305.

D. J. Barnes and J. M. Lough. On the nature and causes of density banding in massive coral skeletons. *J. Exp. Mar. Biol. Ecol.*, 167(1):91–108, 1993. ISSN 0022-0981. doi: 10.1016/0022-0981(93)90186-R.

A. R. Basu, S. B. Jacobsen, R. J. Poreda, C. B. Dowling, and P. K. Aggarwal. Large groundwater strontium flux to the oceans from the bengal basin and the marine strontium isotope record. *Science*, 293:1470–1473, 2001. doi: 10.1126/science.1060524.

J. H. Baumann, J. B. Ries, J. P. Rippe, T. A. Courtney, H. E. Aichelman, I. Westfield, and K. D. Castillo. Nearshore coral growth declining on the mesoamerican barrier reef system. *Glob. Change Biol.*, 25:3932–3945, 2019. doi: 10.1111/gcb.14784.

J. A. Beard, L. C. Ivany, and B. Runnegar. Gradients in seasonality and seawater oxygen isotopic composition along the early permian gondwanan coast, se australia. *Earth Planet. Sc. Lett.*, 425:219–231, 2015. ISSN 0012-821X. doi: 10.1016/j.epsl.2015.06.004.

R. E. Bernstein, P. R. Betzer, R. A. Feely, R. H. Byrne, M. F. Lamb, and A. F. Michaels. Acantharian fluxes and strontium to chlorinity ratios in the north pacific ocean. *Science*, 237:1490–1494, 1987. doi: 10.1126/science.237.4821.1490.

R. E. Bernstein, R. H. Byrne, P. R. Betzer, and A. M. Greco. Morphologies and transformations of celestite in seawater: The role of acantharians in strontium and barium geochemistry. *Geochim. Cosmochim. Acta*, 56(8):3273–3279, 1992. doi: 10.1016/0016-7037(92)90304-2.

A. G. Beu. Molluscan evidence of warm sea temperatures in new zealand during kapitean (late miocene) and waipipian (middle pliocene) time. *New Zeal. J. Geol. Geop.*, 17(2):465–479, 1974. ISSN 0028-8306. doi: 10.1080/00288306.1974.10430403.

A. Bolton, N. F. Goodkin, K. Hughen, D. R. Ostermann, S. T. Vo, and H. K. Phan. Paired porites coral sr/ca and 18o from the western south china sea: Proxy calibration of sea surface temperature and precipitation. *Palaeogeogr. Palaeocl.*, 410:233–243, 2014. ISSN 0031-0182. doi: 10.1016/j.palaeo.2014.05.047.

U. Brand. The oxygen and carbon isotope composition of carboniferous fossil components: sea-water effects. *Sedimentology*, 29(1):139–147, 1982. ISSN 0037-0746. doi: 10.1111/j.1365-3091.1982.tb01715.x.

G. F. N. Braniecki, D. Surge, E. G. Hyland, and D. H. Goodwin. Reconstructed seasonality during the mid piacenzian warm interval and early pleistocene cooling as recorded by growth temperatures from mercenaria shells. *Quat. Sci. Rev.*, 328:108524, 2024. ISSN 0277-3791. doi: 10.1016/j.quascirev.2024.108524.

S. R. Brennan, D. P. Fernandez, G. Mackey, T. E. Cerling, C. P. Bataille, G. J. Bowen, and M. J. Wooller. Strontium isotope variation and carbonate versus silicate weathering in rivers from across alaska: Implications for provenance studies. *Chem. Geol.*, 389:167–181, 2014. doi: 10.1016/j.chemgeo.2014.08.018.

P. G. Butler, C. A. Richardson, J. D. Scourse, A. D. Wanamaker, T. M. Shammon, and J. D. Bennell. Marine climate in the irish sea: analysis of a 489-year marine master chronology derived from growth increments in the shell of the clam arctica islandica. *Quat. Sci. Rev.*, 29(13):1614–1632, 2010. ISSN 0277-3791. doi: 10.1016/j.quascirev.2009.07.010.

S. Y. Cahyarini, M. Pfeiffer, O. Timm, W.-C. Dullo, and D. G. Schönberg. Reconstructing seawater 18o from paired coral 18o and sr/ca ratios: Methods, error analysis and problems, with examples from tahiti (french polynesia) and timor (indonesia). *Geochim. Cosmochim. Acta*, 72(12):2841–2853, 2008. ISSN 0016-7037. doi: 10.1016/j.gca.2008.04.005.

L. M. Cargnelli, S. J. Griesbach, D. B. Packer, and E. Weissberger. Atlantic surfclam, spisula solidissima, life history and habitat characteristics. Report, NOAA, 1999.

H. Cesar, L. Burke, and L. Pet-Soede. The economics of worldwide coral reef degradation. 2003.

D. Chan. Combining statistical, physical, and historical evidence to improve historical sea surface temperature records. *Harvard Data Science Review*, 3(1), 2021. doi: 10.1162/99608f92.edcee38f.

H. Clarke, J. P. D'Olivo, J. Falter, J. Zinke, R. Lowe, and M. McCulloch. Differential response of corals to regional mass-warming events as evident from skeletal sr/ca and mg/ca ratios. *Geochem. Geophys. Geosyst.*, 18(5):1794–1809, 2017. ISSN 1525-2027. doi: 10.1002/2016GC006788.

H. Clarke, J. P. D'Olivo, M. Conde, R. D. Evans, and M. T. McCulloch. Coral records of variable stress impacts and possible acclimatization to recent marine heat wave events on the northwest shelf of australia. *Paleoceanogr. Paleoclimatol.*, 34(11):1672–1688, 2019. ISSN 2572-4517. doi: 10.1029/2018PA003509.

K. M. Cobb, C. D. Charles, H. Cheng, and R. L. Edwards. El niño/southern oscillation and tropical pacific climate during the last millennium. *Nature*, 424:271, 2003. doi: 10.1038/nature01779.

J. E. Cole and R. G. Fairbanks. The southern oscillation recorded in the 18o of corals from tarawa atoll. *Paleoceanography and Paleoclimatology*, 5:669–683, 1990. doi: 10.1029/PA005i005p00669.

B. I. Cook, J. S. Mankin, K. Marvel, A. P. Williams, J. E. Smerdon, and K. J. Anchukaitis. Twenty-first century drought projections in the cmip6 forcing scenarios. *Earth's Future*, 8(6):e2019EF001461, 2020. doi: https://doi.org/10.1029/2019EF001461.

C. E. Cornwall, S. Comeau, N. A. Kornder, C. T. Perry, R. van Hooidonk, T. M. DeCarlo, M. S. Pratchett, K. D. Anderson, N. Browne, R. Carpenter, G. Diaz-Pulido, J. P. D'Olivo, S. S. Doo, J. Figueiredo, S. A. V. Fortunato, E. Kennedy, C. A. Lantz, M. T. McCulloch, M. González-Rivero, V. Schoepf, S. G. Smithers, and R. J. Lowe. Global declines in coral reef calcium carbonate production under ocean acidification and warming. *Proc. Natl. Acad. Sci. U.S.A.*, 118(21):e2015265118, 2021. doi: 10.1073/pnas.2015265118.

T. Corrège. Sea surface temperature and salinity reconstruction from coral geochemical tracers. *Palaeogeogr. Palaeoclimatol. Palaeoecol.*, 232:408–428, 2006. ISSN 0031-0182. doi: 10.1016/j.palaeo.2005.10.014.

K. Cowtan and R. G. Way. Coverage bias in the hadcrut4 temperature series and its impact on recent temperature trends. *Q. J. Roy. Meteor. Soc.*, 140:1935–1944, 2014. doi: 10.1002/qj.2297.

G. Crippa, L. Angiolini, C. Bottini, E. Erba, F. Felletti, C. Frigerio, J. A. I. Hennissen, M. J. Leng, M. R. Petrizzo, I. Raffi, G. Raineri, and M. H. Stephenson. Seasonality fluctuations recorded in fossil bivalves during the early pleistocene: Implications for climate change. *Palaeogeogr. Palaeocl.*, 446:234–251, 2016. ISSN 0031-0182. doi: 10.1016/j.palaeo.2016.01.029.

L. L. B. Davis, D. W. J. Thompson, J. J. Kennedy, and E. C. Kent. The importance of unresolved biases in twentieth-century sea surface temperature observations. *Bull. Amer. Meteor. Soc.*, 100(4):621–629, 2019. ISSN 0003-0007. doi: 10.1175/BAMS-D-18-0104.1.

E. de Boisséson, M. A. Balmaseda, and M. Mayer. Ocean heat content variability in an ensemble of twentieth century ocean reanalyses. *Clim. Dynam.*, 50(9):3783–3798, 2018. ISSN 1432-0894. doi: 10.1007/s00382-017-3845-0.

S. de Villiers. Seawater strontium and sr/ca variability in the atlantic and pacific oceans. *Earth Planet. Sc. Lett.*, 171: 623–634, 1999. ISSN 0012-821X. doi: 10.1016/S0012-821X(99)00174-0.

S. de Villiers, G. T. Shen, and B. K. Nelson. The sr/ca-temperature relationship in coralline aragonite: Influence of variability in (sr/ca) seawater and skeletal growth parameters. *Geochim. Cosmochim. Acta*, 58:197–208, 1994. doi: 10.1016/0016-7037(94)90457-X.

T. M. DeCarlo, G. A. Gaetani, A. L. Cohen, G. L. Foster, A. E. Alpert, and J. A. Stewart. Coral sr-u thermometry. *Paleoceanogr. Paleoclimatol.*, 31:626–638, 2016. doi: 10.1002/2015PA002908.

K. L. DeLong, J. A. Flannery, C. R. Maupin, R. Z. Poore, and T. M. Quinn. A coral sr/ca calibration and replication study of two massive corals from the gulf of mexico. *Palaeogeogr. Palaeoclimatol. Palaeoecol.*, 307:117–128, 2011. doi: 10.1016/j.palaeo.2011.05.005. Cailbration study shows that SidSids are great for intra and inter colony replication. Buoys are better than satellite data for temperature calibration in the Dry Tortugas.

K. L. DeLong, T. M. Quinn, F. W. Taylor, C. C. Shen, and K. Lin. Improving coral-base paleoclimate reconstructions by replicating 350 years of coral sr/ca variations. *Palaeogeogr. Palaeoclimatol. Palaeoecol.*, 373:6–24, 2013. ISSN 0031-0182. doi: 10.1016/j.palaeo.2012.08.019.

K. L. DeLong, C. R. Maupin, J. A. Flannery, T. M. Quinn, and C.-C. Shen. Refining temperature reconstructions with the atlantic coral siderastrea siderea. *Palaeogeogr. Palaeoclimatol. Palaeoecol.*, 462:1–15, 2016. doi: 10.1016/j.palaeo.2016.08.028.

T. L. Delworth and M. E. Mann. Observed and simulated multidecadal variability in the northern hemisphere. *Clim. Dynam.*, 16:661–676, 2000. doi: 10.1007/s003820000075.

D. L. Dettman, A. K. Reische, and K. C. Lohmann. Controls on the stable isotope composition of seasonal growth bands in aragonitic fresh-water bivalves (unionidae). *Geochim. Cosmochim. Acta*, 63(7):1049–1057, 1999. ISSN 0016-7037. doi: 10.1016/S0016-7037(99)00020-4.

F. R. S. Dittmar. On alkali-proof vessels. *J. Soc. Chem. Ind.*, 3(5):303–307, 1884. ISSN 0368-4075. doi: 10.1002/jctb.5000030510.

J. P. D'Olivo, D. J. Sinclair, K. Rankenburg, and M. T. McCulloch. A universal multi-trace element calibration for reconstructing sea surface temperatures from long-lived porites corals: Removing 'vital-effects'. *Geochim. Cosmochim. Acta*, 239:109–135, 2018. doi: 10.1016/j.gca.2018.07.035.

M. G. Donat, L. V. Alexander, H. Yang, I. Durre, R. Vose, R. J. H. Dunn, K. M. Willett, E. Aguilar, M. Brunet, J. Caesar, B. Hewitson, C. Jack, A. M. G. Klein Tank, A. C. Kruger, J. Marengo, T. C. Peterson, M. Renom, C. Oria Rojas, M. Rusticucci, J. Salinger, A. S. Elrayah, S. S. Sekele, A. K. Srivastava, B. Trewin, C. Villarroel, L. A. Vincent, P. Zhai, X. Zhang, and S. Kitching. Updated analyses of temperature and precipitation extreme indices since the beginning of the twentieth century: The hadex2 dataset. *J. Geophys. Res-Atmospheres*, 118(5): 2098–2118, 2013. ISSN 2169-897X. doi: 10.1002/jgrd.50150.

H. Douville, K. Raghavan, J. Renwick, R. P. Allan, P. A. Arias, M. Barlow, R. Cerezo-Mota, A. Cherchi, T. Y. Gan, J. Gergis, D. Jiang, A. Khan, W. Pokam Mba, D. Rosenfeld, J. Tierney, and O. Zolina. *Water Cycle Changes*, page 1055–1210. Cambridge University Press, Cambridge, United Kingdom and New York, NY, USA, 2021. doi: 10.1017/9781009157896.010.

J. P. D'Olivo and M. T. McCulloch. Response of coral calcification and calcifying fluid composition to thermally induced bleaching stress. *Scientific reports*, 7:2207, 2017. doi: 10.1038/s41598-017-02306-x.

M. Elliot, P. B. deMenocal, B. K. Linsley, and S. S. Howe. Environmental controls on the stable isotopic composition of mercenaria mercenaria: Potential application to paleoenvironmental studies. *Geochem. Geophys. Geosyst.*, 4(7):1–16, 2003. ISSN 1525-2027. doi: 10.1029/2002GC000425.

M. Elliot, K. Welsh, C. Chilcott, M. McCulloch, J. Chappell, and B. Ayling. Profiles of trace elements and stable isotopes derived from giant long-lived tridacna gigas bivalves: Potential applications in paleoclimate studies. *Palaeogeogr. Palaeocl.*, 280(1):132–142, 2009. ISSN 0031-0182. doi: 10.1016/j.palaeo.2009.06.007.

C. Emiliani. Pleistocene temperatures. *J. Geol.*, 63(6):538–578, 1955. doi: 10.1086/626295.

S. Epstein, R. Buchsbaum, H. Lowenstam, and H. C. Urey. Carbonate-water isotopic temperature scale. *GSA Bulletin*, 62(4):417–426, 1951. ISSN 0016-7606. doi: 10.1130/0016-7606(1951)62[417:Cits]2.0.Co;2.

R. G. Fairbanks, C. D. Charles, and J. D. Wright. Origin of global meltwater pulses, 1992.

P. G. Falkowski, Z. Dubinsky, L. Muscatine, and J. W. Porter. Light and the bioenergetics of a symbiotic coral. *BioScience*, 34(11):705–709, 1984. ISSN 0006-3568. doi: 10.2307/1309663.

T. Felis, J. Pätzold, Y. Loya, M. Fine, A. H. Nawar, and G. Wefer. A coral oxygen isotope record from the northern red sea documenting nao, enso, and north pacific teleconnections on middle east climate variability since the year 1750. *Paleoceanography*, 15:679–694, 2000. doi: 10.1029/1999PA000477.

D. L. Ficklin, S. E. Null, J. T. Abatzoglou, K. A. Novick, and D. T. Myers. Hydrological intensification will increase the complexity of water resource management. *Earth's Future*, 10(3):e2021EF002487, 2022. doi: https://doi.org/10.1029/2021EF002487.

G. Forchhammer and E. Sabine. Iv. on the composition of sea-water in the different parts of the ocean. *Philos. T. R. Soc. Lond.*, 155:203–262, 1865. doi: 10.1098/rstl.1865.0004.

S. E. Fowell, K. Sandford, J. A. Stewart, K. D. Castillo, J. B. Ries, and G. L. Foster. Intrareef variations in li/mg and sr/ca sea surface temperature proxies in the caribbean reef-building coral siderastrea siderea. *Paleoceanography*, 31:1315–1329, 2016. doi: 10.1002/2016PA002968.

E. Freeman, S. D. Woodruff, S. J. Worley, S. J. Lubker, E. C. Kent, W. E. Angel, D. I. Berry, P. Brohan, R. Eastman, L. Gates, W. Gloeden, Z. Ji, J. Lawrimore, N. A. Rayner, G. Rosenhagen, and S. R. Smith. Icoads release 3.0: a major update to the historical marine climate record. *Int. Jour. Climat.*, 37:2211–2232, 2017. doi: 10.1002/joc.4775.

L. W. Fritz. *Chapter 2 Shell structure and age determination*, volume 31, pages 53–76. Elsevier, Amsterdam, 2001. ISBN 0167-9309. doi: https://doi.org/10.1016/S0167-9309(01)80030-2.

G. A. Gaetani, A. L. Cohen, Z. Wang, and J. Crusius. Rayleigh-based, multi-element coral thermometry: A biomineralization approach to developing climate proxies. *Geochim. Cosmochim. Acta*, 75:1920–1932, 2011. doi: 10.1016/j.gca.2011.01.010.

C. Garcia-Soto, L. Cheng, L. Caesar, S. Schmidtko, E. B. Jewett, A. Cheripka, I. Rigor, A. Caballero, S. Chiba, J. C. Báez, T. Zielinski, and J. P. Abraham. An overview of ocean climate change indicators: Sea surface temperature, ocean heat content, ocean ph, dissolved oxygen concentration, arctic sea ice extent, thickness and volume, sea level and strength of the amoc (atlantic meridional overturning circulation). *Front. Mar. Sci.*, Volume 8 - 2021, 2021. ISSN 2296-7745. doi: 10.3389/fmars.2021.642372.

D. P. Gillikin, A. Lorrain, S. Bouillon, P. Willenz, and F. Dehairs. Stable carbon isotopic composition of mytilus edulis shells: relation to metabolism, salinity, 13cdic and phytoplankton. *Organic Geochemistry*, 37(10):1371–1382, 2006. ISSN 0146-6380. doi: 10.1016/j.orggeochem.2006.03.008.

D. H. Goodwin, B. R. SchoNe, and D. L. Dettman. Resolution and fidelity of oxygen isotopes as paleotemperature proxies in bivalve mollusk shells: Models and observations. *PALAIOS*, 18(2):110–125, 2003. ISSN 0883-1351. doi: 10.1669/0883-1351(2003)18⟨110:RAFOOI⟩2.0.CO;2.

E. Gosling. *Bivalve molluscs: biology, ecology and culture*. John Wiley Sons, 2008. ISBN 1405147571.

E. L. Grossman and T.-L. Ku. Oxygen and carbon isotope fractionation in biogenic aragonite: Temperature effects. *Chem. Geol.*, 59:59–74, 1986. ISSN 0168-9622. doi: 10.1016/0168-9622(86)90057-6.

C. A. Grove, S. Kasper, J. Zinke, M. Pfeiffer, D. Garbe-Schönberg, and G. A. Brummer. Confounding effects of coral growth and high sst variability on skeletal sr/ca: Implications for coral paleothermometry. *Geochem. Geophys. Geosyst.*, 14:1277–1293, 2013. doi: 10.1002/ggge.20095.

M. E. Harte. *Chapter 1 Systematics and taxonomy*, volume 31, pages 3–51. Elsevier, 2001. ISBN 0167-9309. doi: 10.1016/S0167-9309(01)80029-6.

E. C. Hathorne, T. Felis, A. Suzuki, H. Kawahata, and G. Cabioch. Lithium in the aragonite skeletons of massive porites corals: A new tool to reconstruct tropical sea surface temperatures. *Paleoceanography*, 28:143–152, 2013. doi: 10.1029/2012PA002311.

Z. Hausfather, H. F. Drake, T. Abbott, and G. A. Schmidt. Evaluating the performance of past climate model projections. *Geophys. Res. Lett.*, 47(1):e2019GL085378, 2020. ISSN 0094-8276. doi: 10.1029/2019GL085378.

J. P. Hawkins and C. M. Roberts. Effects of recreational scuba diving on coral reefs: Trampling on reef-flat communities. *J. Appl. Ecol.*, 30(1):25–30, 1993. ISSN 00218901, 13652664. doi: 10.2307/2404267.

S. Hetzinger, M. Pfeiffer, W.-C. Dullo, N. Keenlyside, M. Latif, and J. Zinke. Caribbean coral tracks atlantic multidecadal oscillation and past hurricane activity. *Geology*, 36:11–14, 2008. doi: 10.1130/G24321A.1.

S. Hetzinger, M. Pfeiffer, W.-C. Dullo, J. Zinke, and D. Garbe-Schönberg. A change in coral extension rates and stable isotopes after el niño-induced coral bleaching and regional stress events. *Sci. Rep.*, 6:32879, 2016. doi: 10.1038/srep32879.

S. Hirabayashi, Y. Yokoyama, A. Suzuki, Y. Kawakubo, Y. Miyairi, T. Okai, and S. Nojima. Coral growth-rate insensitive sr/ca as a robust temperature recorder at the extreme latitudinal limits of porites. *Geochem. J.*, 47:e1–e5, 2013. doi: 10.2343/geochemj.2.0259.

Y. Horibe, K. Endo, and H. Tsubota. Calcium in the south pacific, and its correlation with carbonate alkalinity. *Earth Planet. Sc. Lett.*, 23:136–140, 1974. doi: 10.1016/0012-821X(74)90040-5.

B. Huang, P. W. Thorne, V. F. Banzon, T. Boyer, G. Chepurin, J. H. Lawrimore, M. J. Menne, T. M. Smith, R. S. Vose, and H.-M. Zhang. Extended reconstructed sea surface temperature, version 5 (ersstv5): upgrades, validations, and intercomparisons. *J. Clim.*, 30:8179–8205, 2017. doi: 10.1175/jcli-d-16-0836.1.

J. Huang and R. Zhang. The mineralization of molluscan shells: Some unsolved problems and special considerations. *Front. Mar. Sci.*, Volume 9 - 2022, 2022. ISSN 2296-7745. doi: 10.3389/fmars.2022.874534.

D. K. Hubbard. *Reef Drilling*, pages 856–869. Springer Netherlands, Dordrecht, 2011. ISBN 978-90-481-2639-2. doi: 10.1007/978-90-481-2639-2_54.

H. P. Hughes, D. Surge, I. J. Orland, M. L. Zettler, and D. K. Moss. Seasonal sims 18o record in astarte borealis from the baltic sea tracks a modern regime shift in the nao. *Frontiers in Marine Science*, 10, 2023. ISSN 2296-7745. doi: 10.3389/fmars.2023.1293823.

T. P. Hughes, J. T. Kerry, A. H. Baird, S. R. Connolly, A. Dietzel, C. M. Eakin, S. F. Heron, A. S. Hoey, M. O. Hoogenboom, and G. Liu. Global warming transforms coral reef assemblages. *Nature*, 556:492, 2018. doi: 10.1038/s41586-018-0041-2.

L. Ivany and B. Runnegar. Early permian seasonality from bivalve 18o and implications for the oxygen isotopic composition of seawater. *Geology*, 38(11):1027–1030, 2010. ISSN 0091-7613. doi: 10.1130/g31330.1.

M. Y. Jimenez, L. C. Ivany, E. J. Judd, and G. Henkes. Low and seasonally variable salinity in the pennsylvanian equatorial appalachian basin. *Earth Planet. Sc. Lett.*, 519:182–191, 2019. ISSN 0012-821X. doi: 10.1016/j.epsl.2019.04.051.

D. S. Jones and I. R. Quitmyer. Marking time with bivalve shells: Oxygen isotopes and season of annual increment formation. *PALAIOS*, 11(4):340–346, 1996. ISSN 08831351, 19385323. doi: 10.2307/3515244.

P. D. Jones, K. R. Briffa, T. J. Osborn, J. M. Lough, T. D. van Ommen, B. M. Vinther, J. Luterbacher, E. R. Wahl, F. W. Zwiers, M. E. Mann, G. A. Schmidt, C. M. Ammann, B. M. Buckley, K. M. Cobb, J. Esper, H. Goosse, N. Graham, E. Jansen, T. Kiefer, C. Kull, M. Kuttel, E. Mosley-Thompson, J. T. Overpeck, N. Riedwyl, M. Schulz, A. W. Tudhope, R. Villalba, H. Wanner, E. Wolff, and E. Xoplaki. High-resolution palaeoclimatology of the last millennium: a review of current status and future prospects. *The Holocene*, 19:3–49, 2009. doi: 10.1177/0959683608098952.

D. C. Jose and H. Michael JR. Stable isotope geochemistry of corals from costa rica as proxy indicator of the el nino/southern oscilation (enso). *Geochim. Cosmochim. Acta*, 58:335–351, 1994. doi: 10.1016/0016-7037(94)90468-5.

J. J. Kennedy. A review of uncertainty in in situ measurements and data sets of sea surface temperature. *Rev. Geophys.*, 52:1–32, 2014. doi: 10.1002/2013RG000434.

J. J. Kennedy, N. A. Rayner, R. O. Smith, D. E. Parker, and M. Saunby. Reassessing biases and other uncertainties in sea surface temperature observations measured in situ since 1850: 2. biases and homogenization. *J. Geophys. Res.*, 116:D14104, 2011. doi: 10.1029/2010JD015220.

E. C. Kent, J. J. Kennedy, T. M. Smith, S. Hirahara, B. Huang, A. Kaplan, D. E. Parker, C. P. Atkinson, D. I. Berry, G. Carella, Y. Fukuda, M. Ishii, P. D. Jones, F. Lindgren, C. J. Merchant, S. Morak-Bozzo, N. A. Rayner, V. Venema, S. Yasui, and H.-M. Zhang. A call for new approaches to quantifying biases in observations of sea surface temperature. *Bull. Amer. Meteor. Soc.*, 98(8):1601–1616, 2017. ISSN 0003-0007. doi: 10.1175/BAMS-D-15-00251.1.

A. Khare, H. P. Hughes, K. H. Kilbourne, and J. Schijf. An icp-aes method for routine high-precision measurement of seawater sr/ca ratios to validate coral paleothermometry calibrations. *Limnol. Oceanogr. Methods*, 19:416–430, 2021. doi: 10.1002/lom3.10434.

A. Khare, H. P. Hughes, J. Schijf, and K. H. Kilbourne. Apparently seasonal variations of the seawater sr/ca ratio across the florida keys reef tract. *Geochem. Geophys. Geosyst.*, 24(3):e2022GC010728, 2023. doi: 10.1029/2022GC010728.

M. Khaska, C. L. G. La Salle, J. Lancelot, A. Mohamad, P. Verdoux, A. Noret, and R. Simler. Origin of groundwater salinity (current seawater vs. saline deep water) in a coastal karst aquifer based on sr and cl isotopes. case study of the la clape massif (southern france). *Appl. Geochem.*, 37:212–227, 2013. doi: 10.1016/j.apgeochem.2013.07.006.

K. H. Kilbourne, T. M. Quinn, and F. W. Taylor. A fossil coral perspective on western tropical pacific climate 350 ka. *Paleoceanography*, 19(1), 2004a. ISSN 0883-8305. doi: 10.1029/2003PA000944.

K. H. Kilbourne, T. M. Quinn, F. W. Taylor, T. Delcroix, and Y. Gouriou. El nino-southern oscillation-related salinity variations recorded in the skeletal geochemistry of a porites coral from espiritu santo, vanuatu. *Paleoceanography*, 19:1–8, 2004b. ISSN 0883-8305. doi: 10.1029/2004PA001033.

R. T. Klein, K. C. Lohmann, and C. W. Thayer. Bivalve skeletons record sea-surface temperature and 18o via mg/ca and 18o/16o ratios. *Geology*, 24(5):415–418, 1996. ISSN 0091-7613. doi: 10.1130/0091-7613(1996)024⟨0415:Bsrsst⟩2.3.Co;2.

J. A. Kleypas, J. W. McManus, and L. A. B. Menez. Environmental limits to coral reef development: where do we draw the line? *Am. Zool.*, 39:146–159, 1999. doi: 10.1093/icb/39.1.146.

D. W. Knutson, R. W. Buddemeier, and S. V. Smith. Coral chronometers: seasonal growth bands in reef corals. *Science*, 177:270–272, 1972. doi: 10.1126/science.177.4045.270.

H. Krawczyk, J. Zinke, N. Browne, U. Struck, J. McIlwain, M. O'Leary, and D. Garbe-Schönberg. Corals reveal enso-driven synchrony of climate impacts on both terrestrial and marine ecosystems in northern borneo. *Sci. Rep.*, 10(1):3678, 2020. ISSN 2045-2322. doi: 10.1038/s41598-020-60525-1.

M. Kucera. *Chapter Six Planktonic Foraminifera as Tracers of Past Oceanic Environments*, volume 1, pages 213–262. Elsevier, 2007. ISBN 1572-5480. doi: 10.1016/S1572-5480(07)01011-1.

I. B. Kuffner, P. L. Jokiel, K. S. Rodgers, A. J. Andersson, and F. T. Mackenzie. An apparent "vital effect" of calcification rate on the sr/ca temperature proxy in the reef coral montipora capitata. *Geochem. Geophys. Geosyst.*, 13:Q08004, 2012. doi: 10.1029/2012GC004128.

K. D. Lafferty. The ecology of climate change and infectious diseases. *Ecology*, 90(4):888–900, 2009. ISSN 0012-9658. doi: 10.1890/08-0079.1.

A. N. LeGrande and G. A. Schmidt. Global gridded data set of the oxygen isotopic composition in seawater. *Geophys. Res. Lett.*, 33(12), 2006. ISSN 0094-8276. doi: 10.1029/2006GL026011.

B. K. Linsley, G. M. Wellington, D. P. Schrag, L. Ren, M. J. Salinger, and A. W. Tudhope. Geochemical evidence from corals for changes in the amplitude and spatial pattern of south pacific interdecadal climate variability over the last 300 years. *Clim. Dynam.*, 22(1):1–11, 2004. ISSN 1432-0894. doi: 10.1007/s00382-003-0364-y.

L. E. Lisiecki and M. E. Raymo. A pliocene-pleistocene stack of 57 globally distributed benthic 18o records. *Paleoceanography*, 20(1), 2005. ISSN 0883-8305. doi: 10.1029/2004PA001071.

K. A. Lubarsky, N. J. Silbiger, and M. J. Donahue. Effects of submarine groundwater discharge on coral accretion and bioerosion on two shallow reef flats. *Limnol. Oceanogr.*, 63:1660–1676, 2018. doi: 10.1002/lno.10799.

J. I. Macdonald and D. A. Crook. Variability in sr: Ca and ba: Ca ratios in water and fish otoliths across an estuarine salinity gradient. *Mar. Ecol. Prog. Ser.*, 413:147–161, 2010. doi: 10.3354/meps08703.

M. E. Mann, Z. Zhang, S. Rutherford, R. S. Bradley, M. K. Hughes, D. Shindell, C. Ammann, G. Faluvegi, and F. Ni. Global signatures and dynamical origins of the little ice age and medieval climate anomaly. *Science*, 326:1256–1260, 2009. doi: 10.1126/science.1177303.

I. Manolis, C. Makropoulos, A. Sfetsos, and A. Skouloudis. Development and application of a methodological framework for assessing the resilience of military infrastructure against climate change impacts. *E3S Web Conf.*, 585:01018, 2024. doi: 10.1051/e3sconf/202458501018.

V. Masson-Delmotte, M. Schulz, A. Abe-Ouchi, J. Beer, A. Ganopolski, J. F. González Rouco, E. Jansen, K. Lambeck, J. Luterbacher, T. Naish, T. Osborn, B. Otto-Bliesner, T. Quinn, R. Ramesh, M. Rojas, X. Shao, and A. Timmermann. Information from paleoclimate archives. Report, Cambridge University Press, 2013.

M. T. McCulloch, J. P. D'Olivo, J. Falter, M. Holcomb, and J. A. Trotter. Coral calcification in a changing world and the interactive dynamics of ph and dic upregulation. *Nat. Commun.*, 8:15686, 2017. doi: 10.1038/ncomms15686.

W. G. Mook and J. C. Vogel. Isotopic equilibrium between shells and their environment. *Science*, 159(3817):874–875, 1968. doi: 10.1126/science.159.3817.874.

D. K. Moss, L. C. Ivany, E. J. Judd, P. W. Cummings, C. E. Bearden, W.-J. Kim, E. G. Artruc, and J. R. Driscoll. Lifespan, growth rate, and body size across latitude in marine bivalvia, with implications for phanerozoic evolution. *Proc. R. Soc. Lond.*, 283(1836):20161364, 2016. doi: 10.1098/rspb.2016.1364.

M. Mudelsee, T. Bickert, C. H. Lear, and G. Lohmann. Cenozoic climate changes: A review based on time series analysis of marine benthic 18o records. *Rev. Geophys.*, 52(3):333–374, 2014. ISSN 8755-1209. doi: 10.1002/2013RG000440.

N. Muehllehner, C. Langdon, A. Venti, and D. Kadko. Dynamics of carbonate chemistry, production, and calcification of the florida reef tract (2009–2010): Evidence for seasonal dissolution. *Global Biogeochem. Cy.*, 30:661–688, 2016. doi: 10.1002/2015GB005327.

L. Muscatine and J. W. Porter. Reef corals: Mutualistic symbioses adapted to nutrient-poor environments. *BioScience*, 27(7):454–460, 1977. ISSN 0006-3568. doi: 10.2307/1297526.

P. A. O'Gorman. Precipitation extremes under climate change. *Curr. Clim. Change Rep.*, 1(2):49–59, 2015. ISSN 2198-6061. doi: 10.1007/s40641-015-0009-3.

M. S. Pratchett, K. D. Anderson, M. O. Hoogenboom, E. Widman, A. H. Baird, J. M. Pandolfi, P. J. Edmunds, and J. Lough. *Spatial, Temporal and Taxonomic Variation in Coral Growth—Implications for the Structure and Function of Coral Reef Ecosystems*, pages 187–212. CRC Press, 2015. doi: 10.1201/b18733-8.

I. R. Quitmyer, D. S. Jones, and W. S. Arnold. The sclerochronology of hard clams,mercenariaspp., from the south-eastern u.s.a.: A method of elucidating the zooarchaeological records of seasonal resource procurement and seasonality in prehistoric shell middens. *J. Archaeol. Sci.*, 24(9):825–840, 1997. ISSN 0305-4403. doi: 10.1006/jasc.1996.0163.

L. J. Raymundo, W. L. Licuanan, and A. M. Kerr. Adding insult to injury: Ship groundings are associated with coral disease in a pristine reef. *PLoS ONE*, 13(9):e0202939, 2018. doi: 10.1371/journal.pone.0202939.

E. V. Reed, D. M. Thompson, J. E. Cole, J. M. Lough, N. E. Cantin, A. H. Cheung, A. Tudhope, L. Vetter, G. Jimenez, and R. L. Edwards. Impacts of coral growth on geochemistry: Lessons from the galápagos islands. *Paleoceanogr. Paleoclimatol.*, 36(4):e2020PA004051, 2021. ISSN 2572-4517. doi: 10.1029/2020PA004051.

D. J. Reynolds, V. R. von Biela, K. H. Dunton, D. C. Douglas, and B. A. Black. Sclerochronological records of environmental variability and bivalve growth in the pacific arctic. *Prog. Oceanogr.*, 206:102864, 2022. ISSN 0079-6611. doi: 10.1016/j.pocean.2022.102864.

E. J. Rohling. *Oxygen Isotope Composition of Seawater*, volume 2, pages 915–922. Elsevier, Amsterdam, 2013.

C. L. Ross, T. M. DeCarlo, and M. T. McCulloch. Calibration of sr/ca, li/mg and sr-u paleothermometry in branching and foliose corals. *Paleoceanography and Paleoclimatology*, 34:1271–1291, 2019. doi: 10.1029/2018PA003426.

J. Sadler, G. E. Webb, L. D. Nothdurft, and B. Dechnik. Geochemistry-based coral palaeoclimate studies and the potential of 'non-traditional' (non-massive porites) corals: Recent developments and future progression. *Earth-Sci. Rev.*, 139:291–316, 2014. ISSN 0012-8252. doi: 10.1016/j.earscirev.2014.10.002.

C. Saenger and Z. Wang. Magnesium isotope fractionation in biogenic and abiogenic carbonates: implications for paleoenvironmental proxies. *Quaternary Sci. Rev.*, 90:1–21, 2014. ISSN 0277-3791. doi: 10.1016/j.quascirev.2014.01.014.

H. R. Sayani, K. M. Cobb, K. DeLong, N. T. Hitt, and E. R. M. Druffel. Intercolony 18o and sr/ca variability among porites spp. corals at palmyra atoll: Toward more robust coral-based estimates of climate. *Geochem. Geophys. Geosyst.*, 20(11):5270–5284, 2019. ISSN 1525-2027. doi: 10.1029/2019GC008420.

H. R. Sayani, D. M. Thompson, J. E. Carilli, T. M. Marchitto, A. U. Chapman, and K. M. Cobb. Reproducibility of coral mn/ca-based wind reconstructions at kiritimati island and butaritari atoll. *Geochem. Geophys. Geosyst.*, 22 (3):e2020GC009398, 2021. ISSN 1525-2027. doi: 10.1029/2020GC009398.

R. W. Schmitt. The ocean's role in climate. *Oceanography*, 31(2):32–40, 2018. ISSN 10428275, 2377617X.

K. Schneider, O. Levy, Z. Dubinsky, and J. Erez. In situ diel cycles of photosynthesis and calcification in hermatypic corals. *Limnol. Oceanogr.*, 54:1995–2002, 2009. doi: 10.4319/lo.2009.54.6.1995.

D. P. Schrag. Rapid analysis of high-precision sr/ca ratios in corals and other marine carbonates. *Paleoceanography*, 14:97–102, 1999. doi: 10.1029/1998PA900025.

A. P. Schurer, M. E. Mann, E. Hawkins, S. F. B. Tett, and G. C. Hegerl. Importance of the pre-industrial baseline for likelihood of exceeding paris goals. *Nat. Clim. Change*, 7(8):563–567, 2017. ISSN 1758-6798. doi: 10.1038/nclimate3345.

B. R. Schöne. Arctica islandica (bivalvia): A unique paleoenvironmental archive of the northern north atlantic ocean. *Global Planet. Change*, 111:199–225, 2013. ISSN 0921-8181. doi: 10.1016/j.gloplacha.2013.09.013.

B. R. Schöne and D. P. Gillikin. Unraveling environmental histories from skeletal diaries — advances in sclerochronology. *Palaeogeogr. Palaeocl.*, 373:1–5, 2013. ISSN 0031-0182. doi: 10.1016/j.palaeo.2012.11.026.

N. N. O. Service. What are zooxanthellae?, 2024a.

N. N. O. Service. Where are coral reefs found?, 2024b.

N. J. Shackleton and R. K. Matthews. Oxygen isotope stratigraphy of late pleistocene coral terraces in barbados. *Nature*, 268:618–620, 1977. doi: 10.1038/268618a0.

D. J. Sinclair. Rbme coral temperature reconstruction: An evaluation, modifications, and recommendations. *Geochim. Cosmochim. Acta*, 154:66–80, 2015. ISSN 0016-7037. doi: 10.1016/j.gca.2015.01.006.

D. J. Sinclair, B. Williams, and M. Risk. A biological origin for climate signals in corals—trace element "vital effects" are ubiquitous in scleractinian coral skeletons. *Geophys. Res. Lett.*, 33:L17707, 2006. doi: 10.1029/2006GL027183.

S. V. Smith, R. W. Buddemeier, R. C. Redalje, and J. E. Houck. Strontium-calcium thermometry in coral skeletons. *Science*, 204:404–407, 1979. doi: 10.1126/science.204.4391.404.

M. Spalding, L. Burke, S. A. Wood, J. Ashpole, J. Hutchison, and P. zu Ermgassen. Mapping the global value and distribution of coral reef tourism. *Mar. Policy*, 82:104–113, 2017. ISSN 0308-597X. doi: 10.1016/j.marpol.2017.05.014.

J. C. Stalker, R. M. Price, and P. K. Swart. Determining spatial and temporal inputs of freshwater, including submarine groundwater discharge, to a subtropical estuary using geochemical tracers, biscayne bay, south florida. *Estuaries Coasts*, 32:694–708, 2009. doi: 10.1007/s12237-009-9155-y.

C. D. Standish, J. Trend, J. Kleboe, T. B. Chalk, S. Mahajan, J. A. Milton, T. M. Page, L. F. Robinson, J. A. Stewart, and G. L. Foster. Correlative geochemical imaging of desmophyllum dianthus reveals biomineralisation strategy as a key coral vital effect. *Sci. Rep.*, 14(1):11121, 2024. ISSN 2045-2322. doi: 10.1038/s41598-024-61772-2.

N. J. Steiger and J. E. Smerdon. A pseudoproxy assessment of data assimilation for reconstructing the atmosphere–ocean dynamics of hydroclimate extremes. *Clim. Past*, 13:1435–1449, 2017. doi: 10.5194/cp-13-1435-2017.

N. J. Steiger, J. E. Smerdon, E. R. Cook, and B. I. Cook. A reconstruction of global hydroclimate and dynamical variables over the common era. *Nature Sci. Data*, 5(1):5:180086, 2018. doi: 10.1038/sdata.2018.86.

C. L. Stephans, T. M. Quinn, F. W. Taylor, and T. Corrège. Assessing the reproducibility of coral-based climate records. *Geophys. Res. Lett.*, 31(18), 2004. ISSN 0094-8276. doi: 10.1029/2004GL020343.

J. A. Stewart, L. F. Robinson, R. D. Day, I. Strawson, A. Burke, J. W. B. Rae, P. T. Spooner, A. Samperiz, P. J. Etnoyer, B. Williams, A. Paytan, M. J. Leng, V. Häussermann, L. N. Wickes, R. Bratt, and H. Pryer. Refining trace metal temperature proxies in cold-water scleractinian and stylasterid corals. *Earth Planet. Sc. Lett.*, 545:116412, 2020. ISSN 0012-821X. doi: 10.1016/j.epsl.2020.116412.

F. Strauch. Determination of cenozoic sea-temperatures using hiatella arctica (linné). *Palaeogeogr. Palaeocl.*, 5(2): 213–233, 1968. ISSN 0031-0182. doi: 10.1016/0031-0182(68)90115-6.

D. M. Surge and K. C. Lohmann. Temporal and spatial differences in salinity and water chemistry in sw florida estuaries: effects of human-impacted watersheds. *Estuaries*, 25:393–408, 2002. doi: 10.1007/BF02695982.

D. M. Surge and B. R. Schöne. *Bivalve sclerochronology*, pages 108–115. Springer Netherlands, Berlin-Heidelberg, 2015. doi: 10.1007/978-94-007-6326-5_165-1.

D. M. Thompson. Environmental records from coral skeletons: A decade of novel insights and innovation. *WIREs Clim. Change*, 13(1):e745, 2021. ISSN 1757-7780. doi: 10.1002/wcc.745.

D. M. Thompson, T. R. Ault, M. N. Evans, J. E. Cole, and J. Emile-Geay. Comparison of observed and simulated tropical climate trends using a forward model of coral 18o. *Geophys. Res. Lett.*, 38:L14706, 2011. doi: 10.1029/2011GL048224.

J. E. Tierney, C. J. Poulsen, I. P. Montañez, T. Bhattacharya, R. Feng, H. L. Ford, B. Hönisch, G. N. Inglis, S. V. Petersen, N. Sagoo, C. R. Tabor, K. Thirumalai, J. Zhu, N. J. Burls, G. L. Foster, Y. Goddéris, B. T. Huber, L. C. Ivany, S. Kirtland Turner, D. J. Lunt, J. C. McElwain, B. J. W. Mills, B. L. Otto-Bliesner, A. Ridgwell, and Y. G. Zhang. Past climates inform our future. *Science*, 370(6517):eaay3701, 2020. doi: 10.1126/science.aay3701.

K. E. Trenberth and J. T. Fasullo. Tracking earth's energy: From el niño to global warming. *Surv. Geophys.*, 33(3): 413–426, 2012. ISSN 1573-0956. doi: 10.1007/s10712-011-9150-2.

H. C. Urey. The thermodynamic properties of isotopic substances. *J. Chem. Soc.*, (0):562–581, 1947. ISSN 0368-1769. doi: 10.1039/JR9470000562.

J. W. van Dam, A. P. Negri, S. Uthicke, and J. F. Mueller. *Chemical pollution on coral reefs: exposure and ecological effects*, book section 9, pages 187–211. Bentham Science Publishers Ltd., 2011.

J. A. J. M. van de Water, W. Leggat, D. G. Bourne, M. J. H. van Oppen, B. L. Willis, and T. D. Ainsworth. Elevated seawater temperatures have a limited impact on the coral immune response following physical damage. *Hydrobiologia*, 759(1):201–214, 2015. ISSN 1573-5117. doi: 10.1007/s10750-015-2243-z.

J. E. N. Veron. *Corals of the World*. 2000. ISBN 0642322368.

S. VijayaVenkataRaman, S. Iniyan, and R. Goic. A review of climate change, mitigation and adaptation. *Renew. Sust. Energ. Rev.*, 16(1):878–897, 2012. ISSN 1364-0321. doi: 10.1016/j.rser.2011.09.009.

R. M. Walter, H. R. Sayani, T. Felis, K. M. Cobb, N. J. Abram, A. K. Arzey, A. R. Atwood, L. D. Brenner, P. Dassié, K. L. DeLong, B. Ellis, J. Emile-Geay, M. J. Fischer, N. F. Goodkin, J. A. Hargreaves, K. H. Kilbourne, H. Krawczyk, N. P. McKay, A. L. Moore, S. A. Murty, M. R. Ong, R. D. Ramos, E. V. Reed, D. Samanta, S. C. Sanchez, J. Zinke, and P. C. k. P. M. the. The coralhydro2k database: a global, actively curated compilation of coral 18o and srthinsp;thinsp;ca proxy records of tropical ocean hydrology and temperature for the common era. *Earth Syst. Sci. Data*, 15(5):2081–2116, 2023. ISSN 1866-3516. doi: 10.5194/essd-15-2081-2023.

A. D. Wanamaker, P. G. Butler, J. D. Scourse, J. Heinemeier, J. Eiríksson, K. L. Knudsen, and C. A. Richardson. Surface changes in the north atlantic meridional overturning circulation during the last millennium. *Nat. Commun.*, 3:899, 2012. doi: 10.1038/ncomms1901.

C. Wang. Three-ocean interactions and climate variability: a review and perspective. *Clim. Dynam.*, 53(7):5119–5136, 2019. ISSN 1432-0894. doi: 10.1007/s00382-019-04930-x.

T. Wang, D. Surge, and K. J. Walker. Isotopic evidence for climate change during the vandal minimum from ariopsis felis otoliths and mercenaria campechiensis shells, southwest florida, usa. *The Holocene*, 21(7):1081–1091, 2011. doi: 10.1177/0959683611400458.

J. N. Weber and P. M. J. Woodhead. Temperature dependence of oxygen-18 concentration in reef coral carbonates. *J. Geophys. Res.*, 77:463–473, 1972. doi: 10.1029/jc077i003p00463.

S. Weiner and P. M. Dove. An overview of biomineralization processes and the problem of the vital effect. *Rev. Mineral Geochem.*, 54(1):1–29, 2003. ISSN 1529-6466. doi: 10.2113/0540001.

C. D. Woodroffe and J. M. Webster. Coral reefs and sea-level change. *Marine Geology*, 352:248–267, 2014. ISSN 0025-3227. doi: 10.1016/j.margeo.2013.12.006.

Y.-Y. Xu, S. Pearson, and K. H. Kilbourne. Assessing coral sr/ca–sst calibration techniques using the species diploria strigosa. *Palaeogeogr. Palaeoclimatol. Palaeoecol.*, 440:353–362, 2015. doi: 10.1016/j.palaeo.2015.09.016.

R. Zeebe and D. A. Wolf-Gladrow. *CO2 in Seawater: Equilibrium, Kinetics, Isotopes*, volume 65 of *Elsevier Oceanography Series*. Gulf Professional Publishing, Amsterdam, 2001.

K. B. Ólafsdóttir and M. Mudelsee. More accurate, calibrated bootstrap confidence intervals for estimating the correlation between two time series. *Math. Geosci.*, 46(4):411–427, 2014. ISSN 1874-8953. doi: 10.1007/s11004-014-9523-4.

CHAPTER 2

Seasonal SIMS Oxygen Isotope Record in Astarte borealis from the Baltic Sea Tracks a Modern Regime Shift in the NAO

2.1 Introduction

Over the last 30 years and starting with the work of Dettman and Lohmann (Dettman and Lohmann, 1995), innovations in microsampling techniques for stable isotope analysis of freshwater to marine organisms with accretionary carbonate hard parts (e.g., bivalves, gastropods, corals, and fish) have spurred discoveries in fields such as paleoclimatology, paleobiology, and archaeology (Schöne et al., 2005; Prendergast et al., 2017). The ability to microsample some archives at seasonal-scale resolution gave rise to the broader field of isotope sclerochronology, which combines the use of growth patterns with oxygen and stable carbon isotope ratios (δ^{18}O and δ^{13}C, respectively) recorded in carbonate hard parts (Schöne and Surge, 2012; Surge and Schöne, 2015). In bivalves, shell growth patterns (growth lines and increments) are formed due to changes in the rate of carbonate deposition that is, in turn, a response to environmental and biological conditions at several periodicities: daily, tidal, fortnightly, monthly, and annual (Barker, 1964; Stanley, 1966; Pannella and MacClintock, 1968; Clark, 1974; Pannella, 1976; Jones et al., 1983; Goodwin et al., 2001). In effect, growth increments form a shell calendar that can be used to measure time. When combined with shell oxygen isotope (δ^{18}O) ratios, which are a function of growth temperature and δ^{18}O values of ambient water, shell calendars are rich bioarchives of past environments and climate conditions.

The vast majority of studies using high-resolution, seasonal-scale records from fast- and slow-growing bivalves employ micromilling techniques that generate carbonate powder on the order of 10s of micrograms analyzed on conventional isotope ratio mass spectrometers (IRMS). Micromills are typically computer-aided systems equipped with cameras used to digitize sampling paths along growth lines/increments visible in the shell cross-section. Shell growth is fastest in the first few years of life, so microsampling is often restricted to the ontogenetically youngest part of the shell. This approach is easily achieved in fast growing and/or large bivalves (Weidman et al., 1994; Quitmyer et al., 1997; Surge and Walker, 2006; Schöne and Gillikin, 2013; Goodwin et al., 2021). Although this approach can achieve submonthly resolution on fast-growing shells, species that are small, slow growing, and long-lived, like those from the genus *Astarte*, are potentially untapped resources of paleoclimate information.

Astarte borealis (Schumacher, 1817) is a common constituent of many Arctic and boreal seas, and individuals are reported to live for several decades (Moss et al., 2018, 2021) to over a century (Torres et al., 2011; Reynolds

et al., 2022). Such long lifespans are not uncommon for high-latitude species. Moss et al. (2016) document that across Bivalvia there is a tendency for lifespan to increase and growth rate to decrease from low to high latitudes. Such longevity makes this species attractive as a potential bioarchive for reconstructing changes in past and present climate. Based on previous work, *A. borealis* from the White Sea, Russia, reached 33.5 mm in length and allowed for traditional micromilling techniques (Moss et al., 2018). However, in a subsequent study, (Moss et al., 2021) found that *A. borealis* from the Baltic Sea is smaller than individuals from the White Sea, precluding the use of traditional micromilling techniques. Thus, they employed secondary ion mass spectrometry (SIMS) to allow for a horizontal sampling resolution of 10 μm with a sampled mass of approximately a nanogram, orders of magnitude smaller than traditional micromilling techniques and IRMS analysis. Their study and our study of a 24-year-old *A. borealis* shell from the Baltic Sea add to the growing body of research that applies SIMS to modern marine/estuarine bivalves (Dunca et al., 2009; Olson et al., 2012; Vihtakari et al., 2016) and other modern and fossil marine organisms with accretionary carbonate hard parts (Kozdon et al., 2009; Matta et al., 2013; Linzmeier et al., 2016; Helser et al., 2018; Wycech et al., 2018).

Studies examining *A. borealis* from the Baltic Sea as paleoclimate archives can greatly improve our understanding of regional-scale climate variability across the North Atlantic. In particular, the Baltic Sea is strongly influenced by large-scale atmospheric circulation (e.g., the NAO), hydroclimate in the catchment area, and restricted water exchange with the North Sea (Lehmann et al., 2011). Although scientific research has focused on NAO decadal variability, physical mechanisms, and external forcings over the last 20-30 years, Pinto and Raible (2012) note that a dearth of long-term, high-resolution archives prior to instrumental observations contributes to uncertainties in our understanding of such regional-scale variability on longer timescales. Therefore, developing a (paleo)climate bioarchive in this region is important to improve our understanding of regional-scale climate variability on long timescales and to reduce uncertainties. Here, using SIMS, we find that $\delta^{18}O_{shell}$ values measured from a 24-year-old *A. borealis* shell collected alive in 2001 from the Baltic Sea captures a well-documented regime shift in the NAO circa 1989 (Lehmann et al., 2011). Our study thus showcases the potential for SIMS $\delta^{18}O_{shell}$ values in this species to provide robust paleoclimate information regarding hydroclimate variability from seasonal to decadal timescales.

2.2 Materials and Methods

2.2.1 Shell collection, preparation, and oxygen isotope analysis

Specimen RFP3S-47 was collected alive on 5 May 2001 from 20.9 m depth (54.7967°N, 12.38787°E) using a van Veen grab as part of an earlier benthic ecology study (Zettler, 2002). The aragonitic shell was cut along the maximum axis of growth to expose light and dark growth increments (visible under reflected light; Figure 2.1A) and set in a 2.5 cm-diameter and 4 mm-thick round epoxy mount alongside grains of the calcite standard UWC-3 (Koz-

don et al., 2009). Prior to SIMS analysis, the mount was sent to Wagner Petrographic for polishing with successively finer diamond suspension grits, finishing with a 0.05 μm colloidal alumina solution. The polished sample was then sputter coated with gold to a thickness of ~60 nm.

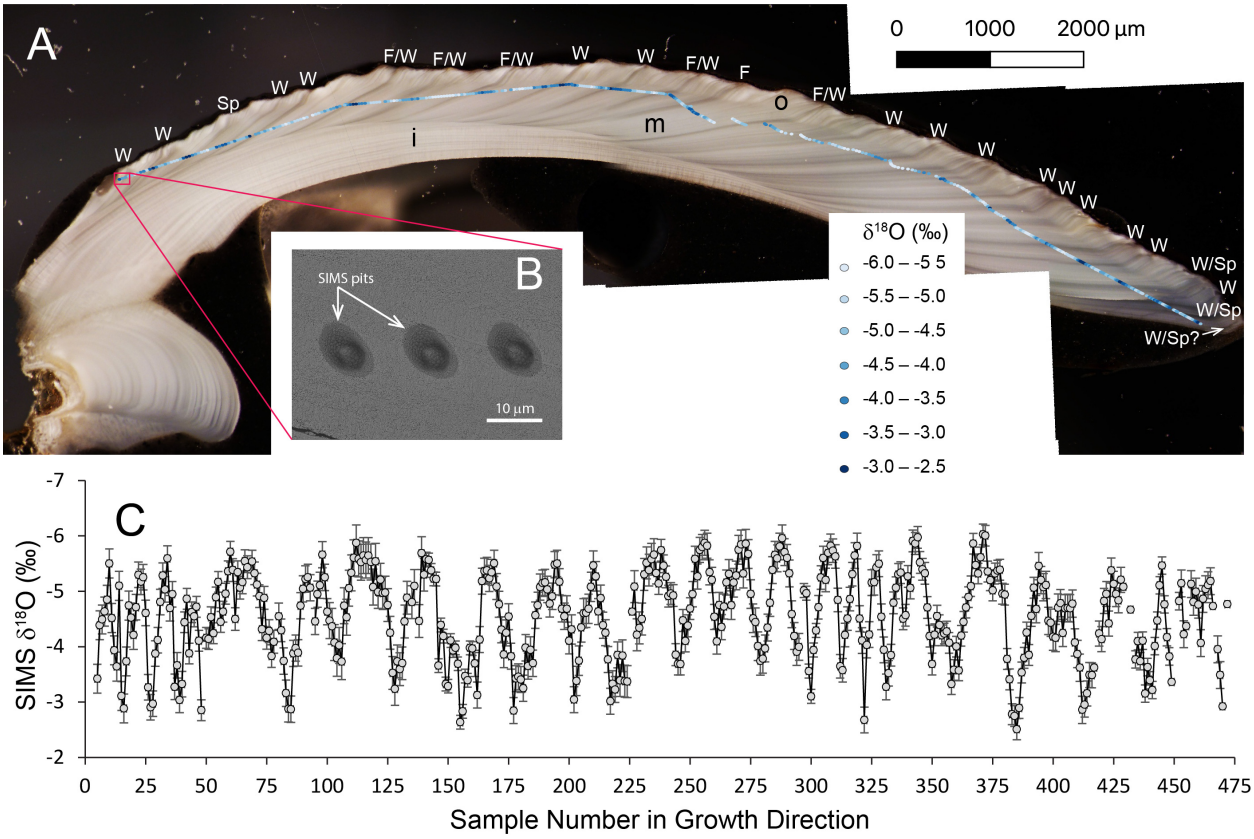

Figure 2.1: Photomicrograph of shell cross-section, location of SIMS sampling pits, SEM image of SIMS pits, and SIMS $\delta^{18}O_{shell}$ values plotted using Quantum-GIS software (QGIS.org, 2023). (A) Cross-section of specimen RFP3S-47 cut along the axis of maximum growth (umbo on left, growth margin on right; growth direction from left to right), showing 3 microstructural layers (i = inner layer, m = middle layer, o = outer layer) and light/dark couplets under reflected light hypothesized to represent annual increments. Approximately 22-24 light/dark couplets are visible. Sampling pits are identified in gradational shades of blue circles (enlarged from true size of 10 μm for ease of visibility), representing 0.5‰ intervals of SIMS $\delta^{18}O_{shell}$ values where lighter blues represent lower values and darker blues are higher values. Estimated season of dark increment formation interpreted from the SIMS $\delta^{18}O_{shell}$ time series (see text for details) are labeled as follows: W = winter; Sp = spring; F = Fall. The last dark increment nearest the growth margin does not include a SIMS $\delta^{18}O_{shell}$ value; thus, the designation W/Sp? is estimated using the relative amount shell growth from the date of harvest. Scale bar = 2000 μm. (B) SEM image of SIMS sampling pits at high resolution (5.5 k magnification) showing examples with no irregularities. Scale bar = 10 μm. (C) SIMS $\delta^{18}O_{shell}$ values sampled along direction of growth (left to right). Gray circles are individual SIMS data points. Bars are standard deviations (2σ). Gaps represent data points removed during quality control.

SIMS analysis was performed at the University of Wisconsin-Madison WiscSIMS laboratory on a Cameca IMS 1280 in August 2018 during the same session as Moss et al. (2021) and following settings described in Wycech et al. (2018). Analysis pits ~10 μm in diameter and ~1 μm deep were sputtered using a 1.0 nA primary beam of 133Cs+. Three Faraday detectors in the double-focusing mass spectrometer simultaneously detected secondary ions of $^{16}O^-$, $^{18}O^-$, and $^{16}OH^-$, with secondary $^{16}O^-$ count rates of ~2.4 Gcps. Values of $\delta^{18}O$ are reported in permil

(‰) relative to the VPDB (Vienna Pee Dee Belemnite) standard. Precision was determined as 2 times the standard deviation (s.d.) of repeated groups of bracketing measurements on the calcite running standard UWC-3, which averaged ±0.24‰ (2 s.d.) across the analysis session. Measured (raw) δ^{18}O values were corrected to the VPDB scale for each group of 15–20 aragonite sample analyses following a 3-step procedure: 1. The instrumental bias of calcite on the VSMOW (Vienna Standard Mean Ocean Water) scale was calculated using the bracketing measurements of UWC-3. 2. An adjustment for the small difference in instrument bias (0.88‰) between calcite and aragonite analyses was applied based on calibration analyses of the aragonite standard UWArg-7 (δ^{18}O = 19.73‰VSMOW Linzmeier et al., 2016) completed at the start of the analysis session. 3. Conversion from the VSMOW to VPDB scales followed procedures outlined in Coplen (1994).

The middle microstructural layer was targeted for SIMS analysis per Moss et al. (2021). SIMS analysis started nearest the umbo and proceeded along growth direction to the growth margin, sampling nearly the entire lifespan of the specimen and yielding 482 SIMS $\delta^{18}O_{shell}$ values. Most of the shell was sampled by manual site selection along growth direction. To maximize machine time by sampling overnight, automated sampling of preselected points was implemented to capture the earliest ontogenetic years (40 samples) and the final 8 light/dark couplets towards the growth margin (∼160 samples).

SIMS data were subjected to a quality-control protocol. First, analytical metrics of each sample measurement – including secondary ion yield, $^{16}OH^-/^{16}O^-$ ratio, and internal variability – were compared to the mean of the bracketing standards. $^{16}OH^-/^{16}O^-$ ratios ranged from 0.0129 to 0.0373, with an average of 0.0243 ± 0.0038 (1σ). Analyses were determined as outliers if they exhibited values that were above (below) the third (first) quartile by more than 1.5 times the interquartile range (Tukey, 1977), and were thus excluded from figures and interpretive discussion. This quality control removed 23 of the 482 total analyses (<5%). An additional 8 duplicate samples were removed from figures and interpretive discussion, resulting in 451 total SIMS $\delta^{18}O_{shell}$ values. Next, SIMS pits were imaged by scanning electron microscopy (SEM) to screen for irregular pit shapes, cracks, or inclusions that may bias the δ^{18}O data. For SEM imaging, the epoxy mount was loaded onto an aluminum receiver with double-sided copper tape. Images were taken using a Zeiss Supra 25 FESEM operating at 5.5 kV, using the SE2 detector, 30 μm aperture, and working distances of 12–15 mm (Carl Zeiss Microscopy, LLC, Peabody, MA). SEM images of SIMS analysis pits revealed no irregularities of either pit morphology or aragonite substrate (Figure 2.1B).

2.3 Results

2.3.1 SIMS δ^{18}O values in *A. borealis*

SIMS $\delta^{18}O_{shell}$ values in specimen RFP3S-47 exhibit a quasi-sinusoidal pattern (Figure 2.1C), with 24 cycles of local minima (-5.58 ± 0.32‰, 1σ) and maxima (-3.15 ± 0.39‰, 1σ) in agreement with the 24 light/dark cou-

plets of annual growth increments visible under reflected light (Figure 2.1A). These SIMS δ^{18}O values are comparable to the SIMS δ^{18}O values measured from another Baltic Sea *A. borealis* specimen in Moss et al. (2021), where the authors noted a negative offset between their SIMS $\delta^{18}O_{shell}$ values relative to coarser resolution IRMS δ^{18}O values measured from the same specimen. Between 9 and 31 SIMS $\delta^{18}O_{shell}$ measurements comprise a full couplet in specimen RFP3S-47, averaging 19 data points per couplet. Most dark increments occur at or near the highest SIMS $\delta^{18}O_{shell}$ values (darker shades of blue circles locating SIMS pits on the shell cross-section in Figure 2.1A). Assuming one light/dark couplet represents an annual cycle, as is often the case in this species (Moss et al., 2018, 2021), our sampling interval equates to sub-monthly resolution on average (see Section 2.4.1 for further discussion of age modeling). However, we note that each discrete sample constitutes a 10 μm spot and a $\sim$5 μm space between spots, and thus one-third of the shell along the sampling path is not represented by the samples presented in this study.

2.3.2 *in situ* Temperature and Salinity

Bottom water temperature (Figure 2.2, top panel) and salinity (Figure 2.2, middle panel) were measured periodically at a location less than 2 km away from our study site (54.79169°N, 13.05831°E) using a calibrated CTD in a previous study (Zettler et al., 2017) between October 1976 and November 2017. The data span the approximate growth years of specimen RFP3S-47 based on counting couplets of light/dark growth increments (1977 to 2001). Prior to 1990, *in situ* temperature and salinity were measured at approximately seasonal resolution (n = 4 $\pm$ 1 per year). During and after 1990, the sampling frequency increased to an average of 7 $\pm$ 3 measurements per year. Throughout all years, eight months were sampled frequently, including the warmest (August) and coldest (March) months of the year (Figure 2.2, bottom panel). However, there is a general dearth of data during the transitional months of April, June, September, and December.

On average, bottom water temperatures ranged from 11.46 $\pm$ 2.63°C (1σ) in August to 2.28 $\pm$ 1.26°C in March, equating to an annual cycle of 9.18°C $\pm$ 3.89°C. However, we note that temperatures collected in July, August, and October are statistically indistinguishable from one another (ANOVA; n = 50, p = 0.41). The same is true for temperatures collected in February, March, and April (n = 46, p = 0.83). The highest bottom water temperature observed was 16.69°C on 5 August 1992, while the lowest temperature observed was -0.30°C on 13 February 1996. Bottom water salinity did not vary with the annual cycle. Salinity measurements exhibited a skewed-right distribution with a median value of 9.83 practical salinity units (psu). Significant deviations above average salinity occur frequently and sporadically throughout the sampling period, with a maximum value of 22.85 psu observed on 26 January 1993. Significant deviations below average salinity were lower in magnitude and frequency, with the minimum value of 7.67 psu observed on 7 May 1999.

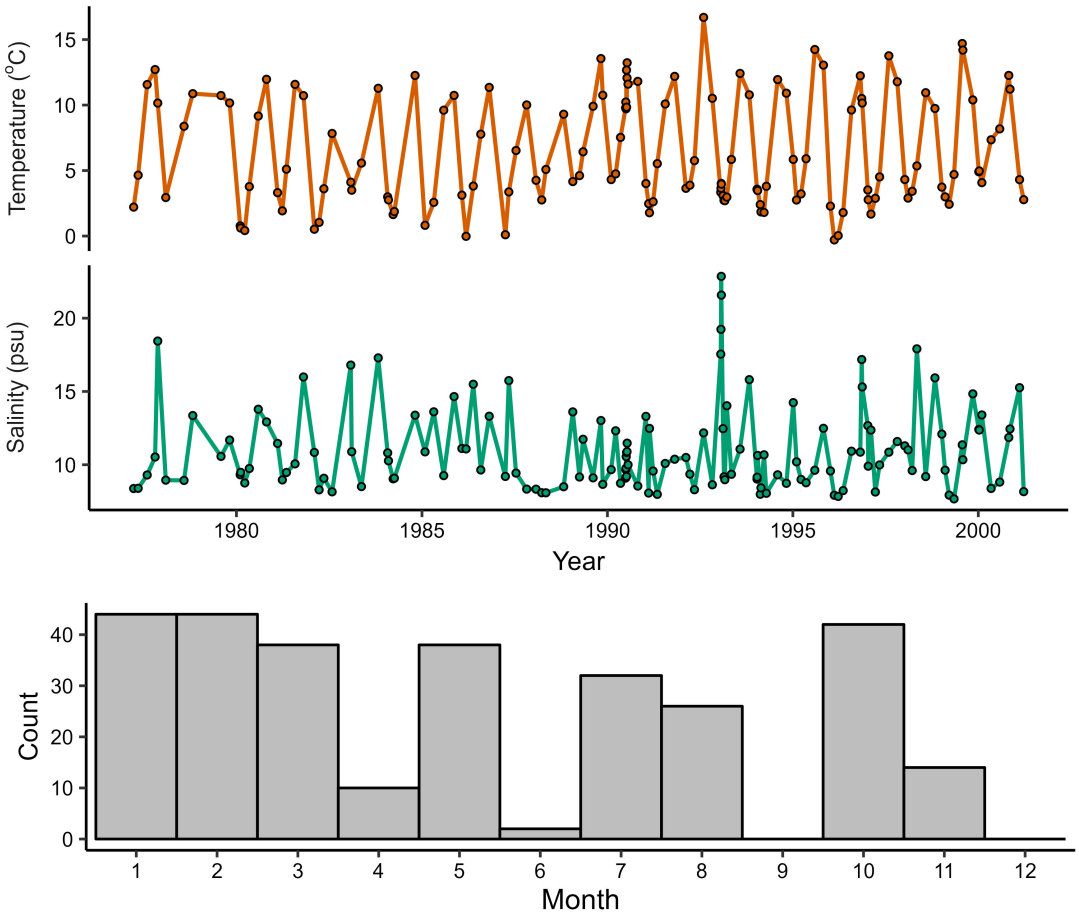

Figure 2.2: Environmental data measured less than 2 km from where specimen RFP3S-47 was collected (54°47'30.1"N, 13°03'29.9"E).(A & B) Bottom water temperature and salinity measured between 23-32 m depth. (C) Number of measurements taken in each month for all years of CTD data.

2.4 Discussion

In this section, we demonstrate that the SIMS $\delta^{18}O_{shell}$ dataset from specimen RFP3S-47 yields quantitative paleoclimate information, validating SIMS $\delta^{18}O_{shell}$ values in *A. borealis* as a new climate archive for mid-to-high latitude coastal environments. First, to associate spatial changes in SIMS $\delta^{18}O_{shell}$ values to temporal changes in environmental conditions, we apply an age-model (described in the next section) to the SIMS $\delta^{18}O_{shell}$ data that aligns local $\delta^{18}O$ maxima with the coldest winter months (Figure 2.3. We then correlate the age-modeled SIMS $\delta^{18}O_{shell}$ dataset with *in situ* temperature and salinity data, as well as with the independent ORAS5 SST dataset (Zuo et al., 2019, Figure 2.4). These correlation analyses, in conjunction with the age model, show that variations in SIMS $\delta^{18}O_{shell}$ values in specimen RFP3S-47 reflect regional hydroclimate conditions. Finally, we correlate the low-frequency variance component of the SIMS $\delta^{18}O_{shell}$ dataset to interannual shifts in the NAO.

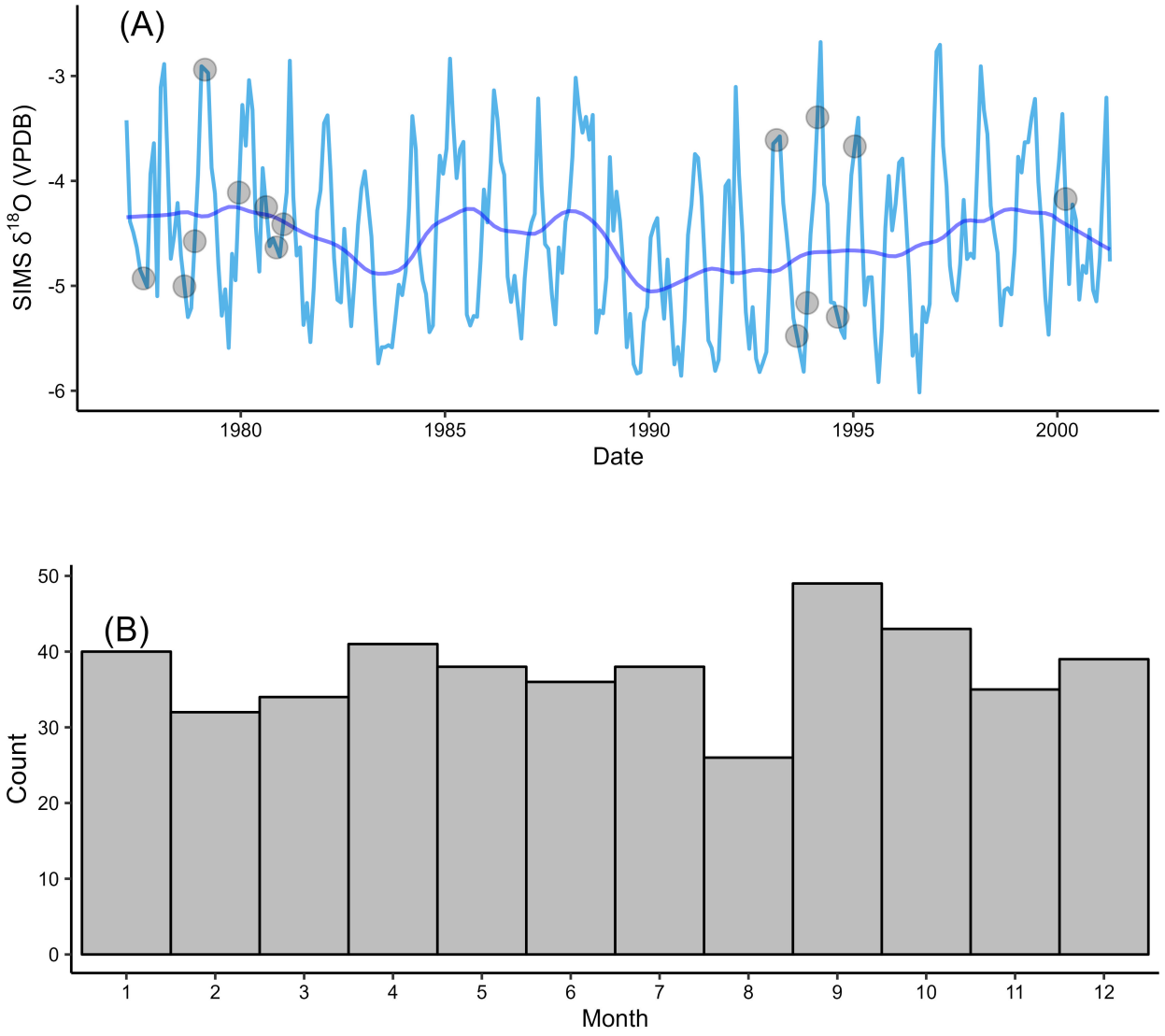

Figure 2.3: (A) Age-modeled SIMS $\delta^{18}O_{shell}$ data from the *A. borealis* specimen. Estimated growth dates are between March 1977 and May 2001. The light blue line is monthly-averaged $\delta^{18}O_{shell}$ values, with gray dots indicating where values were linearly interpolated between bracketing months. The dark blue line represents the data passed through a 36-month LOWESS function. (B) Number of age-modeled growth months for SIMS $\delta^{18}O_{shell}$ data (n = 290) for all growth years (n = 24). Most months (84%) are represented by one or two data points with no bias towards any particular time of year.

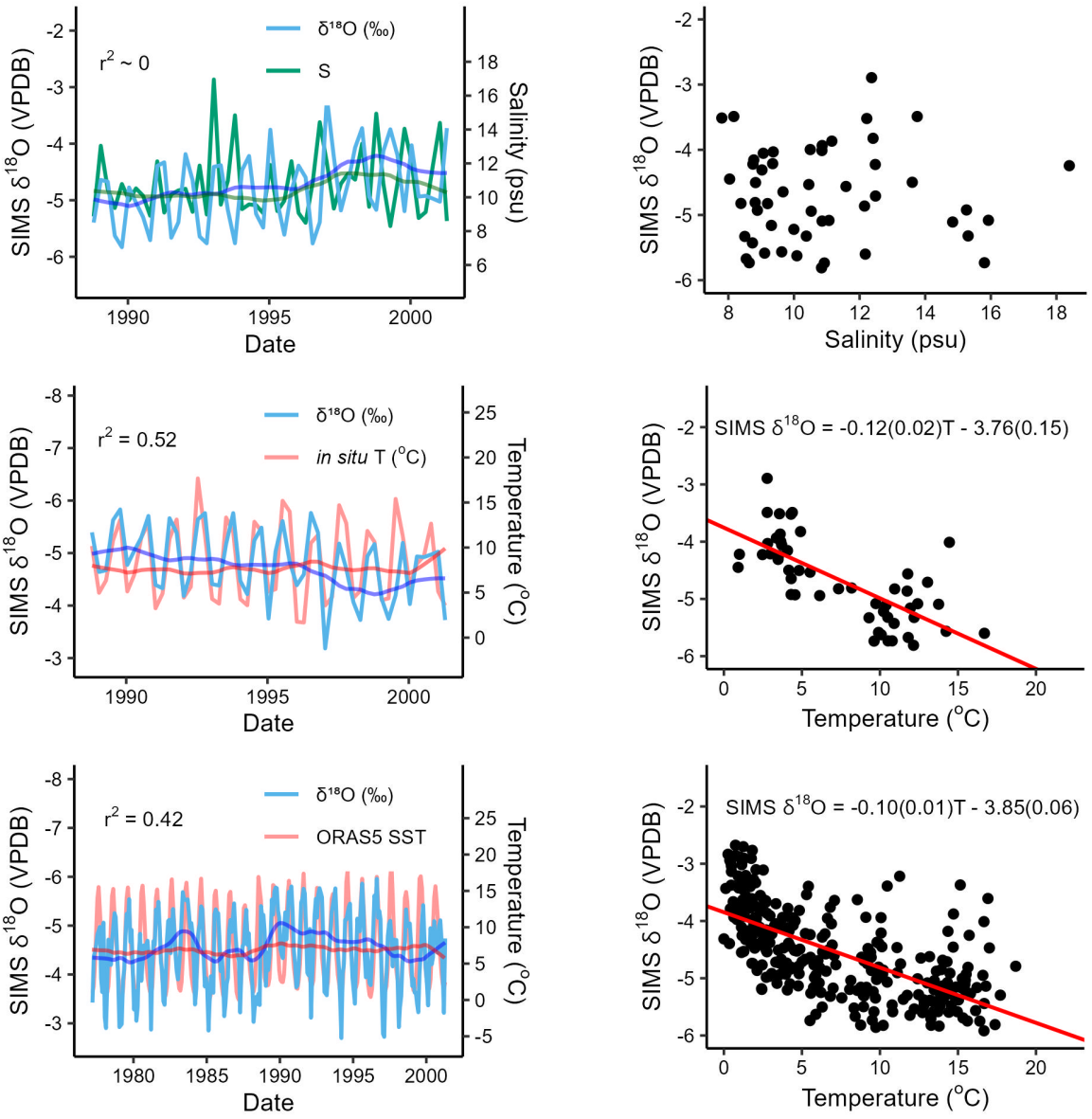

Figure 2.4: Age-modeled SIMS $\delta^{18}O_{shell}$ values compared to *in situ* salinity measurements and two independent temperature datasets from the Baltic Sea.(A–D) Comparison of SIMS $\delta^{18}O_{shell}$ values with *in situ* salinity (A, B) and temperature data (C, D) collected from shipboard measurements between October 1988 and May 2001 (Zettler et al., 2017), mean-averaged over seasonal intervals. (E, F) Comparisons of SIMS $\delta^{18}O_{shell}$ values with sea surface temperature estimates for the entire Baltic Sea region extracted from the ORAS5-SST global reanalysis product at monthly resolution (Zuo et al., 2019). The $\delta^{18}O$ axes in both (C, E) are inverted to better visualize variations in SIMS $\delta^{18}O_{shell}$ values due to temperature. The dark green, blue, and red lines in (A, C, E) show each dataset passed through a 36-month LOWESS function. The equations in (D, F) are displayed to assess correlation, not as proxy calibrations for absolute temperature reconstruction. Parentheses in each equation represent the standard error of the regression coefficients.

2.4.1 Age-modeled SIMS $\delta^{18}O_{shell}$ values

A monthly age model was applied to all $\delta^{18}O_{shell}$ samples throughout the lifespan of specimen RFP3S-47 by aligning the quasi-sinusoidal pattern to the annual cycle of temperature (as recorded by *in situ* CTD measure-

ments) according to well-established methods (Beck et al., 1992; Klein et al., 1996; Surge et al., 2001). The age model assumes that local $\delta^{18}O_{shell}$ maxima occur during the coldest winter months (January, February, March, and April, according to the ORAS5 SST dataset), with the final data point designated as the month of collection (May 2001). All samples between local maxima were assigned months based on linear interpolation of their position between bracketing maxima, which assumes a linear growth rate within years. Counting couplets of light and dark increments backwards from the collection date provides calendar years for all SIMS $\delta^{18}O_{shell}$ samples. We thus infer relative variations in annual growth rates by examining the number of samples collected in each couplet of light and dark increments (Figure 2.5). Excluding the year of collection and the earliest growth year (which do not constitute full light/dark increment couplets), between 9 and 31 samples were collected per year, with periods of notably slow growth in the late 1970s and early 1990s. Given each sample constitutes one 10 μm spot and a 5 μm space between samples, we can approximate an annual growth rate in μm per year (Figure 2.5, secondary y-axis). However, we caution that precisely quantifying growth rates requires a specific protocol where measurements are made perpendicular to growth lines bounding growth increments along the direction of growth (Schöne et al., 2005) and often the hinge plate is used to avoid any biases imparted by the conchoidal shape of the major growth axis (e.g., Winkelstern et al., 2013; Palmer et al., 2021). Given that calculating annual growth rate was not the primary focus of this study and the sampling scheme used did not follow the necessary protocol for such an analysis, our statistical approach provides a relative estimate of growth rates that compliments the more thorough growth assessments of *A. borealis* specimens conducted by Moss et al. (2018, 2021).

For specimen RFP3S-47, all 24 local $\delta^{18}O_{shell}$ maxima occur at or near the dark increment, indicating formation during cold months (i.e., late fall, winter, or early spring; Figure 2.1A). While not a ubiquitous feature for all bivalves across all latitudes, the coincident timing of dark increment formation with $\delta^{18}O_{shell}$ maxima has been observed in other mid- to high-latitude bivalves, including *Arctica islandica* (Witbaard et al., 1994; Schöne et al., 2004) and *Mercenaria mercenaria* (Elliot et al., 2003). Fifteen local $\delta^{18}O_{shell}$ maxima occur exactly at the dark increment (i.e., winter); three occur slightly before the dark increment (i.e., late fall); and six occur slightly after the dark increment (i.e., early spring). Once all data points were age modeled, we calculated that each analysis (10 μm spot and 5 μm space) represents on average 19.5 days.

After the age model was applied, $\delta^{18}O_{shell}$ values were mean-averaged over monthly intervals between March 1977 and April 2001 (Figure 2.3A). Data points are distributed almost uniformly across months, which is a function of both our high sampling resolution and the inherent assumption of constant growth in our age model (Figure 2.3B). Out of 290 months in the time series, 141 are represented by one data point, 103 are represented by two data points, 21 are represented by three data points, 9 are represented by four data points, and one is represented by 5 data points. Only 15 months in the time series were unrepresented by any $\delta^{18}O_{shell}$ samples. For these months, $\delta^{18}O_{shell}$ values were linearly interpolated between bracketing months (gray dots, Figure 2.3A).

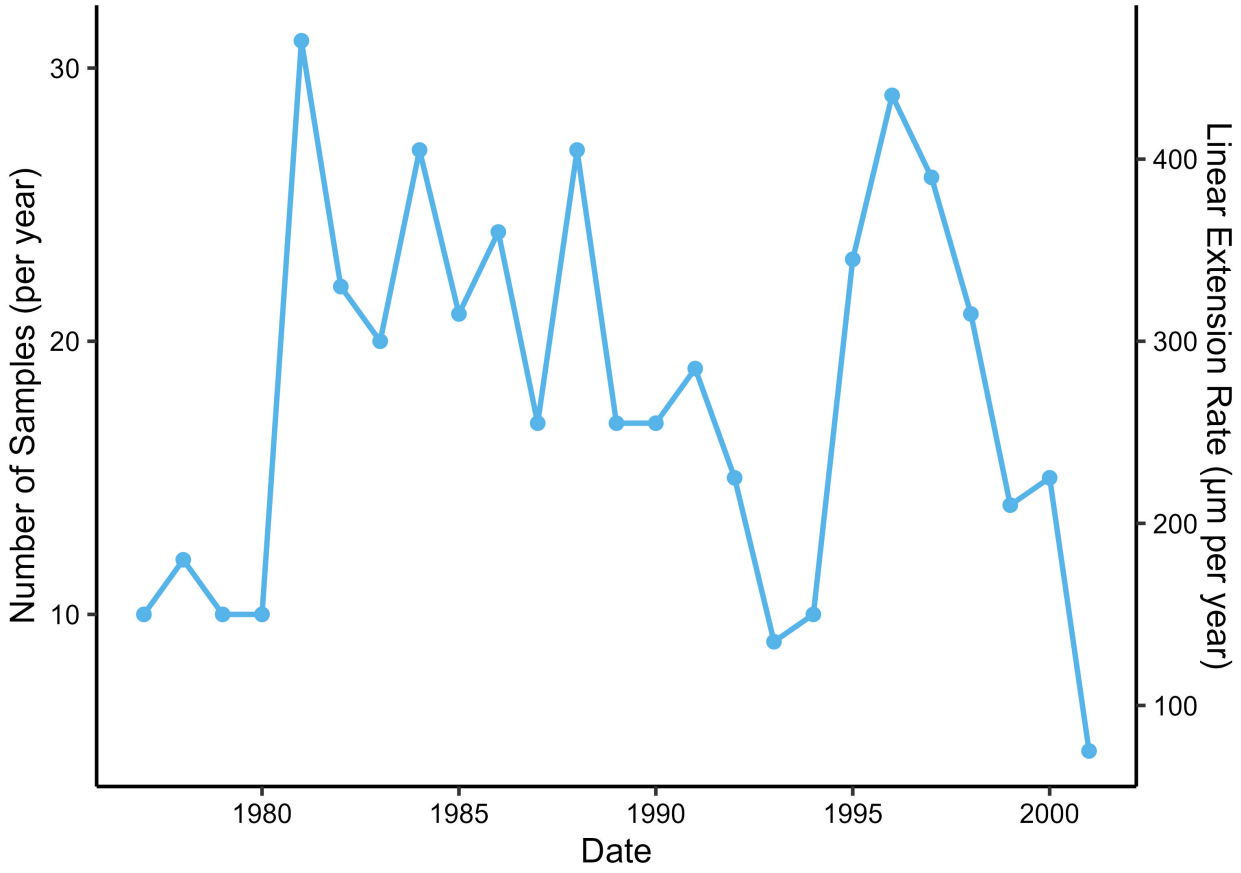

Figure 2.5: Number of data points sampled from specimen RFP3S-47 for each calendar year between the year of collection (2001) and the earliest ontogenetic year (1977). Years were assigned to each growth increment by counting couplets of light and dark increments backwards from the year of collection.

Once the data were averaged into monthly intervals, a 36-month locally weighted scatterplot smoothing (LOWESS) function was applied to highlight the low-frequency variance component (dark blue line, Figure 2.3A). The LOWESS function (Cleveland, 1979) is a non-parametric regression method that replaces each data point in a time series with a weighted average based on a specified window size and the values of the data points in close proximity to the central data point in that window. For the age-modeled SIMS $\delta^{18}O_{shell}$ ¬ time series, we applied a 36-point window size (i.e., a 36-month bandwidth), which is the minimum bandwidth required to mitigate any effects due to seasonality. These smoothed data accentuate interannual variability that peaks within the 3-to-4-year bandwidth over the 24-year time series. The magnitude of the interannual oscillations vary widely, with a few anomalous periods exhibiting cycles as large as 0.64 and 0.76‰ (troughs in 1984 and 1990) or as small as 0.05‰ (troughs in 1993 and 1996). Average interannual variability (0.35‰) in the age-modeled SIMS $\delta^{18}O_{shell}$ dataset is an order of magnitude lower than average seasonal variability (2.43‰). However, interannual variability appears to modulate the seasonal cycle, resulting in seasonal amplitudes as large as 3.31‰ (1997) or as low as 1.44‰ (1990).

2.4.2 Correlating SIMS $\delta^{18}O_{shell}$ values to temperature and salinity

To explore the mechanisms behind the apparent seasonal and interannual variability, age-modeled SIMS $\delta^{18}O_{shell}$ values were compared to salinity and two separate temperature datasets from the Baltic Sea region (Figure 2.4). Although we have correlated age-modeled SIMS $\delta^{18}O_{shell}$ values to two different temperature datasets, we establish this correlation strictly to assess for mechanisms of seasonal and interannual variability. As discussed in Moss et al. (2021), SIMS $\delta^{18}O_{shell}$ values cannot be used to reconstruct absolute temperatures in *A. borealis* shells. Offsets between SIMS-measured $\delta^{18}O$ and IRMS-measured $\delta^{18}O$ values, which are used in temperature calibrations, are reported in a variety of calcite and aragonite biogenic carbonates. The cause of these offsets, commonly ¡1‰, can be due to a variety of factors (Helser et al., 2018; Wycech et al., 2018), including possible inclusion of water or organic material in the carbonate matrix. Here, we do not attempt to characterize or calibrate the absolute $\delta^{18}O$ value from these samples, but instead use the quality-controlled analytical metrics as the basis for our assumption that SIMS faithfully measures relative changes of $\delta^{18}O$ values in specimen RFP3S-47.

Further complications associated with reconstructing temperatures from absolute SIMS $\delta^{18}O$-shell values presented here arise from unconstrained $\delta^{18}O_{water}$ values at this location throughout the study period. Although studies have correlated $\delta^{18}O_{water}$ values to salinity in the Baltic Sea (Frohlich et al., 1988; Harwood et al., 2008), the strength of this correlation is likely variable in space and time. However, given that $\delta^{18}O_{shell}$ values are primarily a function of temperature and the $\delta^{18}O$ value of ambient water, we demonstrate the utility of the combined signal in assessing modes of seasonal to interannual climate variability in the Baltic Sea region. As a general rule, we define strong correlations as those with an r^2 value greater than 0.50 ($|r| > 0.70$), moderate correlations as those with an r^2 value greater than 0.1 ($0.3 < |r| < 0.7$), and weak correlations as those with an r^2 value less than 0.1 ($|r| < 0.3$).

Salinity and temperature depicted in the top four panels of Figure 2.4 were measured simultaneously via shipborne CTD measurements less than two kilometers from our study site, hereafter referred to as *in situ* salinity and temperature (Zettler et al., 2017, see Section 2.3.2). Although *in situ* water data extend back to the earliest estimated growth month for specimen RFP3S-47 (March 1977), the CTD sampling rate is too sparse to support analysis of subannual variance. Therefore, only *in situ* water data collected between October 1988 and May 2001 were used for comparison to age-modeled SIMS $\delta^{18}O_{shell}$ values. To facilitate comparison, age-modeled SIMS $\delta^{18}O_{shell}$ values and *in situ* salinity and temperature were mean-averaged into seasonal values (Winter = DJF, Spring = MAM, Summer = JJA, Fall = SON). The temperature dataset depicted in the bottom four panels of Figure 2.4 was compiled from the ORAS5 SST global reanalysis product (Zuo et al., 2019). The ORAS5 product was chosen above other readily available global SST products primarily for two reasons. First, it is calculated at sufficient spatiotemporal resolution (monthly; 1° x 1°) with reliable data at high latitudes, allowing us to integrate 49 grid-points into a single regional SST estimate for the Baltic Sea (Figure 2.6). Second, ORAS5 is a data assimilation product that

tunes the output of the European Centre for Medium-Range Weather Forecasts' OCEAN5 system to *in situ* observations. Thus, it is well-informed by remote and *in situ* observations, particularly in this dynamic high-latitude coastal region (Carton et al., 2019; Zuo et al., 2019). This is demonstrated by a strong correlation between *in situ* temperature and ORAS5 SST when both datasets are seasonally averaged (n = 51, r^2 = 0.82, $p < 0.001$). The correlation between SIMS $\delta^{18}O_{shell}$ values and each dataset are as follows: no correlation for *in situ* salinity ($r^2 \sim 0$, n = 51, p = 0.99), strong for *in situ* temperature (r^2 = 0.52, n = 51, $p < 0.001$), and moderate for the ORAS5 dataset (r^2 = 0.42, n = 290, $p < 0.001$).

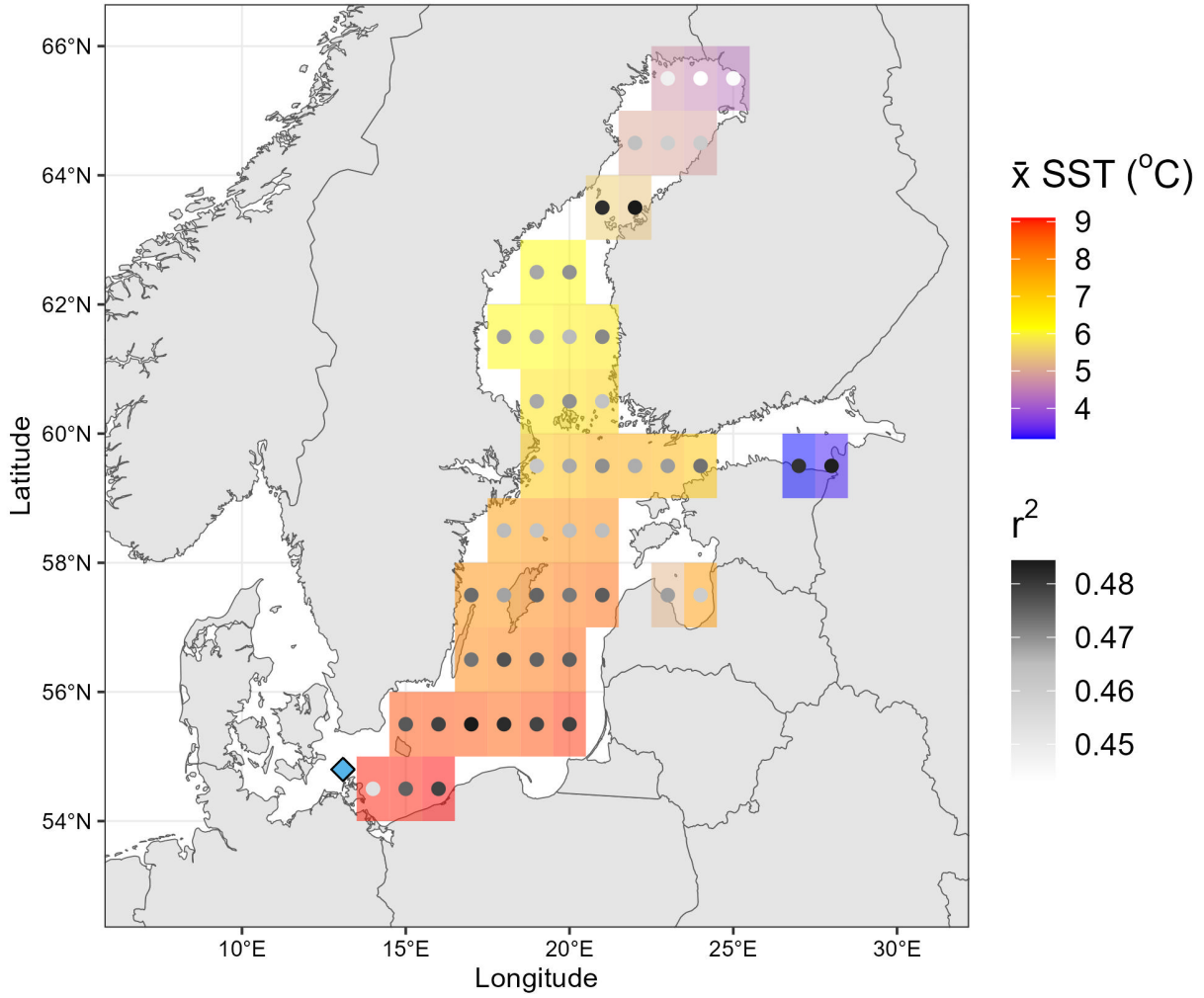

Figure 2.6: Spatial correlation analysis between the SIMS $\delta^{18}O_{shell}$ data and Baltic Sea SST estimates derived from the ORAS5 SST dataset. Mean SST ($\bar{x}$SST; shaded region) and the Pearson correlation coefficients (r^2; points) are shown for each grid point. The blue diamond marks our study site, where specimen RFP3S-47 was collected. The color of each point denotes the r^2 value between age-modeled SIMS $\delta^{18}O_{shell}$ values and SST at that specific location throughout the entire study period (March 1977 to May 2001). The shaded region behind each point indicates the $\bar{x}$SST over the entire study period.

Both temperature datasets exhibit a moderate-to-strong correlation with age-modeled SIMS $\delta^{18}O_{shell}$ values (Pearson's correlation coefficient, $p < 0.001$). Given the assumptions of our age model (aligning local SIMS

δ^{18}O maxima to *in situ* temperature minima), this finding suggests that monthly SIMS $\delta^{18}O_{shell}$ values in specimen RFP3S-47 are varying in part with *in situ* and regional-scale temperature variability, and that temperatures at $\sim$30m depth in the southwest corner of the Baltic Sea covary significantly with SSTs across the entire Baltic Sea. Furthermore, the standard error of the regression coefficients (parentheses in regression equations, bottom two panels in right column of Figure 2.4) overlap between the two temperature models, suggesting the relationship between SIMS δ^{18}O and both temperature datasets is similar. However, a Wilcoxon Rank Sum Test (Bauer, 1972) performed on the regression coefficients from 10,000 bootstrapped resamples suggests that these two equations are statistically distinct ($p < 0.001$). We also note that the slopes of both SIMS δ^{18}O temperature equations are substantially lower than those that are typically observed in other bivalves using IRMS (e.g., -0.22‰ Dettman et al., 1999). We postulate that the lower slope of the relationship between SIMS $\delta^{18}O_{shell}$ values in specimen RFP3S-47 to temperature could be attributed to ontogenetic (growth-related) effects, destructive interference of the temperature signal by $\delta^{18}O_{water}$ values, and by potential seasonal growth cessations (stops).

Ontogenetic effects have been observed in many bivalve species, where the degree to which $\delta^{18}O_{shell}$ values capture the full range of seasonal variation decreases with age (Goodwin et al., 2003). However, our results are not consistent with these ontogenetic effects in specimen RFP3S-47, as neither the amplitude of $\delta^{18}O_{shell}$ couplets nor the number of SIMS $\delta^{18}O_{shell}$ measurements constituting each couplet show a secular negative trend. Therefore, we assume that SIMS $\delta^{18}O_{shell}$ values are capturing the same range of the annual cycle through all growth years and thus do not impose any artifacts on interannual variability.

Variable $\delta^{18}O_{water}$ values could reduce the apparent temperature sensitivity in age-modeled SIMS $\delta^{18}O_{shell}$ values if warmer (cooler) temperatures coincide with higher (lower) $\delta^{18}O_{water}$ values. Previous work has shown that $\delta^{18}O_{water}$ values in the Baltic Sea region are tightly coupled with salinity (Frohlich et al., 1988), and thus could be used as a proxy for $\delta^{18}O_{water}$ values. However, the poor correlation between salinity and the age-modeled SIMS $\delta^{18}O_{shell}$ dataset on seasonal timescales indicate that the relationship between the two at our site is complex. Additionally, we find that adding both temperature and salinity as predictor variables for age-modeled SIMS $\delta^{18}O_{shell}$ values does not yield better estimates than temperature alone ($r^2 = 0.52$, $p < 0.001$). Therefore, we cannot use salinity on seasonal timescales to robustly test whether variations in $\delta^{18}O_{water}$ values are diminishing the temperature sensitivity of SIMS $\delta^{18}O_{shell}$ values. Regardless, we examined the relationship between *in situ* temperature and salinity to verify if seasonal changes in salinity (used here as a proxy for $\delta^{18}O_{water}$) could influence the slope of the relationship between SIMS $\delta^{18}O_{shell}$ values and temperature (Figure A.1 and Table A.1). We find the correlation between *in situ* salinity and temperature is extremely weak (Figure A.1; n = 146, $r^2 = 0.02$, n = 0.14), and there are no significant differences in salinities collected between summer and winter months (Table A.1). While it is likely that SIMS $\delta^{18}O_{shell}$ values are influenced by variations in $\delta^{18}O_{water}$ values, the lack of seasonal variation in salinity (serving here as a proxy for $\delta^{18}O_{water}$) suggests that the influence of $\delta^{18}O_{water}$ variability on SIMS $\delta^{18}O_{shell}$ values is stochastic rather

than systematic. Therefore, we find it highly unlikely that $\delta^{18}O_{water}$ variations can explain the reduced slope in the correlation between SIMS $\delta^{18}O_{shell}$ values and temperature.

Seasonal growth cessations (or stops in growth) and slow downs induced by exceeding growth temperature thresholds are a well-documented phenomena in many bivalve species (e.g., Ansell, 1968; Jones and Quitmyer, 1996; Fritz, 2001, and references therein). It is estimated that Baltic Sea *A. borealis* exhibits an upper temperature threshold between 14 – 17°C and a lower temperature threshold between 0 – 4°C (Oertzen, 1973; Oertzen and Schulz, 1973). Our *in situ* temperature dataset indicates that specimen RFP3S-47 rarely experienced summer temperatures approaching this upper temperature threshold but regularly experienced winter temperatures in the lower threshold range. Furthermore, other environmental and physiological factors can also influence seasonal growth cessation (see Moss et al. (2018) for an overview). Moss et al. (2021) report that temperature stress during cool months could explain the growth slow downs observed in Baltic Sea *A. borealis* during that time; however, winter/spring spawning events could not be ruled out as a possibility.

Seasonal growth cessations would manifest as truncated seasonal amplitudes in $\delta^{18}O_{shell}$ values and, thus, a reduced slope in the correlation between SIMS $\delta^{18}O_{shell}$ values and temperature. To test if seasonal growth cessations were occurring, we conducted two separate statistical analyses. First, if growth cessations were occurring in the winter months, we would expect less variance in SIMS $\delta^{18}O_{shell}$ values during winter months (DJFM = December, January, February, March) than in summer months (JJAS = June, July, August, September). However, we find no significant difference in variance between winter and summer SIMS $\delta^{18}O_{shell}$ values (n = 193, p = 0.58). For the second analysis, we compared the correlation between *in situ* temperature and SIMS $\delta^{18}O_{shell}$ values collected between summer and winter months. We expect that, if growth cessations were occurring during the cold season, winter SIMS $\delta^{18}O$ values would exhibit a weaker correlation with temperature than summer values. However, results are sensitive to which temperature dataset is used. Using the seasonally averaged *in situ* temperature dataset, we find no significant correlation between SIMS $\delta^{18}O_{shell}$ values and *in situ* temperatures for neither winter months (n = 24, r2 ¡ 0.01, p = 0.95) nor summer months (n = 24, r2 = 0.08, p = 0.17). Using the ORAS5 SST dataset, we find a stronger correlation between temperature and winter SIMS $\delta^{18}O_{shell}$ values (n = 97, r2 = 0.36, p ¡ 0.001) than summer values (n = 96, r2 = 0.03, p = 0.07). However, we would expect this stronger correlation due to increased turnover of the Baltic Sea in the winter months, and thus specimen RFP3S-47 at ∼30m depth would likely experience temperatures more similar to Baltic Sea SSTs during the cold season. The inconclusive statistical analyses conducted here, and the difficulty with determining growth cessations via visual inspection, means we cannot rule out that growth cessations are reducing the slope in the correlation between temperature and SIMS $\delta^{18}O_{shell}$ values.

Age-modeled SIMS $\delta^{18}O_{shell}$ values exhibit the greatest interannual variability of all datasets presented in this study, with apparent oscillations occurring every three to four years. Although interannual variability is an order of magnitude smaller than annual variability in the SIMS $\delta^{18}O_{shell}$ dataset, and interannual variability makes up

an even smaller component of the environmental datasets, we find that correlating the interannual components of each dataset yields different results than correlating the monthly- and seasonally-averaged datasets. First, seasonal SIMS $\delta^{18}O_{shell}$ values and *in situ* salinity are strongly correlated when both datasets are passed through a 36-month LOWESS function (r^2 = 0.71, n = 51, $p < 0.001$). The correlation between seasonal SIMS $\delta^{18}O$ and *in situ* temperature actually decreases when we execute the same comparison (r^2 = 0.05, n = 51, p = 0.13), and this same decrease is observed to a lesser extent when comparing the smoothed monthly SIMS $\delta^{18}O$ data and ORAS5 SSTs (r^2 = 0.29, n = 290, $p < 0.001$). These analyses suggest that, while temperature imposes a strong seasonal effect on $\delta^{18}O_{shell}$ values, salinity is predominantly driving interannual variability.

2.4.3 SIMS $\delta^{18}O_{shell}$ values and the NAO

Given the strong influence of temperature and salinity on the SIMS $\delta^{18}O_{shell}$ values at different timescales, we suggest that $\delta^{18}O_{shell}$ values in *A. borealis* from the Baltic Sea may be used to reflect changes in the NAO. The NAO imposes a strong effect on regional temperatures and hydrology as one of the leading modes of interannual climate variability in northern Europe (Hurrell, 1995; Jones et al., 2003). The Baltic Sea is particularly sensitive to the NAO, with stronger (weaker) westerlies bringing increased (decreased) storminess and warmer (colder) winters to the region during the positive (negative) phase (Hurrell, 1995; Lehmann et al., 2011). Because the NAO exhibits a temporal periodicity of approximately 3–4 years, we hypothesize that NAO-related climate changes would work to simultaneously increase SST while decreasing $\delta^{18}O_{water}$ values (and vice versa), effects that would compound to increase the amplitude of the interannual $\delta^{18}O_{shell}$ response of *A. borealis* in the Baltic Sea.

To test this hypothesis, we compared the age-modeled SIMS $\delta^{18}O_{shell}$ dataset from specimen RFP3S-47 to the NAO index for the entire study period (Figure 2.7, left panel). Here, the NAO index is defined as the normalized difference in sea level pressure between Iceland and the Azores (Rogers, 1984; Hurrell, 1995). Additionally, to determine if SIMS $\delta^{18}O_{shell}$ values could track significant changes in the NAO, we conducted a change point analysis on both monthly datasets using the pruned exact linear time (PELT) method (Killick et al., 2012), which is the optimal method for finding exact solutions in change point detection (Truong et al., 2020). These change points are shown in the left panel of Figure 2.7 as blue diamonds on the $\delta^{18}O$ time series and black diamonds on the NAO time series. Although the two datasets are uncorrelated at monthly intervals (r^2 = 0.002, p = 0.49), they are moderately inversely correlated when each monthly dataset are passed through a 36-month LOWESS function (r^2 = 0.46, n = 290, $p < 0.001$; Figure 2.7, left panel). This change in correlation between monthly and interannual timescales observed between SIMS $\delta^{18}O_{shell}$ values and the NAO is very similar to the change in correlation observed between SIMS $\delta^{18}O$ and salinity. However, we note that the correlation between SIMS $\delta^{18}O_{shell}$ values and the NAO is supported by a much larger sample size due to the higher resolution (monthly vs. seasonal) from which the smoothed data were derived.

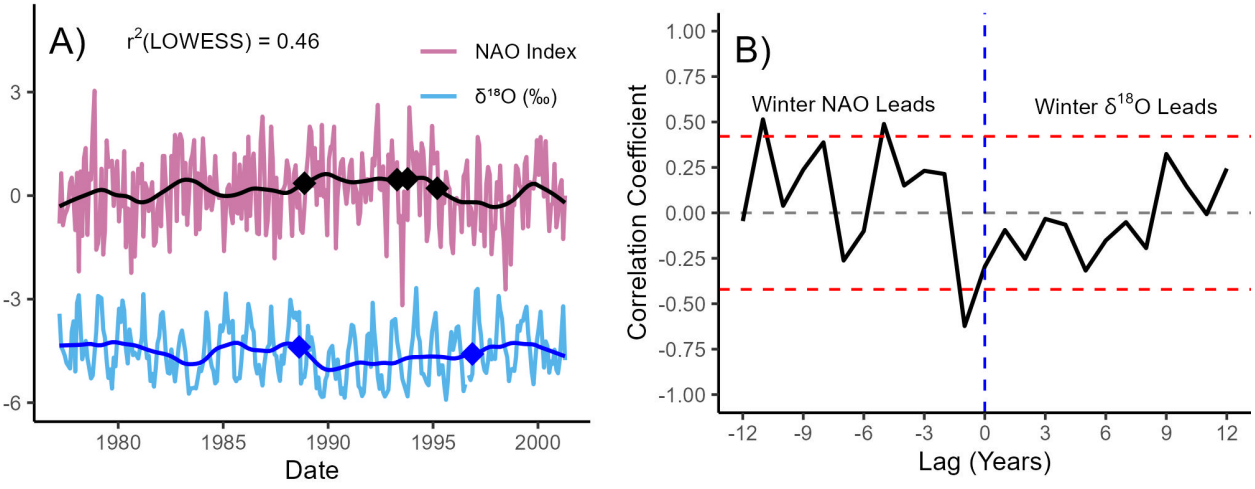

Figure 2.7: SIMS $\delta^{18}O_{shell}$ values compared to the North Atlantic Oscillation (NAO). (Left) Age-modeled $\delta^{18}O_{shell}$ values (blue) and the NAO Index (purple), defined as the normalized difference in sea-level pressures between Iceland and the Azores. The bold blue and black lines represent each dataset passed through a 36-month LOWESS function. Diamonds indicate change points in each monthly time series, identified using a PELT change point detection method. (Right) Lagged correlation analysis between winter (DJFM) $\delta^{18}O_{shell}$ values and the NAO Index. The x-axis values represent the number of years that the NAO lags $\delta^{18}O_{shell}$ values. The red-dotted lines ($r = \pm 0.42$) indicate the point at which the correlation becomes significant at the 95% confidence level (Hu et al., 2017).

The strength of the correlation between the smoothed SIMS $\delta^{18}O_{shell}$ dataset and the NAO is such that SIMS $\delta^{18}O_{shell}$ values track a documented regime shift in the NAO circa 1989 (left panel of Figure 2.7; first black/blue diamonds), where the overall trend in the NAO shifts towards more negative values while winter NAO values remain largely positive (Lehmann et al., 2011). Moreover, the 1989 regime shift is visually striking, particularly in both LOWESS-smoothed time series. The other change point in the SIMS $\delta^{18}O$ time series (circa 1996) occurs within three years of a cluster of change points in the NAO time series, which are associated with a pronounced negative excursion (1994) and an interannual shift towards more negative values (1995). All these latter change points are detected nearly within a 36-month window of each other, which lends further support to our conclusion that $\delta^{18}O_{shell}$ values covary with the NAO on interannual timescales.

The significant correlation on interannual timescales between the NAO index and the SIMS $\delta^{18}O_{shell}$ dataset suggests that positive (negative) phases of the NAO generally bring warmer (cooler) and wetter (dryer) conditions to the Baltic Sea. This finding is consistent with previous studies analyzing modeled and observed temperature and salinity data from the Baltic Sea (Hänninen et al., 2000; Lehmann et al., 2011). In summary, warmer winter SSTs are associated with positive phases of the NAO, as stronger westerly winds bring milder winters and excess precipitation to the region (Hurrell, 1995; Lehmann et al., 2011). Negative phases of the NAO are associated with weaker westerly winds, more extreme winters, and less precipitation in northern Europe (Dickson and Brander, 1993). Additionally, pulses of saline water from the North Sea through the Danish Straits are more likely to occur during a negative NAO

phase (Schinke and Matthäus, 1998). Thus, opposite phases of the NAO propagate conditions where temperature and freshwater flux reinforce one another on interannual timescales, likely amplifying the environmental signal recorded in the SIMS $\delta^{18}O_{shell}$ dataset.

To evaluate the mechanisms behind the correlation between the NAO Index and the SIMS $\delta^{18}O_{shell}$ dataset, particularly during winter when the NAO exhibits the greatest regional impact, we conducted a lagged correlation analysis between winter values (DJFM) from both datasets (Figure 2.7, right panel). We find that winter values from each dataset are moderately correlated when winter NAO leads winter $\delta^{18}O_{shell}$ values by one year (r^2 = 0.39, n = 23, p = 0.002). The significant lagged correlation between winter SIMS $\delta^{18}O_{shell}$ values and the NAO could be attributed to the stepwise hydrologic response observed across the Baltic Sea region to freshwater forcing from the NAO. Freshwater runoff into the Baltic Sea lags the NAO index by a few months, with salinity lagging further behind freshwater runoff within one year (Hänninen et al., 2000). The spread in these lag times is largely due to the broad range of residence times (hours to years) that water exhibits across the Baltic Sea region, both in the Baltic Sea itself and in its various watersheds (Ehlin, 1981; Bergström and Carlsson, 1994; Hänninen et al., 2000). Given that our site is located in the Arkona basin subregion near the mouth of the Baltic Sea, we hypothesize that the SIMS $\delta^{18}O_{shell}$ dataset is capturing an integrated signal of freshwater flux derived from melting snow and ice, the volume of which is largely controlled by the state of previous years' NAO. This hydroclimatic link between the NAO and SIMS $\delta^{18}O_{shell}$ values on interannual timescales is further supported by the significant correlation between SIMS $\delta^{18}O_{shell}$ values and *in situ* salinity when both datasets are binned annually and salinity leads by one-year (Figure A.2; n = 23, r^2 = 0.29, p = 0.007). We observe that the lagged correlation analysis conducted specifically on winter $\delta^{18}O_{shell}$ values and the NAO index exhibits a higher coefficient of determination than the lagged correlation analysis conducted between annually binned $\delta^{18}O_{shell}$ values and salinity. We postulate this could be due to: (a) the coarser sampling resolution in the *in situ* salinity dataset precluding a winter-only comparison with SIMS $\delta^{18}O_{shell}$ values, and (b) the influence of the NAO index on both temperature and $\delta^{18}O_{water}$.

2.4.4 Conclusions

This study presents the first multidecadal $\delta^{18}O$ time series generated from an *A. borealis shell* using SIMS. At sub-monthly resolution, we find that the SIMS $\delta^{18}O_{shell}$ time series is significantly correlated to *in situ* temperatures at the mouth of the Baltic Sea (r^2 = 0.52), as well as regional SST across the Baltic Sea based on ORAS5 SST estimates (r^2 = 0.42). The strongest correlation emerges when comparing the interannual components of the SIMS $\delta^{18}O_{shell}$ dataset and salinity (r^2 = 0.71). We observe a moderate correlation between the interannual components of the SIMS $\delta^{18}O_{shell}$ dataset and the NAO Index (r^2 = 0.46), where SIMS $\delta^{18}O_{shell}$ values capture a well-documented regime shift circa 1989 (Lehmann et al., 2011). We hypothesize that this coupling emerges as a result of NAO-related climate effects creating constructive interference between SST and $\delta^{18}O_{water}$ values at the southern

margin of the Baltic Sea on interannual timescales, thereby imposing a strong environmental signal onto the SIMS $\delta^{18}O_{shell}$ dataset. The integrated hydroclimate signal captured at our site by the SIMS $\delta^{18}O_{shell}$ dataset is further supported by a significant correlation between binned DJFM winter $\delta^{18}O_{shell}$ values with the previous years' winter NAO Index (r^2 = 0.39). Our analyses indicate that SIMS $\delta^{18}O_{shell}$ values in *A. borealis* from the Baltic Sea are a potentially rich source of paleoclimate information, with capabilities of reconstructing the mid-to-high latitude component of the NAO during the Holocene at sub-monthly resolution over decadal timescales.

2.5 Funding

Funding for this study was provided by the US National Science Foundation (NSF) to Surge (EAR-1656974). The WiscSIMS Laboratory is supported by the US NSF (Grant EAR-1355590 and EAR-1658823). Long-term environmental data for Figure 2.2A, B were obtained within the framework of the German Baltic Sea Monitoring financed by the Federal Maritime and Hydrographic Agency (BSH) and carried out by the Leibniz Institute for Baltic Sea Research (IOW).

2.6 Acknowledgments

Dr. Jonathan Lees is gratefully acknowledged for his helpful suggestions towards analyzing temporal variations in the SIMS $\delta^{18}O_{shell}$ dataset. We also thank Garrett Braniecki for helpful insights into analyzing growth variations in specimen RFP3S-47. Comments from three anonymous reviewers helped improve this manuscript and were greatly appreciated.

BIBLIOGRAPHY

A. D. Ansell. The rate of growth of the hard clam mercenaria mercenaria) throughout the geographical range. *ICES J. Mar. Sci.*, 31(3):364–409, 1968. ISSN 1054-3139. doi: 10.1093/icesjms/31.3.364.

R. Barker. Microtextural variation in pelecypod shells. *Malacologia*, 2:69–86, 1964.

D. F. Bauer. Constructing confidence sets using rank statistics. *J. Am. Stat. Assoc.*, 67(339):687–690, 1972. ISSN 0162-1459. doi: 10.1080/01621459.1972.10481279.

J. Beck, R. L. Edwards, E. Ito, F. W. Taylor, J. Recy, F. Rougerie, P. Joannot, and C. Henin. Sea-surface temperature from coral skeletal strontium/calcium ratios. *Science*, 257:644–647, 1992. doi: 10.1126/science.257.5070.644.

S. Bergström and B. Carlsson. River runoff to the baltic sea - 1950-1990. *Ambio*, 23(4-5):280–287, 1994. ISSN 00447447 (ISSN) 16547209 (EISSN).

J. A. Carton, S. G. Penny, and E. Kalnay. Temperature and salinity variability in the soda3, ecco4r3, and oras5 ocean reanalyses, 1993–2015. *J. Clim.*, 32(8):2277–2293, 2019. ISSN 0894-8755. doi: 10.1175/jcli-d-18-0605.1.

G. R. Clark. Growth lines in invertebrate skeletons. *Ann. Rev. Earth Planet Sci.*, 2(1):77–99, 1974. doi: 10.1146/annurev.ea.02.050174.000453.

W. S. Cleveland. Robust locally weighted regression and smoothing scatterplots. *J. Am. Stat. Assoc.*, 74(368):829–836, 1979. ISSN 0162-1459. doi: 10.1080/01621459.1979.10481038.

T. B. Coplen. Reporting of stable hydrogen, carbon, and oxygen isotopic abundances (technical report). *Pure Appl. Chem.*, 66(2):273–276, 1994. doi: 10.1351/pac199466020273.

D. L. Dettman and K. C. Lohmann. Seasonal change in paleogene surface water : Fresh-water bivalves of western north america. In P. K. Swart, K. C. Lohmann, J. McKenzie, and S. Savin, editors, *American Geophysical Union*, pages 153–163. doi: 10.1029/GM078p0153.

D. L. Dettman and K. C. Lohmann. Microsampling carbonates for stable isotope and minor element analysis: Physical separation of samples on a 20 micrometer scale. *J. Sed. Res.*, 65A(3):566–569, 1995.

D. L. Dettman, A. K. Reische, and K. C. Lohmann. Controls on the stable isotope composition of seasonal growth bands in aragonitic fresh-water bivalves (unionidae). *Geochim. Cosmochim. Acta*, 63(7):1049–1057, 1999. ISSN 0016-7037. doi: 10.1016/S0016-7037(99)00020-4.

R. R. Dickson and K. M. Brander. Effects of a changing windfield on cod stocks of the north atlantic. *Fish. Oceanogr.*, 2(3-4):124–153, 1993. ISSN 1054-6006. doi: 10.1111/j.1365-2419.1993.tb00130.x.

E. Dunca, H. Mutvei, P. Göransson, C.-M. Mörth, B. R. Schöne, M. J. Whitehouse, M. Elfman, and S. P. Baden. Using ocean quahog (arctica islandica) shells to reconstruct palaeoenvironment in Öresund, kattegat and skagerrak, sweden. *Int. J. Earth Sci.*, 98(1):3–17, 2009. ISSN 1437-3262. doi: 10.1007/s00531-008-0348-6.

U. Ehlin. *Hydrology of the Baltic Sea*, volume 30, book section 2, pages 123–134. Elsevier, Amsterdam, 1981. ISBN 0422-9894. doi: 10.1016/S0422-9894(08)70139-9.

M. Elliot, P. B. deMenocal, B. K. Linsley, and S. S. Howe. Environmental controls on the stable isotopic composition of mercenaria mercenaria: Potential application to paleoenvironmental studies. *Geochem. Geophys. Geosyst.*, 4(7):1–16, 2003. ISSN 1525-2027. doi: 10.1029/2002GC000425.

L. W. Fritz. *Chapter 2 Shell structure and age determination*, volume 31, pages 53–76. Elsevier, Amsterdam, 2001. ISBN 0167-9309. doi: https://doi.org/10.1016/S0167-9309(01)80030-2.

K. Frohlich, J. Grabczak, and K. Rozanski. Deuterium and oxygen-18 in the baltic sea. *Chem. Geol.*, 72(1):77–83, 1988. ISSN 0168-9622. doi: 10.1016/0168-9622(88)90038-3.

D. H. Goodwin, K. Flessa, B. R. Schöne, and D. L. Dettman. Cross-calibration of daily growth increments, stable isotope variation, and temperature in the gulf of california bivalve mollusk chione cortezi: implications for paleoenvironmental analysis. *PALAIOS*, 16(4):387–398, 2001. doi: 10.1669/0883-1351(2001)016⟨0387:CCODGI⟩2.0.CO;2.

D. H. Goodwin, B. R. SchoNe, and D. L. Dettman. Resolution and fidelity of oxygen isotopes as paleotemperature proxies in bivalve mollusk shells: Models and observations. *PALAIOS*, 18(2):110–125, 2003. ISSN 0883-1351. doi: 10.1669/0883-1351(2003)18⟨110:RAFOOI⟩2.0.CO;2.

D. H. Goodwin, D. P. Gillikin, E. N. Jorn, M. C. Fratian, and A. D. Wanamaker. Comparing contemporary biogeochemical archives from mercenaria mercenaria and crassostrea virginica: Insights on paleoenvironmental reconstructions. *Palaeogeogr. Palaeocl.*, 562:110110, 2021. ISSN 0031-0182. doi: 10.1016/j.palaeo.2020.110110.

A. J. P. Harwood, P. F. Dennis, A. D. Marca, G. M. Pilling, and R. S. Millner. The oxygen isotope composition of water masses within the north sea. *Estuar. Coast.*, 78(2):353–359, 2008. ISSN 0272-7714. doi: 10.1016/j.ecss.2007.12.010.

T. E. Helser, C. R. Kastelle, J. L. McKay, I. J. Orland, R. Kozdon, and J. W. Valley. Evaluation of micromilling/conventional isotope ratio mass spectrometry and secondary ion mass spectrometry of 18o values in fish otoliths for sclerochronology. *Rapid Commun. Mass. Sp.*, 32(20):1781–1790, 2018. ISSN 0951-4198. doi: 10.1002/rcm.8231.

J. Hu, J. Emile-Geay, and J. Partin. Correlation-based interpretations of paleoclimate data–where statistics meet past climates. *Earth Planet. Sc. Lett.*, 459:362–371, 2017. doi: 10.1016/j.epsl.2016.11.048.

J. Hurrell. Decadal trends in the north atlantic oscillation: Regional temperatures and precipitation. *Science*, 269 (5224):676–679, 1995. doi: 10.1126/science.269.5224.676.

J. Hänninen, I. Vuorinen, and P. Hjelt. Climatic factors in the atlantic control the oceanographic and ecological changes in the baltic sea. *Limnol. Oceanogr.*, 45(3):703–710, 2000. ISSN 0024-3590. doi: 10.4319/lo.2000.45.3.0703.

D. S. Jones and I. R. Quitmyer. Marking time with bivalve shells: Oxygen isotopes and season of annual increment formation. *PALAIOS*, 11(4):340–346, 1996. ISSN 08831351, 19385323. doi: 10.2307/3515244.

D. S. Jones, D. F. Williams, and M. A. Arthur. Growth history and ecology of the atlantic surf clam, spisula solidissima (dillwyn), as revealed by stable isotopes and annual shell increments. *J. Exp. Mar. Biol. Ecol.*, 73(3):225–242, 1983. ISSN 0022-0981. doi: 10.1016/0022-0981(83)90049-7.

P. D. Jones, T. J. Osborn, and K. R. Briffa. *Pressure-Based Measures of the North Atlantic Oscillation (NAO): A Comparison and an Assessment of Changes in the Strength of the NAO and in its Influence on Surface Climate Parameters*, pages 51–62. 2003. doi: 10.1029/134GM03.

R. Killick, P. Fearnhead, and I. A. Eckley. Optimal detection of changepoints with a linear computational cost. *J. Am. Stat. Assoc.*, 107(500):1590–1598, 2012. ISSN 0162-1459. doi: 10.1080/01621459.2012.737745.

R. T. Klein, K. C. Lohmann, and C. W. Thayer. Bivalve skeletons record sea-surface temperature and 18o via mg/ca and 18o/16o ratios. *Geology*, 24(5):415–418, 1996. ISSN 0091-7613. doi: 10.1130/0091-7613(1996)024⟨0415:Bsrsst⟩2.3.Co;2.

R. Kozdon, T. Ushikubo, N. T. Kita, M. Spicuzza, and J. W. Valley. Intratest oxygen isotope variability in the planktonic foraminifer *N. pachyderma*: Real vs. apparent vital effects by ion microprobe. *Chem. Geol.*, 258(3):327–337, 2009. ISSN 0009-2541. doi: 10.1016/j.chemgeo.2008.10.032.

A. Lehmann, K. Getzlaff, and J. Harlaß. Detailed assessment of climate variability in the baltic sea area for the period 1958 to 2009. *Clim. Res.*, 46(2):185–196, 2011. ISSN 0936-577X. doi: 10.3354/cr00876.

B. J. Linzmeier, R. Kozdon, S. E. Peters, and J. W. Valley. Oxygen isotope variability within nautilus shell growth bands. *PLoS ONE*, 11(4):e0153890, 2016. doi: 10.1371/journal.pone.0153890.

M. E. Matta, I. J. Orland, T. Ushikubo, T. E. Helser, B. A. Black, and J. W. Valley. Otolith oxygen isotopes measured by high-precision secondary ion mass spectrometry reflect life history of a yellowfin sole (limanda aspera). *Rapid Commun. Mass. Sp.*, 27:691–699, 2013. doi: 10.1002/rcm.6502.

D. K. Moss, L. C. Ivany, E. J. Judd, P. W. Cummings, C. E. Bearden, W.-J. Kim, E. G. Artruc, and J. R. Driscoll. Lifespan, growth rate, and body size across latitude in marine bivalvia, with implications for phanerozoic evolution. *Proc. R. Soc. Lond.*, 283(1836):20161364, 2016. doi: 10.1098/rspb.2016.1364.

D. K. Moss, D. Surge, and V. Khaitov. Lifespan and growth of astarte borealis (bivalvia) from kandalaksha gulf, white sea, russia. *Polar Biol.*, 41(7):1359–1369, 2018. ISSN 1432-2056. doi: 10.1007/s00300-018-2290-9.

D. K. Moss, D. Surge, M. L. Zettler, I. J. Orland, A. Burnette, and A. Fancher. Age and growth of astarte borealis (bivalvia) from the southwestern baltic sea using secondary ion mass spectrometry. *Mar. Biol.*, 168(8):133, 2021. ISSN 1432-1793. doi: 10.1007/s00227-021-03935-7.

J. Oertzen. Abiotic potency and physiological resistance of shallow and deep water bivalves. *Oikos*, pages 261–266, 1973.

J. Oertzen and S. Schulz. Beitrag zur geographischen verbreitung und ökologischen resistenz von bivalviern der ostsee. *Beitr. Meereskd.*, 32:75–88, 1973.

I. C. Olson, R. Kozdon, J. W. Valley, and P. U. P. A. Gilbert. Mollusk shell nacre ultrastructure correlates with environmental temperature and pressure. *J. Am. Chem. Soc.*, 134(17):7351–7358, 2012. ISSN 0002-7863. doi: 10.1021/ja210808s.

K. L. Palmer, D. K. Moss, D. Surge, and S. Turek. Life history patterns of modern and fossil mercenaria spp. from warm vs. cold climates. *Palaeogeogr. Palaeocl.*, 566:110227, 2021. ISSN 0031-0182. doi: 10.1016/j.palaeo.2021.110227.

G. Pannella. Tidal growth patterns in recent and fossil mollusc bivalve shells: a tool for the reconstruction of paleotides. *The Science of Nature*, 63(12):539–543, 1976. ISSN 1432-1904. doi: 10.1007/BF00622786.

G. Pannella and C. MacClintock. Biological and environmental rhythms reflected in molluscan shell growth. *Memoir (The Paleontological Society)*, 2:64–80, 1968. ISSN 00788597, 19372833.

J. G. Pinto and C. C. Raible. Past and recent changes in the north atlantic oscillation. *WIREs Clim. Change*, 3(1):79–90, 2012. ISSN 1757-7780. doi: 10.1002/wcc.150.

A. L. Prendergast, E. A. A. Versteegh, and B. R. Schöne. New research on the development of high-resolution palaeoenvironmental proxies from geochemical properties of biogenic carbonates. *Palaeogeogr. Palaeocl.*, 484:1–6, 2017. ISSN 0031-0182. doi: 10.1016/j.palaeo.2017.05.032.

I. R. Quitmyer, D. S. Jones, and W. S. Arnold. The sclerochronology of hard clams,mercenariaspp., from the south-eastern u.s.a.: A method of elucidating the zooarchaeological records of seasonal resource procurement and seasonality in prehistoric shell middens. *J. Archaeol. Sci.*, 24(9):825–840, 1997. ISSN 0305-4403. doi: 10.1006/jasc.1996.0163.

D. J. Reynolds, V. R. von Biela, K. H. Dunton, D. C. Douglas, and B. A. Black. Sclerochronological records of environmental variability and bivalve growth in the pacific arctic. *Prog. Oceanogr.*, 206:102864, 2022. ISSN 0079-6611. doi: 10.1016/j.pocean.2022.102864.

J. C. Rogers. The association between the north atlantic oscillation and the southern oscillation in the northern hemisphere. *Mon. Weather Rev.*, 112(10):1999–2015, 1984. ISSN 0027-0644. doi: 10.1175/1520-0493(1984)112⟨1999:TABTNA⟩2.0.CO;2.

H. Schinke and W. Matthäus. On the causes of major baltic inflows —an analysis of long time series. *Cont. Shelf Res.*, 18(1):67–97, 1998. ISSN 0278-4343. doi: 10.1016/S0278-4343(97)00071-X.

C.-F. Schumacher. *Essai d'un nouveau système des habitations des vers testacés: avec XXII planches*. Imprimeire de M. le directeur Schultz, Copenhagen, 1817.

B. R. Schöne and D. P. Gillikin. Unraveling environmental histories from skeletal diaries — advances in sclerochronology. *Palaeogeogr. Palaeocl.*, 373:1–5, 2013. ISSN 0031-0182. doi: 10.1016/j.palaeo.2012.11.026.

B. R. Schöne and D. Surge. *Bivalve Schlerochronology and Geochemistry*, volume 1, book section 14. Paleontological Institute, Lawrence, Kansas, 2012.

B. R. Schöne, A. D. Freyre Castro, J. Fiebig, S. D. Houk, W. Oschmann, and I. Kröncke. Sea surface water temperatures over the period 1884–1983 reconstructed from oxygen isotope ratios of a bivalve mollusk shell (arctica islandica, southern north sea). *Paleoceanogr. Paleoclimatol.*, 212(3):215–232, 2004. ISSN 0031-0182. doi: 10.1016/j.palaeo.2004.05.024.

B. R. Schöne, J. Fiebig, M. Pfeiffer, R. Gle, J. Hickson, A. L. A. Johnson, W. Dreyer, and W. Oschmann. Climate records from a bivalved methuselah (arctica islandica, mollusca; iceland). *Palaeogeogr. Palaeocl.*, 228(1):130–148, 2005. ISSN 0031-0182. doi: 10.1016/j.palaeo.2005.03.049.

S. M. Stanley. Paleoecology and diagenesis of key largo limestone, florida. *AAPG Bull.*, 50:1927–1947, 1966. doi: 10.1306/5d25b6a9-16c1-11d7-8645000102c1865d.

D. Surge and K. J. Walker. Geochemical variation in microstructural shell layers of the southern quahog (mercenaria campechiensis): Implications for reconstructing seasonality. *Palaeogeography, Palaeoclimatology, Palaeoecology*, 237(2):182–190, 2006. ISSN 0031-0182. doi: https://doi.org/10.1016/j.palaeo.2005.11.016.

D. Surge, K. C. Lohmann, and D. L. Dettman. Controls on isotopic chemistry of the american oyster, crassostrea virginica: implications for growth patterns. *Palaeogeogr. Palaeocl.*, 172(3):283–296, 2001. ISSN 0031-0182. doi: 10.1016/S0031-0182(01)00303-0.

D. M. Surge and B. R. Schöne. *Bivalve sclerochronology*, pages 108–115. Springer Netherlands, Berlin-Heidelberg, 2015. doi: 10.1007/978-94-007-6326-5_165-1.

M. E. Torres, D. Zima, K. K. Falkner, R. W. Macdonald, M. O'Brien, B. R. Schöne, and T. I. M. Siferd. Hydrographic changes in nares strait (canadian arctic archipelago) in recent decades based on 18o profiles of bivalve shells. *Arctic*, 64(1):45–58, 2011. ISSN 00040843.

C. Truong, L. Oudre, and N. Vayatis. Selective review of offline change point detection methods. *Signal Processing*, 167:107299, 2020. ISSN 0165-1684. doi: 10.1016/j.sigpro.2019.107299.

J. W. Tukey. *Exploratory Data Analysis*, volume 2. Addison-Wesley, Reading, MA, 1977.

M. Vihtakari, P. E. Renaud, L. J. Clarke, M. J. Whitehouse, H. Hop, M. L. Carroll, and W. G. Ambrose. Decoding the oxygen isotope signal for seasonal growth patterns in arctic bivalves. *Palaeogeogr. Palaeocl.*, 446:263–283, 2016. ISSN 0031-0182. doi: 10.1016/j.palaeo.2016.01.008.

C. R. Weidman, G. A. Jones, and Kyger. The long-lived mollusc arctica islandica: A new paleoceanographic tool for the reconstruction of bottom temperatures for the continental shelves of the northern north atlantic ocean. *J. Geophys. Res-Oceans*, 99(C9):18305–18314, 1994. ISSN 0148-0227. doi: 10.1029/94JC01882.

I. Winkelstern, D. Surge, and J. W. Hudley. Multiproxy sclerochronological evidence for plio-pleistocene regional warmth: United states mid-atlantic coastal plain. *PALAIOS*, 28(9):649–660, 2013. ISSN 0883-1351. doi: 10.2110/palo.2013.p13-010r.

R. Witbaard, M. I. Jenness, K. Van Der Borg, and G. Ganssen. Verification of annual growth increments in arctica islandica l. from the north sea by means of oxygen and carbon isotopes. *Neth. J. Sea. Res.*, 33(1):91–101, 1994. ISSN 0077-7579. doi: 10.1016/0077-7579(94)90054-X.

J. B. Wycech, D. C. Kelly, R. Kozdon, I. J. Orland, H. J. Spero, and J. W. Valley. Comparison of 18o analyses on individual planktic foraminifer (orbulina universa) shells by sims and gas-source mass spectrometry. *Chem. Geol.*, 483:119–130, 2018. ISSN 0009-2541. doi: 10.1016/j.chemgeo.2018.02.028.

M. L. Zettler. Ecological and morphological features of the bivalve astarte borealis (schumacher, 1817) in the baltic sea near its geographical range. *J. Shellfish Res.*, 21(1):33–40, 2002. ISSN ISSN: 0730-8000 EISSN: 1943-6319.

M. L. Zettler, R. Friedland, M. Gogina, and A. Darr. Variation in benthic long-term data of transitional waters: Is interpretation more than speculation? *PLoS ONE*, 12(4):e0175746, 2017. doi: 10.1371/journal.pone.0175746.

H. Zuo, M. A. Balmaseda, S. Tietsche, K. Mogensen, and M. Mayer. The ecmwf operational ensemble reanalysis–analysis system for ocean and sea ice: a description of the system and assessment. *Ocean Sci.*, 15(3):779–808, 2019. ISSN 1812-0792. doi: 10.5194/os-15-779-2019.

CHAPTER 3

Synthetic and Practical Reconstructions of SST and Seawater pH Using the Novel Multiproxy SMITE Method

3.1 Introduction

Tropical sea surface temperature (SST) is a critical component of the climate system, linked to a multitude of key variables such as atmospheric moisture content and temperature, cloud cover, and patterns of atmospheric circulation (Hastenrath, 2012). However, the evolution of tropical SST prior to and during the industrial era remains uncertain due to poor data coverage and changing measurement technology (Kent and Kennedy, 2021). This uncertainty has significant consequences for attempts to establish a baseline for present-day climate change, impacting our abilities to meet internationally agreed-upon climate targets (Hawkins et al., 2017). Towards this end, massive reef-building (scleractinian) corals have been extensively utilized to reconstruct variations in SST throughout the Holocene (Thompson, 2021), thereby filling a critical gap in our knowledge with respect to tropical SST variability.

Over the past several decades, numerous geochemical tracers in scleractinian coral skeletons have been calibrated to local environmental parameters (Sadler et al., 2014), which in turn have been used to reconstruct regional climate variability from seasonal to centennial timescales (Jones et al., 2009). Under ideal conditions, a single coral geochemical proxy is largely a function of the climate target of interest, with minimal influence from other variables such as coral growth variations, analytical error, or age model uncertainty. When these conditions are met, coral skeletal geochemistry can be used to robustly reconstruct climate targets such as SST, sea surface salinity (SSS), and seawater pH (pH_{sw}), often at monthly resolution (D'Olivo et al., 2019; Grothe et al., 2020; Ong et al., 2022).

The degree of accuracy, precision, correlation, and reproducibility in any coral-based climate reconstruction is often a function of many factors, including (but not limited to): how much natural variability the climate target of interest exhibits in a given location; the uncertainty associated with the chosen observations of the climate target (e.g., *in situ* SST observations versus those derived from remote sensing products); the concentrations of the geochemical proxy in the coral skeleton; how sensitive the geochemical proxy is to the climate target; whether this sensitivity is consistent, both between coral colonies as well as throughout the skeleton of an individual colony; the degree to which other internal or external processes create interference in the relationship between the proxy and the climate target; and whether the age model error is reasonable within the resolution and length of the climate reconstruction.

For example, skeletal strontium-to-calcium ratios (Sr/Ca) are the most commonly used coral-based paleothermometer to date (Beck et al., 1992; Walter et al., 2023). SST exhibits strong annual cycles even in tropical oceans ($\sim$2°C), and while *in situ* observations of SST in the tropical oceans can be scarce, remote sensing products are becoming increasingly better at capturing SST variations on coral reefs (Merchant et al., 2019), thereby reducing uncertainty with respect to the climate target. Despite a relatively low temperature sensitivity ($\sim$0.06 mmol $mol^{-1}{}^{o}C^{-1}$ Corrège, 2006), the high degree of analytical precision for measuring Sr/Ca using inductively coupled plasma optical emission spectrometry (ICP-OES Schrag, 1999) often yields high precision Sr/Ca-based SST estimates (e.g. $\pm$ 0.16°C, 1σ). However, analytical uncertainty for Sr/Ca increases by an order of magnitude when using inductively coupled plasma mass spectrometry (ICP-MS), particularly when coupled with laser ablation (Kawakubo et al., 2014). This is but one contributing factor to the high degree of uncertainty around the regression coefficients for the Sr/Ca – SST relationship, which often vary between taxa, regions, regression techniques, and even different laboratories using similar analytical equipment (Corrège, 2006; Hathorne et al., 2013b; Xu et al., 2015; Fowell et al., 2016; Ross et al., 2019; Stewart et al., 2020). Uncertainty surrounding the Sr/Ca – SST relationship have also been attributed to biological controls on Sr uptake into the coral aragonite crystal lattice (Sinclair et al., 2006; Kuffner et al., 2012; Grove et al., 2013; Hirabayashi et al., 2013; Alpert et al., 2016; Hetzinger et al., 2016; Clarke et al., 2017; D'Olivo and McCulloch, 2017; Clarke et al., 2019; Reed et al., 2021). Recent work also suggests that nutrient conditions can create substantial non-SST-related variability in coral Sr/Ca ratios (Standish et al., 2023). While much work has gone into improving the reproducibility of coral Sr/Ca-derived SST estimates (Stephans et al., 2004; Allison and Finch, 2009; DeLong et al., 2013, 2016; Sayani et al., 2019; Stewart et al., 2020), the wide distribution of coral Sr/Ca regression coefficients often necessitates colony-specific Sr/Ca – SST calibrations, making applications of coral Sr/Ca paleothermometry to fossil coral material challenging at the present time (Goodkin et al., 2007; DeLong et al., 2010).

In the last decade, calibrations using multiple temperature-sensitive proxies, or multiproxy calibrations, have been developed specifically to minimize or even circumvent non-SST-related variability (Gaetani et al., 2011; Hathorne et al., 2013a; Saenger and Wang, 2014; DeCarlo et al., 2016; D'Olivo et al., 2018; Sinclair, 2015). These multiproxy paleothermometers often produce regression coefficients that are more consistent across corals from different regions and taxa (DeCarlo et al., 2016; D'Olivo et al., 2018; Wu et al., 2021). However, this reproducibility comes at the expense of sampling resolution (DeCarlo et al., 2016) or reconstruction skill relative to the best single-proxy estimator from any given location (D'Olivo et al., 2018; Sinclair, 2015; Wu et al., 2021). Furthermore, these multiproxy calibration methods have exclusively focused on SST, leaving other important climate targets such as pH_{sw} untested (McCulloch et al., 2017; Gagnon et al., 2021). This is especially relevant, as the primary coral geochemical proxy for pH_{sw} is its boron isotopic composition ($\delta^{11}B$). However, it is becoming increasingly apparent that coral skeletal $\delta^{11}B$ ratios are a function of SST, SSS, and the pH of the coral calcifying fluid (pH_{cf}), which is up-

regulated by the coral organism and exhibits increased seasonal variance relative to the pH_{sw} (D'Olivo et al., 2019; McCulloch et al., 2017; Zeebe and Wolf-Gladrow, 2001; Gagnon et al., 2021).

This study presents a novel multiproxy method for reconstructing SST and pH_{sw} across an array of coral geochemical variables. Utilizing the generalized inverse solution (Moore, 1920; Penrose, 1955), our novel Scleractinian Multivariate Isotope and Trace Element (SMITE) method leverages covariance across multiple proxies to improve the correlation, accuracy, and precision of the reconstruction (henceforth referred to as 'reconstruction skill') while yielding reproducible and mechanistically sensible regression coefficients. We first explain how the SMITE method applies the generalized inverse solution to calibrate coral geochemical data (or any coral variable) to SST and pH_{sw}. Next, we utilize a synthetic proxy dataset (Sr/Ca, δ^{18}O, and δ^{11}B) where the climate targets used to create each 'pseudoproxy' are known (SST, SSS, pH_{sw}) to explore the effects of analytical noise (random and autocorrelated) and calibration period length on both SMITE SST and pH_{sw} reconstructions. Then, as proof-of-concept, we apply the SMITE method to an array of seven coral variables (B/Ca, δ^{11}B, Li/Ca, Mg/Ca, Sr/Ca, U/Ca & Li/Mg) measured on two *Porites astreoides* corals collected from the northern fringing reef of Bermuda. These six unique geochemical variables (with the addition of Li/Mg) were chosen to capture a wide array of potential temperature and pH_{sw} dependencies to maximize covariance between the coral variable field and the reconstruction targets. We then examine two ways in which users can exercise control on SMITE reconstruction skill: through selective exclusion of coral variables in the SMITE method, and through a regularization technique that helps constrain SMITE model parameters with minimal impact on reconstruction skill. Finally, based on these findings, we provide a list of recommendations for new SMITE users while suggesting key areas where its use would best improve coral-based climate reconstructions.

3.2 Materials and methods

3.2.1 SMITE method theory and derivation

Multivariate estimations of any climate target from an array of coral variables (e.g., Sr/Ca, δ^{11}B, linear extension rate) can be represented as a classic inverse problem:

$$Ax = b \tag{3.1}$$

Where *A* is a matrix of age-modeled coral variables, with *p* columns denoting each unique variable and *t* rows denoting time. Vector *b* is of length *t* denoting the climate target across time; and *x* is a vector of length *p* denoting the model parameters that relate *A* to *b*. Thus, *x* contains the regression coefficients that correspond to each coral vari-

able in the A matrix and its relationship to b. Ideally, the matrix-vector product, or dot-product, of A and x would yield a perfect estimate of the climate target of interest, b.

If A has an inverse (A'), then x could easily be solved as $A'b$. Since only square matrices have inverses, one approach is to calculate the inverse of the square p by p correlation matrix of A, assign b as a vector of length p containing the correlation coefficients of each coral variable to the climate target, and then solve. However, coral variable data are often highly collinear, and so the model parameters (i.e., the regression coefficients contained in x) estimated by this approach would be highly unstable and non-reproducible across space and time.

To bypass the issue of collinearity, the SMITE method utilizes the generalized inverse, or pseudoinverse, solution (Moore, 1920; Penrose, 1955) to calculate model parameters for SST and pH_{sw} estimates from a non-specific array of coral variables. It begins by performing a singular value decomposition (SVD Lanczos, 1996; Golub and Van Loan, 2013) on the coral variable field.

$$A_a = USV^T \tag{3.2}$$

Where A_a is a matrix of age-modeled z-score normalized ($\mu = 0$, $\sigma = 1$) coral variables, with p columns denoting each variable and t rows denoting time. According to the SVD, A_a can be decomposed into three orthogonal matrices: U, S, and V, where U and V contain basis vectors spanning the data space and the column space, respectively. They are thus column-orthogonal to each other, and each contain the loadings or eigenvectors of the coral variable field. The diagonal matrix S contains the singular values of the coral variable field in descending order, representing the variance explained by each eigenvector (or percent variance explained, when normalized by the sum of the diagonal). The SVD and the eigendecomposition, a perhaps more familiar technique that is often used during Empirical Orthogonal Function analysis (North et al., 1982), yield identical results when applied to the covariance matrix of a particular data field. In this case, the eigenvalues calculated from the eigendecomposition are identical to the singular values calculated from the SVD, and the eigenvectors are identical to the U and V matrices. However, the SVD offers a number of additional benefits over the eigendecomposition, one of which is that it can be applied to non-square matrices (Susanto et al., 1998). Therefore, all information between coral variables is retained when calculating SMITE model parameters utilizing the SVD.

As mentioned before, A' cannot be determined because A is not square, and calculating the inverse of the covariance matrix of A creates collinearity and violates one of the basic assumptions of regression (independent predictor variables). However, we have shown that the z-score normalized coral variable field matrix A_a can be decomposed into three orthogonal matrices, for which an inverse does exist. Thus, a generalized inverse, or 'pseudoin-

verse', of the *A* matrix ($A_\dagger$) can be calculated by rearranging the terms of the decomposed *A* matrix.

$$A_\dagger = VS^{-1}U^T \tag{3.3}$$

Consequently, a pseudoinverse solution (Aster et al., 2018) can be calculated from the dot-product of $A_\dagger$ and *b*.

$$x_\dagger = A_\dagger b = VS^{-1}U^T b \tag{3.4}$$

Where $x_\dagger$ is a vector of length *p* containing the SMITE model parameters for each unique coral variable. Henceforth, we will simply refer to the $x_\dagger$ vector as SMITE model parameters. We will refer to the specific value of each SMITE model parameter as its '$x_\dagger$ value'. Thus, the dot-product of the z-score normalized coral variable field matrix and SMITE model parameters yield normalized estimates of the climate target of interest.

$$A_a x_\dagger = \hat{b}_a \tag{3.5}$$

These can then easily be converted to absolute estimates using the standard deviation (σ) and mean (μ) of the climate target in the calibration dataset.

$$\hat{b} = (\hat{b}_a * \sigma_b) + \mu_b \tag{3.6}$$

Importantly, the pseudoinversion of the *A* matrix and the calculation of $x_\dagger$ assumes that the columns of *A* exhibit a linear relationship to *b*. In the case of coral SST proxy data, the assumption of linearity often holds within a particular temperature range (Cuny-Guirriec et al., 2019). However, if nonlinearity is observed in a particular variable's relationship to the climate target of interest, it may be necessary to transform the coral variable prior to its entry into the *A* matrix so that it exhibits a more linear relationship to the climate target of interest.

Prior to calculating SMITE model parameters in Eq 3.4, higher order singular values (i.e., ones describing less variance in the dataset) and their corresponding basis vectors in *U* and *V* can be 'truncated' from the pseudoinverse of the coral variable field.

$$A_{\dagger T} = V_T S_T^{-1} U_T^T b_a \tag{3.7}$$

Where subscript *T* denotes that the corresponding matrix has had certain columns removed or truncated. This is a common regularization technique used in Principal Components Regression (Jolliffe, 1982). The accuracy, precision, correlation, and reproducibility of any SMITE reconstruction can vary depending on the level of regularization im-

plemented (see sections 3.3.3 and 3.4.2). Ideally, this step is taken to remove singular values that are close to zero and prevent the SMITE method from overfitting the model to random noise and variability not related to the climate target of interest. We provide guidance for choosing the optimum level of regularization in section 3.4.3.

The procedure for reconstructing SST or pH_{sw} from an array of coral variables using the SMITE method is listed below, along with a procedural diagram (Fig 3.1).

1. Age-modeled coral variables are arranged into a matrix with columns denoting each coral variable and rows denoting time (A).
2. A subset of A is created for calibration (A_c).
3. A_c is z-score normalized (A_{ac}; mean-subtracted, divided by the standard deviation).
4. SST is (if necessary) resampled to the same frequency as the coral variable data and z-score normalized (b_a).
5. An SVD is performed on A_{ac} to yield three orthogonal matrices, U, S, and V (Eq 3.2).
6. (OPTIONAL) The U, S, and V matrices are truncated to remove higher order singular values (Eq 3.7).
7. SMITE model parameters ($x_\dagger$) are calculated by rearranging the terms of the SVD (Eq 3.4).
8. A_{ac} and $x_\dagger$ are dot-multiplied to yield predicted climate target anomalies during the calibration period ($\hat{b}_a$) (Eq 3.5). To yield predicted climate anomalies for the entire length of the record, A must be z-score normalized using the mean and standard deviation of the calibration dataset (A_a) before it is dot-multiplied to $x_\dagger$.
9. Predicted climate target anomalies are converted to absolute climate target estimates ($\hat{b}$) using the mean and standard deviation from the calibration dataset (Eq 3.6).

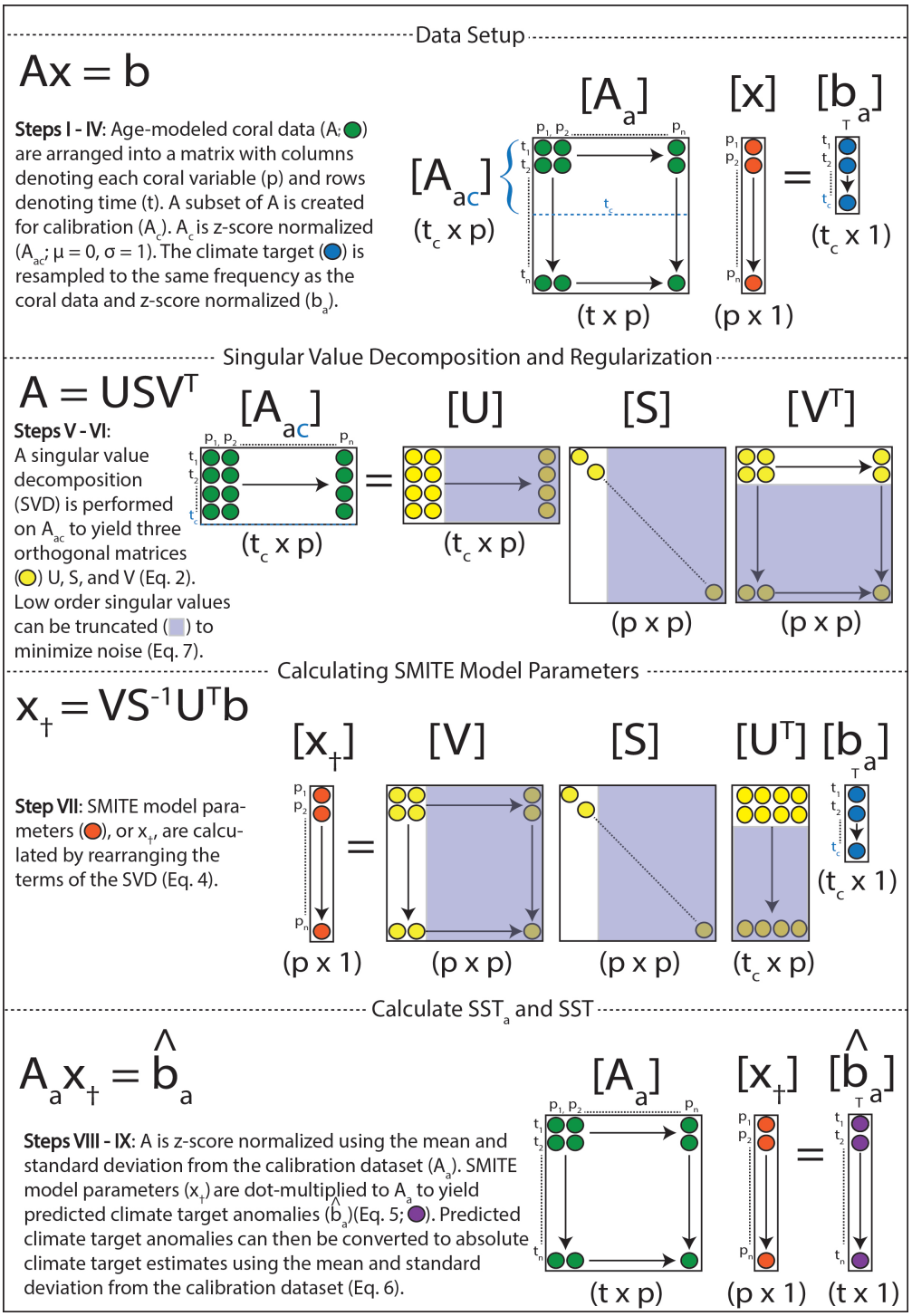

Figure 3.1: Procedural diagram for implementing the SMITE method on a coral variable dataset.

3.2.2 Synthetic pseudoproxy dataset

We created three synthetic 'pseudoproxies' (Sr/Ca, δ^{18}O, δ^{11}B) with various amounts of environmental information encoded into each, based on their theoretical dependence on SST, SSS and pH_{sw} (Fig 3.2). Because we

created this dataset with three coral variables and three potential climate targets, this is considered a square system (i.e., the number of predictor variables equals the number of unknown variables), which is important when considering regularization (see sections 3.3.3 and 3.4.2). The means by which we calculated these three synthetic pseudoproxies are highly idealized, meaning that each pseudoproxy has a near-perfect relationship with its corresponding climate target(s). However, the uncertainty in each proxy's relationship to the climate target is considered in our experimental design, which examines how uncertainty in reconstructed SST and pH_{sw} estimates increases as the degree of Gaussian and autocorrelated noise increases. The magnitude of Gaussian noise and autocorrelation considered in our experiment (Table 3.1) is beyond the typical range observed in most coral-based paleoclimate studies (Hathorne et al., 2013b; Jones et al., 2015; Standish et al., 2019). We expect therefore that all linear sources of uncertainty, and their subsequent impacts on SST and pH_{sw} estimates, are accounted for in this conservative analysis. The minimum uncertainty for each synthetic pseudoproxy was taken from the literature as analytical uncertainty. For synthetic Sr/Ca values, this was taken to be 0.009 mmol/mol, or approximately 0.1% RSD (Schrag, 1999). For synthetic $\delta^{18}O$ values, we used an analytical uncertainty of 0.1‰(Epstein and Mayeda, 1953). For synthetic $\delta^{11}B$ values, analytical uncertainty was taken to be 0.09‰(Stewart et al., 2021).

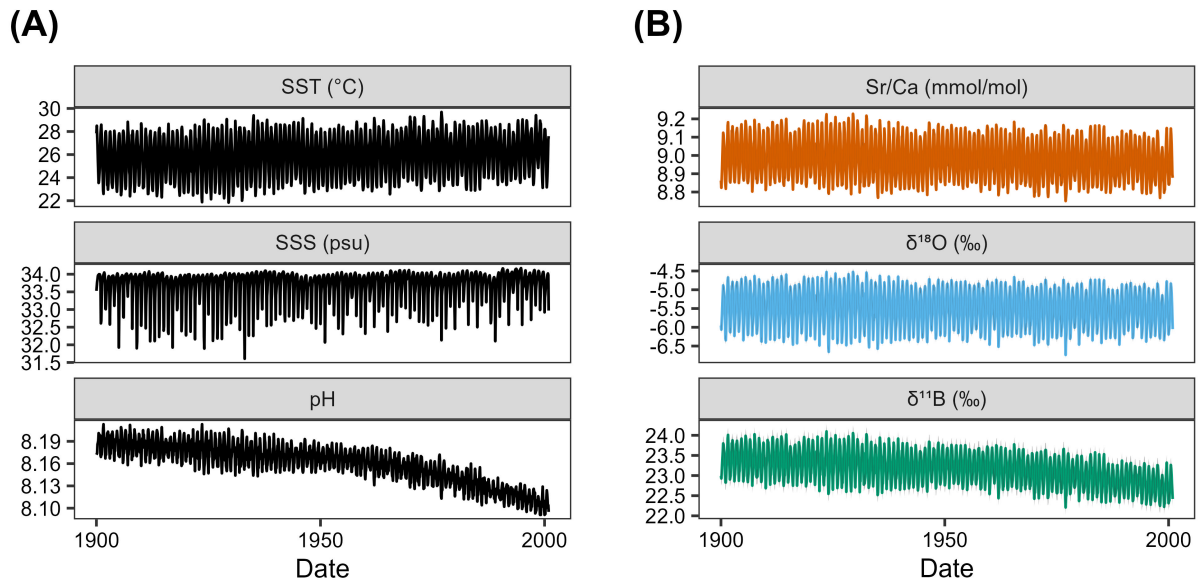

Figure 3.2: Monthly time series of three synthetic pseudoproxies (B) calculated from environmental information spanning the 20th century off the east coast of Australia (A) (Lenton et al., 2016; de Boisséson et al., 2018). The gray shaded region in each panel, which is barely visible, indicates the minimum (analytical) uncertainty associated with each pseudoproxy. All three pseudoproxies exhibit an idealized relationship with their corresponding environmental variable(s) of interest (Sr/Ca $\sim$ SST; $\delta^{18}O \sim$ SST + SSS; $\delta^{11}B \sim$ SST + SSS + pH_{sw}).

Monthly SST and pH_{sw} data from the Great Barrier Reef (18.5°S, 149.5°E) between 1900 and 2000 were acquired from Lenton et al. (2016), a 20th century reconstruction of SST, SSS and pH_{sw} across the Great Barrier

Table 3.1: Mean (μ), standard deviation (σ), range of analytical errors (ϵ), and correlation coefficients (r) for all synthetic proxies to each environmental variable.

Synthetic Proxy	μ	σ	ϵ_{min} - ϵ_{max} **(RSD)**	**r - SST**	**r - SSS**	**r - pH_{sw}**
Sr/Ca (mmol/mol)	8.98	0.12	0.009–0.180 (0.1–1.9%)	−1.00	0.68	0.54
δ^{18}**O (‰)**	−5.49	0.51	0.10–0.21 (1.8–3.7%)	−0.98	0.80	0.50
δ^{11}**B (‰)**	22.90	0.66	0.18–0.62 (0.78–2.68%)	−0.92	0.63	0.82

Reef (n = 1212). SSTs ranged from 21.83°C to 29.69°C (μ = 25.92°C ± 1.91, 1σ), with a minor but significant warming trend of 0.08°C per decade ($p < 0.0001$). Seawater pH ranged from 8.09 to 8.21 (μ = 8.16 ± 0.03) and exhibits two significant negative trends pre-1950 (0.004 units per decade) and post-1950 (0.014 units per decade). Although SSS data are also available from this dataset for the same time interval, these data simply repeat the same annual cycle of SSS throughout the 20th century with no interannual or decadal variability. To better reproduce long-term changes in SSS, we used SSS data from the ORA20C dataset (de Boisséson et al., 2018) from the same location and time interval. This dataset extends back through the 20th century and is an advanced data assimilation product that tunes the output of the European Center for Medium-range Weather Forecasts twentieth century reanalysis, ERA-20C, to *in situ* observations. SSS variations from this location in the ORA20C dataset exhibit a highly skewed left distribution (μ = 33.69 ± 0.43 psu), with values ranging from 31.61 to 34.17 due to episodic freshwater runoff events.

According to hindcast archived data from the CSIRO Environmental Modelling Suite implemented by the Australian Institute of Marine Science (https://research.csiro.au/cem/software/ems/), SSS in this region between 2010 and 2022 ranged from 34.7 to 35.6 psu and exhibit a slightly skewed left distribution (μ = 35.23 ± 0.16 psu). We acknowledge that the distributions of ORA20C and CSIRO SSS are statistically distinct from one another, both in terms of mean and variance ($p < 0.001$). However, the purpose of including SSS in the synthetic experiment is to create interference in both synthetic δ^{18}O and δ^{11}B values for reconstructing SST and pH_{sw}, respectively. Thus, there are two important aspects of SSS that we wish to reproduce for the purposes of this experiment: long-term variability (interannual to decadal), and the covariance between SSS and SST. The ORA20C SSS dataset for this region exhibits substantial interannual and decadal-scale variability, while the Lenton et al. (2016) SSS dataset exhibits none. With respect to covariance, the CSIRO dataset shows that SST and SSS are moderately anti-correlated in this region (r = −0.58). SST and SSS data from Lenton et al. (2016) exhibit a slightly weaker anti-correlation (r

= −0.53), while SST data from Lenton et al. (2016) and ORA20C SSS exhibit a slightly stronger anti-correlation (r = −0.68). Since ORA20C SSS exhibits both long-term variability and similar covariance to SST as the observed CSIRO data, we chose to use the ORA20C SSS dataset for our synthetic experiment.

Synthetic Sr/Ca ratios were calculated as a function of SST using the mean slopes and intercepts for the Sr/Ca ∼ SST relationship from Corrège (2006).

$$Sr/Ca_c = -0.0607(0.0090)SST + 10.553(0.292)SSS \tag{3.8}$$

Where *SST* is sea surface temperature in degrees Celsius. Synthetic Sr/Ca (Sr/Ca_c) ratios ranged from 8.75 to 9.23 mmol/mol (μ = 8.98 mmol/mol ± 0.12).

Synthetic δ^{18}O values were calculated as a function of both SST and SSS using equation 1 from Thompson et al. (2011).

$$\delta^{18}O_c = -0.22SST + 0.27SSS \tag{3.9}$$

The regression slopes for SST and SSS were chosen using the same criteria from Thompson et al. (2011). The SST slope is the organic slope of the δ^{18}O and SST relationship, while the SSS slope is based on basin-scale seawater δ^{18}O and SSS regression estimates (LeGrande and Schmidt, 2006). Synthetic δ^{18}O values ranged from −6.74 to −4.52‰(μ = −5.49 ± 0.51‰).

Synthetic δ^{11}B values were calculated as a function of SST, SSS and pH_{cf}. They were determined by re-arranging the pH-dependent equation from Zeebe and Wolf-Gladrow (2001) to solve for the boron isotope ratio of carbonate ($\delta^{11}B_c$).

$$\delta^{11}B_c = pK_B - log(\frac{\delta^{11}B_{sw} - \delta^{11}B_c}{\delta^{11}B_c - \delta^{11}B_{sw} + 1000(\alpha - 1)}) \tag{3.10}$$

Where the boron isotope ratio of seawater ($\delta^{11}B_{sw}$) is 39.61‰(Foster et al., 2010), and the mass fraction factor between boric acid and borate ion (α) is 1.0272 (Klochko et al., 2006). The negative log of the dissociation constant between boric acid and borate ion (pK_B) is a function of both temperature and salinity (Dickson, 1990). We therefore calculated pK_B at each time interval by taking the negative log of the K_B equation from Dickson (1990)(Dickson, 1990). The values of pK_B ranged between 8.56 and 8.64 given a temperature range between 21.83 and 29.69°C and a salinity range between 31.61 and 34.17 psu.

These calculations yield synthetic δ^{11}B values between 18.30 and 19.64‰, which is expected given the pH of seawater. However, corals upregulate their internal pH relative to seawater (McCulloch et al., 2017) while also often exhibiting increased seasonal variance (Ross et al., 2017). Thus, to yield synthetic δ^{11}B values consis-

tent with those observed in coral aragonite, we calculated pH_{cf} from pH_{sw} using equation 13 from D'Olivo et al. (2019)(D'Olivo et al., 2019).

$$pH_{cf} = 0.49pH_{sw} + 4.93 - 0.02SST \tag{3.11}$$

Note that the temperature sensitivity of synthetic δ^{11}B values is realized in its dependence on both pK_B as well as pH_{cf} as specified in Eq 3.11. Meanwhile, the salinity sensitivity of synthetic δ^{11}B values is only realized in its dependence on pK_B. Synthetic δ^{11}B values ranged from 22.21 - 24.10‰ (μ = 23.17‰± 0.41).

3.2.3 *P. astreoides* application study

Coral sampling and sample preparation

In November 2014 a 5 cm diameter core was sampled from two *P. astreoides* colonies (1B and 3B, respectively) located on Hog Reef, Bermuda (32.457°N, 64.835°W), at a depth of 10 and 12 m using a 1 horsepower handheld pneumatic air drill with a custom made 5-by-15 cm diamond core bit (Fig 3.3). Corals were sampled as close to the National Oceanographic and Atmospheric Administration's PMEL MAPCO2 buoy moored at Hog Reef as possible (within 5 m). After sampling, voids in the coral skeleton were filled with cement plugs to prevent boring organisms from inhabiting the holes, and to encourage further coral growth. Cores were then transported to the University of Southampton for geochemical analyses. The outer tissue layers of each coral core were removed using a WaterPik before being left to soak in pure ethanol for 5 minutes followed by deionised water. A clean sintered diamond cut-off wheel was used to cut the cores into $\sim$7 mm thick slabs, both of which were then divided into two sections. Each section was polished using a rotary diamond grinder followed by silicon carbide grinding paper down to 4 μm. Samples were cleaned over two days in a solution of 20% H_2O_2 and 2.0 M NH_3 before being rinsed, ultrasonicated for 10 minutes, then rinsed again in 18.2 MΩ (ultrapure) water and left to dry in a flow box. Finally, the topmost sections containing the most recent growth were mounted onto glass slides in preparation for geochemical analyses.

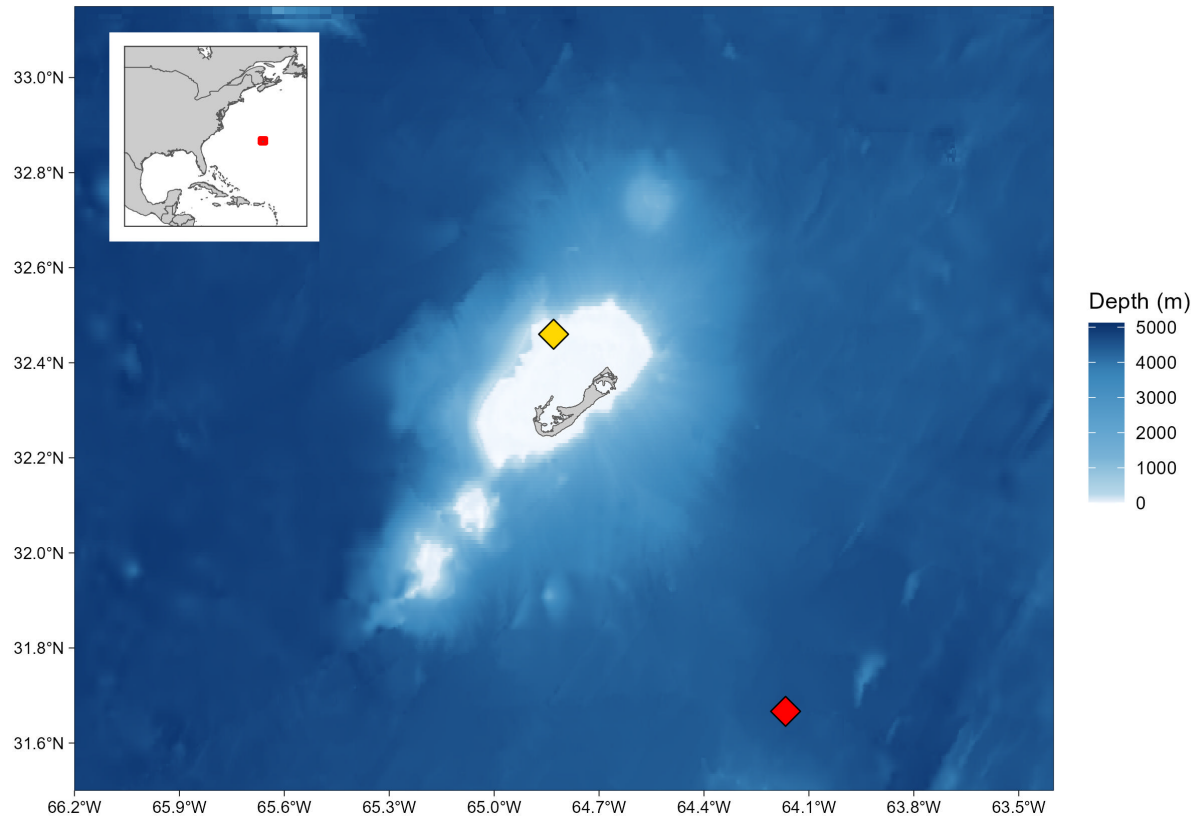

Figure 3.3: Collection site of *P. astreoides* corals 1B and 3B on the northern fringing reef of Bermuda. The yellow diamond indicates the location of National Oceanographic and Atmospheric Administration's PMEL MAPCO2 buoy moored at Hog Reef (32.457°N, 64.835°W), meters from where corals 1B and 3B were cored. The red diamond indicates the location of the Bermuda Atlantic Time-series Study (BATS) sampling station (∼32.67°N, 64.17°W. The red box on the inlayed map indicates the borders of the larger map. Bathymetry data displayed was collected from the National Oceanographic and Atmospheric Association via the open-source R package ggOceanMaps (Vihtakari, 2024). Shoreline data are republished from Wessel and Smith (1996) under a CC BY license, with permission from Dr. Walter H.F. Smith, original copyright 1996.

Geochemical analysis

Geochemical analyses were carried out at the Geochemistry laboratory, School of Ocean and Earth Sciences, University of Southampton. Elemental analyses (Li, B, Mg, Ca, Sr, U) were performed on an Agilent (Agilent Technologies Inc., CA, USA) 8900 Triple Quadrupole ICP-MS coupled to an Elemental Scientific Lasers (Bozeman, MT, USA) NWR193 excimer laser ablation system with a TwoVol2 ablation chamber. On-peak blank corrections based on the mean intensities of preceding and succeeding blank measurements were applied offline, as was instrumental drift and mass bias corrections which employed sample-standard bracketing with coral reference material JCp-1 (*Porites sp.* coral) using the values published by Hathorne et al. (2013b) (Hathorne et al., 2013a). Samples and standards were ablated in line mode, with sample analyses ablating the same tracks previously used for the δ^{11}B analyses (see below). Standard analysis consisted of approximately 285 integration cycles of 0.42 s. Samples were analyzed along 30 parallel and adjoining tracks amounting to ∼6 mm long transects that each consisted of ∼1400

Table 3.2: Typical operating conditions for laser ablation ICP-MS analysis.

	δ^{11}**B isotope analysis**	**Trace element analysis**
Instrument		
Mass Spectrometer	Thermo Scientific Neptune Plus multi-collector inductively coupled plasma mass spectrometer	Agilent 8900 Triple Quadrupole inductively coupled plasma mass spectrometer
Laser Ablation System	Elemental Scientific Lasers NWR193 excimer laser ablation system with a TwoVol2 ablation chamber	Elemental Scientific Lasers NWR193 excimer laser ablation system with a TwoVol2 ablation chamber
RF Power	1400 W	1550 W
Cones	Nickel skimmer (X) and jet sample	Standard nickel sample cone and XT skimmer
Gas Flows		
Cooling gas (argon)	16 l min^{-1}	13 l min^{-1}
Auxiliary gas (argon)	0.7 l min^{-1}	0.8 l min^{-1}
Make-up gas (argon)	1.0 l min^{-1}	0.6 l min^{-1}
Ablation cell carrier gas (helium)	0.85–1.00 l min^{-1}	0.5 l min^{-1}
Additional gas (nitrogen)	0.004–0.007 l min^{-1}	0.01 l min^{-1}
Ablation Conditions		
Laser power density	$\sim$4 J cm^{-2}	$\sim$1.8 J cm^{-2}
Laser repetition rate	12 Hz	5 Hz
Laser beam size	100–150 μm diameter	150 μm diameter
Laser tracking speed	10 μm s^{-1}	10 μm s^{-1}
Ablation mode	Line	Line

integration cycles of 0.42 s. Operating conditions are detailed in Table 3.2. Reference material PS69/318-1, a cold-water calcitic scleraxonian octocoral coral, was ablated throughout the analytical session as a guide to accuracy, internal precision, and external reproducibility (n = 10). Internal precision, expressed as 2 standard errors (SE) of the mean of 1200 integration cycles, was $\leq$ 7% for B/Ca, Mg/Ca, and Sr/ Ca, and $\leq$ 16% for Li/Ca, U/Ca and Li/Mg. External reproducibility, expressed as 2σ of the mean of the 10 analyses, was $<$ 6% for B/Ca, Mg/Ca, Sr/ Ca and Ba/Ca, 12% for Li/Ca and Li/Mg, and 29% for U/Ca. Mean accuracy was within 10% of solution values for all ratios except Li/Mg which was within 11% (Foster et al., 2013).

Boron isotope analyses were performed on a Thermo Scientific Neptune Plus MC-ICP mass spectrometer coupled to an Elemental Scientific Lasers NWR193 excimer laser ablation system with a TwoVol2 ablation chamber, broadly following previously described analytical protocols (Standish et al., 2019; Chalk et al., 2021). Data were collected in static mode, with ^{10}B and ^{11}B measured on the L3 and H3 Faraday cups, both of which were installed with 10^{12} Ω resistors. The laser system was again operated in line mode, with standard measurements consisting of 100 integration cycles of 2.194 s (100–120 μm laser beam diameter) and sample measurements consisting of $\sim$282 integration cycles of 2.194 s (150 μm laser beam diameter). Prior to data collection, standards and samples were ablated to remove any surface contamination (laser power density of $\sim$2 J cm^{-2}, laser repetition rate of 10 Hz, laser tracking speed of 200 μm s^{-1}). Dynamic blank corrections were applied cycle by cycle assuming a linear relationship between preceding and succeeding blank measurements (each consisting of 22 integration cycles of 2.194 s); instrumental mass bias was corrected by sample-standard bracketing with glass reference material NIST SRM610 and the isotope composition published by le Roux et al. (2004) and Standish et al. (2019); and matrix interferences from scattered ions (Standish et al., 2019) were corrected based on the power-relationship between δ^{11}B inaccuracy and ^{11}B/Ca$_{\text{interference}}$ for pressed pellets of carbonate reference materials JCp-1 and JCt-1 (*Tridacna gigas*), and where Ca$_{\text{interference}}$ was measured at m/z of 10.10 on the L2 Faraday cup. All corrections were applied offline. Standard data were screened, with cycles falling outside 2σ of the mean removed. Internal reference material PS69/318-1 was ablated throughout the analytical session as a guide to internal precision, external reproducibility, and accuracy. Internal precision, expressed as 2SE of the mean of the 100 integration cycles, was $\leq$ 0.4‰. The mean δ^{11}B of the repeat analysis (n = 18) was 13.61 ± 0.54‰(2σ), consistent with a solution measurement of 13.83 ± 0.29‰(2σ Standish et al., 2019).

Age model and environmental reconstructions

For each coral we combined 10 adjoining and parallel laser transects into a single time series for each geochemical variable by averaging data in depth space. We report the uncertainty on the mean for each measurement as the SE of the 10 parallel laser transects. An age model was then constructed based firstly upon consideration of an x-ray image showing density banding and the date of collection. This was then refined by tuning annual variations

in Sr/Ca to SST, where minima, maxima, and mid-points were considered contemporaneous with SST maxima, minima, and mid-points, respectively. Using this method, we calculate that data from coral 1B ranges from June 2010 to April 2013, and data from coral 3B ranges from June 2010 to September 2013.

We created an *in situ* SST and pH_{sw} dataset ranging throughout the study period (May 2010 to September 2013) by combining two independent *in situ* environmental datasets from the northern fringing reef of Bermuda. The first dataset (from January 2011 to September 2013) was acquired from the National Oceanographic and Atmospheric Administration PMEL MAPCO2 buoy moored at Hog Reef (32.457°N, 64.835°W). Corals 1B and 3B grew several meters away from the Hog Reef Buoy, which has been continuously measuring seawater partial pressure CO_2, SSS and SST since 2011 with only minor interruptions (https://www.pmel.noaa.gov/co2/story/Hog+Reef). A continuous record of SST and pH_{sw} was calculated from these data by assuming a constant seawater alkalinity of 2357 μmol/kg (Courtney et al., 2017) for most of the study interval (July 2011 to March 2013) and solving the full carbonate system using alkalinity and the partial pressure of CO_2 using the seacarb package in R (Gattuso et al., 2022). This assumption is justified because both CO_2 and pH_{sw} are determined by the alkalinity / dissolved inorganic carbon ratio (Hain et al., 2018), therefore using a range of alkalinity from 2300 to 2400 μmol/L (the range observed by Courtney et al. (2017)) changes our estimate of pH_{sw} by only 0.015 pH units.

To extend our environmental data beyond the interval covered by the Hog Reef Buoy to the bottom of our time series, we utilized a second dataset consisting of shipboard SST and pH_{sw} data acquired from the Bermuda Atlantic Time-series Study (BATS; $\sim$32.67°N, 64.17°W Steinberg et al., 2001), which has been measuring SST and pH_{sw} at monthly intervals since 1983. Due to both the discontinuous nature of the BATS data, and the lack of Hog Reef data prior to 2011, we established a linear model between BATS and Hog Reef SST (n = 41, r = 0.78, $p < 0.001$) as well as BATS and Hog Reef pH_{sw} (n = 41, r = 0.83, $p < 0.001$). We then created an *in situ* SST and pH_{sw} calibration dataset by combining the predicted values of Hog Reef data (when BATS data was available) and observed Hog Reef data (when BATS data was not available).

Finally, we calculate Sr/Ca-derived SST estimates for corals 1B and 3B using ordinary least squares regression, and we calculate δ^{11}B-derived pH_{sw} using Eq 3.10 and Eq 3.11. To estimate pK_B, we use our combined BATS and Hog Reef *in situ* SST dataset, as well as SSS data from BATS alone. SSS on Hog Reef is relatively invariant, and there is little offset between Hog Reef SSS and BATS SSS. Missing SSS values from the BATS dataset (3 out of 40 months) were linearly interpolated between adjacent months for the purposes of generating a continuous pK_B dataset.

3.2.4 Error assessments

We use three metrics to quantitatively compare SMITE SST and pH_{sw} estimates with those derived from Sr/Ca ratios and δ^{11}B values, respectively: the correlation coefficient (r), the root-mean squared error (RMSE), and the standard error of prediction (SEP). Each metric provides a measure of the correlation, accuracy, and precision of

the reconstruction, respectively. The SEP is defined as the uncertainty in derived SST estimates based on the uncertainty in both the climate target (SST, pH_{sw}) as well as the uncertainty in the corresponding coral variable(s). Given that our SST measurements are derived from, or modeled after, temperatures derived from *in situ* loggers, uncertainty for temperature was fixed at 0.02°C (https://www.onsetcomp.com/products/data-loggers/u22-001). Uncertainty for our pH_{sw} measurements were fixed at 0.02 units. Uncertainty for SSS measurements (used in calculating pK_B for δ^{11}B-derived pH_{sw} estimates) were based on BATS CTD measurements and also fixed at 0.02 psu.

The SEP for each climate target reconstruction is calculated using a bootstrap Monte Carlo approach. At each iteration (i = 1,. . . ,10000), each individual measurement in both the coral variable and climate target fields are randomly resampled from a normal distribution with a mean equal to the given variable/climate target value (μ_i) and a standard deviation equal to the specified error (s_i). Model parameters are then estimated from the perturbed coral variable and climate target fields, and SST/pH_{sw} estimates for each data point are stored. The 95% confidence interval for each predicted value is determined from the distribution of predicted values derived from each Monte Carlo iteration. The SEP is then determined as the average distance from the mean to the upper and lower bounds of the 95% confidence interval, divided by 1.96 (Fisher, 1970). The 95% confidence interval for the SEP itself is then defined as the standard deviation of the SEP throughout each calibration dataset, multiplied by 1.96.

3.3 Results

3.3.1 Synthetic study

We utilized our synthetic proxy dataset (Sr/Ca, δ^{18}O, δ^{11}B) to assess the relative impact of Gaussian noise on SMITE SST and pH_{sw} reconstructions (Fig 3.4). The top panels (A-B) show the SMITE SST and pH_{sw} reconstructions relative to their respective climate targets throughout the 20th century as we progressively increased Gaussian noise by relative standard deviation (RSD). The bottom panels (C-D) show the maximum and minimum RMSE (translucent regions) and SEP (opaque regions) for SMITE SST and pH_{sw} estimates (black), Sr/Ca SST (orange) and δ^{11}B pH_{sw} (green) at each noise increment. We emphasize that the mean value of each synthetic proxy measurement exhibits the ideal relationship with the climate target, while the upper and lower bounds of the 95% confidence interval for each measurement (which increases as Gaussian noise increases) represent maximum deviation from the ideal. The minimum RMSEs depicted in Fig 3.4C and Fig 3.4D (lower bounds of the translucent regions) are calculated from the idealized mean values of each measurement. In practice, these minimum RMSEs would be achieved under two conditions: a perfect relationship between the proxy and the climate target, and a near-limitless number of repeat sample analyses.

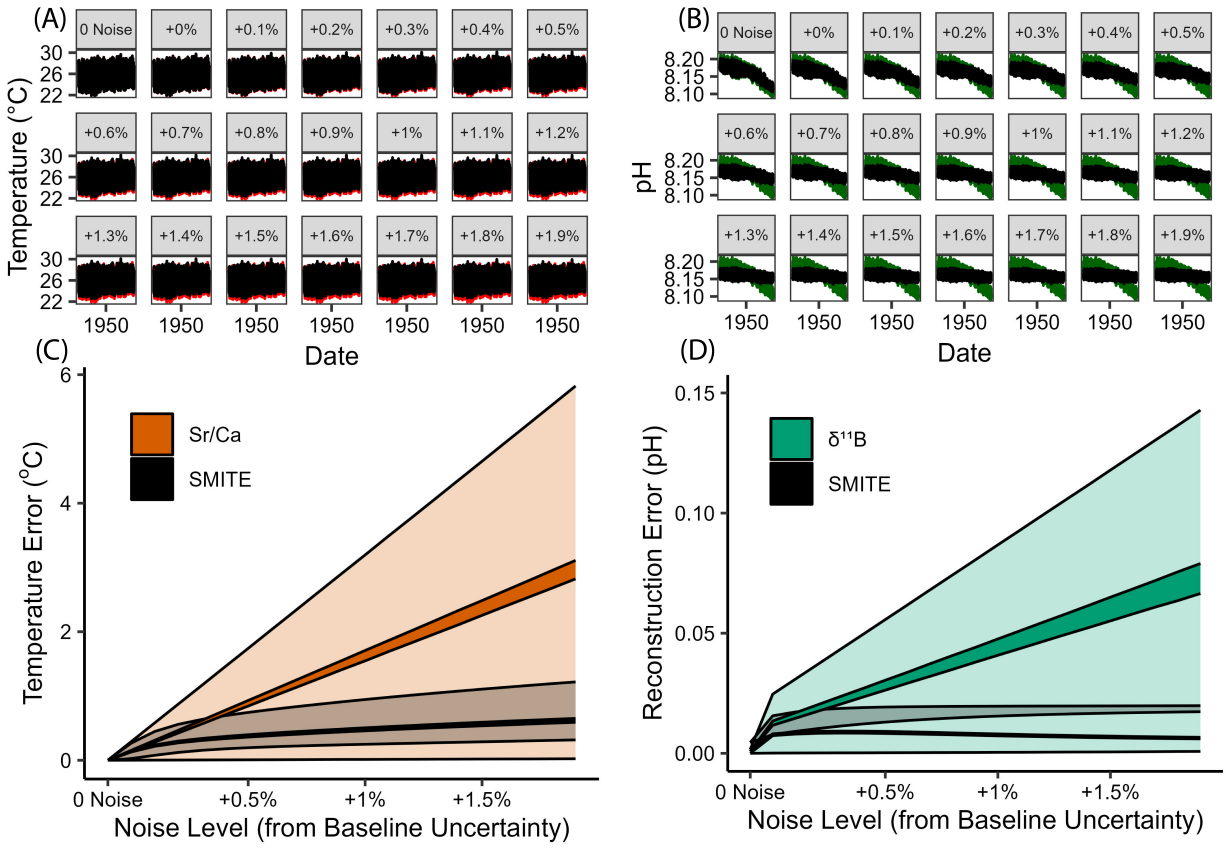

Figure 3.4: SMITE SST and pH_{sw} reconstructions for the 20th century (A-B), and reconstruction statistics for SMITE SST, Sr/Ca SST (C), SMITE pH_{sw}, and $\delta^{11}B$ pH_{sw} (D) across various levels of Gaussian noise. (A-B) Each panel represents the factor by which Gaussian (analytical) was increased in terms of relative standard deviation (RSD). Black lines represent the SMITE reconstruction for the 20th century at each noise increment. Colored lines represent the climate targets over the same period (SST = red, pH_{sw} = green). (C-D) The RMSE (translucent shaded region) and SEP (opaque shaded region) for SST and pH_{sw} estimates derived from the SMITE method are black, while the colored regions represent the RMSE and SEP for Sr/Ca SST (orange) and $\delta^{11}B$ pH_{sw} (green). Like the panels in A and B, the x-axis represents the factor by which Gaussian (analytical) noise was increased in terms of RSD. The upper and lower bounds of each shaded region represent the maximum and minimum values for the RMSE and SEP at each noise increment.

Conversely, the maximum RMSEs (the upper bounds of translucent regions) are calculated from the average RMSE between the upper and lower bounds of the 95% confidence interval for each reconstruction. They are thus representative of how high RMSEs could be, given a certain level of noise and disregarding the benefits of repeat sample analysis. Therefore, the maximum and minimum RMSEs for each reconstruction method represent two extremes. Given a certain level of noise, any study would exhibit RMSEs closer to one or extreme or the other depending on the quality of the 'true' relationship between the proxy and the climate target, as well as how many repeat analyses could be conducted on a particular sample. A companion assessment examining the effect of autocorrelated noise is available in the supplemental material (Figures B.1 and B.2), which shows far less impact than Gaussian noise except for at very high values of the lag-1 autocorrelation coefficient (> 0.9).

We observe from the similarities between SMITE SST estimates and 'true' SST in Fig 3.4A (red and black lines, respectively), as well as the shallow slope of the SEP and RMSE in response to noise in Fig 3.4C, that SMITE SST estimates in the synthetic dataset are highly robust to even exceptionally high levels of Gaussian noise. For synthetic Sr/Ca SST, the SEP and the maximum RMSE exhibit a linear relationship with Gaussian noise, which is expected given the linearity between synthetic Sr/Ca ratios and SST. At low levels of noise ($< +0.2\%$ RSD), SMITE follows this same pattern of linearity between reconstruction statistics and noise. However, as noise continues to increase, the slope of SMITE's reconstruction statistics shoals, leading to significant improvements in SMITE SST reconstructions relative to Sr/Ca alone. This shallowing of the reconstruction statistics in response to noise can be directly attributed to SMITE's increasing dependence on δ^{18}O as noise increases (Fig 3.5), which in turn is due to the improved sensitivity of synthetic δ^{18}O as a paleothermometer relative to Sr/Ca at higher noise levels.

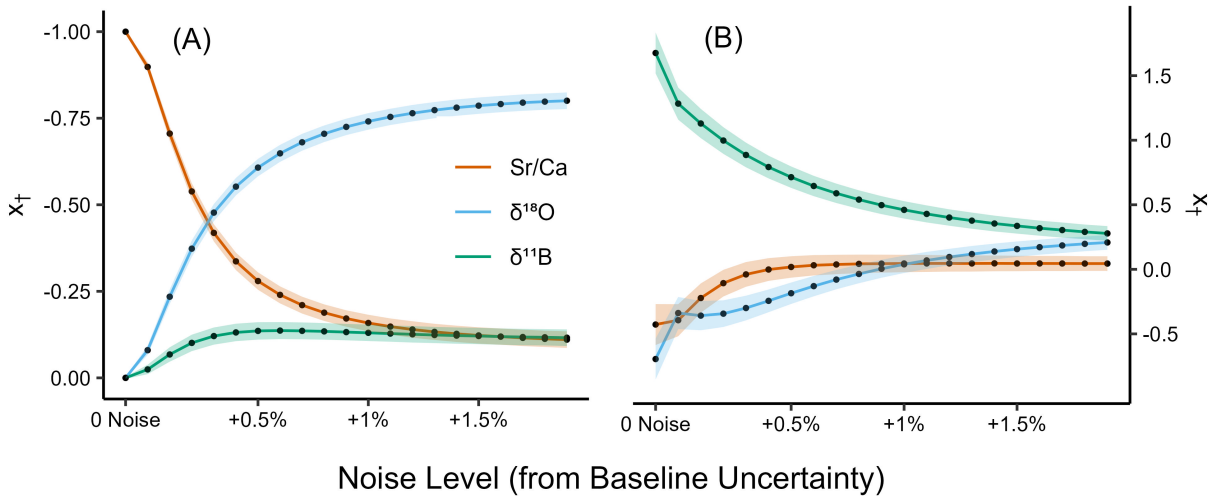

Figure 3.5: Synthetic SMITE model parameters for SST (A) and pH_{sw} (B) as Gaussian noise is increased from minimum (analytical) uncertainty in terms of relative standard deviation (RSD). The color of each line denotes the proxy associated with each model parameter (orange = Sr/Ca, blue = δ^{18}O, green = δ^{11}B). The shaded region around each line indicates the 95% confidence interval associated with that model parameter.

For the synthetic pH_{sw} reconstructions (Fig 3.4B and Fig 3.4D), δ^{11}B reconstruction statistics also exhibit a linear relationship with increasing noise levels, like the reconstruction statistics observed from synthetic Sr/Ca SST. The rapid increase in pH_{sw} reconstruction error at the first noise increment (+0% RSD) can be explained by the higher baseline uncertainty for synthetic δ^{11}B (0.40% RSD) relative to Sr/Ca (0.10% RSD), and the 0.1% RSD increase at each noise increment thereafter. We also observe that SMITE pH_{sw} SEP and maximum RMSEs remain well below that of δ^{11}B alone, with the difference in reconstruction skill increasing as noise increases. This remains true at all noise increments, even as SMITE model parameters remain preferentially weighted towards δ^{11}B (Fig 3.5B).

However, we note two key differences between the synthetic SST and pH_{sw} reconstructions. First, we observe that when no noise is implemented into the system, synthetic $\delta^{11}B$ pH_{sw} estimates outperform those derived from SMITE by a small margin. This is due to the idealized relationship between synthetic $\delta^{11}B$ values and pH_{sw}, which follows Eq 3.10 and Eq 3.11. Conversely, SMITE simply treats $\delta^{11}B$ as linearly correlated with pH_{sw} and considers its covariance with Sr/Ca and $\delta^{18}O$. Thus, SMITE makes no assumptions regarding the relationship between pH_{sw} and pH_{cf} nor changes pK_B, which would confound the pH_{sw} signal due to interference from SST and SSS. SMITE only considers the uncertainties in the coral variable field, which we have defined at each noise increment as a percent-RSD increase from baseline uncertainty. Second, SMITE pH_{sw} estimates are far less skillful than SMITE SST estimates, particularly when considering the long-term trend as noise levels increase (Fig 3.4A and Fig 3.4B).

The loss in both long-term and short-term variance for SMITE pH_{sw} estimates results from the compounding effects of relatively high uncertainty in synthetic $\delta^{11}B$, as well as the distribution of SMITE model parameters. Unlike SST (which is encoded in all three synthetic variables), information associated with pH_{sw} is only reflected in synthetic $\delta^{11}B$. Thus, SMITE is fully dependent on synthetic $\delta^{11}B$ to capture the long-term trend in pH_{sw}. At the first noise increment, the long-term trend in SMITE pH_{sw} estimates ($\sim$0.085 units) is approximately 70% of the long-term pH_{sw} trend ($\sim$0.12 units). Nearly 0.02 pH units of this 0.035-unit discrepancy can be explained by the uncertainty in synthetic $\delta^{11}B$ (0.18‰ at the first noise increment). The remaining discrepancy of 0.015 pH units can be explained by the fact that $\delta^{11}B$ only contributes to 57% of SMITE pH_{sw} estimates at the first noise increment (Fig 3.5B). The remaining 43% are divested into synthetic Sr/Ca and $\delta^{18}O$, both of which exhibit virtually no long-trend. Thus, only a fraction of the long-term trend in pH_{sw} captured by synthetic $\delta^{11}B$ is propagated through the SMITE model. As noise increases throughout the experiment, the sum of the SMITE model parameters decreases, uncertainty in synthetic $\delta^{11}B$ values continues to rise, and the resulting SMITE pH_{sw} reconstruction exhibits progressively smaller variance.

Despite the loss of long-term variance, SMITE still yields more accurate and precise predictions of pH_{sw} at all noise increments where noise is present relative to synthetic $\delta^{11}B$ alone. This is due to the large 95% confidence interval associated with synthetic $\delta^{11}B$ pH_{sw} estimates once noise is introduced into the system, which is propagated by the uncertainty in synthetic $\delta^{11}B$, SST and SSS (which influence pK_B and pH_{cf}), and pH_{sw}. However, as mentioned before, the negative effects of the large confidence interval in synthetic $\delta^{11}B$ can be mitigated by repeat sample analysis. Thus, given a certain number of repeat analyses according to the central limit theorem, it is possible for both synthetic $\delta^{11}B$ pH_{sw} and synthetic Sr/Ca SST estimates to outperform estimates derived from SMITE, since minimum SMITE RMSEs remain higher than both throughout the experiment. However, in practice, this would require both an idealized relationship between the proxy and the climate target in addition to repeat sample analyses.

We also assessed how SMITE model parameters varied with different calibration period lengths (Fig 3.6). In this experiment, we fixed the noise level at +0% RSD (baseline uncertainty) and increased the calibration period

for the SMITE method from 5 to 100 years in five-year increments. For the SST reconstruction, $x_\dagger$ values for each SMITE model parameter remain fixed at -0.92 (Sr/Ca), -0.08 (δ^{18}O), and -0.01 (δ^{11}B) throughout the course of the experiment. This suggests that SMITE SST model parameters are stable with only five years of calibration data (the first increment we tested). Conversely, model parameters for the SMITE pH_{sw} reconstruction take approximately 30 years to stabilize due to high levels of uncertainty. Again, this is likely because δ^{11}B is the only synthetic proxy in this dataset that is sensitive to pH_{sw}, and the long-term trend in pH_{sw} increases in magnitude halfway through the 20th century.

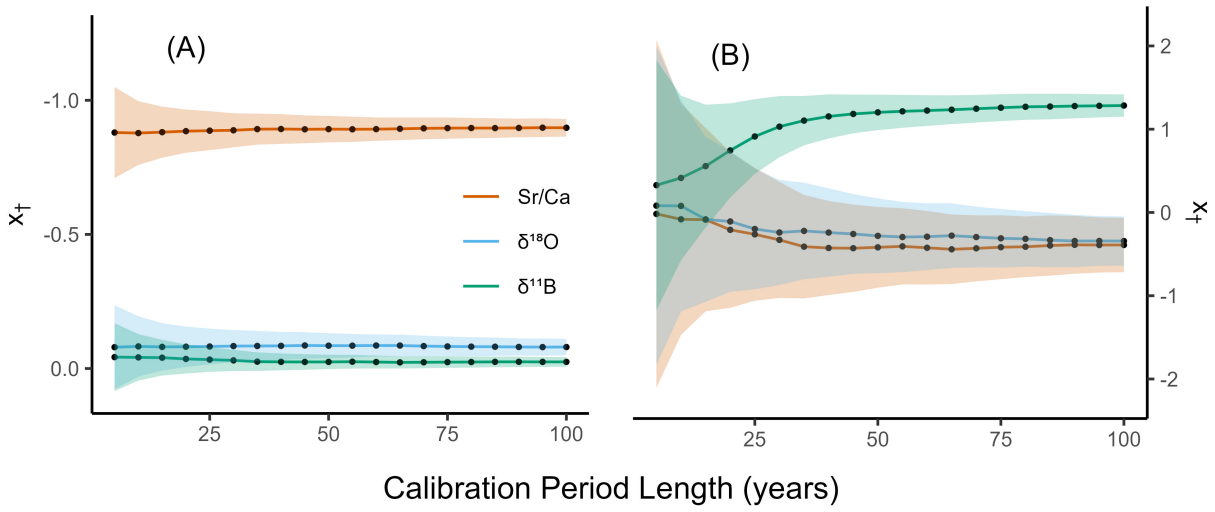

Figure 3.6: Synthetic SMITE model parameters for SST (A) and pH_{sw} (B) as the calibration period is increased from five to one hundred years in five-year increments. The color of each line denotes the proxy associated with each $x_\dagger$ value (orange = Sr/Ca, blue = δ^{18}O, green = δ^{11}B). The shaded region around each line indicates the 95% confidence interval associated with that model parameter.

3.3.2 Application study

Seven coral skeletal geochemical variables (B/Ca, Li/Ca, Mg/Ca, Sr/Ca, U/Ca, δ^{11}B + Li/Mg) were measured and age-modeled from both Bermudan *P. astreoides* corals between June 2010 and September 2013 (Fig 3.7). For ease of interpretation, each coral variable was z-score normalized (black lines) and plotted alongside mean-standardized SST (orange lines) and pH_{sw} (green line). The mean and variance of each coral variable, their respective analytical errors, and their correlations to both SST and pH_{sw} are provided in Table B.1. In both coral cores (1B and 3B), Sr/Ca and Li/Mg ratios exhibit the strongest individual correlations to SST (Sr/Ca, r = -0.85 and -0.77; Li/Mg, r = -0.83 and -0.85). B/Ca also exhibits moderately strong correlations with SST in both corals (r = -0.75

and -0.77, respectively). For pH_{sw}, Sr/Ca and Li/Mg also emerge as the strongest pH_{sw} indicators, likely due to the moderate anti-correlation of SST and pH_{sw} at this site ($r = -0.85$).

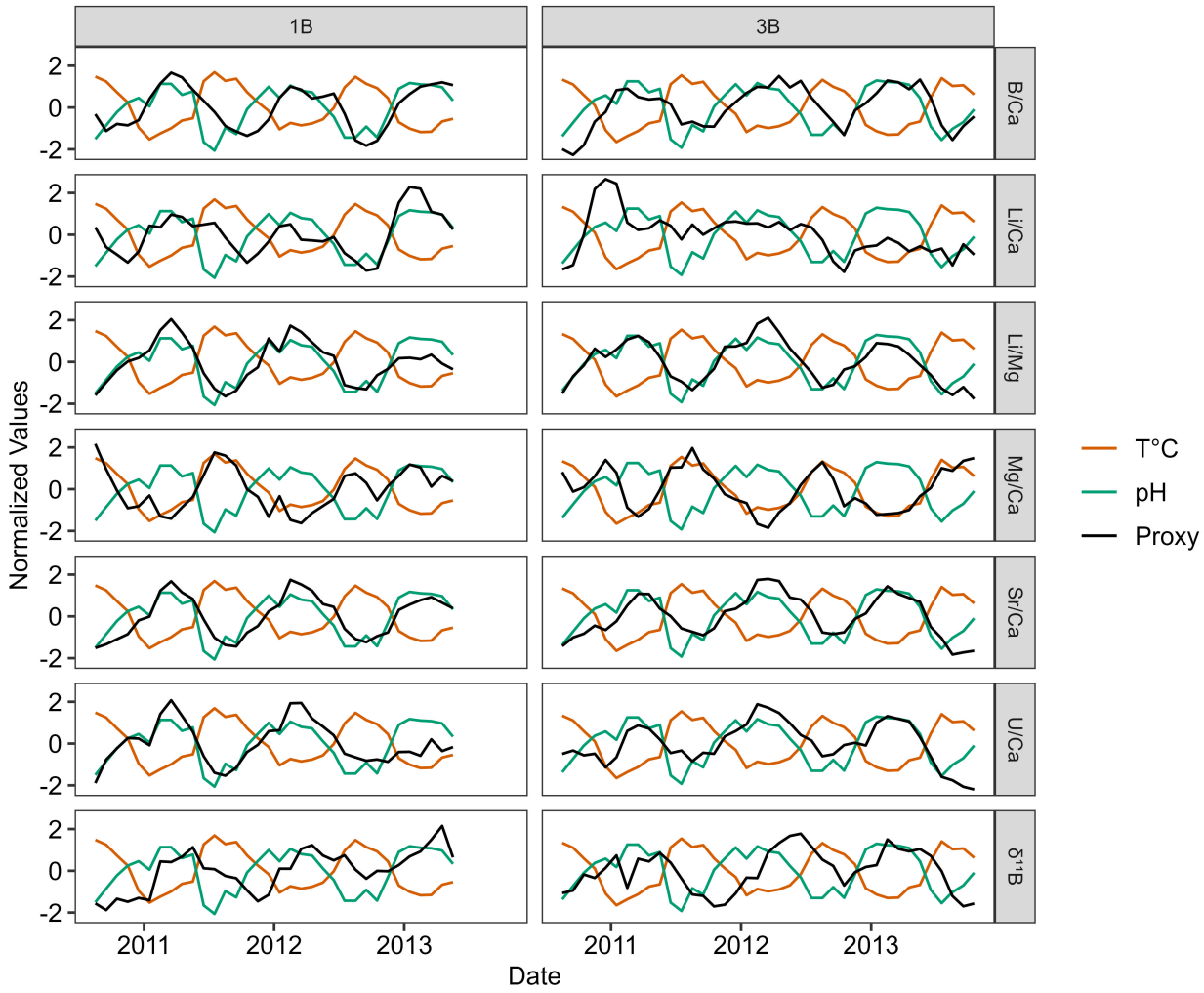

Figure 3.7: Z-score normalized monthly-averaged coral variable data (black lines) from *P. astreoides* corals 1B (left) and 3B (right). *In situ* normalized SST (orange lines) and pH_{sw} (green lines) are plotted inside each panel to show each proxy's relative correlation to the climate target. Data from coral 1B were assigned ages between June 2010 and April 2013 (n = 35). Data from coral 3B were assigned ages between June 2010 and September 2013 (n = 40).

SMITE SST and pH_{sw} reconstructions for corals 1B and 3B are shown in Fig 3.8 (red lines and shaded region). For comparison, we also plot Sr/Ca-derived SST estimates (calculated using ordinary least squares regression) and δ^{11}B-derived pH_{sw} (calculated using Eq 3.10). Note that for the SMITE reconstructions, we have performed a regularization procedure that slightly reduces reconstruction skill as a tradeoff for reduced uncertainty in SMITE model parameters (Eq 3.7). For an in-depth discussion on the effects of this regularization procedure, see sections

3.2.1 and 3.4.2. For all reconstructions, the SMITE method is more accurate (RMSE), precise (SEP), and better correlated to each climate target (r^2) than the best or most common single-proxy estimators.

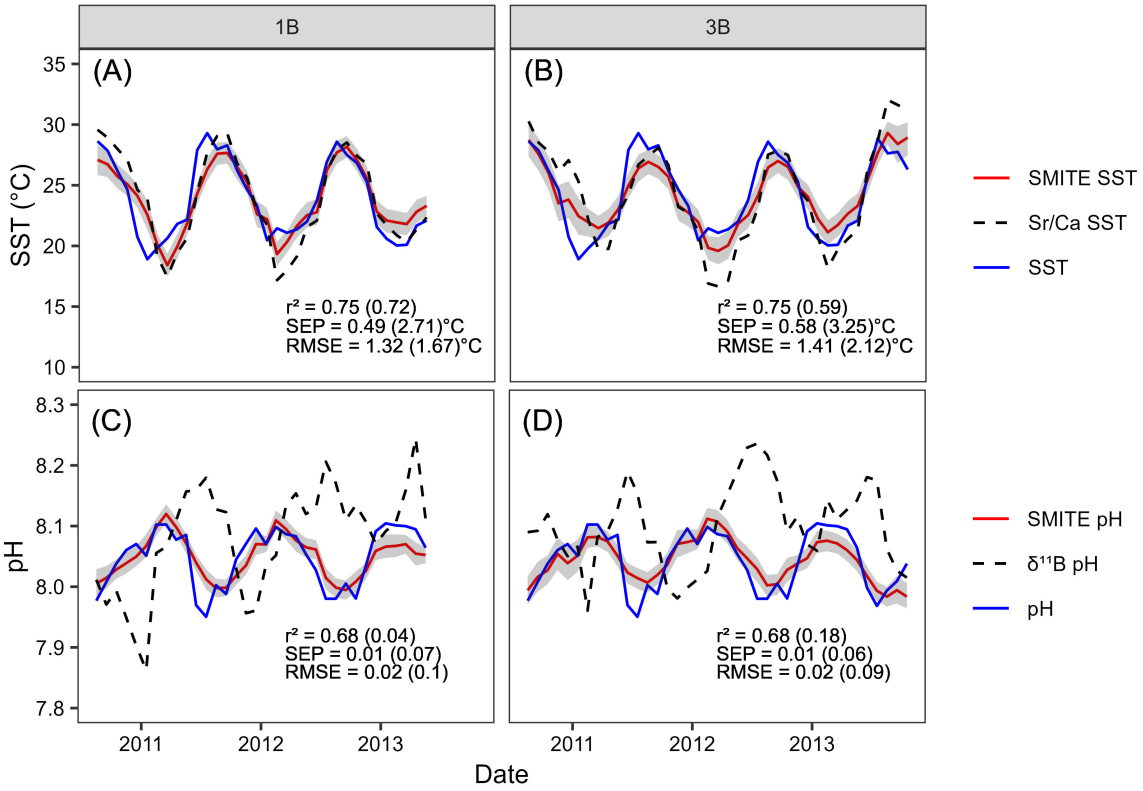

Figure 3.8: SMITE-derived SST (A-B) and pH_{sw} (C-D) estimates (red lines) from corals 1B (left) and 3B (right) compared to *in situ* SST and pH_{sw} (blue lines). SST and pH_{sw} estimates from the best or most common single-proxy estimators in these corals are plotted as dashed lines in each panel (SST = Sr/Ca; $pH_{sw} = \delta^{11}B$). The gray shaded region indicates the 95% confidence interval for each SMITE reconstruction. SMITE reconstruction statistics are listed at the bottom of each panel, with the equivalent statistics for Sr/Ca- and $\delta^{11}B$-derived estimates given in parentheticals.

Between corals 1B and 3B, SMITE SST estimates are 5 and 6 times more precise and 21% and 33% more accurate than those derived from Sr/Ca. Importantly, this notable improvement in reconstruction skill is not fully realized in the r^2 value, where SMITE SST estimates in coral 1B are only marginally better than those derived from Sr/Ca. For the pH_{sw} reconstructions between corals 1B and 3B, the SMITE method is 7 and 6 times more precise and 5 times more accurate than $\delta^{11}B$. This vast improvement can largely be attributed to the relatively poor performance of $\delta^{11}B$ as a proxy for pH_{sw} in these systems, particularly in coral 1B. However, while Li/Mg is the strongest pH_{sw} proxy in both corals, it is not often used for pH_{sw} reconstructions given its known dependence on temperature (Cuny-Guirriec et al., 2019). Regardless, we still observe large improvements in SMITE pH_{sw} estimates relative to Li/Mg pH_{sw} estimates, with 5 times better precision and 33% and 50% better accuracy in SMITE than from Li/Mg (Table B.2). We reiterate that this improvement is not fully realized in the correlation coefficient alone, where SMITE and Li/Mg-derived pH_{sw} estimates are comparable.

Next, we compare SMITE model parameters between corals 1B and 3B to assess their reproducibility (Fig 3.9). All SMITE model parameters in both the SST and pH_{sw} reconstructions are highly reproducible between corals, exhibiting $x_{\dagger}$ values that are nearly identical and/or within error of each other. Notably, the uncertainty in each SMITE model parameter tends to decrease as the absolute $x_{\dagger}$ value increases. For reproducibility, it is crucial that variables with the highest $x_{\dagger}$ values (i.e., have the strongest impact on the reconstruction) are statistically indistinguishable from one another between corals. Indeed, we see this is the case for the SMITE SST reconstruction, where $x_{\dagger}$ values associated with Li/Ca, Li/Mg, Mg/Ca, Sr/Ca, and U/Ca are nearly identical between corals. Consequently, SMITE SST estimates are highly reproducible between corals, exhibiting significantly better correlations, accuracy, and precision than the relatively more direct Sr/Ca method (Fig 3.10A and Fig 3.10B). We also find that SMITE pH_{sw} model parameters exhibit very similar $x_{\dagger}$ values between Li/Ca, Li/Mg, Sr/Ca, and U/Ca. This results in highly skillful SMITE cross-compared pH_{sw} estimates that exhibit similar correlations with superior precision and accuracy relative to those derived from Li/Mg (Fig 3.10C and Fig 3.10D). While this is a relatively small sample size (two corals over a few annual cycles), the level of reproducibility of both the SMITE SST and pH_{sw} reconstructions between corals is highly encouraging and warrants more rigorous testing in future studies.

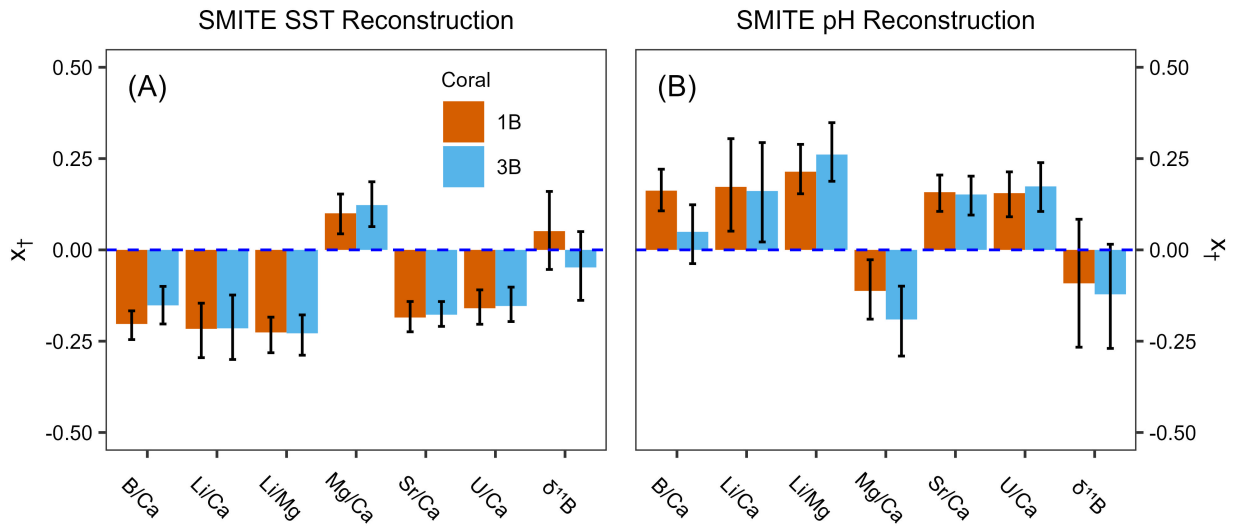

Figure 3.9: SMITE model parameters for each coral variable corresponding to the SMITE SST reconstruction (A) and pH_{sw} reconstruction (B). The loadings for each coral (1B & 3B) are indicated by the orange and blue colors, respectively. Error bars represent the 95% confidence interval for each loading.

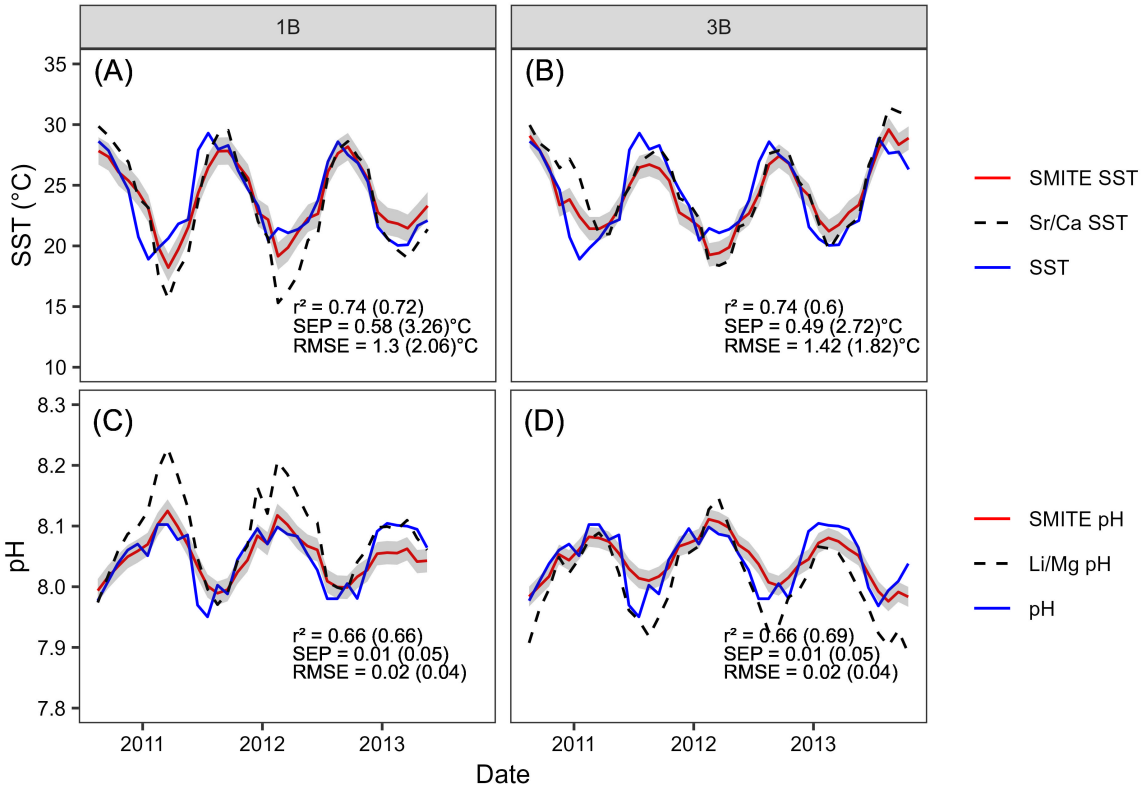

Figure 3.10: SMITE-derived SST (A-B) and pH_{sw} (C-D) estimates (red lines) compared to *in situ* SST and pH_{sw} (blue lines) when using regression coefficients derived *from the opposite corals*. SST and pH_{sw} estimates from the best single-proxy estimators in these corals are plotted as dashed lines in each panel (SST = Sr/Ca; pH_{sw} = Li/Mg). The gray shaded region indicates the 95% confidence interval for each SMITE reconstruction. SMITE reconstruction statistics are listed at the bottom of each panel, with the equivalent statistics for Sr/Ca- and Li/Mg-derived estimates given in parentheticals.

3.3.3 User-based approaches for modifying SMITE reconstruction skill

Systematic inclusion of coral variables on the SMITE SST reconstruction

An intuitive procedure that new SMITE users might implement to optimize reconstruction skill would be to selectively exclude certain coral variables. Therefore, we applied the SMITE method to every possible combination of 2-7 coral variables (n = 120) in the two Bermudan corals and examined the subsequent impact on the correlation (r), accuracy (RMSE), and precision (SEP) of the SMITE SST reconstruction (Fig 3.11). This experiment was performed with no regularization implemented (Eq 3.7). We also provide a complimentary analysis regarding SMITE pH_{sw} reconstructions in the supplemental information (Figure B.3).

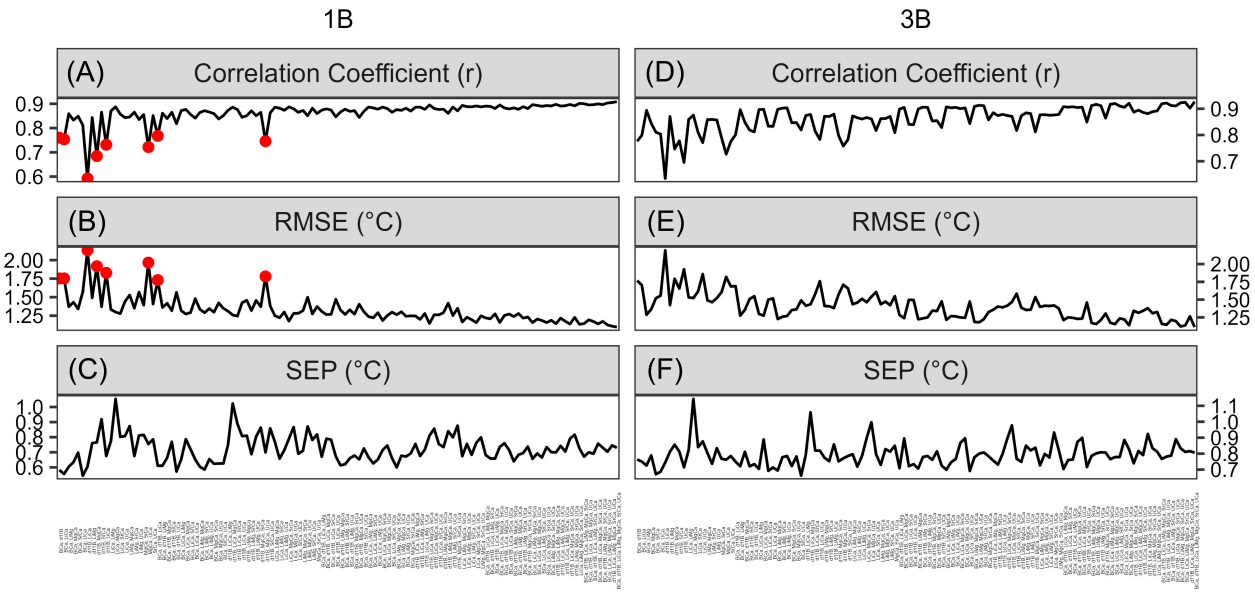

Figure 3.11: The correlation coefficient (r; A and D), the root-mean-square-error (RMSE; B and E), and standard error of prediction (SEP; C and F) for each SMITE SST reconstruction from the Bermudan *P. astreoides* corals through every combination of the seven coral geochemical variables (n = 120). The left side of each plot begins with only two coral variables (B/Ca and δ^{11}B). Each line then tracks the corresponding reconstruction statistic as variables are systematically replaced and added to the SMITE SST reconstruction. Each line thus ends on the final value of each reconstruction statistic when all seven coral variables are used.

Throughout the experiment, two notable patterns emerge. First, we observe a small but statistically significant trend ($p < 1e-9$) towards higher r-values and lower RMSEs for both corals as more variables are added to the SMITE method. Second, we note that there are certain combinations of coral variables that yield poorer quality reconstructions, indicated by 'spikes' in each of the reconstruction statistics. These spikes are particularly noticeable in coral 1B, which interestingly coincide with when both Li/Mg and Sr/Ca are excluded from the model (Panels A and B, red points). Furthermore, we note that the magnitude of these spikes decreases significantly as more coral variables are added to the SMITE SST reconstruction.

Regularization through truncation of singular values

SMITE method users can reduce uncertainty in SMITE model parameters by removing, or 'truncating', higher order (or less dominant) singular values from the coral variable field dataset (Eq 3.7). Here we demonstrate the effects of sequentially truncating singular values on the coral 1B SMITE SST and pH_{sw} reconstructions (Fig 3.12). The singular values of both Bermudan coral datasets are shown in Figure B.4, and a complimentary regularization analysis of coral 3B is provided in Figure B.4. At first glance, regularization has similar effects between the SMITE SST and pH_{sw} reconstructions. With each singular value truncated, uncertainty with respect to each SMITE model parameter is reduced, the correlation coefficient and SEP decrease, and the RMSE increases. In short, regularization compromises accuracy and correlation in exchange for precision and reduced uncertainty in SMITE model parame-

ters. The optimum level of regularization depends on two factors. First, the size of the coral dataset determines how many singular values can be truncated. Thus, a dataset with a greater number of variables offers greater control over how much information users could omit from the calibration. Second, regularization may vary depending on how information related to the climate target of interest is spread among the singular values.

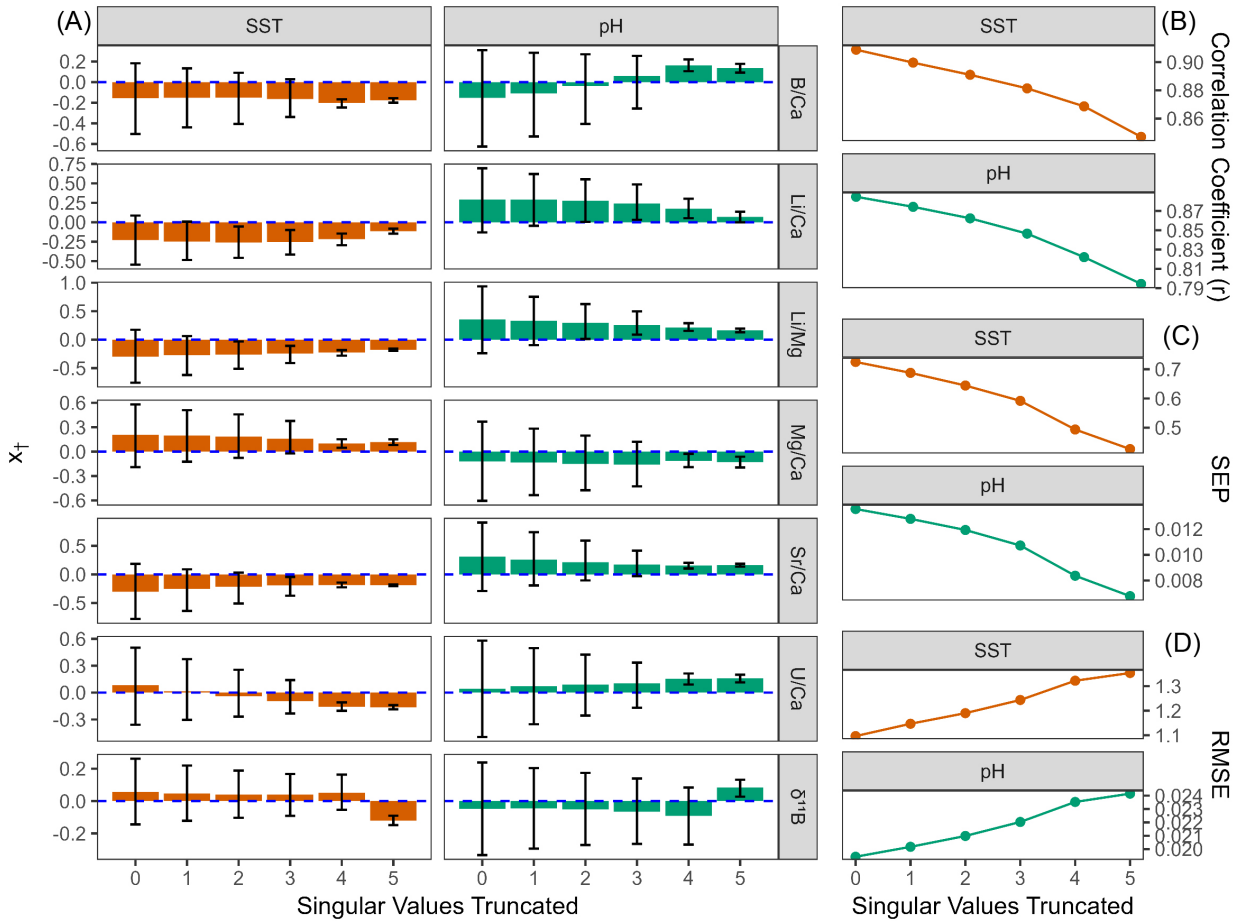

Figure 3.12: The effects of truncating singular values from coral 1B on the SMITE SST and pH_{sw} reconstruction. The x-axis in each plot denotes the number of singular values truncated. Each plot thus shows the progressive effects from no truncation (left) to maximum truncation (right). Truncation occurs from the highest (least dominant) singular values to the lowest (most dominant) singular values. The first two singular values can never be truncated. Colors distinguish the results from the SST reconstructions (orange) versus the pH_{sw} reconstructions (green). (A) SMITE model parameters, or $x_\dagger$ values, at each successive level of truncation. Rows denote the SMITE model parameter. The colored bar within each plot indicates the $x_\dagger$ value of the corresponding SMITE model parameter at a given level of truncation. Error bars for each $x_\dagger$ value denote the 95% confidence interval based on a Monte Carlo approach. (B – D) The correlation coefficient (r; B), the standard error of prediction (SEP; C), and the root-mean-square-error (RMSE; D) at each successive level of truncation.

It is important to note that results from the synthetic dataset are shown with no regularization implemented (section 3.2.1). With only three coral variables in the dataset (Sr/Ca, $\delta^{18}O$, $\delta^{11}B$) and three potential climate targets (SST, SSS, pH_{sw}), only one singular value can be truncated from the synthetic dataset. As expected, truncating the highest order singular value in the synthetic dataset results in greatly reduced uncertainty in SMITE model parame-

ters that, in the case of SST, are more stable across noise treatments. However, we also observe a significant reduction in reconstruction skill. This is likely because in a square system such as this (i.e., an equal number of climate targets and predictor variables), important climate information could be stored in even the highest order singular value. Therefore, we recommend only implementing truncation in overdetermined systems, where the number of coral variables is significantly higher than the number of climate targets.

3.4 Discussion

Here we used a variety of data types to assess the quality of SST and pH_{sw} estimates derived from the SMITE method, a novel multivariate calibration method that leverages covariance across a coral variable field to optimize reconstruction skill. Using two Bermudan *P. astreoides* corals as a proof-of-concept, we show that SMITE SST and pH_{sw} estimates are more accurate and precise than those derived from the best single-proxy estimators in each system. Furthermore, we find a high degree of inter-colony reproducibility in SMITE model parameters, and consequently reconstruction skill, when the SMITE method is applied to two corals that were collected near one another under identical environmental conditions. The reproducibility of SMITE model parameters across cores, which is achieved at higher levels of regularization (i.e., more singular values truncated), suggests that this method may hold great promise for application to the fossil record (i.e., when no calibration data are available for a particular core). In this section, we will discuss why the inclusion of different coral variables and regularization exhibit their observed effects on the accuracy, precision, correlation, and reproducibility of each reconstruction in the Bermuda coral datasets. As we examine the effects of these user-controlled procedures, we will use the results from the synthetic proxy studies to better inform our discussion of their effects on reconstruction skill. We conclude this section with a list of recommendations for those who wish to implement the SMITE method in their own datasets.

3.4.1 Properties of the coral variable field and their effects on SMITE reconstruction skill

Our findings in this study suggest that the quality of the SMITE reconstruction is contingent on both the quality and quantity of coral variables included in the reconstruction. The quantity effect is most clearly observed in the systematic inclusion experiment, where SMITE reconstruction skill improves as more coral variables are added to the SMITE dataset. However, there is a sense of 'diminishing returns' with how much the reconstruction improves after a certain threshold. The exact position of this 'threshold' warrants more rigorous testing in future studies. We observe the effect of coral variable quality in this same systematic inclusion experiment, specifically in the 'baseline' stability of the SMITE reconstruction (i.e., the overall variance of the reconstruction statistics throughout the experiment). We hypothesize that this baseline stability is a function of the coral variables with the strongest relationship to the climate target. For coral 1B, the presence of two robust SST proxies (Sr/Ca and Li/Mg) leads to many different

combinations of variables that produce strong SMITE SST reconstructions. Therefore, the main source of variance in the correlation and accuracy of the reconstructions is observed when neither Sr/Ca nor Li/Mg are included in the reconstruction (red dots, Fig. 11). While SMITE SST reconstructions for coral 3B still exhibit a high degree of skill throughout the course of the experiment, the greater variability we observe in the baseline SST reconstruction may be due to the relatively poorer performance of Sr/Ca, since Li/Mg remains a strong SST proxy in both corals.

We see further evidence for the importance of both the quantity and quality of the coral variables in the SMITE dataset when we consider how Gaussian noise impacts the synthetic proxy dataset. At a noise factor of 0, we observed how Sr/Ca and δ^{11}B were the greatest contributors to the SMITE SST and pH_{sw} reconstructions, respectively (Fig 3.5). This is logical, as synthetic Sr/Ca and δ^{11}B exhibit the strongest correlations with SST and pH_{sw}, respectively. As noise increased, the SMITE SST reconstructions maintained a high level of skill due to the additional presence of δ^{18}O as a very strong and sensitive SST proxy. However, SMITE pH_{sw} estimates did not capture the long-term trend after only a relatively small increase in noise. This stark contrast in reconstruction skill is due to the presence of multiple strong SST proxies in the synthetic dataset (Sr/Ca and δ^{18}O), with the added benefit of δ^{18}O being very robust to analytical noise. Conversely, synthetic δ^{11}B exhibits only a moderate correlation with pH_{sw} (r^2 = 0.68). Because SMITE treats δ^{11}B as linearly correlated to pH_{sw} and does not consider the relationship between pH_{sw} and pH_{cf} nor changes in pK_B, SMITE pH_{sw} reconstructions were significantly less skillful than the SST reconstructions. Therefore, even though we used the same exact calibration scheme for both climate target reconstructions, the stronger and more numerous SST proxies in the synthetic dataset result in stronger SMITE SST reconstructions relative to pH_{sw}.

3.4.2 The effects of truncation on SMITE reconstruction skill

SMITE reconstruction skill is also dependent on the degree of regularization, or the number of singular values truncated from the coral variable field (Eq 3.7; Fig 3.12). The underlying principle behind the SMITE method is that information associated with the climate target is encoded as covariance between the coral variables. Thus, climate target information is spread out between the singular values of the coral variable dataset. For coral 1B, we find multiple lines of evidence suggesting that most of the SST information is stored in the lower order, or dominant, singular values (i.e., singular values in which SST describes a large portion of variance in the data). First, the $x_\dagger$ value for most SMITE model parameters remains relatively constant at all levels of regularization, with U/Ca and δ^{11}B as the exception. Second, accuracy and correlation decrease linearly from 0–4 singular values truncated, after which the values continue to decrease less linearly. We also note a significant reduction in SMITE model parameter uncertainty at this same level of truncation. These observations suggest that removing the upper four singular values (i.e., truncation level 4) removes a significant amount of non-SST-related variability from the system, thus preventing SMITE from overfitting model parameters to potential noise. We find further evidence for this interpretation when examining

the singular values of the coral 1B dataset (Figure B.4), where we observe a subtle drop-off between the third singular value (74% cumulative variance explained) and the fourth singular value (82% cumulative variance explained). This drop-off also exists in the coral 3B dataset, with only minor differences in cumulative variance explained (69% and 80%, respectively). All these lines of evidence suggest that, for both the 1B and 3B SMITE SST reconstructions, the optimum trade-off of reconstruction skill and model parameter uncertainty occurs once the upper four singular values are truncated. Thus, this was the chosen level of regularization for both the 1B and 3B SMITE SST reconstructions in section 3.3.2.

For the SMITE pH_{sw} reconstruction, we find that pH_{sw} information is also likely stored in the lower order singular values. However, we note that the only SMITE pH_{sw} model parameters that do not change significantly throughout the experiment are Li/Mg, Mg/Ca, and Sr/Ca. These model parameters also have the least amount of uncertainty associated with them at each level of truncation. We also observe that the same shift in model parameter uncertainty and reconstruction skill that occurs in the SMITE SST reconstructions occurs in the SMITE pH_{sw} reconstructions at the exact same level of truncation (4). This finding further supports that the upper four singular values contain non-climate-related variability, specifically pH_{sw} in this case. Thus, we truncated the upper four singular values for the SMITE pH_{sw} reconstructions in section 3.3.2 as well. However, we speculate that the higher degree of uncertainty in SMITE pH_{sw} model parameters indicates that covariance in this particular coral variable field is not as strongly influenced by pH_{sw} as it is by SST.

3.4.3 Recommendations for implementers of the SMITE method

The results presented in this study show that SMITE SST and pH_{sw} estimates are more accurate, precise, and better correlated to *in situ* SST and pH_{sw} than those derived from the best or most-commonly-used single- and dual-proxy estimators. Furthermore, SMITE model parameters are highly reproducible between both Bermudan corals, and synthetic SMITE SST model parameters are stable across a large range of calibration periods (in this study, 5 to 100 years). The stability and reproducibility of the SMITE method makes it a promising candidate for fossil coral applications, where model parameters derived from modern cores would be applied to fossil material. Moreover, the SMITE method is computationally inexpensive and can be readily implemented into any paleoclimate reconstruction where multivariate coral data is available. Therefore, we provide here a list of recommendations for those who wish to utilize the SMITE method in their own datasets. Within this list, we provide some promising directions and potential limitations of the SMITE method for future studies.

Include as many coral variables as possible. While it may seem counterintuitive to include coral variables that are weakly associated with the climate target, our results show that SMITE reconstruction skill increases as the number of predictor variables increases. Additionally, increasing the number of coral variables pushes the system towards overdetermination, which increases flexibility when it comes to choosing the appropriate level of regular-

ization. However, our results also indicate that SMITE reconstruction skill is contingent upon the performance of the best predictors of the climate target. We therefore recommend users carefully examine the relationship between each coral variable and the climate target(s) prior to implementing the SMITE method (e.g., via scatter plots, covariance structure, etc.). Coral variables may need to be transformed for optimum results, as the SMITE method is a linear regression and thus assumes linearity between the predictor variables and the climate target. Therefore, certain coral variables that exhibit a non-linear relationship to the climate target (e.g., Li/Mg to SST over wide temperature ranges) may need to be transformed prior to entry in the calibration dataset.

Optimum regularization. Given the high level of uncertainty in SMITE model parameters when no singular values are truncated, we recommend users implement some level of regularization when applying the SMITE method in an overdetermined system (i.e., more coral variables than climate targets). Our results show that, even at high levels of regularization in such an overdetermined system, there is a minimal trade-off in reconstruction skill for large improvements in SMITE model parameter uncertainty, which in turn results in better reproducibility between corals. Future studies could apply the SMITE method to fossil coral material and potentially improve upon existing reconstructions. To determine the optimum level of regularization, users should qualitatively assess the distribution of the singular values in the coral dataset. Users should also systematically assess the reconstruction skill and model parameter uncertainty at each level of truncation (e.g., Fig 3.12). We recommend implementing regularization at the point when (a) the uncertainty associated with SMITE model parameters decreases significantly; and (b) when there is an inflection point in the distribution of the singular values (for the Bermuda corals, this occurred at $\sim$70% cumulative variance explained).

The degree of improvement in SMITE reconstruction skill over conventional calibration methods depends on the quality of the calibration dataset. Without regularization, it is mathematically impossible for the SMITE method to perform worse than the single best linear predictor of the climate target in any coral variable dataset. This is because as the performance of the best predictor in the dataset improves, SMITE utilizes that information and improves accordingly. However, our results indicate that, to a point, the magnitude of the improvement in SMITE reconstruction skill over conventional univariate regression techniques increases as the quality of the coral dataset decreases. If the best predictor for the climate target in the coral variable dataset is very robust (e.g., Sr/Ca to SST in coral 1B), then SMITE's improvement on that reconstruction will be modest. In contrast, SMITE drastically improves the reconstruction for datasets where the best predictor variable is relatively weak (e.g., δ^{11}B to pH_{sw} in the synthetic dataset), or where the signal-to-noise ratio is relatively low (e.g., Sr/Ca to SST in the synthetic dataset when analytical noise is increased). This is extremely promising for potential SMITE SST reconstructions implemented on tropical corals utilizing ICP-MS methods, where the annual SST range is relatively small ($\sim$2–3^{o}C) and where the analytical uncertainty for Sr/Ca is many factors higher than for ICP-OES. However, we acknowledge that the impact of noise on a tropical coral variable dataset may not scale linearly (as modeled in the synthetic experi-

ment) due to increased age-model uncertainties when the annual SST range is subdued. These nonlinear processes could influence the robustness of SMITE reconstructions. Thus future work is needed to address the utility of SMITE SST reconstructions using tropical corals. Additionally, for climate targets such as pH_{sw} where the linear correlation to a coral variable is relatively poor and covariance associated with the climate target may not be as pronounced, we speculate that users will need to be more strategic in which coral variables are included in the SMITE calibration dataset. Which specific coral variables are included for SMITE pH_{sw} reconstructions in particular should be rigorously tested in future studies.

Further testing is needed for the SMITE method's ability to capture long-term trends in pH_{sw}. Using the synthetic dataset, we show that SMITE SST model parameters are insensitive to the length of the calibration period between 5 and 100 years (in five-year increments). Conversely, SMITE pH_{sw} loadings did not stabilize until 30 years of calibration data were available. This is an unrealistic calibration period length for most coral-based pH_{sw} reconstruction. Unfortunately, SMITE pH_{sw} reconstructions calculated prior to the 30-year calibration period fail to capture the long-term trend in pH_{sw}. This could be due to the complications associated with SMITE treating $\delta^{11}B$ as a linear proxy for pH_{sw} and not accounting for variability in pK_B, which is both temperature and salinity dependent. Alternatively, it could be due to the rapid decrease in pH_{sw} partway through the 20th century. While it is encouraging that SMITE pH_{sw} estimates were highly skillful and reproducible between the Bermuda corals, this could be due to either the strong covariance of pH_{sw} and SST at Hog Reef ($r^2 = 0.82$), or the relatively small sample size of the Bermuda coral dataset. Thus, it cannot be ruled out that significant changes in long-term trends may further complicate the SMITE pH_{sw} reconstruction, at least in square systems when little-to-no regularization can be implemented. Furthermore, the *P. astreoides* coral datasets in this study were relatively short (35 and 40 months, respectively), and the synthetic dataset is highly idealized in its relationships between the synthetic proxies and the reconstruction targets. Additional testing of the SMITE method is needed on multi-decadal coral datasets at lower sampling resolutions (e.g., annual rather than monthly), which could elucidate how SMITE can help with broader climate interpretations.

SMITER - an open-source package in R for implementing the SMITE method on coral datasets. The SMITE method is computationally inexpensive and can be readily performed on a variety of statistical software programs. However, we aim to facilitate rapid dissemination of the SMITE method with the release of the open-source SMITER package in R (`https://hphughescraft.github.io/SMITER`). The SMITER package gives researchers a user-friendly tool to implement the SMITE method in their own datasets, which could quickly advance the community's understanding of SMITE's utility on tropical corals and its ability to capture long-term trends in pH_{sw}, as well as how the method performs on longer datasets with coarser sampling resolution. Furthermore, application of the SMITE method on the large (and growing) number of existing coral records will generate an equally large number of SMITE model parameters. These model parameters can be independently assessed to determine

the extent of the SMITE method's reproducibility among corals of varying taxa and location. Such reproducibility-focused research questions could ultimately improve coral-based paleoclimate reconstructions on fossil material.

3.5 Acknowledgments

We gratefully acknowledge Sarah Fowell and Nick Bates for collecting the coral cores from Hog Reef, Bermuda. Dan Doran and Matthew Beverly-Smith are gratefully acknowledged for sample preparation, whilst Andy Milton is thanked for analytical support. We thank the British Ocean Sediment Core Research Facility (BOSCORF) for supporting the generation of X-radiography data used in this study. We also thank Garrett Braniecki, Marissa Hughes, and Richard Smith for their contributions and helpful suggestions towards interpreting SMITE method uncertainties and output. Comments from two reviewers helped improve this manuscript and were greatly appreciated.

BIBLIOGRAPHY

N. Allison and A. A. Finch. Reproducibility of minor and trace element determinations in porites coral skeletons by secondary ion mass spectrometry. *Geochem. Geophys. Geosyst.*, 10(4), 2009. ISSN 1525-2027. doi: 10.1029/2008GC002239.

A. E. Alpert, A. L. Cohen, D. W. Oppo, T. M. DeCarlo, J. M. Gove, and C. W. Young. Comparison of equatorial pacific sea surface temperature variability and trends with sr/ca records from multiple corals. *Paleoceanography*, 31:252–265, 2016. doi: 10.1002/2015PA002897.

R. C. Aster, B. Borchers, and C. H. Thurber. *Parameter estimation and inverse problems*. Elsevier, 2018. ISBN 0128134232.

J. Beck, R. L. Edwards, E. Ito, F. W. Taylor, J. Recy, F. Rougerie, P. Joannot, and C. Henin. Sea-surface temperature from coral skeletal strontium/calcium ratios. *Science*, 257:644–647, 1992. doi: 10.1126/science.257.5070.644.

T. B. Chalk, C. D. Standish, C. D'Angelo, K. D. Castillo, J. A. Milton, and G. L. Foster. Mapping coral calcification strategies from in situ boron isotope and trace element measurements of the tropical coral siderastrea siderea. *Sci. Rep.*, 11:472, 2021. doi: 10.1038/s41598-020-78778-1.

H. Clarke, J. P. D'Olivo, J. Falter, J. Zinke, R. Lowe, and M. McCulloch. Differential response of corals to regional mass-warming events as evident from skeletal sr/ca and mg/ca ratios. *Geochem. Geophys. Geosyst.*, 18(5):1794–1809, 2017. ISSN 1525-2027. doi: 10.1002/2016GC006788.

H. Clarke, J. P. D'Olivo, M. Conde, R. D. Evans, and M. T. McCulloch. Coral records of variable stress impacts and possible acclimatization to recent marine heat wave events on the northwest shelf of australia. *Paleoceanogr. Paleoclimatol.*, 34(11):1672–1688, 2019. ISSN 2572-4517. doi: 10.1029/2018PA003509.

T. Corrège. Sea surface temperature and salinity reconstruction from coral geochemical tracers. *Palaeogeogr. Palaeoclimatol. Palaeoecol.*, 232:408–428, 2006. ISSN 0031-0182. doi: 10.1016/j.palaeo.2005.10.014.

T. A. Courtney, M. Lebrato, N. R. Bates, A. Collins, S. J. de Putron, R. Garley, R. Johnson, J.-C. Molinero, T. J. Noyes, C. L. Sabine, and A. J. Andersson. Environmental controls on modern scleractinian coral and reef-scale calcification. *Sci. Adv.*, 3(11):e1701356, 2017. doi: 10.1126/sciadv.1701356.

K. Cuny-Guirriec, E. Douville, S. Reynaud, D. Allemand, L. Bordier, M. Canesi, C. Mazzoli, M. Taviani, S. Canese, and M. McCulloch. Coral li/mg thermometry: Caveats and constraints. *Chem. Geol.*, 523:162–178, 2019. doi: 10.1016/j.chemgeo.2019.03.038.

E. de Boisséson, M. A. Balmaseda, and M. Mayer. Ocean heat content variability in an ensemble of twentieth century ocean reanalyses. *Clim. Dynam.*, 50(9):3783–3798, 2018. ISSN 1432-0894. doi: 10.1007/s00382-017-3845-0.

T. M. DeCarlo, G. A. Gaetani, A. L. Cohen, G. L. Foster, A. E. Alpert, and J. A. Stewart. Coral sr-u thermometry. *Paleoceanogr. Paleoclimatol.*, 31:626–638, 2016. doi: 10.1002/2015PA002908.

K. L. DeLong, T. M. Quinn, C. Shen, and K. Lin. A snapshot of climate variability at tahiti at 9.5 ka using a fossil coral from iodp expedition 310. *Geochem. Geophys. Geosyst.*, 11:Q06005, 2010. ISSN 1525-2027. doi: 10.1029/2009GC002758.

K. L. DeLong, T. M. Quinn, F. W. Taylor, C. C. Shen, and K. Lin. Improving coral-base paleoclimate reconstructions by replicating 350 years of coral sr/ca variations. *Palaeogeogr. Palaeoclimatol. Palaeoecol.*, 373:6–24, 2013. ISSN 0031-0182. doi: 10.1016/j.palaeo.2012.08.019.

K. L. DeLong, C. R. Maupin, J. A. Flannery, T. M. Quinn, and C.-C. Shen. Refining temperature reconstructions with the atlantic coral siderastrea siderea. *Palaeogeogr. Palaeoclimatol. Palaeoecol.*, 462:1–15, 2016. doi: 10.1016/j.palaeo.2016.08.028.

A. G. Dickson. Thermodynamics of the dissociation of boric acid in synthetic seawater from 273.15 to 318.15 k. *Deep Sea Res. Part A*, 37(5):755–766, 1990. ISSN 0198-0149. doi: 10.1016/0198-0149(90)90004-F.

J. P. D'Olivo, D. J. Sinclair, K. Rankenburg, and M. T. McCulloch. A universal multi-trace element calibration for reconstructing sea surface temperatures from long-lived porites corals: Removing 'vital-effects'. *Geochim. Cosmochim. Acta*, 239:109–135, 2018. doi: 10.1016/j.gca.2018.07.035.

J. P. D'Olivo, G. Ellwood, T. M. DeCarlo, and M. T. McCulloch. Deconvolving the long-term impacts of ocean acidification and warming on coral biomineralisation. *Earth Planet. Sc. Lett.*, 526:115785, 2019. ISSN 0012-821X. doi: 10.1016/j.epsl.2019.115785.

J. P. D'Olivo and M. T. McCulloch. Response of coral calcification and calcifying fluid composition to thermally induced bleaching stress. *Scientific reports*, 7:2207, 2017. doi: 10.1038/s41598-017-02306-x.

S. Epstein and T. Mayeda. Variation of o18 content of waters from natural sources. *Geochim. Cosmochim. Acta*, 4 (5):213–224, 1953. ISSN 0016-7037. doi: 10.1016/0016-7037(53)90051-9.

R. A. Fisher. *Statistical Methods for Research Workers*, pages 66–70. Springer New York, New York, NY, 1970. ISBN 978-1-4612-4380-9. doi: 10.1007/978-1-4612-4380-9_6.

G. L. Foster, P. A. E. Pogge von Strandmann, and J. W. B. Rae. Boron and magnesium isotopic composition of seawater. *Geochem. Geophys. Geosyst.*, 11, 2010. doi: 10.1029/2010GC003201.

G. L. Foster, B. Hönisch, G. Paris, G. S. Dwyer, J. W. B. Rae, T. Elliott, J. Gaillardet, N. G. Hemming, P. Louvat, and A. Vengosh. Interlaboratory comparison of boron isotope analyses of boric acid, seawater and marine caco3 by mc-icpms and ntims. *Chem. Geol.*, 358:1–14, 2013. ISSN 0009-2541. doi: 10.1016/j.chemgeo.2013.08.027.

S. E. Fowell, K. Sandford, J. A. Stewart, K. D. Castillo, J. B. Ries, and G. L. Foster. Intrareef variations in li/mg and sr/ca sea surface temperature proxies in the caribbean reef-building coral siderastrea siderea. *Paleoceanography*, 31:1315–1329, 2016. doi: 10.1002/2016PA002968.

G. A. Gaetani, A. L. Cohen, Z. Wang, and J. Crusius. Rayleigh-based, multi-element coral thermometry: A biomineralization approach to developing climate proxies. *Geochim. Cosmochim. Acta*, 75:1920–1932, 2011. doi: 10.1016/j.gca.2011.01.010.

A. C. Gagnon, A. M. Gothmann, O. Branson, J. W. B. Rae, and J. A. Stewart. Controls on boron isotopes in a cold-water coral and the cost of resilience to ocean acidification. *Earth Planet. Sc. Lett.*, 554:116662, 2021. ISSN 0012-821X. doi: 10.1016/j.epsl.2020.116662.

J.-P. Gattuso, J.-M. Epitalon, H. Lavigne, and J. Orr. seacarb, 2022.

G. H. Golub and C. F. Van Loan. *Matrix computations*. JHU press, 2013. ISBN 1421408597.

N. F. Goodkin, K. A. Hughen, and A. L. Cohen. A multicoral calibration method to approximate a universal equation relating sr/ca and growth rate to sea surface temperature. *Paleoceanography*, 22, 2007. doi: 10.1029/2006PA001312.

P. R. Grothe, K. M. Cobb, G. Liguori, E. Di Lorenzo, A. Capotondi, Y. Lu, H. Cheng, R. L. Edwards, J. R. Southon, G. M. Santos, D. M. Deocampo, J. Lynch-Stieglitz, T. Chen, H. R. Sayani, D. M. Thompson, J. L. Conroy, A. L. Moore, K. Townsend, M. Hagos, G. O'Connor, and L. T. Toth. Enhanced el niño–southern oscillation variability in recent decades. *Geophys. Res. Lett.*, 47(7):e2019GL083906, 2020. ISSN 0094-8276. doi: 10.1029/2019GL083906.

C. A. Grove, S. Kasper, J. Zinke, M. Pfeiffer, D. Garbe-Schönberg, and G.-J. A. Brummer. Confounding effects of coral growth and high sst variability on skeletal sr/ca: Implications for coral paleothermometry. *Geochem. Geophys. Geosyst.*, 14(4):1277–1293, 2013. ISSN 1525-2027. doi: 10.1002/ggge.20095.

M. P. Hain, G. L. Foster, and T. Chalk. Robust constraints on past co2 climate forcing from the boron isotope proxy. *Paleoceanogr. Paleoclimatol.*, 33(10):1099–1115, 2018. ISSN 2572-4517. doi: 10.1029/2018PA003362.

S. Hastenrath. *Climate dynamics of the tropics*, volume 8. Springer Science & Business Media, 2012. ISBN 9401131562.

E. C. Hathorne, T. Felis, A. Suzuki, H. Kawahata, and G. Cabioch. Lithium in the aragonite skeletons of massive porites corals: A new tool to reconstruct tropical sea surface temperatures. *Paleoceanography*, 28:143–152, 2013a. doi: 10.1029/2012PA002311.

E. C. Hathorne, A. Gagnon, T. Felis, J. Adkins, R. Asami, W. Boer, N. Caillon, D. Case, K. M. Cobb, E. Douville, P. DeMenocal, A. Eisenhauer, D. Garbe-Schönberg, W. Geibert, S. Goldstein, K. Hughen, M. Inoue, H. Kawahata, M. Kölling, F. L. Cornec, B. K. Linsley, H. V. McGregor, P. Montagna, I. S. Nurhati, T. M. Quinn, J. Raddatz, H. Rebaubier, L. Robinson, A. Sadekov, R. Sherrell, D. Sinclair, A. W. Tudhope, G. Wei, H. Wong, H. C. Wu, and C.-F. You. Interlaboratory study for coral sr/ca and other element/ca ratio measurements. *Geochem. Geophys. Geosyst.*, 14:3730–3750, 2013b. doi: 10.1002/ggge.20230.

E. Hawkins, P. Ortega, E. Suckling, A. Schurer, G. Hegerl, P. Jones, M. Joshi, T. J. Osborn, V. Masson-Delmotte, J. Mignot, P. Thorne, and G. J. van Oldenborgh. Estimating changes in global temperature since the preindustrial period. *Bull. Amer. Meteor. Soc.*, 98(9):1841–1856, 2017. ISSN 0003-0007. doi: 10.1175/bams-d-16-0007.1.

S. Hetzinger, M. Pfeiffer, W.-C. Dullo, J. Zinke, and D. Garbe-Schönberg. A change in coral extension rates and stable isotopes after el niño-induced coral bleaching and regional stress events. *Sci. Rep.*, 6:32879, 2016. doi: 10.1038/srep32879.

S. Hirabayashi, Y. Yokoyama, A. Suzuki, Y. Kawakubo, Y. Miyairi, T. Okai, and S. Nojima. Coral growth-rate insensitive sr/ca as a robust temperature recorder at the extreme latitudinal limits of porites. *Geochem. J.*, 47:e1–e5, 2013. doi: 10.2343/geochemj.2.0259.

I. T. Jolliffe. A note on the use of principal components in regression. *J. Roy. Stat. Soc.*, 31(3):300–303, 1982. ISSN 00359254, 14679876. doi: 10.2307/2348005.

J. P. Jones, J. P. Carricart-Ganivet, R. Iglesias Prieto, S. Enríquez, M. Ackerson, and R. I. Gabitov. Microstructural variation in oxygen isotopes and elemental calcium ratios in the coral skeleton of orbicella annularis. *Chem. Geol.*, 419:192–199, 2015. ISSN 0009-2541. doi: 10.1016/j.chemgeo.2015.10.044.

P. D. Jones, K. R. Briffa, T. J. Osborn, J. M. Lough, T. D. van Ommen, B. M. Vinther, J. Luterbacher, E. R. Wahl, F. W. Zwiers, M. E. Mann, G. A. Schmidt, C. M. Ammann, B. M. Buckley, K. M. Cobb, J. Esper, H. Goosse, N. Graham, E. Jansen, T. Kiefer, C. Kull, M. Kuttel, E. Mosley-Thompson, J. T. Overpeck, N. Riedwyl, M. Schulz, A. W. Tudhope, R. Villalba, H. Wanner, E. Wolff, and E. Xoplaki. High-resolution palaeoclimatology of the last millennium: a review of current status and future prospects. *The Holocene*, 19:3–49, 2009. doi: 10.1177/0959683608098952.

Y. Kawakubo, Y. Yokoyama, A. Suzuki, T. Okai, C. Alibert, L. Kinsley, and S. Eggins. Precise determination of sr/ca by laser ablation icp-ms compared to icp-aes and application to multi-century temperate corals. *GEOCHEMICAL JOURNAL*, 48(2):145–152, 2014. ISSN 0016-7002. doi: 10.2343/geochemj.2.0295.

E. C. Kent and J. J. Kennedy. Historical estimates of surface marine temperatures. *Annual Review of Marine Science*, 13(1):283–311, 2021. doi: 10.1146/annurev-marine-042120-111807.

K. Klochko, A. J. Kaufman, W. Yao, R. H. Byrne, and J. A. Tossell. Experimental measurement of boron isotope fractionation in seawater. *Earth Planet. Sc. Lett.*, 248:276–285, 2006. doi: 10.1016/j.epsl.2006.05.034.

I. B. Kuffner, P. L. Jokiel, K. S. Rodgers, A. J. Andersson, and F. T. Mackenzie. An apparent "vital effect" of calcification rate on the sr/ca temperature proxy in the reef coral montipora capitata. *Geochem. Geophys. Geosyst.*, 13: Q08004, 2012. doi: 10.1029/2012GC004128.

C. Lanczos. *Linear differential operators*. SIAM, 1996. ISBN 0898713706.

P. J. le Roux, S. B. Shirey, L. Benton, E. H. Hauri, and T. D. Mock. In situ, multiple-multiplier, laser ablation icp-ms measurement of boron isotopic composition () at the nanogram level. *Chem. Geol.*, 203(1):123–138, 2004. ISSN 0009-2541. doi: 10.1016/j.chemgeo.2003.09.006.

A. N. LeGrande and G. A. Schmidt. Global gridded data set of the oxygen isotopic composition in seawater. *Geophys. Res. Lett.*, 33(12), 2006. ISSN 0094-8276. doi: 10.1029/2006GL026011.

A. Lenton, B. Tilbrook, R. J. Matear, T. P. Sasse, and Y. Nojiri. Historical reconstruction of ocean acidification in the australian region. *Biogeosciences*, 13:1753–1765, 2016. doi: 10.5194/bg-13-1753-2016.

M. T. McCulloch, J. P. D'Olivo, J. Falter, M. Holcomb, and J. A. Trotter. Coral calcification in a changing world and the interactive dynamics of ph and dic upregulation. *Nat. Commun.*, 8:15686, 2017. doi: 10.1038/ncomms15686.

C. J. Merchant, O. Embury, C. E. Bulgin, T. Block, G. K. Corlett, E. Fiedler, S. A. Good, J. Mittaz, N. A. Rayner, D. Berry, S. Eastwood, M. Taylor, Y. Tsushima, A. Waterfall, R. Wilson, and C. Donlon. Satellite-based time-series of sea-surface temperature since 1981 for climate applications. *Scientific Data*, 6(1):223, 2019. ISSN 2052-4463. doi: 10.1038/s41597-019-0236-x.

E. Moore. On the reciprocal of the general algebraic matrix. *Bull. Amer. Math. Soc.*, 26:394–395, 1920.

G. R. North, T. L. Bell, R. F. Cahalan, and F. J. Moeng. Sampling errors in the estimation of empirical orthogonal functions. *Mon. Weather Rev.*, 110(7):699–706, 1982. ISSN 0027-0644. doi: 10.1175/1520-0493(1982)110⟨0699:Seiteo⟩2.0.Co;2.

M. R. Ong, N. F. Goodkin, R. Guppy, and K. A. Hughen. Colpophyllia natans from tobago, a novel paleoclimate archive for reconstructing sea surface temperature in the tropical atlantic. *Paleoceanogr. Paleoclimatol.*, 37(12): e2022PA004483, 2022. ISSN 2572-4517. doi: 10.1029/2022PA004483.

R. Penrose. A generalized inverse for matrices. *Proc. Cambridge Phil. Soc.*, 51:406–413, 1955.

E. V. Reed, D. M. Thompson, J. E. Cole, J. M. Lough, N. E. Cantin, A. H. Cheung, A. Tudhope, L. Vetter, G. Jimenez, and R. L. Edwards. Impacts of coral growth on geochemistry: Lessons from the galápagos islands. *Paleoceanogr. Paleoclimatol.*, 36(4):e2020PA004051, 2021. ISSN 2572-4517. doi: 10.1029/2020PA004051.

C. L. Ross, J. L. Falter, and M. T. McCulloch. Active modulation of the calcifying fluid carbonate chemistry (, b/ca) and seasonally invariant coral calcification at sub-tropical limits. *Sci. Rep.*, 7:1–11, 2017. doi: 10.1038/s41598-017-14066-9.

C. L. Ross, T. M. DeCarlo, and M. T. McCulloch. Calibration of sr/ca, li/mg and sr-u paleothermometry in branching and foliose corals. *Paleoceanography and Paleoclimatology*, 34:1271–1291, 2019. doi: 10.1029/2018PA003426.

J. Sadler, G. E. Webb, L. D. Nothdurft, and B. Dechnik. Geochemistry-based coral palaeoclimate studies and the potential of 'non-traditional' (non-massive porites) corals: Recent developments and future progression. *Earth-Sci. Rev.*, 139:291–316, 2014. ISSN 0012-8252. doi: 10.1016/j.earscirev.2014.10.002.

C. Saenger and Z. Wang. Magnesium isotope fractionation in biogenic and abiogenic carbonates: implications for paleoenvironmental proxies. *Quaternary Sci. Rev.*, 90:1–21, 2014. ISSN 0277-3791. doi: 10.1016/j.quascirev.2014.01.014.

H. R. Sayani, K. M. Cobb, K. DeLong, N. T. Hitt, and E. R. M. Druffel. Intercolony and sr/ca variability among porites spp. corals at palmyra atoll: Toward more robust coral-based estimates of climate. *Geochem. Geophys. Geosyst.*, 20(11):5270–5284, 2019. ISSN 1525-2027. doi: 10.1029/2019GC008420.

D. P. Schrag. Rapid analysis of high-precision sr/ca ratios in corals and other marine carbonates. *Paleoceanography*, 14:97–102, 1999. doi: 10.1029/1998PA900025.

D. J. Sinclair. Rbme coral temperature reconstruction: An evaluation, modifications, and recommendations. *Geochim. Cosmochim. Acta*, 154:66–80, 2015. ISSN 0016-7037. doi: 10.1016/j.gca.2015.01.006.

D. J. Sinclair, B. Williams, and M. Risk. A biological origin for climate signals in corals—trace element "vital effects" are ubiquitous in scleractinian coral skeletons. *Geophys. Res. Lett.*, 33:L17707, 2006. doi: 10.1029/2006GL027183.

C. D. Standish, T. B. Chalk, T. L. Babila, J. A. Milton, M. R. Palmer, and G. L. Foster. The effect of matrix interferences on in situ boron isotope analysis by laser ablation multi-collector inductively coupled plasma mass spectrometry. *Rapid Commun. Mass. Sp.*, 33(10):959–968, 2019. ISSN 0951-4198. doi: 10.1002/rcm.8432.

C. D. Standish, T. B. Chalk, M. Saeed, F. Lei, M. C. Buckingham, C. D'Angelo, J. Wiedenmann, and G. L. Foster. Geochemical responses of scleractinian corals to nutrient stress. *Geochim. Cosmochim. Acta*, 351:108–124, 2023. ISSN 0016-7037. doi: 10.1016/j.gca.2023.04.011.

D. K. Steinberg, C. A. Carlson, N. R. Bates, R. J. Johnson, A. F. Michaels, and A. H. Knap. Overview of the us jgofs bermuda atlantic time-series study (bats): a decade-scale look at ocean biology and biogeochemistry. *Deep Sea Res. Part II*, 48(8):1405–1447, 2001. ISSN 0967-0645. doi: 10.1016/S0967-0645(00)00148-X.

C. L. Stephans, T. M. Quinn, F. W. Taylor, and T. Corrège. Assessing the reproducibility of coral-based climate records. *Geophys. Res. Lett.*, 31(18), 2004. ISSN 0094-8276. doi: 10.1029/2004GL020343.

J. A. Stewart, L. F. Robinson, R. D. Day, I. Strawson, A. Burke, J. W. B. Rae, P. T. Spooner, A. Samperiz, P. J. Etnoyer, B. Williams, A. Paytan, M. J. Leng, V. Häussermann, L. N. Wickes, R. Bratt, and H. Pryer. Refining trace metal temperature proxies in cold-water scleractinian and stylasterid corals. *Earth Planet. Sc. Lett.*, 545:116412, 2020. ISSN 0012-821X. doi: 10.1016/j.epsl.2020.116412.

J. A. Stewart, S. J. Christopher, J. R. Kucklick, L. Bordier, T. B. Chalk, A. Dapoigny, E. Douville, G. L. Foster, W. R. Gray, R. Greenop, M. Gutjahr, F. Hemsing, M. J. Henehan, P. Holdship, Y.-T. Hsieh, A. Kolevica, Y.-P. Lin, E. M. Mawbey, J. W. B. Rae, L. F. Robinson, R. Shuttleworth, C.-F. You, S. Zhang, and R. D. Day. Nist rm 8301 boron isotopes in marine carbonate (simulated coral and foraminifera solutions): Inter-laboratory and trace element ratio value assignment. *Geostand. Geoanal. Res.*, 45(1):77–96, 2021. ISSN 1639-4488. doi: 10.1111/ggr.12363.

R. D. Susanto, Q. Zheng, and X.-H. Yan. Complex singular value decomposition analysis of equatorial waves in the pacific observed by topex/poseidon altimeter. *Journal of Atmospheric and Oceanic Technology*, 15(3):764–774, 1998. ISSN 0739-0572. doi: 10.1175/1520-0426(1998)015⟨0764:CSVDAO⟩2.0.CO;2.

D. M. Thompson. Environmental records from coral skeletons: A decade of novel insights and innovation. *WIREs Clim. Change*, 13(1):e745, 2021. ISSN 1757-7780. doi: 10.1002/wcc.745.

D. M. Thompson, T. R. Ault, M. N. Evans, J. E. Cole, and J. Emile-Geay. Comparison of observed and simulated tropical climate trends using a forward model of coral . *Geophys. Res. Lett.*, 38:L14706, 2011. doi: 10.1029/2011GL048224.

M. Vihtakari. ggoceanmaps: Plot data on oceanographic maps using 'ggplot2', 2024.

R. M. Walter, H. R. Sayani, T. Felis, K. M. Cobb, N. J. Abram, A. K. Arzey, A. R. Atwood, L. D. Brenner, E. P. Dassié, K. L. DeLong, B. Ellis, J. Emile-Geay, M. J. Fischer, N. F. Goodkin, J. A. Hargreaves, K. H. Kilbourne, H. Krawczyk, N. P. McKay, A. L. Moore, S. A. Murty, M. R. Ong, R. D. Ramos, E. V. Reed, D. Samanta, S. C. Sanchez, J. Zinke, and the PAGES CoralHydro2k Project Members. The coralhydro2k database: a global, actively curated compilation of coral δ^{18}o and sr / ca proxy records of tropical ocean hydrology and temperature for the common era. *Earth Syst. Sci. Data*, 15(5):2081–2116, 2023. doi: 10.5194/essd-15-2081-2023.

P. Wessel and W. H. F. Smith. A global, self-consistent, hierarchical, high-resolution shoreline database. *Journal of Geophysical Research: Solid Earth*, 101(B4):8741–8743, 1996. ISSN 0148-0227. doi: 10.1029/96JB00104.

Y. Wu, S. J. Fallon, N. E. Cantin, and J. M. Lough. Assessing multiproxy approaches (sr/ca, u/ca, li/mg, and b/mg) to reconstruct sea surface temperature from coral skeletons throughout the great barrier reef. *Sci. Total. Environ.*, 786:147393, 2021. ISSN 0048-9697. doi: 10.1016/j.scitotenv.2021.147393.

Y.-Y. Xu, S. Pearson, and K. H. Kilbourne. Assessing coral sr/ca–sst calibration techniques using the species diploria strigosa. *Palaeogeogr. Palaeoclimatol. Palaeoecol.*, 440:353–362, 2015. doi: 10.1016/j.palaeo.2015.09.016.

R. Zeebe and D. A. Wolf-Gladrow. *CO2 in Seawater: Equilibrium, Kinetics, Isotopes*, volume 65 of *Elsevier Oceanography Series*. Gulf Professional Publishing, Amsterdam, 2001.

CHAPTER 4

Beyond the Seasonal Cycle: Fidelity Testing Coral SST Calibration Methods Across Time and Space

4.1 Introduction

The tropical oceans serve as the heat engine of the global climate system, absorbing the majority of incoming solar radiation and driving large-scale exchanges of heat between the ocean and atmosphere. These processes fuel global circulation patterns and exert strong controls on regional hydroclimate variability across the tropics and beyond (Hastenrath, 2012; Loeb et al., 2012). As such, tropical sea surface temperatures (SSTs) are considered an essential climate variable and are closely linked to the occurrence and intensity of extreme events such as heat waves, hurricanes, droughts, and floods (Trenberth and Fasullo, 2012).

In the absence of long-term instrumental records, paleoclimate reconstructions derived from the geochemistry of coral skeletons offer a powerful and independent means of estimating past SST variability (Sadler et al., 2014; Thompson, 2021). As corals grow, they incorporate trace elements and isotopic ratios that reflect ambient environmental conditions, particularly SST, into their aragonite skeletons (Beck et al., 1992; Weber and Woodhead, 1972). Like tree rings, corals form annual growth bands, enabling precise chronological alignment of high-resolution geochemical records (DeLong et al., 2013; Walter et al., 2023). When collected from strategically selected sites, these coral records can be linked to large-scale climate phenomena such as the El Niño-Southern Oscillation (ENSO), the dominant mode of interannual climate variability outside the seasonal cycle (Grothe et al., 2020). Coral-based reconstructions from the 20th century thus provide a critical, observationally independent benchmark for assessing SST variability, complementing both instrumental data and model-based climate estimates (Chen et al., 2019; Davis et al., 2019; Lough, 2010).

Despite the valuable insights coral skeletal geochemistry provides for reconstructing historical tropical SST variability, converting these geochemical signals into robust SST estimates remains a significant challenge. A central issue is the reproducibility of regression coefficients used to convert geochemical proxies to temperature (Corrège, 2006; Cuny-Guirriec et al., 2019; Gagan et al., 2012; Sayani et al., 2019). While some studies demonstrate that reproducibility is possible with careful sampling and methodological rigor (Allison and Finch, 2009; DeLong et al., 2013, 2016; Sayani et al., 2019; Stephans et al., 2004; Stewart et al., 2020), many others report substantial variability in regression slopes even among colonies of the same species growing in close proximity, often necessitating colony-

specific calibrations (DeLong et al., 2010; Goodkin et al., 2007). Moreover, regression parameters derived during the calibration period have been shown to drift over time, varying across decadal and longer timescales (Gagan et al., 2012; Wilson et al., 2006). This lack of reproducibility, both spatially (between corals) and temporally (within individual cores), significantly raises uncertainty in reconstructions that extend beyond the instrumental period.

In recent years, many studies have adopted multiproxy approaches in an effort to improve the reproducibility of regression coefficients. These methods often demonstrate greater consistency across locations and coral taxa (DeCarlo et al., 2016; D'Olivo et al., 2018; Hughes et al., 2024; Wu et al., 2021). However, this improvement in reproducibility frequently comes at the expense of reduced sampling resolution or diminished reconstruction skill relative to the best-performing univariate estimators in a given system (Sinclair, 2015; DeCarlo et al., 2016; D'Olivo et al., 2018). More recently, machine learning has emerged as a promising tool for achieving reproducible regression parameters in coral-based paleothermometry (Wei et al., 2024). Using a 'universal' calibration involving taxon and region-specific hyperparameters, the authors were able to achieve an impressive best RMSE under 1°C. Yet these models required extensive training datasets with broad regional coverage and a large suite of geochemical variables to perform effectively. Additionally, many machine learning models remain empirically driven, and while some offer interpretability tools (Karamperidou, 2024), they often lack the mechanistic transparency traditionally sought in climate studies (O'Loughlin et al., 2025). This tradeoff between predictive skill and interpretability remains an open and active area of research in applying machine learning to proxy system modeling (e.g., Murray et al., 2023).

Hughes et al. (2024) proposed the Scleractinian Multivariate Isotope and Trace Element (SMITE) method as a means of achieving skillful SST reconstructions at the individual record level while also yielding reproducible and mechanistically sensible regression coefficients. The authors suggest that the generalized inverse solution (Moore, 1920; Penrose, 1955) can be used to leverage the covariance among multiple geochemical variables in coral skeletons to reconstruct SST, thereby improving correlation, accuracy, precision, and reproducibility relative to standard univariate methods such as Sr/Ca or Li/Mg. However, SMITE has thus far only been tested on two corals over a few annual cycles. Rigorous evaluation of its performance and reproducibility, particularly in comparison to conventional methods, remains outstanding and is a primary focus of this study.

In addition to concerns about reproducibility, it is standard practice for coral-based SST calibrations to be performed with the seasonal cycle intact. Indeed, the ability to resolve seasonal-scale variability is one of the key strengths of coral-derived SST records. However, calibrating models with the seasonal cycle included risks overfitting to a well-constrained signal when, in many cases, it is the deviations from this signal that are of greatest interest, such as interannual variability associated with ENSO or the Indian Ocean Dipole (IOD). To my knowledge, while many comparisons of coral-based SST calibration methods exist (e.g., Chen et al., 2019; D'Olivo et al., 2018; Xu et al., 2015), no systematic assessment has evaluated coral SST calibrations using exclusively deseasonalized datasets, despite this representing the temporal scale most relevant to interannual climate variability. A focused 'fi-

delity test' of this kind would complement existing studies that demonstrate the ability of coral-based reconstructions to capture interannual modes of variability (DeLong et al., 2013; Evans et al., 2002).

Assessing how coral SST calibration methods perform on deseasonalized datasets would also facilitate the integration of coral records into climate field reconstructions (CFRs). CFRs are gridded datasets of climate variables, such as temperature or precipitation, that span broad geographic regions and temporal scales (Smerdon et al., 2023). By assimilating extensive networks of proxy records using myriad statistical techniques, often in combination with advanced climate models, these datasets help characterize key spatiotemporal patterns over the Common Era (Evans et al., 2002; Steiger et al., 2018).

There is both precedent and strong rationale for incorporating coral-based SST records into CFRs. Many coral sites are situated in key hotspots of interannual climate variability, including regions influenced by ENSO and IOD. Their capacity to resolve spatial patterns at subannual resolution in these dominant modes of variability offers particular value for climate diagnostics, adaptation planning, and early warning systems (Hargreaves and Annan, 2009; Schmidt et al., 2013; Tierney et al., 2020; Watkins, 2024). This relevance further motivates evaluating SST reconstruction skill on deseasonalized datasets, especially since most CFR frameworks remove the seasonal cycle prior to proxy assimilation (Smerdon et al., 2023).

Previous work has shown that coral-based CFRs using skeletal oxygen isotopes can skillfully capture interannual variability across the tropical Pacific when employing reduced-space approaches that isolate dominant climate modes (Evans et al., 2000, 2002). Coral records have also been incorporated into various hemispheric CFRs, often alongside terrestrial proxies (Mann et al., 1998, 1999; Rutherford et al., 2005). However, many coral synthesis efforts have focused on producing composite time series for broad ocean basins or ENSO-sensitive regions, rather than developing spatially explicit field reconstructions (Sanchez et al., 2020; Tierney et al., 2015; Wilson et al., 2006; Emile-Geay et al., 2013). Since the popularization of data assimilation methods in paleoclimate studies such as Paleoclimate Data Assimilation (PDA; Hakim et al., 2016), coral-specific CFRs have received relatively little attention, despite their potential to resolve fine-scale spatial patterns in tropical climate variability.

This study evaluates the performance of three coral-based calibration methods (Sr/Ca, Li/Mg, and SMITE) in estimating deseasonalized SST variability. Using records primarily from the Great Barrier Reef (GBR), along with selected cores from the Galápagos Archipelago, I assess each method across three levels of inference. First, I compare performance within individual records (i.e., intrarecord comparisons), quantifying correlation, accuracy, and relative accuracy. Second, I assess how model parameters estimated by each method perform across coral records, testing reproducibility across colonies and regions. Finally, I integrate each method into a PDA synthetic CFR experiment to evaluate how calibration error propagates through field reconstructions of the GBR. In doing so, this study provides a systematic evaluation of each method's fidelity, emphasizing reconstruction skill and suitability for cli-

mate reconstructions within records, across records, and for spatially resolved field reconstructions targeting ENSO and IOD variability on the GBR.

4.2 Methods

4.2.1 Data Set Sources

Coral Records

Data from 15 coral records were obtained from the GBR region across three studies (D'Olivo and McCulloch, 2017; D'Olivo et al., 2018; Wu et al., 2021), along with data from two coral records from the Galápagos archipelago (Thompson et al., 2022). These records were specifically selected because they include measurements of five key geochemical variables critical for applying the SMITE method: Sr/Ca, Li/Ca, Mg/Ca, U/Ca, and B/Ca. The concentration of records within the GBR also provides an important regional focus necessary for the subsequent synthetic CFR experiment (see Section 4.2.5).

The coral records assessed in this study vary in temporal resolution, coverage, and analytical methodology. GBR1-12 (D'Olivo and McCulloch, 2017; D'Olivo et al., 2018) are bimonthly and span relatively short periods, ranging from about 4 to 13 years. GBR13-15 (Wu et al., 2021) are of monthly resolution and extend across several decades, from 42 years to over 110 years. The two Galápagos coral records (GI1 & GI2; Thompson et al., 2022) are also of monthly resolution and cover periods of approximately 5 and 34 years, respectively. Most coral records span the late twentieth century, with the exception of GBR14 and GBR15, which extend into the mid- and early twentieth century, respectively. Table 4.1 summarizes key metadata associated with each record, including location, temporal coverage, and original study attribution. The geographic distribution of these records is shown in Figure 4.1.

I used reported analytical errors from each coral record to help refine the regression parameters calculated from all three calibration methods using Weighted Least Squares (see Section 4.2.3). Notably, GBR1-12 as well as GI1-2 were collected via standard solution-based ICP-MS, while GBR13-15 were collected via LA-ICP-MS. This has a significant impact on the analytical errors and, consequently, on the quality of the calibrations, which is particularly noticeable when comparing the GBR coral records (see Section 4.3.1).

Table 4.1: Summary of coral records used in this study. Coral IDs follow a naming convention where an abbreviated region name (GBR = Great Barrier Reef; GI = Galápagos Islands) is followed by a numeric identifier ordered by latitude within each region (lower numbers correspond to more northerly locations).

Coral ID	Species	Latitude	Longitude	Start Year	End Year	Study
GI1	*P. lobata*	1.39	269.83	1995	2000	Thompson et al., 2022
GI2	*P. lobata*	1.39	269.83	1976	2010	Thompson et al., 2022
GBR1	*P. australiensis*	-14.67	145.46	2003	2013	D'Olivo et al., 2018
GBR2	*P. australiensis*	-16.93	145.99	1990	1994	D'Olivo et al., 2018
GBR3	*P. lutea*	-17.92	146.51	1990	1994	D'Olivo et al., 2018
GBR4	*P. solida*	-18.27	147.38	1996	2001	D'Olivo et al., 2018
GBR5	*P. lutea*	-18.27	147.38	2003	2012	D'Olivo et al., 2018
GBR6	*P. lutea*	-18.27	147.38	2005	2012	D'Olivo et al., 2018
GBR7	*P. lutea*	-18.27	147.38	2004	2009	D'Olivo et al., 2018
GBR8	*P. mayeri*	-18.48	146.87	1996	2008	D'Olivo et al., 2018
GBR9	*P. lutea*	-18.82	147.65	1996	2009	D'Olivo et al., 2018
GBR10	*P. lobata*	-18.82	147.65	2007	2013	D'Olivo et al., 2018
GBR11	*P. lobata*	-18.82	147.65	2006	2013	D'Olivo et al., 2018
GBR12	*P. lutea*	-18.84	146.54	1999	2008	D'Olivo & McCulloch, 2017
GBR13	*P. spp.*	-19.52	149.07	1949	2017	Wu et al., 2021
GBR14	*P. spp.*	-19.74	148.83	1975	2017	Wu et al., 2021
GBR15	*P. spp.*	-22.47	151.74	1907	2017	Wu et al., 2021

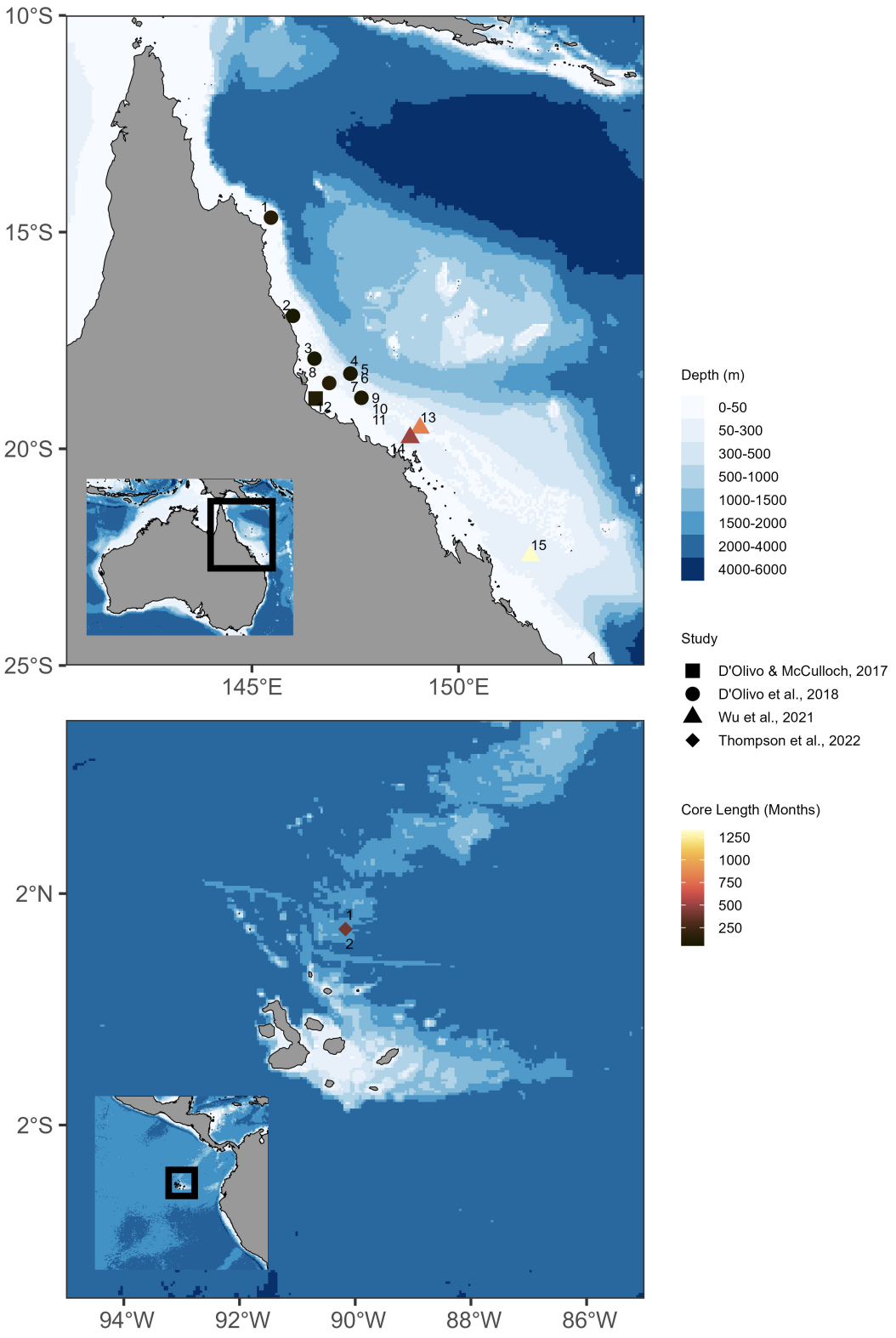

Figure 4.1: Location, record length, and source manuscript for all corals used in this study. Plots were rendered using the ggOceanMaps package in R.

CCI SST

All coral records were calibrated against a single, consistent SST product: the European Space Agency's Climate Change Initiative SST dataset (CCI SST; Merchant et al., 2019). CCI SST is a high resolution data product that adjusts for differences between multiple satellite-based instruments, with limited validation against *in situ* SST measurements. CCI SST provides daily SST estimates at a spatial resolution of 0.05° × 0.05°, with associated uncertainties estimated as standard deviations of the error distribution. Recent studies have found that CCI SST is highly suitable for assessing SST variability in coastal reef environments (Hu et al., 2021; Margaritis et al., 2025), with estimates that are comparable or superior to more commonly utilized SST data products such as OISST (Banzon et al., 2016; Reynolds et al., 2007) or the National Oceanographic and Atmospheric Administration's Coral Reef Watch (Heron et al., 2014). While *in situ* SST logger data exist for several sites, these records vary in coverage, often spanning only partial segments of the coral records. To ensure methodological consistency and comparable error treatment across all sites, I calibrated all corals against CCI SST data. For details regarding calibration, see Section 4.2.3.

I note that satellite-derived SST products such as CCI SST are known to exhibit certain systemic biases, particularly in nearshore environments where retrievals are complicated by land proximity. Consequently, CCI SST exhibits a longitudinal error gradient on the GBR, with elevated errors nearshore and depressed errors offshore (Figure C.1). Furthermore, CCI SST generally demonstrates a characteristic seasonal bias, with slightly elevated winter SST estimates and slightly depressed summer estimates relative to *in situ* measurements (Figure C.2). This seasonal bias is also reflected in CCI SST error estimates, with higher uncertainty during the austral summer (December through February) due to increased cloud prevalence. Despite these limitations, CCI SST is well-correlated with available *in situ* logger data across all sites ($r^2 = 0.91$, $n = 1382$), providing confidence that it serves as a robust calibration target across the study region.

ORA-20C SST

I used the twentieth century Ocean ReAnalyses dataset (ORA-20C; de Boisséson et al., 2018) as the "true" SST signal in the synthetic CFR experiment (see Section 4.2.5 for details). ORA-20C is an ocean reanalysis product, assimilating *in situ* temperature and salinity profiles with estimates from the NEMO 3.4 ocean model (Madec, 2008) and driven by surface boundary conditions from the European Centre for Medium-Range Weather Forecasts' twentieth century atmospheric reanalysis. ORA-20C provides monthly SST fields at a spatial resolution of 1°×1°, with uncertainties estimated from an ensemble of simulations that begin with slightly different initial ocean conditions. This dataset provides continuous coverage from 1900 to 2010 and is particularly well suited for capturing decadal-scale variability throughout the twentieth century (de Boisséson et al., 2018).

I selected ORA-20C over gridded observational products like OISST because its model-based framework avoids spatial infilling techniques used in observation-only datasets, which tend to smooth over important spatial structure across the GBR. Capturing such spatial variations is a central focus of the synthetic CFR experiment. However, we note that prior to the 1980s, ORA-20C exhibits considerable uncertainty in the tropical oceans that exceeds interannual-to-decadal scale variability (de Boisséson et al., 2018). Given the geographic boundaries of the GBR (see Section 4.2.5) and the spatial resolution of ORA-20C, we use 31 grid points in total from ORA-20C to represent the Great Barrier Reef. Further details on the use of ORA-20C in the synthetic CFR experiment are provided in Section 4.2.5.

CMIP6 SST Ensemble

I constructed an ensemble of eleven CMIP6 models to serve as the prior for the synthetic CFR experiment (Table 4.2). Model descriptions are available from their respective references (ACCESS-CM2: Bi et al. 2020; AWI-CM-1-1: Semmler et al. 2020; CanESM5: Swart et al. 2019; EC-Earth3: Döscher et al. 2022; FIO-ESM-2: Bao et al. 2020; IPSL-CM6A-LR: Boucher et al. 2020; MIROC6: Tatebe et al. 2019; MPI-ESM1-2-HR: Müller et al. 2018; NESM3: Cao et al. 2018; NorESM2-MM: Seland et al. 2020; TaiESM1: Wang et al. 2021). These models were selected based on their availability at the time of analysis and their sufficiently high spatial resolution to be comparable with the ORA-20C dataset. This selection prioritized models with native output fields at or finer than 1°×1° resolution to minimize interpolation artifacts.

Table 4.2: CMIP6 ensemble members used to generate the prior for synthetic CFR experiment.

Model	Institution	Native Resolution (°latitude x °longitude)
ACCESS-CM2	CSIRO-BOM	1.25°×1.875°
AWI-CM-1-1-MR	AWI	0.25°×0.25°
CanESM5	CCCma	1°×1°
EC-Earth3	EC-Earth Consortium	0.9°×0.9°
FIO-ESM-2	FIO-QLD	0.27-0.54°×1.1°
IPSL-CM6A-LR	IPSL	0.9°×0.9°
MIROC6	JAMSTEC	0.9°×0.9°
MPI-ESM1-2-HR	MPI-M	0.9°×0.4°
NESM3	NUIST	0.9°×0.9°
NorESM2-MM	NCC	0.9°×0.9°
TaiESM1	Academia Sinica	0.9°×0.9°

Each CMIP6 model provides monthly-mean SST fields over the twentieth century. During preprocessing, all ensemble members were spatially regridded to match the ORA-20C SST grid (1°×1°) using a weighted averaging approach based on haversine distance (i.e., latitude-corrected). For TaiESM1, the longitudinal resolution was too coarse to resolve 3 of the 31 grid cells. For these grid cells, I interpolated the missing grid cells based on adjacent grid cells. Temporally, three of the models (CanESM5, FIO-ESM-2, NESM3) exhibited minor discrepan-

cies between calendar days and model days, resulting in a small number of missing months (typically 3 months out of 1320). These missing points were linearly interpolated from adjacent months to maintain consistent time series lengths. Although this introduced minor seasonal artifacts, these effects were largely removed during the deseasonalization process (see Section 4.2.2).

I note that the CMIP6 ensemble members unanimously exhibited higher interannual variability than ORA-20C along the GBR region, consistent with expectations from free-running global climate models versus constrained data assimilation products. To mitigate this effect and ensure fair comparison, I applied a variance scaling adjustment to match the target interannual variance of ORA-20C (see Maraun, 2016). Additionally, capturing tropical interannual SST variability, especially related to ENSO, is still a challenge for many CMIP6 models (Gu and Sun, 2025; Liao et al., 2021; Planton et al., 2021; Rashid et al., 2022). Therefore, even after variance scaling, the CMIP6 ensemble exhibits substantial spread in interannual SST variability over the GBR throughout the twentieth century (see Section 4.4.3 for a detailed discussion).

4.2.2 Deseasonalization

Many experiments in this study use deseasonalized SST reconstructions to focus on interannual to decadal variability. Deseasonalization was performed by removing the monthly climatological mean from each month of the time series, thus eliminating the seasonal cycle without compromising the number of observations, as annual binning might. This non-parametric approach preserves variability on timescales longer than one year and avoids edge effects commonly introduced by high-frequency filtering. In this study, "deseasonalized SST reconstructions" refer to cases where the input data were deseasonalized prior to calibration, ensuring that the calibration is based solely on interannual and longer-timescale variability, rather than being dominated by the seasonal cycle. Alternative approaches exist, including calibrating against the full seasonal data and then deseasonalizing afterward. While both strategies have merits, deseasonalizing prior to calibration is theoretically preferable when the goal is to optimize reconstruction of non-seasonal variability.

4.2.3 Calibration

This study implements three calibration approaches that incorporate increasing amounts of information to reconstruct SST from coral geochemical records: Sr/Ca, Li/Mg, and SMITE.

Sr/Ca calibration follows a standard univariate linear regression, based on the assumption of an inverse relationship between SST and the distribution coefficient, K(T), of Sr in coral aragonite versus ambient seawater (Beck et al., 1992; Kinsman and Holland, 1969; Smith et al., 1979). In most cases, the seawater Sr/Ca ratio is assumed constant, yielding a single linear regression between Sr/Ca measured from coral aragonite and SST (e.g., Corrège, 2006).

For Li/Mg, I also employ a univariate calibration framework but normalize Li/Ca to Mg/Ca prior to regression with SST (Cuny-Guirriec et al., 2019; Hathorne et al., 2013; Montagna et al., 2014). This normalization is intended to remove common non-SST-related variability associated with coral physiology or microscale skeletal variations between centers of calcifications and fibrous aragonite (Cuny-Guirriec et al., 2019). Given the relatively narrow temperature range observed along the GBR (17-31°C), I found that a linear calibration worked just as well as an exponential calibration, similar to what was found by D'Olivo et al. (2018). Thus I proceeded with a univariate linear regression between Li/Mg and CCI SST. However, the incorporation of two distinct elemental proxies effectively makes Li/Mg a multiproxy method, albiet with univariate calibration.

The SMITE method employs a multivariate calibration framework that simultaneously incorporates all five measured TE/Ca ratios, with the addition of Li/Mg. SMITE leverages the covariance of the multitude of geochemical variables to optimize predictive skill (correlation, accuracy, reproducibility). To perform the SMITE calibration, coral skeletal geochemical variables are age modeled, z-score normalized, and transformed using a singular value decomposition (SVD). Singular values can then be truncated (or regularized) to circumvent collinearity between the coral variables and thus prevent overfitting. The degree of regularization is an important consideration, and the cumulative variance explained by each singular value should be used in part to inform how many singular values to truncate. Following Hughes et al. (2024), I chose to truncate all singular values except the two lowest, a strategy that maximizes reproducibility at the small expense of predictive skill. For the seasonal data, the first two singular values explained more than 90% of the variance in all but three corals (GBR13-15), where it explained more than 80% of the variance. For the deseasonalized data, there is considerably more spread in the cumulative variance explained (CVE) by the first two singular values. However, only one record yields less than 70% CVE by the first two singular values (GBR15; 68%). The other 16 records exhibit more than 70% CVE by the first two singular values.

All calibrations were performed against the CCI SST product (Section 4.2.1), using the nearest available CCI grid point for each coral location. For GBR1-12, which are at bimonthly resolution, CCI SST was averaged into bimonthly bins prior to calibration. For GBR13-15 and GI1-2, monthly resolution was retained. Regression parameters were determined for all reconstruction methods using a Weighted Least Squares (WLS) approach, which accounts for uncertainty in both the predictor (CCI SST) as well as the response (geochemical variables). An initial estimate of the regression parameters (slopes for Sr/Ca and Li/Mg, loadings for SMITE) are obtained using Ordinary Least Squares. Weights were then calculated by inverting the combined uncertainty of each geochemical variable and CCI SST error. This method effectively accounts for uncertainty in both the x and y directions, and minimizes residuals with respect to the combined error structure of the calibration data.

To robustly estimate calibration uncertainties and prevent overfitting, I employed a block-bootstrap cross-validation approach (e.g., Politis et al., 2004). In each iteration ($i = 1 \ldots 10,000$), I randomly resampled (with replacement) the coral and SST fields in contiguous blocks of 24 months, then collated them to create new synthetic

coral and SST fields. I chose a block size of 24 months so as to preserve autocorrelation on interannual timescales. I then removed one of these blocks, calibrated the model on the remaining data, and validated against the held-out blocks. The resulting distributions of fitted model parameters, residuals, reconstructed SST values, singular values, and skill statistics were then summarized by extracting 95% confidence intervals from the bootstrap distributions of the cross-validated blocks.

4.2.4 Skill Metrics

To assess the performance of each coral-based SST reconstruction method (Sr/Ca, Li/Mg, and SMITE), I implemented what I and others have called a "fidelity" testing framework (e.g., Canesi et al., 2024). By this, I mean that I applied each calibration method independently to each individual coral record and evaluated the resulting reconstructions using a suite of skill metrics. This approach enables a direct comparison of how different calibration strategies perform at the single-record level under block-bootstrap cross-validation.

Skill was assessed using several summary statistics that capture different aspects of reconstruction skill. These metrics include the Pearson correlation coefficient (r) as a measure of linear association or correlation, the root-mean-square error (RMSE) as a measure of average accuracy, and the normalized RMSE (nRMSE) as an indicator of relative accuracy (i.e., variance-adjusted). For the CFR experiments, I additionally calculated the coefficient of efficiency (CE) to evaluate reconstruction skill during the validation period.

Confidence intervals for all skill metrics used in the intrarecord and interrecord comparisons were calculated from the bootstrap distributions obtained through the block-bootstrap cross-validation approach described in Section 4.2.3. Confidence intervals for all skill metrics used in the synthetic CFR experiment were derived from the distribution of ensemble realizations. For details, see Sections 4.2.4 and 4.2.5.

Pearson Correlation Coefficient (r)

The Pearson correlation coefficient (r; Rogers and Hopkins, 1988) quantifies the strength and direction of the linear relationship between two variables:

$$r = \frac{\sum_{i=1}^{n}(x_i - \bar{x})(y_i - \bar{y})}{\sqrt{\sum_{i=1}^{n}(x_i - \bar{x})^2}\sqrt{\sum_{i=1}^{n}(y_i - \bar{y})^2}} \tag{4.1}$$

In this study, x_i and y_i are the reconstructed and observed SST values, respectively, and $\bar{x}$ and $\bar{y}$ are their means. High absolute r values indicate strong agreement between reconstructed and observated SSTs. I also report r^2, which intuitively expresses the amount of variance explained between the x and y variables, albeit without expressing the direction of the linear relationship.

Root Mean Square Error (RMSE)

RMSE (Hodson, 2022) measures the average difference between two variables:

$$\text{RMSE} = \sqrt{\frac{1}{n}\sum_{i=1}^{n}(x_i - y_i)^2} \tag{4.2}$$

I thus use RMSE to measure the average magnitude of the reconstruction errors. Lower RMSE values indicate higher accuracy in reconstructed SSTs (i.e., a smaller difference between reconstructed and observed SSTs). Additionally, I calculate the normalized RMSE (nRMSE), which measures the average magnitude of reconstruction errors normalized to the standard deviation of the reconstruction.

$$\text{nRMSE} = \frac{\text{RMSE}}{\sqrt{\frac{1}{n}\sum_{i=1}^{n}(x_i - \bar{x})^2}} \tag{4.3}$$

By normalizing to the standard deviation of each reconstruction, nRMSE values indicate how well a reconstruction captures the *pattern* of SST anomalies, prioritizing accuracy in timing and variability over absolute magnitude.

Coefficient of Efficiency (CE)

CE (Cook et al., 1994, 1999) evaluates reconstruction skill relative to the mean of the validation period:

$$\text{CE} = 1 - \frac{\sum_{i=1}^{n}(x_i - y_i)^2}{\sum_{i=1}^{n}(y_i - \bar{y}_{\text{val}})^2} \tag{4.4}$$

where $\bar{y}_{\text{val}}$ is the mean of observed SST during the validation period. CE values range from $-\infty$ to 1, where 1 indicates a perfect reconstruction and 0 indicates no improvement over using the validation period mean. Negative values suggest that the reconstruction performs worse than the validation mean.

Climate Field Summary Statistics

For the synthetic CFRs, summary statistics (r, RMSE, CE) between reconstructed and observed SSTs were computed at each individual grid point. Confidence intervals for these CFR-based summary statistics differ from those estimated from the fidelity testing experiments. As previously mentioned, in the fidelity testing experiments, I estimated the confidence intervals for each summary statistic from the bootstrap distributions of a block-bootstrap cross-validation approach, which accounts for temporal autocorrelation and sampling variability in the calibration

period. For the synthetic CFR experiment, I derive 95% confidence intervals from the distribution of summary statistics across the ensemble of CFR realizations (see Section 4.2.5).

While ensemble or field-mean summary statistics may be used for visualization or benchmarking in certain contexts, all analyses in the synthetic CFR experiment are based on grid-point-level comparisons between the reconstructed and observed SST fields. That is, each summary statistic is calculated independently at each grid cell by comparing the reconstructed and observed SST time series at that location. This approach preserves the spatial structure of the reconstruction and enables identification of regions where model skill is consistently strong or uncertain.

4.2.5 Synthetic CFR Experiment

Experimental Design

I aimed to evaluate how different coral calibration methods (Sr/Ca, Li/Mg, SMITE) impact SST field reconstruction skill. Specifically, I focus on understanding when coral-derived SST reconstructions are sufficiently accurate enough to resolve variability associated with ENSO and IOD. Initially, two experimental approaches were developed: a modern, observationally anchored "practical CFR" using GBR1-15 and CCI SST (see Section 4.2.6); and an empirically-modeled "synthetic CFR" using pseudo-observations of SST derived from structured noise added to ORA-20C and a CMIP6 ensemble as the prior. Ultimately, the practical CFR results were deemed inconclusive due to high sensitivity to a range of reasonable design assumptions (e.g., observation error structure, proxy weighting), and those results are not presented in this study. The primary analysis and skill assessments are therefore based on the synthetic CFR experiment. See Section 4.4.3 for further discussion of the limitations of the GBR1-15 dataset in the context of the practical CFR.

The synthetic CFR was designed to empirically quantify coral-based SST field reconstruction skill using a PDA framework with an offline ensemble Kalman Filter (PDA-enKF). A schematic of the experimental design is provided in Figure 4.2. For each method (SMITE, Sr/Ca, Li/Mg), pseudo-observations were generated by modeling the residuals of the deseasonalized GBR1-12 SST regressions. Ensembles of pseudo-coral records were created by randomly assigning them spatial and temporal coverage across the GBR over the 20th century and perturbing ORA-20C SSTs with structured autocorrelated noise specific to each calibration method. Each pseudo-observation ensemble was paired with a randomly selected member of an 11-model CMIP6 prior ensemble, regridded and variance-adjusted to match ORA-20C SST variability over the GBR. This process was repeated 500 times per increment of network size (i.e., number of coral records) to produce 500-member ensembles, enabling robust, uncertainty-quantified skill estimates as a function of proxy density.

In this experiment, I focused not just on general reconstruction performance, but on a more functional question: when does a coral-based CFR on the GBR attain sufficient skill to resolve SST variability associated with ENSO

and IOD? To address this, I introduced a spatially explicit signal recoverability metric (Section 4.2.5) that compares the sensitivity of the climate signal to the uncertainty inherent in the synthetic CFR ensemble. By mapping the ratio of effective signal strength (variance-adjusted β^2) to reconstruction uncertainty (RMSE^2), I identify when and where reconstructed SST fields can reliably capture interannual climate variability. This approach yields clear, application-focused insight into the skill requirements for detecting large-scale climate modes using coral paleoclimate archives from the GBR.

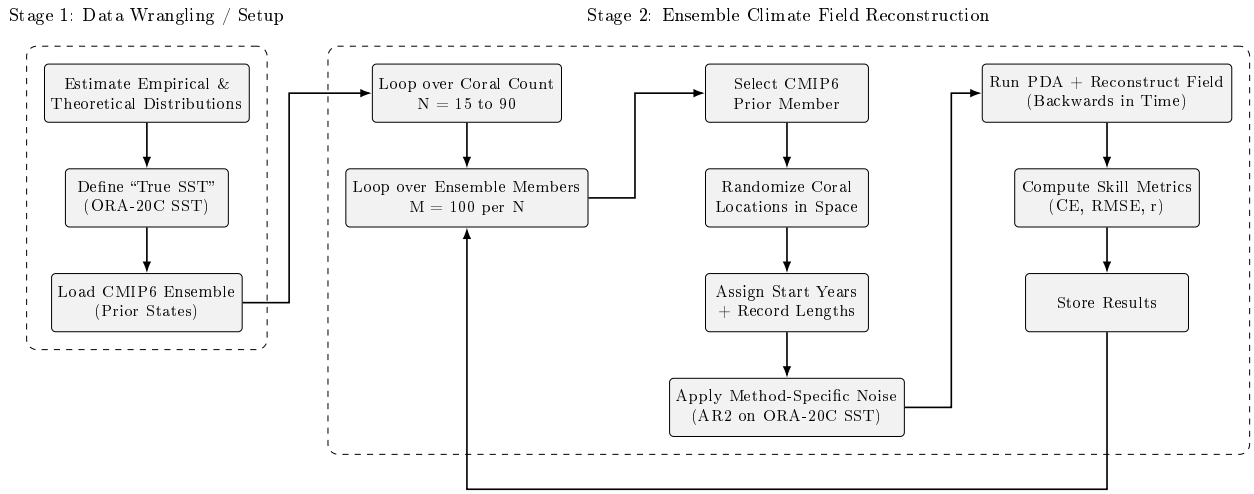

Figure 4.2: Schematic of the synthetic climate field reconstruction experiment workflow.

Spatial and Temporal Domains

I define the spatial domain for the synthetic CFR experiment using the Great Barrier Reef shapefile provided by the World Heritage Marine Programme (`https://www.marineregions.org/gazetteer.php?p=details&id=26847`). To ensure consistency between the ORA-20C reanalysis product and the CMIP6 prior ensemble, all data fields were regridded onto a common $1^\circ \times 1^\circ$ latitude-longitude resolution within the GBR region (31 grid cells in total). Spatial regridding was performed using a weighted averaging scheme based on haversine distance, with minor adjustments for coarse-grid models as described in Section 4.2.1.

The temporal domain spanned from January 1900 to December 2000, covering 1212 months at native monthly resolution. No temporal coarsening was necessary, although several CMIP6 models exhibited minor missing months due to calendar discrepancies; these were infilled by linear interpolation (Section 4.2.1). All datasets (ORA-20C and each CMIP6 ensemble member) were deseasonalized prior to analysis following the procedure outlined in Section 4.2.2. While linear interpolation and deseasonalization may introduce minor high-frequency artifacts, these effects were minimal and are unlikely to affect the interannual variability that is the primary focus of this study.

Network Size and Ensemble Design

For each ensemble member in the synthetic CFR experiment, I generated N synthetic coral records by randomly sampling space, theoretically sampling time from an exponential decay function, and empirically sampling reconstruction skill based on the residual structure of the GBR1-12 dataset. N was increased sequentially from a minimum of 15 synthetic records (to replicate the number of records in GBR1-15) to a maximum of 90 records in increments of 15, with each N consisting of 500 ensemble realizations. For each realization, the prior (a CMIP6 model) and the observations (the synthetic coral records) were resampled and the entire climate field was reconstructed using an inverse PDA-enKF approach. This approach ensures that the synthetic proxy network encompasses a wide range of possible sampling scenarios, enabling a robust assessment of reconstruction skill across methods.

Synthetic Records: Spatiotemporal Assignment

The grid cell for each synthetic coral record was selected randomly with replacement from the 31 available grid cells within the GBR domain. The random and independent approach to spatial sampling allows for spatial clustering or sparsity to emerge naturally across ensemble members. Temporal coverage for each synthetic coral record was determined through independently assigning record duration and a starting year. I modeled record lengths using an exponentially decaying distribution, constrained by the maximum and minimum durations observed in the GBR1-15 dataset (50 months and 1327 months, respectively). Shorter records were more probable, consistent with real-world coral core collections where longer, continuous records are relatively more rare. The starting year of each synthetic record was likewise sampled from an exponentially-decaying distribution biased towards more recent decades (1900-2009). This mimics the higher prevalence of coral records in the late twentieth century while ensuring sufficient coverage across the full twentieth century. The maximum start year of 2009 was used to ensure that records would still have a high chance of capturing the year 2000. The starting years and durations of all synthetic records within each ensemble member were repeatedly resampled until full 20th century coverage was achieved with no gaps.

Notably, any synthetic records that were collocated in both time and space (i.e., assigned to the same grid cell and overlapping in time) were combined into a single pseudo-observation prior to assimilation, but after each record had been generated through the addition of structured noise to the ORA-20C "true" SST signal (see the following Section for details). These combined SST estimates were calculated as a weighted average, with weights proportional to the inverse of the observation errors.

Synthetic Records: Structured Noise Assignment

To model the reconstruction skill of each synthetic coral record, I perturbed the ORA-20C SST signal using empirical estimates of residual structure derived from the deseasonalized GBR1-12 regressions. Separate structured noise models were constructed from the 5th, 50th, and 95th of the cross-validated residuals for each calibration method. I discuss the characteristics of these distributions in Section 4.3.3. Importantly, only GBR1-12 were used to generate the residuals and autoregressive (AR) coefficients for each synthetic coral record. This restriction was deemed necessary because GBR13-15 were generated using LA-ICP-MS, which exhibits different error characteristics compared to the solution-based ICP-MS approach used for corals GBR1-12. Moreover, GBR13-15 exhibit monthly resolution and span significantly greater lengths of time than GBR1-12, resulting in a disproportionate influence on the total number of residuals (69% of the residual dataset by count). By restricting the sampling pool to GBR1-12, I ensured that all calibration residuals were measured with comparable analytical methods typically employed in coral-based SST reconstructions, and thus calibration errors were modeled on a consistent basis.

Structured noise for each calibration method was modeled according to an AR process of order two (AR2), reflecting the autocorrelation structure observed in cross-validated calibration residuals. For each synthetic coral record, AR2 model parameters (the two autoregressive coefficients) were randomly drawn from empirical distributions obtained by fitting AR2 models to the deseasonalized residuals of the GBR1-12 records for each method separately. All AR1 and AR2 coefficients were found to be significantly higher than 0 except SMITE's AR2 coefficients for the 5th and 50th percentile, as well as Li/Mg's AR2 coefficients for the 95th percentile. The white noise term for each AR2 model was determined using the standard deviation of the residuals, tempered by the randomly drawn AR coefficients. This random resampling approach captures realistic variability in calibration noise structure while preserving the distinct noise characteristics of each reconstruction method.

Formally, the perturbed SST time series at each time step ($\hat{\text{SST}}_t$) for each synthetic coral record was generated according to:

$$\hat{\text{SST}}_t = \text{SST}_{\text{true},t} + \hat{e}_t \tag{4.5}$$

where the synthetic residual $\hat{e}_t$ was generated recursively by:

$$\hat{e}_t = \phi_1 \hat{e}_{t-1} + \phi_2 \hat{e}_{t-2} + \epsilon_t \tag{4.6}$$

with ϕ_1 and ϕ_2 (the AR1 and AR2 coefficients, respectively) drawn randomly from the AR coefficients estimated from the deseasonalized GBR1-12 residuals. The white noise term (ϵ_t) was drawn from a normal distribution $\mathcal{N}(0, \sigma_\epsilon^2)$, with σ_ϵ^2 approximated as:

$$\sigma_\epsilon^2 = \sigma_{\text{res}}^2(1 - \phi_1^2 - \phi_2^2) \tag{4.7}$$

where σ_{res}^2 is the variance of the raw calibration residuals for each method.

For SMITE-based synthetic records, I applied an additional variance scaling adjustment after perturbing ORA-20C SST with the SMITE-specific AR2 noise model. Unlike Sr/Ca and Li/Mg reconstructions, which generally overestimate SST variance relative to observations, SMITE reconstructions consistently underestimate variance. To replicate this behavior, I scaled down the variance of SMITE-based synthetic records by a factor randomly drawn from the observed variance ratio (σ_{SMITE}^2 / σ_{CCI}^2) among the GBR1-12 reconstructions. Such a variance adjustment was not necessary for Sr/Ca or Li/Mg, since adding structured noise to an existing signal increases the variance relative to the original signal. This adjustment ensures that synthetic SMITE reconstructions reflect realistic variance suppression observed in this study.

Once the synthetic coral records were generated, I defined the observation error for each synthetic record as the squared RMSE plus a small Gaussian white noise term with a standard deviation of 0.05°C. This white noise term was added in order to mimic uncertainties associated with instrumental SST observations, such as *in situ* loggers or gridded SST products while maintaining consistency across all reconstruction methods. I note that this Gaussian perturbation represents a simplified estimate of real-world uncertainties. Historical SST measurements, particularly prior to the satellite era, are spatially heterogeneous and can exhibit structural uncertainties on the order of 0.1°C (Smith and Reynolds, 2002; Chan, 2021; Chan and Huybers, 2021). However, because all synthetic records were generated and perturbed identically across calibration methods, relative skill comparisons remain robust despite this simplification.

I acknowledge that a more complex approach, such as simulating incomplete or temporally sparse calibration intervals, could more faithfully represent real-world calibration scenarios. However, such an approach would introduce additional assumptions and asymmetries among methods, particularly Sr/Ca and Li/Mg which exhibit higher AR coefficients than SMITE. Therefore, I opted for this streamlined framework to minimize differences arising from external factors rather than purely from calibration method.

Assimilation Framework

I employed Paleoclimate Data Assimilation with an offline ensemble Kalman filter (PDA-enKF; Hakim et al., 2016) to reconstruct SST fields across the GBR using synthetic coral records. The PDA-enKF method generates a posterior estimate of the climate field (x_a) by updating a prior estimate of the climate field (x_b) using synthetic coral-based SST observations (y) according to:

$$x_a = x_b + K(y - y_e) \tag{4.8}$$

Here, $(y - y_e)$ is referred to as "the innovation", with y_e representing the prior estimate of the same point in space and time as a given observation y. K is the Kalman gain matrix, given by:

$$K = BH^T(HBH^T + R)^{-1} \tag{4.9}$$

where B is the prior covariance matrix, and R is the observation (i.e., proxy) error covariance matrix. For each ensemble realization, x_b and B were randomly selected together from one of the preprocessed CMIP6 ensemble members described in Section 4.2.1. Each ensemble consisted of 500 members per coral network size (N), providing a wide range of skill estimates and uncertainty across different calibration methods and proxy network densities.

In a standard PDA approach, prior estimates are forward-modeled into the proxy observation space, meaning the climate variables (e.g., SST) is first converted into proxy values (e.g., Sr/Ca). This allows for detailed error treatments at the proxy level. In this study, I adopted an "inverse" approach in which both the prior and the observations are in temperature space (°C). Specifically, I assimilated synthetic coral SST records directly modeled after the calibration errors derived from the GBR1-12 regressions (Section 4.2.5). This inverse approach was necessary given the complexity of forward-modeling the five TE/Ca ratios used in the SMITE method. Forward modeling each geochemical variable and propagating their associated uncertainties would have introduced prohibitive complexity and compounded statistical challenges.

By working solely in the prior space (SST, °C), calibration uncertainties were incorporated directly into R, dynamically defined at each time step as the covariance matrix of the squared RMSEs and modeled instrumental noise. I emphasize that the RMSEs themselves were based on block-boostrapped cross-validated residual structures modeled using an AR2 process, with the addition of a non-negligible "instrumental" white noise term. This process ensures that temporal autocorrelation and random noise are captured in the observation error. The resulting observation error thus inherently captures a wide range of uncertainties relevant to coral paleothermometry, including analytical error, age model uncertainty, instrumental SST uncertainty, and other systemic effects that can decouple coral geochemical SST proxies from the "true" SST signal. Since the errors of each synthetic coral record are strategically redefined across 500 ensemble realizations, this framework enables a robust statistical assessment of reconstruction skill as a function of proxy density and calibration strategy.

Although this approach does not forward-model proxy systems explicitly, and thus cannot separately model uncertainties arising from individual geochemical processes such as trace-element partitioning behavior, metabolic or kinetic effects, or diagenetic alteration, the structure of R provides a conservative, physically grounded representation of realistic proxy errors, without modeling those errors explicitly. However, I acknowledge that it implicitly

assumes stationary calibration errors through time and may not capture potential low-frequency proxy drifts or biases that are difficult to capture fully within the study period. These limitations are discussed further in Section 4.4.3.

Climate Mode Signal Recoverability

To evaluate the ability of each coral-based SST reconstruction method to resolve interannual climate variability on the GBR over the 20th century, I computed a spatially explicit effective signal recoverability (ESR) metric, defined as the ratio of the effective signal variance to CFR uncertainty at each $1° \times 1°$ grid cell across the GBR.

$$\mathrm{ESR}_i = \frac{\beta_i^2 \gamma_i}{\mathrm{RMSE}_i^2} \tag{4.10}$$

$$\gamma_i = \frac{\sigma^2_{\text{recon},i}}{\sigma^2_{\text{ORA-20C},i}} \tag{4.11}$$

Where β_i^2 is the squared regression slope of the ith grid cell between deseasonalized CCI SST and the climate mode index of interest (Niño3.4 for ENSO, Kumar et al., 2020, for IOD) over the period 1981-2016. γ_i is the variance ratio of the ith grid cell between reconstructed SST and "true" SST (ORA-20C). RMSE_i^2 is the squared root mean square error of the ith grid cell in the field reconstruction. This variance-ratio correction ensures that ESR is appropriately penalized when reconstructed variance is low, reflecting the reduced ability to detect climate mode signals under such conditions. To reduce the impact of short-term noise and improve consistency with the smoothed climate indices, both the SST and index time series were subjected to a 3-month running mean prior to slope calculation. However, this smoothing had minimal impact on the final ESR values, given that all data were already monthly averaged.

To estimate confidence intervals for ESR, I calculate ESR for each member of the ensemble and derive the 95% confidence interval from the 5th, 50th, and 95th percentiles of the ensemble spread, as described in Section 4.2.4. To incorporate uncertainty in the β term, I estimate the standard error of β using the same block-bootstrap cross-validation framework described in Section 4.2.3, and randomly resample it at each ensemble realization from a normal distribution centered on β. This approach thus accounts for uncertainty in all three components of the ESR formula. Because β^2 has units of °C² per index unit², RMSE² is in °C², and γ is dimensionless, the ESR itself is dimensionless, making it a normalized metric of reconstruction fidelity relative to the strength of the underlying climate signal.

I interpret an ESR $\geq$1 as the threshold for successfully resolving a climate mode at a given grid point. This means that the reconstruction uncertainty is smaller than the expected signal amplitude, and thus the reconstruction has sufficient fidelity to detect SST variability related to the climate mode. This is a deliberately conservative criterion: it does not require perfect phase tracking of the climate mode, only that the magnitude of SST variability ex-

plained by the mode exceeds reconstruction error. This framework enables a direct, spatially resolved assessment of where and under what observational conditions coral-based CFRs can be expected to recover key climate fingerprints. I applied this signal recoverability metric to ENSO and IOD, but not to PDO. PDO exhibited extremely weak regression slopes throughout the GBR region, yielding ESRs well below one across all methods and network sizes, and therefore was excluded from further analysis.

4.2.6 Practical CFR Experiment

In parallel to the synthetic CFR experiment, I attempted a practical CFR using corals GBR1-15 and CCI SST. Although this experiment shared many methodological similarities with the synthetic CFR experiment (Section 4.2.5), the results ultimately proved too sensitive to reasonable design choices to yield robust, reproducible, and statistically significant skill estimates. As a result, the limitations of the practical CFR are discussed qualitatively in Section 4.4.3.

The spatial domain for the practical CFR matched the GBR boundaries defined by the World Heritage Marine Programme (`https://www.marineregions.org/gazetteer.php?p=details&id=26847`), regridded to a $0.7° \times 0.7°$ grid (62 grid cells) in order to preserve the relative balance between spatial and temporal variability in the deseasonalized CCI SST dataset. The temporal domain spanned 1981-2016, with the final five years (2012-2016) used to estimate prior climatology (x_b and B). The preceding thirty years (1981-2011) were used for validation. Datasets were deseasonalized to focus on interannual to decadal variability (Section 4.2.2).

Assimilation was performed using a PDA-KF framework (no ensemble), with the prior defined as the mean climatological SST field over the calibration period (2012-2016), derived from CCI SST. Unlike the synthetic CFR, which assimilated synthetic SST records, the practical CFR directly assimilated coral SST reconstructions generated via SMITE, Sr/Ca and Li/Mg from GBR1-15 (Section 4.2.3). Like in the synthetic CFR experiment, I took an inverse approach to the PDA framework, expressing the observations, prior, and reconstructions in temperature units (°C).

The observation error covariance matrix (R) was defined for each coral record using one of four different combinations: RMSE, RMSE^2, as well as each RMSE iteration combined with the respective standard error of prediction (SEP; Hughes et al., 2024). When multiple proxies overlapped within a grid cell and timestep, they were combined using either using a non-weighted or weighted average based on their cross-validated uncertainties. Validation was conducted against the deseasonalized CCI SST fields.

While this framework preserved internal consistency and faithfully incorporated proxy calibration uncertainties, the practical CFR results proved highly sensitive to choices about proxy weighting and error assignment. Skill spread was large, and which method yielded the best results varied depending on specific assumptions. Therefore, while this experiment demonstrated that a practical coral-based CFR over the GBR is feasible in principle,

it also highlights the challenges of achieving statistically significant results when spatiotemporal coverage is low ($\sim$5%).

4.3 Results

4.3.1 Intrarecord Comparisons

Summary

I evaluated the performance of three reconstruction methods (SMITE, Sr/Ca and Li/Mg) across all 15 GBR corals records (GBR1-15) and 2 Galápagos coral records (GI1 & GI2). For SMITE, I applied the maximum level of regularization to each coral record when calculating the model parameters (see Hughes et al., 2024, for details), prioritizing reproducibility and minimizing overfitting at the expense of some reconstruction skill. Detailed results for each individual reconstruction, including the full proxy field, correlation matrix, reconstruction time series, SMITE model loadings, and skill metrics (RMSE, r), are provided in Appendices C.2 and C.3 for all seasonal and deseasonalized records, respectively. For a more holistic view of how each reconstruction compares across all records, I provide additional summary figures in the appendices (Figures C.3 through C.8).

Throughout this section examining the intrarecord comparisons, I frequently reference 95% confidence intervals across different groups of coral records. These groups are divided by analytical method (GBR1-12, GBR13-15) and by region (GI1 and GI2). When referencing these intervals, I use the notation "95CI" to denote the 5th, 50th, and 95th percentiles. When I report a mean 95CI for a particular method (e.g., $\mu_{\text{SMITE-95CI}}$), I am referring to the simple arithmetic mean from the group of 95CIs in question (e.g., GBR1-12).

Seasonal Intrarecord Comparison

Across all 17 coral records, SMITE SST estimates yield the highest correlation to CCI SST in 16 cases (Figure 4.3, top panels), outperformed by Li/Mg in only one record (GBR4). However, only one of these comparisons (GBR7) yields a statistically significant difference at the 95% confidence level, favoring SMITE. This particular record is also among the shortest in the dataset, spanning only 62 months. Among GBR1-12, which yielded more skillful reconstructions (top-left panel, unshaded region), median correlation coefficients fall within a relatively narrow range across all methods. SMITE reconstructions yield median r-values between 0.92 and 0.99 with relatively tight confidence intervals ($\mu_{\text{SMITE-95CI}}$ = 0.92 / 0.96 / 0.99). Sr/Ca and Li/Mg reconstructions exhibit similar performance to each other with nearly identical 95% confidence intervals ($\mu_{\text{Sr/Ca-95CI}}$ = 0.90 / 0.95 / 0.98, $\mu_{\text{Li/Mg-95CI}}$ = 0.90 / 0.96 / 0.98).

For GBR13-15 (top-left panel, shaded region), the correlation coefficients decrease modestly relative to GBR1-12, while confidence intervals increase substantially. This behavior is consistent with the higher analytical

uncertainty present in GBR13-15 despite their larger sample size, due to being longer records with higher temporal resolution. SMITE reconstructions for these corals yield an average 95% confidence interval of 0.70 / 0.87 / 0.95. Sr/Ca reconstructions yield the least skillful correlations in this group, with an average 95% confidence interval of 0.53 / 0.77 / 0.91. Li/Mg reconstructions perform slightly better than Sr/Ca in GBR13-15, with an average 95% confidence interval of 0.60 / 0.81 / 0.93.

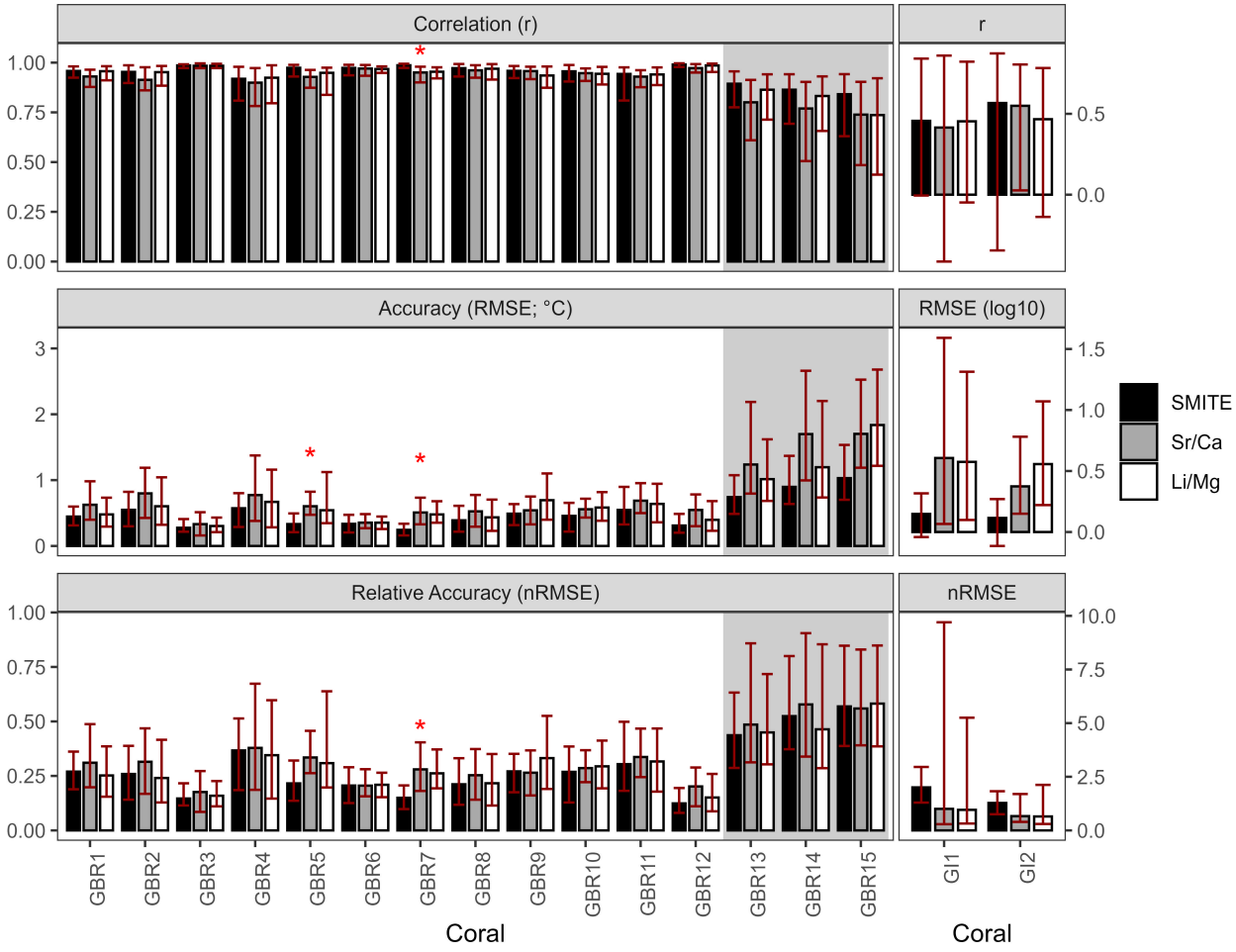

Figure 4.3: Summary statistics for each reconstruction method (SMITE, Sr/Ca, Li/Mg) performed on each seasonal coral record. Reconstruction methods are separated by color (black = SMITE, grey = Sr/Ca, white = Li/Mg). Great Barrier Reef corals (GBR1-15) and Galápagos corals (GI1-2) are in separate panels for scaling. The shaded region behind GBR13-15 is a visual tool to distinguish them from GBR1-12, given the stark contrast in summary statistics due to different analytical methodologies. Red error bars indicate the 95% confidence interval on each summary statistic. Asterisks indicate when the improvement in SMITE summary statistics is significant over Sr/Ca or Li/Mg at the 95% confidence level. There were no instances where Sr/Ca or Li/Mg were significantly better than SMITE, nor where Sr/Ca or Li/Mg were significantly different from one another.

Correlations are lower and confidence intervals widen in the Galápagos corals relative to the GBR corals (GI1 and GI2; top-right panel). Here, the lower bounds of the confidence intervals for all three methods approach or fall below zero, indicating limited predictive skill. All methods yield average r-values of moderate strength for

these corals (μ_{SMITE} = 0.51, $\mu_{Sr/Ca}$ = 0.48, $\mu_{Li/Mg}$ = 0.46). However, all of their confidence intervals range from a high greater than 0.8 to a low under 0.10.

Focusing on absolute accuracy (RMSE; Figure 4.3, middle panels), SMITE yields the lowest RMSE in all 17 reconstructions, with two shorter records (GBR4 and GBR7) exhibiting statistically significant improvements at the 95% confidence level. Among the more skillful GBR1-12 records (middle-left panel, unshaded region), SMITE reconstructions yield RMSEs ranging from 0.24°C to 0.57°C, with relatively tight uncertainty bounds ($\mu_{SMITE\text{-}95CI}$ = 0.25 / 0.41 / 0.60°C). Sr/Ca and Li/Mg reconstructions display similar median RMSEs, although Li/Mg's RMSEs are slightly lower ($\mu_{Sr/Ca\text{-}95CI}$ = 0.36 / 0.57 / 0.84°C; $\mu_{Li/Mg\text{-}95CI}$ = 0.31 / 0.51 / 0.82°C).

For the less skillful GBR13-15 records (middle-left panel, shaded region), RMSEs increase by a factor of two to three across all methods. SMITE reconstructions for these corals yield broader 95% confidence intervals ($\mu_{SMITE\text{-}95CI}$ = 0.61 / 0.89 / 1.33°C), though they remain narrower and lower in magnitude than Sr/Ca (0.99 / 1.55 / 2.46°C) or Li/Mg (0.88 / 1.35 / 2.17°C). Absolute accuracy is lowest in corals GI1 and GI2 (middle-right panel), where RMSEs increase sharply and confidence intervals widen substantially across all methods. Nonetheless, SMITE continues to yield lower RMSEs than Li/Mg or Sr/Ca, both of which reach upper 95% confidence bounds over 16 and 22°C ($\mu_{SMITE\text{-}95CI}$ = 0.84 / 1.35 / 1.97°C; $\mu_{Sr/Ca\text{-}95CI}$ = 1.29 / 3.20 / 22.54°C; $\mu_{Li/Mg\text{-}95CI}$ = 1.46 / 3.68 / 16.18°C). However, given the large size of the confidence intervals, none of these comparisons proved statistically significant.

Turning to relative accuracy (nRMSE; Figure 4.3, bottom panels), which normalizes RMSEs to the standard deviation of the reconstructed SSTs, SMITE achieves the lowest nRMSE in 8 of 17 records, compared to 3 for Sr/Ca and 6 for Li/Mg. Of these, only GBR7 shows a statistically significant improvement in nRMSE favoring SMITE. Among the more skillful GBR1-12 records (bottom-left panel, unshaded region), SMITE shows the lowest average median nRMSEs across records with tight uncertainty around each of those estimates ($\mu_{SMITE\text{-}95CI}$ = 0.14 / 0.23 / 0.34). Sr/Ca and Li/Mg reconstructions yield slightly higher nRMSEs, with Li/Mg averaging slightly lower nRMSEs than Sr/Ca ($\mu_{Sr/Ca\text{-}95CI}$ = 0.18 / 0.28 / 0.41; $\mu_{Li/Mg\text{-}95CI}$ = 0.15 / 0.26 / 0.41).

nRMSEs roughly double among GBR13-15 relative to GBR1-12, with little differences among methods (bottom-left panel, shaded region). SMITE's average 95% confidence interval spans 0.35 / 0.51 / 0.76, nearly identical to Sr/Ca (0.35 / 0.54 / 0.86) and Li/Mg (0.32 / 0.50 / 0.81). In the Galápagos records (bottom-right panel), nRMSEs are the highest among all groups of corals. SMITE exhibits median nRMSEs that are twice as high as Sr/Ca or Li/Mg for both corals, primarily due to low reconstructed variance in SMITE SST estimates (see Appendices C.2 or Figure C.3). However, SMITE's confidence intervals remain many factors smaller than Sr/Ca or Li/Mg, indicating robust estimates under block-bootstrap cross-validation.

Deseasonalized Intrarecord Comparison

Next, I evaluated the performance of SMITE, Sr/Ca, and Li/Mg SST reconstructions using all 17 *deseasonalized* coral records (GBR1-15 and GI1-2; Figure 4.4). The purpose of this comparison is to determine how well reconstruction skill across all methods is maintained after the seasonal cycle has been removed. The deseasonalization process is described in Section 4.2.2. Across all 17 coral records, SMITE produces the highest correlation coefficient in 13 cases, compared to 3 for Sr/Ca and 1 for Li/Mg (Figure 4.4, top panel). However, none of these comparisons yielded a statistically significant difference at the 95% confidence level, primarily due to large uncertainties in the correlation estimates. Even among the more skillful GBR1-12 records (top panel, left of shaded region), correlation coefficients span a wide range, with SMITE median r values falling between 0.61 and 0.91 and relatively broad confidence intervals ($\mu_{\text{SMITE-95CI}}$ = 0.31 / 0.79 / 0.93). Sr/Ca and Li/Mg reconstructions perform worse than SMITE on average, particularly in their lower confidence bounds ($\mu_{\text{Sr/Ca-95CI}}$ = 0.03 / 0.71 / 0.91, $\mu_{\text{Li/Mg-95CI}}$ = 0.18 / 0.72 / 0.91).

For GBR13-15 (top panel, shaded region), correlation coefficients are approximately half of those observed in GBR1-12, with lower 95% confidence bounds falling well-below 0, indicating little to no predictive skill. SMITE reconstructions in GBR13-15 yield an average 95CI of −0.37 / 0.28 / 0.71, while Sr/Ca and Li/Mg reconstructions are similarly broad (−0.33 / 0.22 / 0.68 and −0.41 / 0.21 / 0.68, respectively). The loss of predictive skill is even more pronounced in GI1 and GI2 (top panel, right of shaded region), where all methods produce median correlations near zero and confidence intervals spanning approximately −0.60 to 0.70.

In terms of absolute accuracy (Figure 4.4, middle panel), SMITE again yields the lowest RMSE in all 17 deseasonalized reconstructions. However, none of those comparisons are statistically significant. Among GBR1-12 (middle panel, left of shaded region), SMITE reconstructions show tight RMSE confidence intervals ($\mu_{\text{SMITE-95CI}}$ = 0.13 / 0.21 / 0.35°C). Sr/Ca and Li/Mg exhibit significantly higher confidence intervals than SMITE in this group, particularly with respect to the upper bounds ($\mu_{\text{Sr/Ca-95CI}}$ = 0.20 / 0.42 / 2.45°C; $\mu_{\text{Li/Mg-95CI}}$ = 0.21 / 0.39/ 1.34°C).

For GBR13-15 (middle panel, shaded region), RMSEs increase two- to three-fold for all methods. SMITE RMSEs remain the lowest and most constrained ($\mu_{\text{SMITE-95CI}}$ = 0.25 / 0.38 / 0.59°C), while Sr/Ca and Li/Mg exhibit broad error bounds and elevated central estimates (0.74 / 1.49 / 5.36°C and 0.85 / 1.94 / 20.12°C, respectively). Li/Mg performs worse than Sr/Ca in this group, despite yielding slightly better accuracy among GBR1-12. The decline in absolute accuracy is most pronounced in the Galápagos corals. While SMITE RMSEs remain below 1°C ($\mu_{\text{SMITE-95CI}}$ = 0.32 / 0.44 / 0.62°C), Sr/Ca and Li/Mg reconstructions exhibit extremely large confidence intervals ($\mu_{\text{Sr/Ca-95CI}}$ = 0.81 / 2.92 / 54.66°C; $\mu_{\text{Li/Mg-95CI}}$ = 0.84 / 3.44 / 76.17°C). Such unstable RMSE values are due to the extremely low sensitivity to SST for Sr/Ca and Li/Mg in GI1 and GI2, indicating a near-total breakdown of predictive skill when the seasonal cycle has been removed from the data.

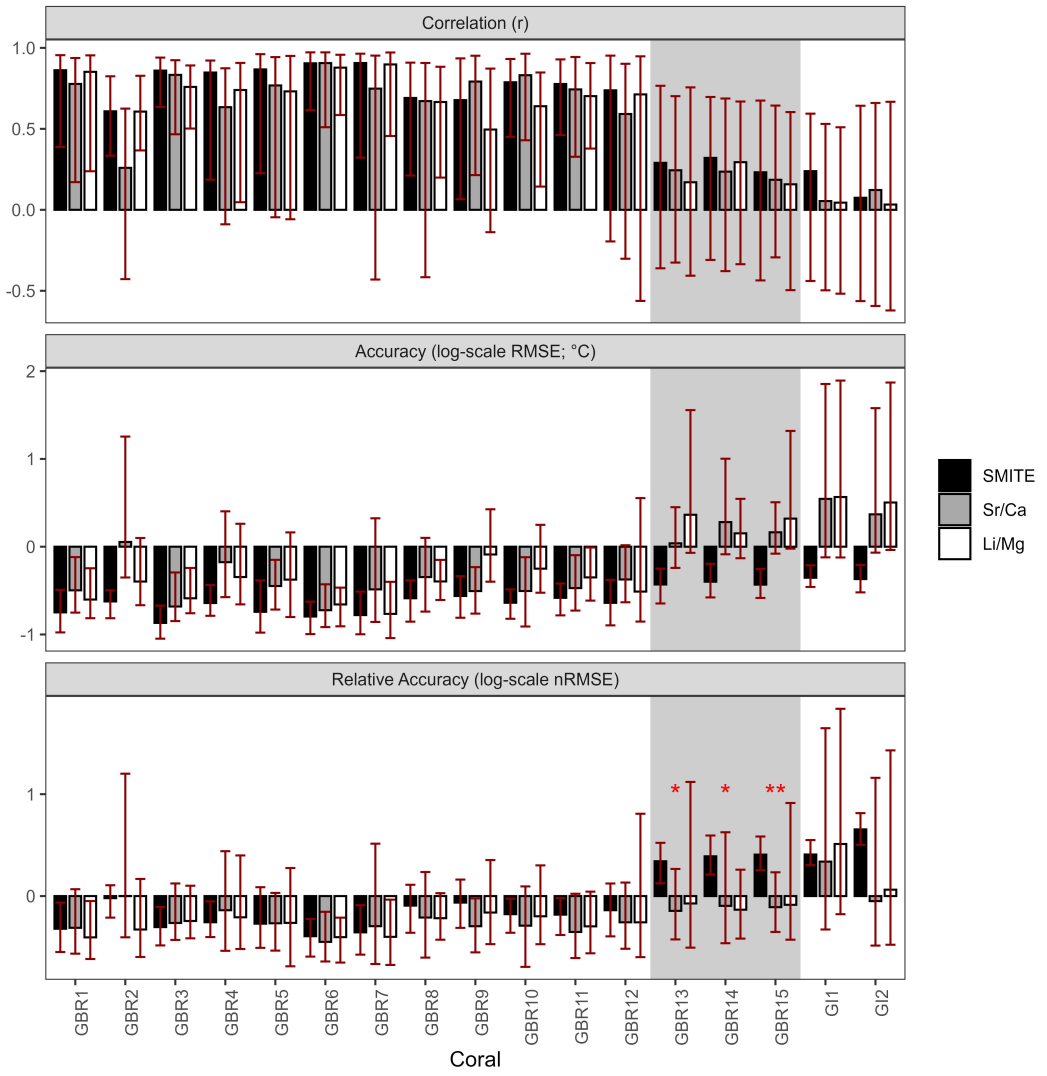

Figure 4.4: Summary statistics for each reconstruction method (SMITE, Sr/Ca, Li/Mg) performed on each *deseasonalized* coral record. Reconstruction methods are separated by color (black = SMITE, grey = Sr/Ca, white = Li/Mg). RMSE and nRMSE panels are log-scaled to better visualize differences among methods. The shaded region behind GBR13-15 is a visual tool to distinguish them from GBR1-12, given the stark contrast in summary statistics due to different analytical methodologies. Red error bars indicate the 95% confidence interval on each summary statistic. Asterisks indicate when the corresponding comparison is statistically significant (* = 0.05, ** = 0.01).

Turning to relative accuracy (Figure 4.4, bottom panel), SMITE yields the lowest nRMSE in only 2 cases, compared to 9 for Sr/Ca and 6 for Li/Mg. GBR13-15 all show SMITE yielding significantly higher nRMSEs than Sr/Ca or Li/Mg. Again, this is due to low reconstructed variance in SMITE SST estimates, which is particularly evident in GBR13-15. Among the more skillful GBR1-12 records (bottom panel, left of shaded region), SMITE and Sr/Ca exhibit similar ranges of median nRMSEs (0.40–0.95 and 0.36–1.00, respectively), while Li/Mg displays the narrowest range of median nRMSEs (0.39–0.69). However, although SMITE's average median and lower bound are

slightly elevated relative to Sr/Ca and LI/Mg, its upper bound is far lower than either Sr/Ca or Li/Mg in this group ($\mu_{\text{SMITE-95CI}}$ = 0.39 / 0.63 / 1.03, $\mu_{\text{Sr/Ca-95CI}}$ = 0.28 / 0.57 / 2.71, $\mu_{\text{Li/Mg-95CI}}$ = 0.28 / 0.53 / 1.87).

Among the less skillful GBR13-15 records (bottom panel, shaded region), where comparisons are statistically significant, SMITE nRMSEs become more erratic due to extremely low reconstructed SST variance (see Appendices C.3 or Figure C.4). Its average 95CI increases substantially ($\mu_{\text{SMITE-95CI}}$ = 1.56 / 2.40 / 3.70), more than tripling from the GBR1-12 group. In contrast, Sr/Ca and Li/Mg exhibit only modest increases in relative error, with nRMSE 95CIs that remain broadly comparable to those of GBR1-12 except for their upper bounds ($\mu_{\text{Sr/Ca-95CI}}$ = 0.39 / 0.77 / 2.60; $\mu_{\text{Li/Mg-95CI}}$ = 0.36 / 0.80 / 7.73). For GI1 and GI2 (bottom panel, right of shaded region), nRMSEs increase sharply for all methods. SMITE reconstructions are heavily penalized by low SST variance, resulting in high median values with relatively constrained uncertainty ($\mu_{\text{SMITE-95CI}}$ = 2.60 / 3.54 / 5.03). Sr/Ca and Li/Mg show lower median nRMSEs for both GI1 and GI2, though their confidence intervals extend well beyond 10, highlighting limited predictive skill and substantial instability under block-bootstrap cross-validation ($\mu_{\text{Sr/Ca-95CI}}$ = 0.40 / 1.54 / 29.43, $\mu_{\text{Li/Mg-95CI}}$ = 0.50 / 2.20 / 47.87).

SMITE Model Parameters

To better understand which coral geochemical variables drive SMITE SST reconstructions, I examined the SMITE model parameters (or loading scores) between seasonal and deseasonalized calibrations across all 17 coral records (Figure 4.5). The loading scores indicate the relative contribution of each TE/Ca ratio to the SST reconstruction. Near-zero values suggest little to no contribution, while larger absolute values reflect stronger influence. The top panel displays loading scores from the seasonal reconstructions, while the bottom panel shows those from the deseasonalized reconstructions. For comparison, model parameters from the linear univariate Sr/Ca and Li/Mg reconstructions are provided in the Appendix (Figures C.9 and C.10).

Across the seasonal GBR models, Sr/Ca and Li/Mg consistently emerged as the strongest contributors to SMITE SST reconstructions. This is reflected in their high mean and low variance in absolute loading scores ($\mu_{x\dagger}$ = −0.18, $\sigma_{x\dagger}$ = 0.02), suggesting they reliably influence the reconstructions across different coral records. Mg/Ca and U/Ca also exhibit relatively high mean absolute loadings (0.18), but with variances two to three times greater ($\sigma_{x\dagger}$ = 0.05 for U/Ca; $\sigma_{x\dagger}$ = 0.08 for Mg/Ca), indicating that their contributions are more variable between sites. Notably, Mg/Ca displays uniformly positive loading scores across the GBR, consistent with its commonly observed direct relationship to SST. B/Ca ranks fifth in terms of mean loading strength ($\mu_{x\dagger}$ = −0.17) but contributes relatively consistently ($\sigma_{x\dagger}$ = 0.04). In contrast, Li/Ca shows the lowest mean loading ($\mu_{x\dagger}$ = −0.15) and the highest variance ($\sigma_{x\dagger}$ = 0.08), suggesting its influence on SST reconstructions varies substantially across coral sites.

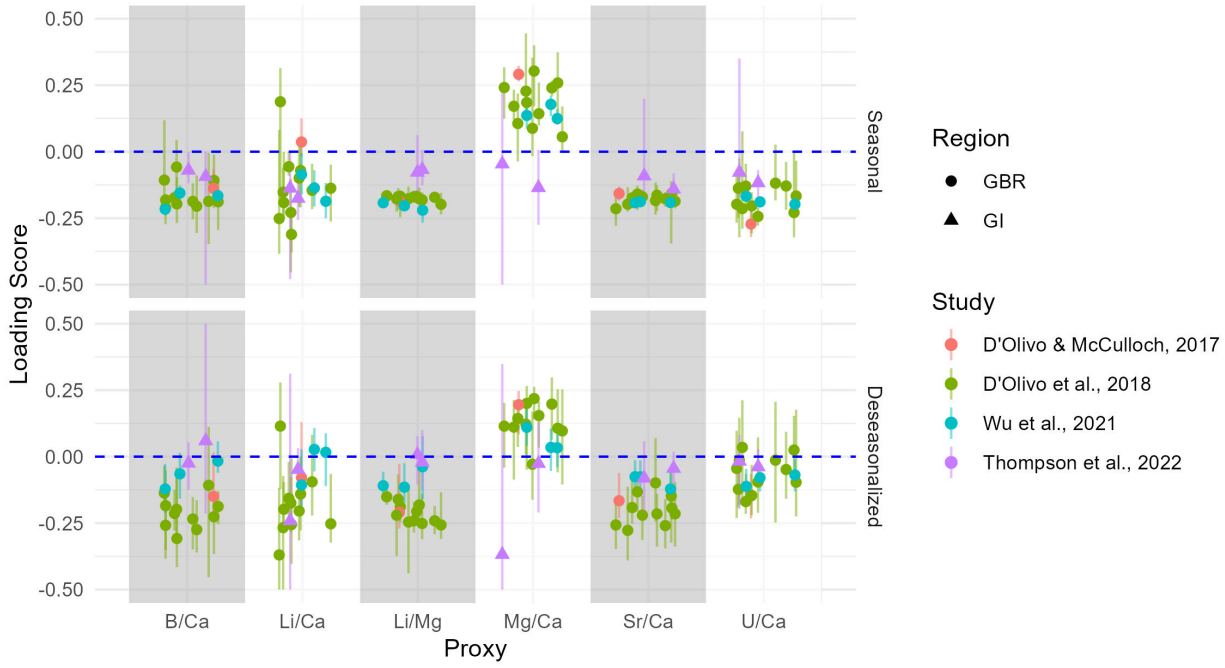

Figure 4.5: SMITE model parameters, or loading scores, for all six TE/Ca ratios across all 17 coral records in this study. Shape denotes the region that the coral record came from (GBR = Great Barrier Reef, GI = Galápagos Islands). Color denotes the study that the coral came from. Vertical lines attached to each point denote the 95% confidence interval for that particular model parameter. The blue dashed line indicates a loading score of 0, which infers that the TE/Ca in question is not contributing any information to the SST reconstruction. The shaded regions are visual tools to distinguish loading scores between TE/Ca ratios. The top panel shows the loading scores from the unaltered seasonal reconstructions, while the bottom panel shows the loading scores after the seasonal cycle has been removed.

In the deseasonalized GBR models, the relative ranking of TE/Ca contributions remains broadly similar, though some subtle shifts emerge. Li/Mg still shows the highest mean absolute loading score ($\mu_{x\dagger} = -0.19$), with Sr/Ca and B/Ca following closely behind ($\mu_{x\dagger} = -0.18$). Li/Ca rises to fourth ($\mu_{x\dagger} = -0.16$), while Mg/Ca and U/Ca show the lowest mean contributions after deseasonalization ($\mu_{x\dagger} = 0.12$ and -0.08, respectively), suggesting weaker relationships with SST once the seasonal signal is removed. More importantly, variance increases for half of the variables, reflecting reduced coherence between SST and coral geochemistry at interannual to decadal timescales. For Sr/Ca and Li/Mg, loading score variance increases more than three-fold ($\sigma_{x\dagger} = 0.07$ and 0.06, respectively), and B/Ca doubles ($\sigma_{x\dagger} = 0.08$). Li/Ca shows a slight increase in variance ($\sigma_{x\dagger} = 0.10$), while U/Ca show no change in variance relative to the seasonal loading scores ($\sigma_{x\dagger} = 0.05$). Mg/Ca is the only variable that exhibits a decrease in variance after deseasonalization ($\sigma_{x\dagger} = 0.06$).

One striking feature is the strong convergence of Li/Mg loading scores in the deseasonalized GBR models, particularly across GBR1-12. Among these corals, Li/Mg exhibits a slightly higher absolute mean loading score than Sr/Ca ($\mu_{x\dagger} = -0.21$ vs. -0.20) combined with lower variance ($\sigma_{x\dagger} = 0.04$ versus 0.05). This consistency suggests a robust inverse relationship between Li/Mg and SST at interannual timescales. However, this pattern may in part

reflect the relatively short duration of these coral records, which limits the expression of long-term variability, and the use of solution-based ICP-MS methods, which are generally less precise for Sr/Ca than for Li/Mg.

As expected, the Galápagos corals stand apart from their GBR counterparts in terms of TE/Ca contributions to SST reconstructions. Many of the loading scores for GI1 and GI2 exhibit confidence intervals that overlap with zero, indicating insignificant correlations with SST. In the seasonal models, absolute mean loading scores across most TE/Ca ratios are notably lower than those observed in the GBR records. In GI1, all six TE/Ca ratios exhibit similarly weak and consistent loadings ($\mu_{x\dagger} = -0.09$, $\sigma_{x\dagger} < 0.01$), indicating limited and uniform covariance with SST. GI2 shows greater variability: Li/Ca contributes the most ($x_\dagger = -0.18$), followed by Sr/Ca and Mg/Ca ($x_\dagger = -0.14$ for both). U/Ca provides a modest signal ($x_\dagger = -0.12$), while Li/Mg and B/Ca show minimal influence ($x_\dagger = -0.07$ each).

In the deseasonalized models, the pattern reverses between the two corals. GI2 now shows uniformly weak and stable contributions from all TE/Ca ratios ($\mu_{x\dagger} = -0.03$, $\sigma_{x\dagger} < 0.01$), indicating minimal coherence with SST once the seasonal cycle is removed. In contrast, GI1 displays more pronounced and variable loadings: Mg/Ca exhibits the strongest signal ($x_\dagger = 0.37$), followed by Li/Ca ($x_\dagger = -0.24$), with Sr/Ca and B/Ca contributing smaller amounts ($x_\dagger = -0.08$ and -0.06, respectively). U/Ca and Li/Mg have negligible influence in this model ($x_\dagger = -0.02$ and -0.01, respectively).

Together, these results reinforce the dominant role of Sr/Ca and Li/Mg in driving SMITE reconstructions and confirm their consistency across studies and across the GBR. The increased spread of loading scores in deseasonalized models highlights how geochemical proxies of SST become less reliable on interannual-to-decadal timescales. Notably, however, the stability and strength of Li/Mg loadings in the GBR1-12 corals (measured via solution-based ICP-MS) suggest it may be especially well-suited for reconstructing interannual SST variability, even when seasonal signals are removed.

4.3.2 Interrecord Comparisons

To evaluate the reproducibility of each reconstruction method, I conducted a comprehensive cross-application experiment using the deseasonalized coral datasets. Each of the 17 SST models produced from each reconstruction method (SMITE, Sr/Ca, Li/Mg) was applied to all 17 coral records (GBR1-15 and GI1-2), yielding a total of 867 reconstructions (289 model-data pairs across 3 methods). Figure 4.6 presents the distributions of the differences in correlation (Δr^2; top row) and relative accuracy (ΔnRMSE; bottom row) between SMITE and Sr/Ca (left column) and Li/Mg (right column). Positive values indicate that SMITE performs better than the respective univariate method in terms of Δr^2 (higher correlation) but worse in terms of ΔnRMSE (higher relative error). The overall performance of SMITE relative to Sr/Ca and Li/Mg can be inferred by the distance between the median of each distribution (vertical red dashed lines) and the point where Δr^2 or ΔnRMSE equals zero (vertical blue dashed lines). As in the in-

trarecord comparisons (Section 4.3.1), SMITE consistently outperforms both Sr/Ca and Li/Mg in terms of RMSE across all interrecord reconstructions, often by a substantial margin. The full distributions of RMSE differences are provided in Appendix C.11. Given this consistent advantage in absolute error, I focus here on differences in relative error (ΔnRMSE) to provide a more balanced assessment of how each method captures SST anomalies on interannual to decadal timescales.

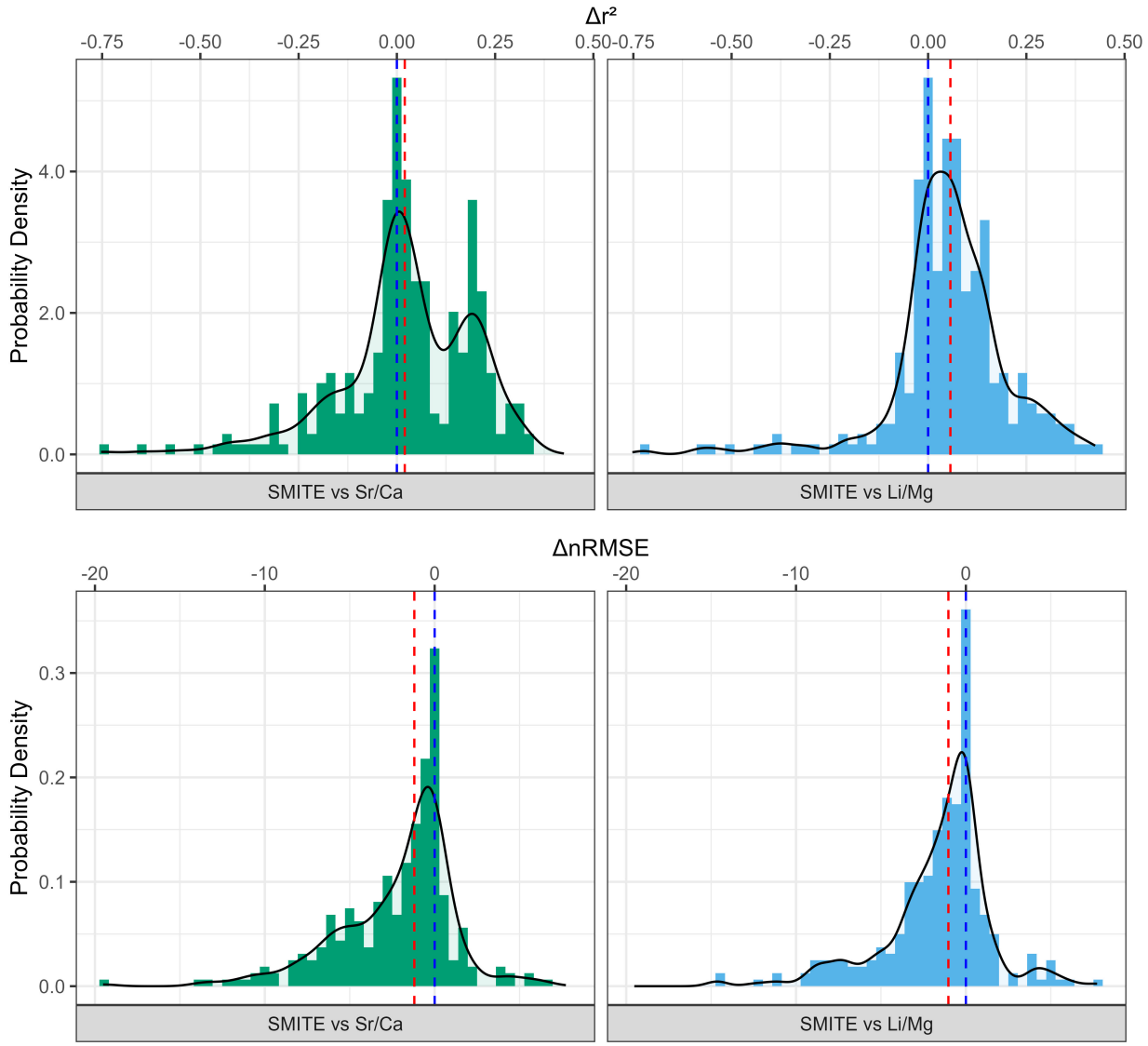

Figure 4.6: Histograms showing the difference in summary statistics between SMITE and Sr/Ca (left column), and between SMITE and Li/Mg (right column), for all possible combinations of deseasonalized SST models and coral datasets. The top panels display differences in the squared Pearson correlation coefficient (Δr^2), while the bottom panels display differences in normalized root mean square error (ΔnRMSE). Black lines overlaying the histograms indicate probability density functions (PDFs). Blue dashed lines mark zero, indicating no difference between SMITE and the corresponding univariate method. Red dashed lines indicate the median of each distribution.

As previously mentioned, this analysis specifically focuses on deseasonalized calibrations in order to focus on calibration fidelity with respect to interannual SST variability. For reference, readers can consult Figure C.12 for the individual values of each summary statistic across methods. I acknowledge that it is not typical in modern calibration practices to apply an SST model from one coral to another, especially across sites or species. However, I posit that such tests are highly informative of method reproducibility for paleoclimate studies, given fossil coral applications will not have paired instrumental SST records. Furthermore, applying SST models between different coral records parallels drifts in reconstruction skill that may emerge from long coral records. Thus, this cross-application framework provides a useful benchmark for assessing the stability of different calibration methods. For a detailed discussions on the implications of this experiment, see Section 4.4.2.

When examining the Δr^2 distributions (Figure 4.6, top row), SMITE yields a higher Δr^2 value than Sr/Ca in 166 out of 289 cases (57%) and 210 cases against Li/Mg (73%). Most values fall within 0.3 units of zero with medians close to zero (0.02 for SMITE vs Sr/Ca, 0.06 for SMITE vs Li/Mg), indicating a modest improvement for SMITE over Sr/Ca and Li/Mg in terms of correlation. However, both distributions exhibit long left tails, indicating isolated cases where SMITE performed substantially worse than the univariate methods, by more than 0.5 units in some comparisons. Conversely, there is also a marked cluster of reconstructions in which SMITE improves upon Sr/Ca by 0.15-0.25 units, suggesting under certain local or analytical conditions, SMITE better preserves SST signal coherence across coral records.

Assessing differences in relative accuracy (ΔnRMSE) reveals a more consistent advantage for SMITE, despite being outperformed by both Sr/Ca and Li/Mg in the deseasonalized intrarecord comparisons (Section 4.3.1). Across the interrecord experiments, SMITE yields lower nRMSE values in 226 cases (78%) compared to Sr/Ca and in 213 cases (74%) compared to Li/Mg. Median ΔnRMSE values exceed one standard deviation in both comparisons, indicating regular and meaningful gains in relative reconstruction accuracy ($\Delta\text{nRMSE}_{\text{Sr/Ca}} = -1.20$, $\Delta\text{nRMSE}_{\text{Li/Mg}} = -1.03$). While over 95% of all pairwise differences fall between -8.5 and 2.5 standard deviations, there are isolated outlier cases where Sr/Ca and Li/Mg ΔnRMSEs exceed 5 or approach -20.

To identify which combinations of models and coral records produce significant results and to elucidate any structural patterns, I constructed a matrix-style visualization comparing SMITE against Sr/Ca and Li/Mg across all possible combinations of deseasonalized models and coral datasets (Figure 4.7). Here, the color of each cell denotes the difference in summary statistics between the corresponding combination of a coral dataset (y-axis) and a SST model (x-axis). When assessing whether each comparison was statistically significant (cells not containing 'x'), I used the uncertainty of the summary statistic associated with the SST model, and not the coral dataset. This choice was made for practical reasons. Under realistic conditions, applying a coral-derived model to a new coral record would typically involve using the error metrics derived from the calibration model because the calibration error metrics on the coral dataset would likely not be available.

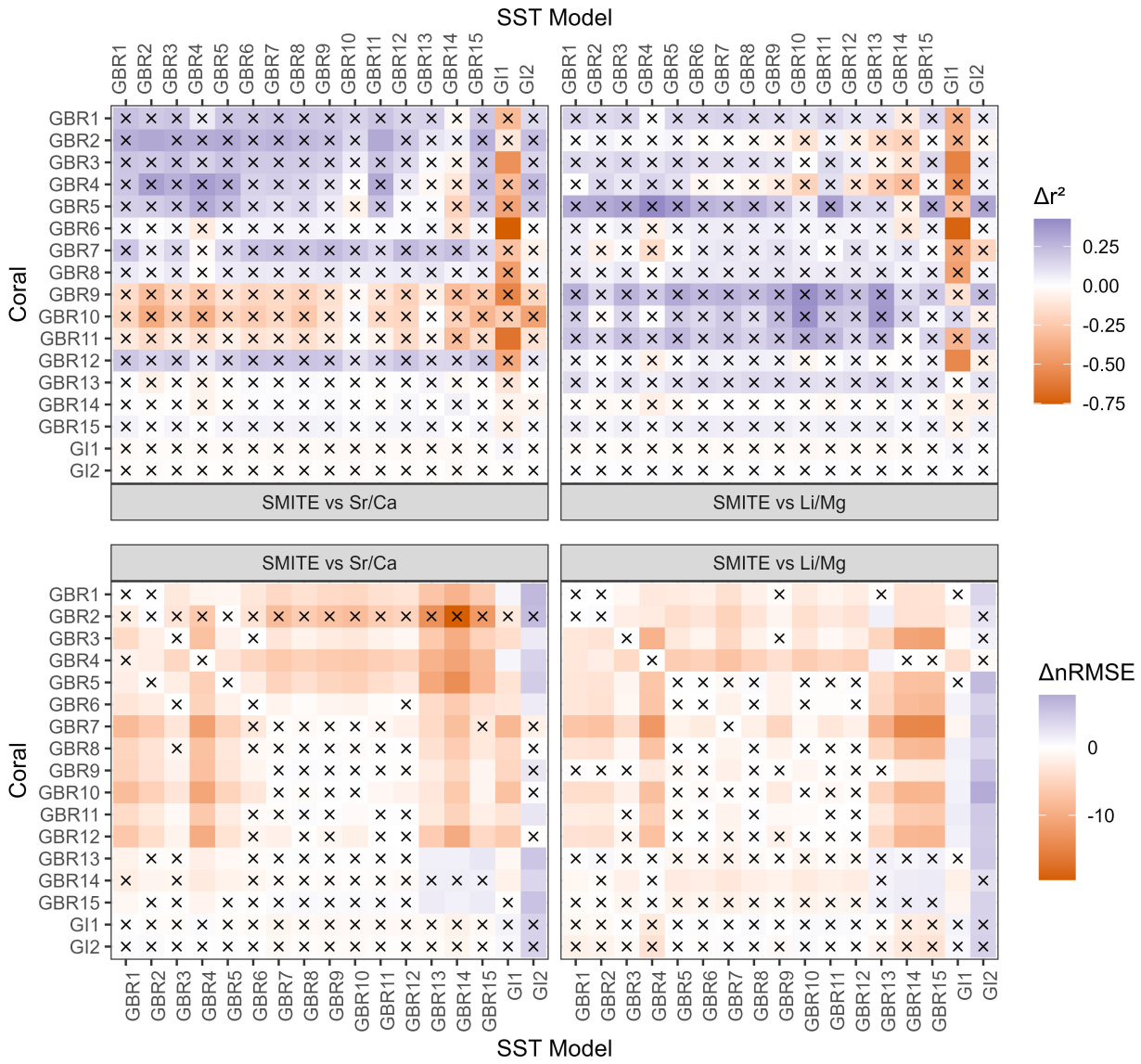

Figure 4.7: The difference in summary statistics between SMITE and Sr/Ca (left column), and between SMITE and Li/Mg (right column), for all possible combinations of deseasonalized SST models (x-axis) and coral datasets (y-axis). The diagonal represents where an SST model is applied to the same coral that it was generated from. Off-diagonal elements thus represent some combination of coral and model. Colors in each cell indicate the value of the difference in the summary statistics. Purple indicates higher values for either the squared correlation coefficient (r^2) or the normalized root mean square error (nRMSE). Cells that contain 'x' indicate when the difference between the corresponding summary statistic is not significant at the 95% confidence level.

As previously noted, SMITE produced higher r^2 values than Sr/Ca in 57% of cases and 73% of cases for Li/Mg. However, the top panels of Figure 4.7 reveals that the vast majorities of these comparisons are not statistically significant (cells containing 'x'). Statistically significant Δr^2 values occur when a model trained on Galápagos coral GI1 is applied to GBR3, GBR6, GBR11, and GBR12 coral datasets. As discussed earlier, the GI1 deseasonalized SMITE model is effectively a bivariate SST model, with strong loadings in Mg/Ca and Li/Ca and near-zero contributions from all other TE/Ca ratios. Unsurprisingly, Sr/Ca and Li/Mg SST regression models from GI1 per-

form significantly better than SMITE when applied to GBR corals using this non-generalizable bivariate regression model.

In contrast, nRMSE comparisons (bottom panels of Figure 4.7) highlight a more consistent and statistically robust advantage for SMITE. As noted in the previous section, SMITE achieves lower nRMSEs in 78% of comparisons against Sr/Ca and 74% against Li/Mg. A substantial fraction of these improvements are statistically significant: 120 of 226 cases for Sr/Ca, and 111 of 213 for Li/Mg. Moreover, the arrangement of these results within Figure 4.7 reveals several consistent patterns. First, coral datasets GBR13-15 contribute relatively few statistically significant comparisons, likely reflecting the large uncertainties in their nRMSE estimates. Second, applying coral models GBR1-12 to many of the GBR datasets yield significantly negative ΔnRMSE values, creating a notable 'n'-shaped pattern in the center of each panel. This indicates significantly better performance when applying SMITE SST models across the more skillful GBR1-12 records. Finally, models trained on GI2 consistently produce significantly positive ΔnRMSE values when applied to any dataset, indicating degraded SMITE performance relative to Sr/Ca and Li/Mg in these cases. This likely stems from the ubiquitously low loading scores for all TE/Ca ratios from the GI2 SMITE model, leaving these reconstructions generally uninformed by temperature variability.

4.3.3 Synthetic CFR

Structured Noise Models

A key component of the synthetic CFR experiment is how the residuals of each calibration method are modeled. Figure 4.8 displays the 5th, 50th, and 95th percentile distributions of the block-bootstrap cross-validated residuals for each calibration method (top panel) and their autocorrelation coefficients (AR1, middle panel; AR2, bottom panel) derived from the GBR1-12 coral records. These form the basis of the pseudo-observation error modeling used in the synthetic CFR experiment. Each percentile distribution constitutes a unique population of residuals and AR coefficients that can be randomly drawn from to create each pseudo-observation. In summary, these residual models indicate the degree of autocorrelation present in each method, with high AR coefficients indicating a high degree of "memory" in the error terms and thus strong systematic non-SST-related variability. For methodological details, including why GBR13-15 were excluded from this modeling, see Section 4.2.5.

With respect to the residual distributions (Figure 4.8, top panel), all methods' median distributions (boxplots with solid-black outlines) cluster tightly around 0. However, the 5th (least opaque, dotted outlines) and 95th (most opaque, dashed outlines) percentile distributions depart significantly from 0 for all methods, with the most extreme outliers observed in Sr/Ca and the most conservative estimates in SMITE. Autocorrelation coefficients vary substantially both across methods and between percentile distributions (middle and bottom panels). Within the median percentile distributions, SMITE exhibits both the lowest AR1 and AR2 coefficients, with the latter being statisti-

cally indistinguishable from 0 ($p = 0.86$). Sr/Ca and Li/Mg exhibit roughly equal AR1 and AR2 coefficients, both of which are significantly above 0 ($p < 0.05$). There is significantly more variability in the 5th and 95th percentile distributions. The only three AR2 coefficients that are not statistically different from 0 are SMITE's 50th percentile ($p = 0.86$), SMITE's 95th percentile ($p = 0.12$), and Li/Mg's 95th percentile ($p = 0.16$). However, across all percentile distributions, Sr/Ca consistently shows higher AR1 and AR2 coefficients than Li/Mg, albeit with considerably less spread. This indicates that Sr/Ca demonstrates the most persistent autocorrelation in its errors, whereas the memory effect in Li/Mg is much more variable, particularly in the AR2 coefficients.

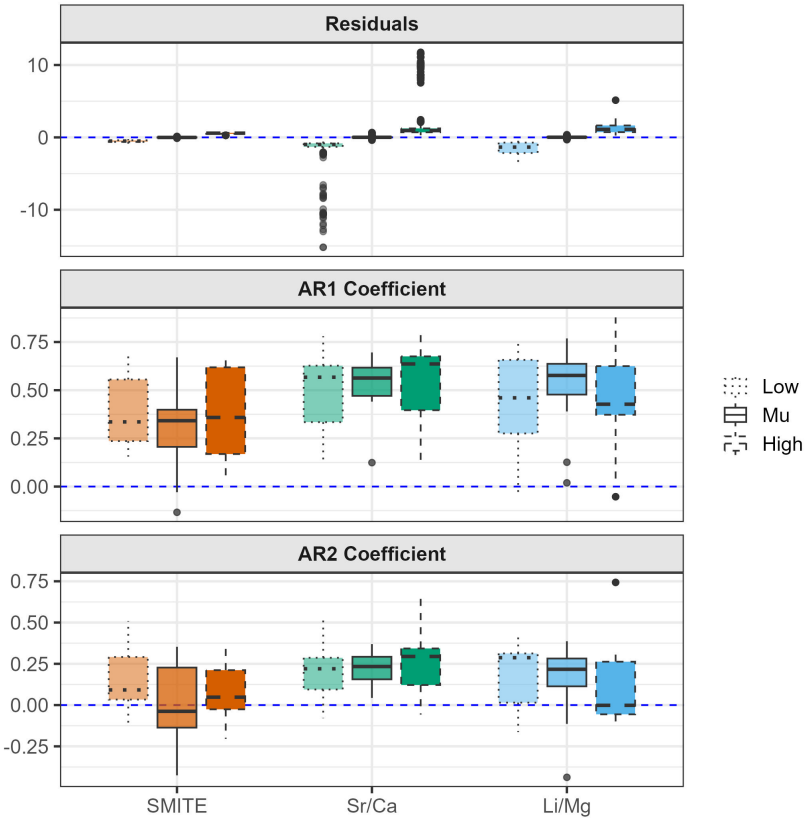

Figure 4.8: Boxplots depicting the 5th, 50th, and 95th percentiles of cross-validated residuals and their autoregression coefficients (AR1 and AR2) from the Great Barrier Reef corals for each calibration method (SMITE = orange, Sr/Ca = green, Li/Mg = blue). Each percentile distribution for each method are shown in different boxplots, with opacity and outlines indicating the 5th (least opaque, dotted), 50th (solid) and 95th (most opaque, dashed) percentiles, respectively. Boxplots depict the interquartile range, with central lines indicating the median. Whiskers extend to values within 1.5-times the interquartile range, with points beyond this range plotted as outliers (Tukey, 1977). The top panel includes 563 residuals per percentile distribution per method, while the bottoms panel summarizes 12 AR coefficients per percentile distribution per method.

Together, these results underscore that SMITE produces smaller and more weakly autocorrelated residuals than Sr/Ca or Li/Mg in the GBR1-12 datasets. While this alone would portend superior performance in the synthetic CFR experiment for SMITE, I penalize synthetic SMITE CFRs by dampening their variance in accordance to the ratio of variance suppression observed in GBR1-12 (see Section 4.2.5 for details).

Climate Mode Signal Recoverability

To evaluate the performance of each synthetic CFR method, I assessed the fraction of the SST field over the GBR in which interannual variability linked to ENSO and IOD could be resolved. Figure 4.9 shows the percentage of grid cells deemed "resolved" as a function of the number of coral records assimilated (N = 15-90) with 95% confidence intervals indicated by the colored shaded regions. A grid cell is deemed resolved with respect to ENSO or IOD variability when it exhibits an ESR greater than or equal to 1 (see Section 4.2.5 for a detailed description of the ESR metric). Results are shown separately by reconstruction method (Sr/Ca, Li/Mg, SMITE; columns) and climate mode (ENSO, IOD; rows). The gray shaded regions indicate the mean proxy coverage of the SST field at each network size.

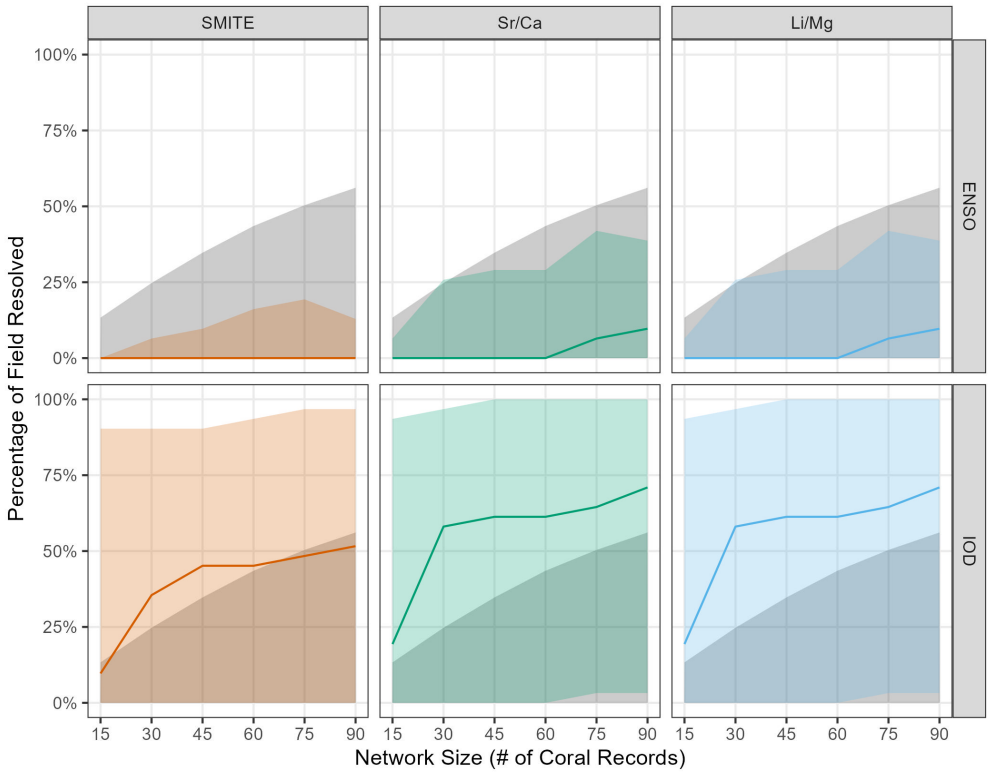

Figure 4.9: Percentage of grid cells on the Great Barrier Reef (GBR) in which synthetic climate field reconstructions (CFRs) successfully resolve interannual SST variability associated with the El Niño-Southern Oscillation (ENSO; top row) and the Indian Ocean Dipole (IOD; bottom row). Columns represent the reconstruction method used to generate the synthetic CFR (Sr/Ca, Li/Mg, and SMITE). A grid cell is considered "resolved" when its effective signal recoverability (ESR; defined as the effective signal variance divided by CFR uncertainty) is greater than or equal to 1 (see Section 4.2.5). Colored shaded regions correspond to the 95% confidence intervals, while solid lines indicate the median. Shaded gray envelopes indicate the mean percentage of the spatiotemporal domain of the SST field covered by the proxy network at each sampling level (i.e., number of assimilated coral records).

The large uncertainty shown in the shaded confidence intervals stems from a multitude of sources, including the ensemble-based uncertainty in the prior CMIP6 models, CFR error, and reconstructed variance ratios. However,

the largest source of uncertainty stems from the error in the SST-climate mode regression slopes estimated during the satellite era (the β^2 term in the ESR calculation). However, these large error bars in the percentage of the field resolved, particularly with respect to IOD, are difficult to diagnose specifically. For instance, there is no apparent relationship between the mean latitude of the synthetic coral records and their ability to resolve ENSO or IOD variability ($p > 0.05$). Therefore, further discussion of Figure 4.9 focuses on the median confidence line (solid lines) and the upper bounds (top portion of the shaded regions).

For ENSO, SMITE is unable to resolve any grid cells at median confidence across the entire experiment. Its upper confidence bound reaches a modest 6 grid cells by N = 75 (covering 50% of the spatiotemporal domain), but then drops slightly to 4 grid cells at N = 90 (56% spatiotemporal coverage). Both Sr/Ca and Li/Mg perform similarly throughout the experiment, resolving 2 grid cells at N = 75 and 3 at N = 90 with median confidence. Their upper confidence bounds show more potential, peaking at 13 grid cells at N = 75 before declining slightly to 12 grid cells at N = 90. This drop at the final increment across all methods suggests diminishing returns in ENSO resolution once the coral network reaches a certain size.

IOD-related variability shows greater potential for spatial reconstruction, though with higher uncertainty. All three methods are able to resolve a meaningful portion of the IOD signal, but Sr/Ca and Li/Mg consistently outperform SMITE. At N = 15, Sr/Ca and Li/Mg each resolve 6 grid cells at median confidence ($\sim$20% of the grid cells), while SMITE resolves just 3. As the network expands, resolution increases rapidly at first. This is particularly true for Sr/Ca and Li/Mg, which triple their resolved grid cells from 6 to 18 between N = 15 and N = 30. Growth slows after this point, with Sr/Ca and Li/Mg resolving 22 grid cells by N = 90. SMITE's performance slows after N = 45 with 14 grid cells resolved , peaking at 16 resolved grid cells by the end of the experiment.

All methods reach high percentages of field resolution for IOD in the upper bounds of their confidence intervals throughout the experiment. However, Sr/Ca and Li/Mg maintain a clear advantage, fully resolving the GBR by N = 45. SMITE, in contrast, never reaches full resolution, falling short by one grid cell at N = 90. This shortfall likely does not reflect a theoretical limit, however, as appears to be the case for ENSO. Rather, given that SMITE's median confidence line continues to increase linearly, full field resolution may still be achievable with a larger coral network.

To visualize where climate signals are most robustly captured, I mapped median ESRs from the initial and final proxy network sizes (N = 15 and N = 90, respectively) across the GBR for both ENSO and IOD (Figure 4.10). These maps show grid-wise ESRs for each method (SMITE, Sr/Ca, Li/Mg), allowing direct comparison of both spatial resolution and regional sensitivity across the minimum and maximum network sizes across the experiment. By examining the evolution of ESRs from a sparse to dense coral network, this figure highlights not only how much of the field each method resolve, but where those climate signals are best captured.

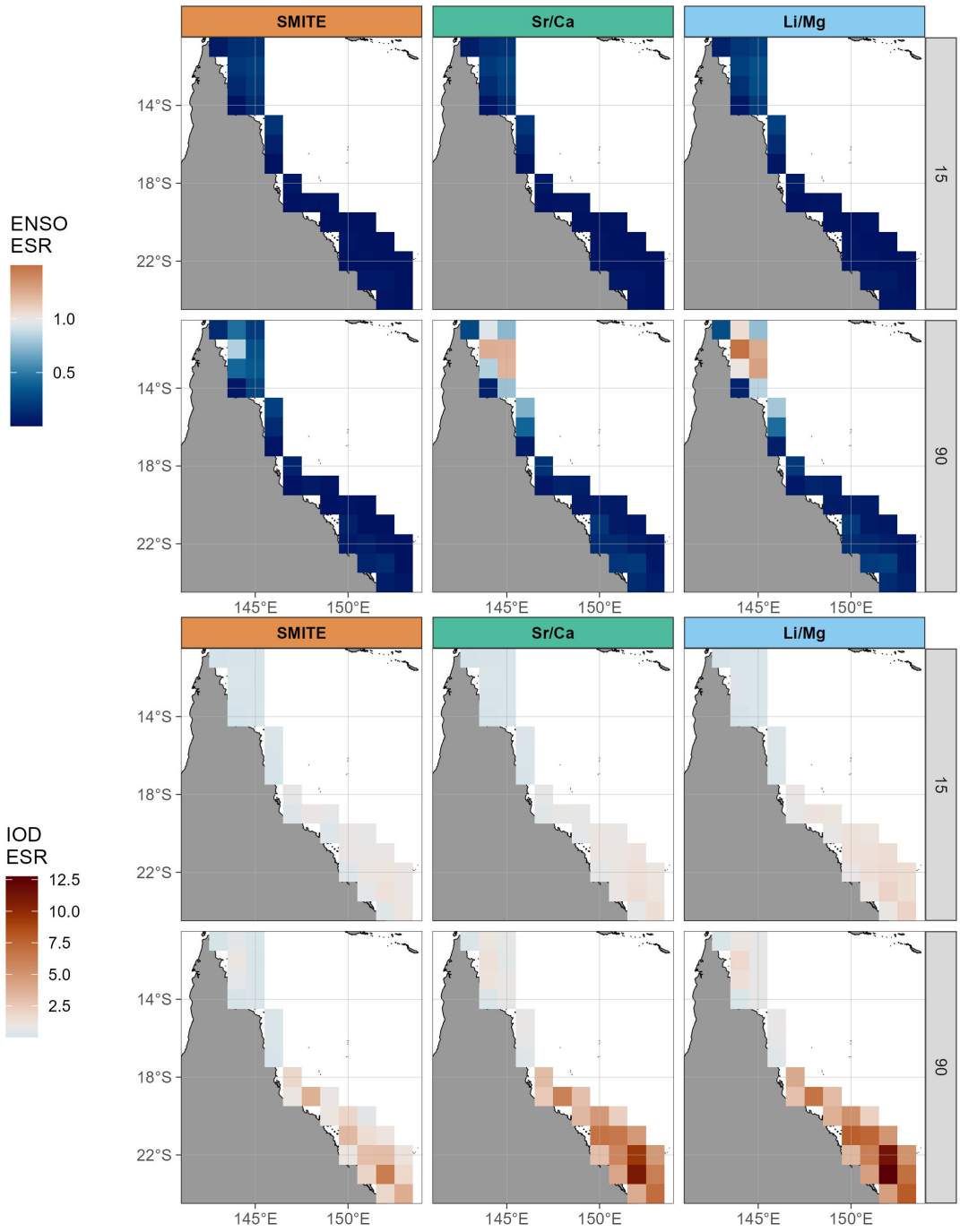

Figure 4.10: Median effective signal recoverability (ESR) for the El Niño-Southern Oscillation (ENSO; top two rows) and the Indian Ocean Dipole (IOD; bottom two rows) based on each method's synthetic climate field reconstructions (columns) across the Great Barrier Reef. Within each climate mode group, each row represents the ESR under different network sizes (15 and 90). The ESR is defined as the variance-adjusted squared regression slope between SST and the climate mode of interest, divided by the squared RMSE of the CFR at each grid cell. An ESR $\geq$1 indicates that the local SST variability attributable to the climate mode is resolved beyond the reconstruction error (see Section 4.2.5).

The ENSO ESR maps indicate that signal recoverability is largely confined to the northernmost portion of the GBR. As mentioned earlier, no method is able to resolve ENSO variability at the minimum network size of N =

15. At N = 90, SMITE shows only a single grid cell approaching an ESR of 1. Sr/Ca and Li/Mg each resolve three grid cells at N = 90, though Li/Mg shows greater potential, with higher ESR values within each resolved cell. Across the southern GBR, ENSO ESR values remain consistently low—even at the maximum network size—suggesting either weak ENSO teleconnections or low signal-to-noise ratios in this region. This highly localized sensitivity may help explain why the upper confidence bounds for all methods show diminishing returns with increasing coral network size: adding more records does not necessarily improve signal recoverability if the signal can only be detected in the northernmost $\sim$10 grid cells.

In contrast, IOD-related signal recoverability appears much stronger, particularly in the southern GBR, with substantial gains extending into the mid-GBR. Both Li/Mg and Sr/Ca achieve ESRs above 10 in two of the southernmost grid cells, indicating strong localized sensitivity to the IOD. All methods are able to resolve at least some grid cells in the northern GBR as well, suggesting robust IOD teleconnections that exhibit coherence across the field.

These spatial patterns reinforce the latitudinal asymmetry in ENSO and IOD expression across the GBR. They also highlight how different modes of variability leave distinct regional fingerprints, an insight not easily gleaned from bulk statistics alone. Furthermore, these results suggest that the Bayesian approach to field reconstruction applied by the PDA-enKF method benefits from noisier records without variance suppression, as reflected in SMITE's poor performance. That said, these spatial ESR metrics are to be interpreted conservatively. The synthetic CFR design incorporates several simplifying assumptions, including the AR2 error model, the criteria for defining a 'resolved' grid cell, and fixed teleconnection patterns based on the calibration period. To account for these choices, the ensemble-based uncertainty estimates are designed to capture a broad range of outcomes, as reflected in the width of the confidence intervals.

Summary Statistics

Finally, to quantitatively contextualize the patterns observed in the ESR maps, I examine summary statistics from the synthetic CFRs as a function of proxy network size (Figure 4.11). The spatial distributions of each summary statistic at the final network size of N = 90 are provided in Figure C.13. Across the most widely used reconstruction metrics—correlation (r), root-mean-square error (RMSE), and coefficient of efficiency (CE)—SMITE outperforms both Sr/Ca and Li/Mg, with Li/Mg consistently showing improvements over Sr/Ca. However, when considering relative accuracy (nRMSE) and variance preservation (γ), a more nuanced picture emerges. While Sr/Ca and Li/Mg show similar curves, with Li/Mg maintaining a slight edge, SMITE's improvement in nRMSE with increasing network size is noticeably slower than that of either univariate method, resulting in significantly higher nRMSE values at the final network size of N = 90. This divergence can be directly linked to the evolution of the variance ratio (γ), since nRMSE is inversely proportional to reconstruction variance (see Equation 4.2.4). While SMITE's γ remains largely constant at approximately 0.5, both Li/Mg and Sr/Ca exhibit progressive gains in γ, along with tight-

ening confidence intervals. These improvements in variance preservation explain the declining nRMSE values—and consequently the enhanced ESR performance—of Sr/Ca and Li/Mg relative to SMITE.

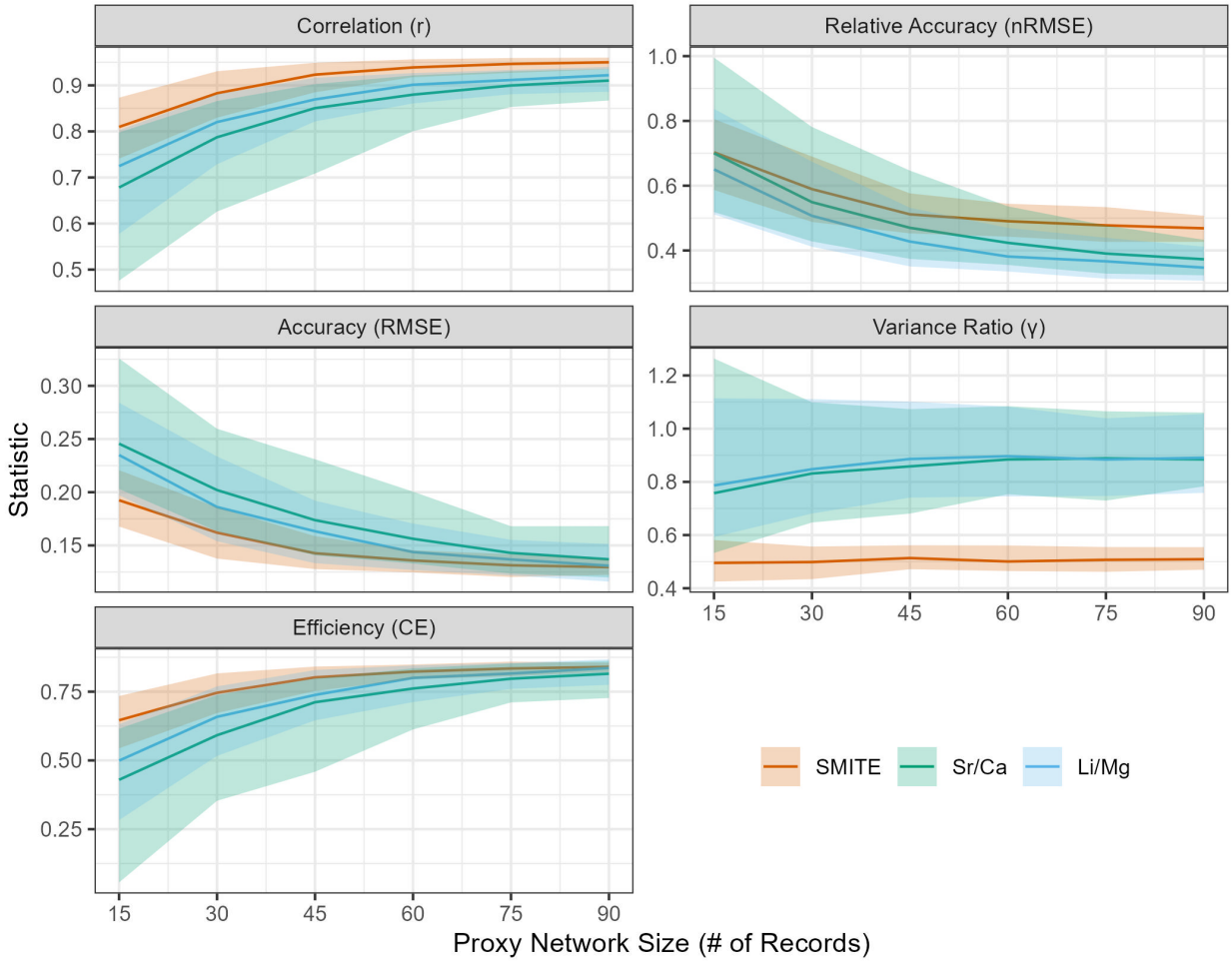

Figure 4.11: Summary statistics for the synthetic climate field reconstruction (CFR) ensembles as the proxy network size (number of coral records assimilated) increases from 15 to 90. Error envelopes around each curve indicate the 95% confidence interval, based off 500-member ensembles.

4.4 Discussion

4.4.1 Conceptual Framing

Seasonal SST calibrations are widespread in coral paleoclimatology and have proven useful for understanding local climate processes, such as annual temperature cycles and seasonal hydroclimate variability. However, many core applications of coral-based SST reconstructions, such as identifying sensitivity to ENSO or IOD events, or conducting climate diagnostics using empirical orthogonal function (EOF) analysis, require sensitivity to interannual anomalies, not the seasonal cycle itself. The seasonal cycle imparts a strong signal onto SST calibrations, often dominating the total variance explained. While this can enhance apparent reconstruction skill, it may obscure the more

subtle climate signals that paleoclimatologists seek to extract, which are deviations from the expected seasonal state. These interannual fluctuations are typically an order of magnitude smaller than the seasonal signal, making them difficult to detect and reconstruct faithfully when the seasonal cycle is retained. Given this, rigorously assessing how different SST proxies and calibration methods perform in capturing deseasonalized variability is essential. This study aims to fill this gap by systematically evaluating the fidelity of multiple calibration methods (SMITE, Sr/Ca, Li/Mg) across different spatial and temporal scales (intrarecord, interrecord, field).

4.4.2 Evaluating Reconstruction Skill Across Scales

Intrarecord Skill: Implications for Tracking Interannual Variability

To evaluate the fidelity of each calibration method at the individual-record level, I compared reconstruction skill before and after deseasonalization. Figures 4.3 and 4.4 illustrate these differences across three calibration methods (SMITE, Sr/Ca, and Li/Mg), revealing how the presence or absence of the seasonal cycle affects correlation (r), accuracy (RMSE), and relative accuracy (nRMSE). Differences can also be observed directly in Appendices C.2 and C.3, as well as in Figures C.3 through C.8. These results serve as a baseline for understanding the ability of coral-based SST reconstructions to resolve interannual variability within each record.

Across all methods, I observe a consistent and often substantial decline in correlation when calibrations are performed on deseasonalized datasets, even among the relatively skillful GBR1-12 records. For SMITE, the median correlation drops by 18% (from 0.96 to 0.79) among these corals, and the width of the 95% confidence interval increases 9-fold (from 0.07 to 0.62). Sr/Ca and Li/Mg exhibit even larger median reductions (from $\sim$0.96 to $\sim$0.72), and their confidence intervals expand by a factor of 11 and 9, respectively.

Among the longer and more continuous laser-ablated GBR13-15 records, the drop in correlation is even more severe. SMITE shows a 68% reduction in median correlation (from 0.87 to 0.28), while Sr/Ca and Li/Mg show comparable declines of 71% (from 0.77 to 0.22) and 74% (from 0.81 to 0.21), respectively. The corresponding increases in confidence interval width (over four-fold for SMITE and approximately three-fold for Sr/Ca and Li/Mg) suggest instability in deseasonalized models. In the Galápagos corals, the shift from seasonal to deseasonalized calibration yields SST correlations for all three methods that are not statistically different from zero. Median correlations decline by 71% for SMITE, 81% for Sr/Ca, and 91% for Li/Mg. Confidence intervals among GI1 and GI2 only grow modestly: by about 9% for SMITE, 12% for Sr/Ca, and 30% for Li/Mg. However, this limited expansion reflects the fact that the lower confidence bounds were already near zero in the seasonal regressions. As a result, models have little remaining room to degrade further without yielding significant negative correlations, which are unlikely in the absence of any meaningful signal.

nRMSE provides a clearer indication of how well each method captures interannual SST anomalies by removing the influence of total reconstructed variance. This makes nRMSE especially useful in comparing methods like SMITE to univariate approaches. Although SMITE consistently produces lower RMSEs than Sr/Ca and Li/Mg, owing to its tendency to suppress reconstructed SST variance in noisy coral datasets, this can result in reconstructions that relax toward zero variance and convey little to no meaningful climate signal. As a result, SMITE performs better in terms of absolute accuracy, but not necessarily relative accuracy. This is why interpreting RMSE alongside nRMSE provides a more comprehensive assessment of reconstruction skill.

Among the relatively skillful GBR1-12 corals, all methods show increases in nRMSE when calibrated on deseasonalized data relative to the seasonal data. However, SMITE exhibits the largest change with nearly a three-fold increase (from 0.23 to 0.63), while Sr/Ca and Li/Mg follow with approximately two-fold increases (0.28 to 0.57 for Sr/Ca, 0.26 to 0.53 for Li/Mg). The confidence interval for Sr/Ca's nRMSEs expands most dramatically (over 10-fold), compared to three-fold for SMITE and six-fold for Li/Mg. This relatively modest increase in SMITE's nRMSE confidence intervals between seasonal and deseasonalized reconstructions suggests greater consistency in tracking interannual variability across cross-validation relative to Sr/Ca and Li/Mg.

For the GBR13-15 corals, SMITE again shows the steepest degradation, with a nearly five-fold increase in median nRMSE (from 0.51 to 2.40). Sr/Ca and Li/Mg exhibit more modest increases by a factor of $\sim$1.5, likely due to high raw variance in their reconstructions, which buffers their nRMSE metrics. However, Sr/Ca exhibits the most modest increase in confidence interval width between seasonal and deseasonalized nRMSEs for GBR13-15 (over four-fold). SMITE's mean confidence interval grows over five-fold, while Li/Mg's mean confidence interval grows nearly 15-fold due to high upper bounds in GBR13 and, to a lesser extent, GBR15.

The Galápagos corals further highlight the variance penalty inherent to nRMSE, particularly with SMITE SST reconstructions. SMITE's median nRMSE rises from ≤ 2 in the seasonal calibrations to 2.6 and 4.5 for corals GI1 and GI2 in the deseasonalized calibrations, respectively. Sr/Ca and Li/Mg also show two-to-three-fold increases in their median nRMSEs across deseasonalization, although the upper bounds of their confidence intervals well-exceed those of SMITE. This suggests that while the univariate methods maintain stable performance, they also retain more extreme cases of overfitting or mismatch in anomaly timing.

Two key patterns emerge from these intrarecord comparisons. First, the general increase in nRMSE and decline in correlation across all methods when moving from seasonal to deseasonalized calibrations indicates that a substantial amount of reconstruction skill is lost when the seasonal cycle is removed. However, under favorable analytical conditions, such as those found in the GBR1-12 corals analyzed via solution-based ICP-MS, the ability to track interannual variability is relatively well preserved, particularly by Sr/Ca and Li/Mg. In contrast, under more challenging conditions, such as laser ablation datasets (GBR13-15) or environmentally complex settings like the Galápagos, SMITE performs poorly with respect to nRMSEs, often failing to capture meaningful anomalies.

Among the more skillful GBR1-12 records in the deseasonalized intrarecord comparisons, Sr/Ca and Li/Mg both produced the lowest nRMSE in 4 and 5 out of 12 cases. While none of these are statistically significant, Li/Mg's relative strength in tracking interannual variability is supported by the SMITE loading score distributions (Figure 4.5) and results from the synthetic CFR experiment. I noted previously that Li/Mg loadings for GBR1-12 cluster tightly around a high absolute loading score for both seasonal and deseasonalized datasets, indicating a consistently strong correlation with SST across timescales. Li/Mg residuals for GBR1-12 also exhibit lower spread and AR coefficients than Sr/Ca, though still higher than SMITE, indicating greater temporal consistency and reduced red-noise behavior. This pattern indicates that within a single coral record and under these specific analytical conditions, Li/Mg can outperform Sr/Ca and SMITE SST estimates (under maximum regularization) with respect to reconstructing interannual anomalies, particularly when those anomalies are the central objective and variance fidelity outweighs absolute accuracy.

Interrecord Skill: Implications for Reproducibility

Understanding how each calibration method performs on deseasonalized datasets within individual coral records provides a critical baseline for evaluating local-scale interannual reconstruction skill. However, this approach is inherently limited by the length of the calibration period. The block-bootstrap cross-validation approach used in this study offers a rigorous framework for estimating uncertainty and addressing autocorrelation, but its effectiveness is ultimately bounded by the duration of the calibration period. True out-of-sample skill, which can only ever be approximated, can refer to two distinct but related phenomena: (1) how well a SST regression model performs when applied to a different coral record from which it was developed, such as in fossil applications, and (2) how stable a regression model remains when applied down-core within a long, continuous record (i.e., temporal regression stability).

While regression parameters are rarely transferred between coral records in modern-era studies due to the availability of gridded SST products like HadISST or ERASST, such transfers are often necessary in fossil reconstructions. The limitations of gridded SST datasets are well-documented, particularly in the early 20th century when observational constraints are sparse (Chan, 2021; Chan and Huybers, 2021; Davis et al., 2019; Kennedy et al., 2011; Smith and Reynolds, 2002). Thus, developing robust SST regression models that can be applied to fossil records remains a core goal of coral paleoclimatology. In this context, the interrecord comparisons provide a rigorous and practical test of how well different regression models generalize across coral datasets, with direct implications for reconstructing historical interannual variability throughout the Common Era.

Temporal regression instability poses a more pernicious challenge when performing long coral-based SST reconstructions. A variety of physical and biological factors can degrade calibration fidelity over time, including changes in local seawater chemistry unrelated to large-scale climate signals (de Villiers et al., 1994), shifts in nu-

trient concentrations (Standish et al., 2023), kinetic or metabolic effects (DeLong et al., 2011; Kuffner et al., 2012; Sinclair et al., 2006), and errors introduced through age-model uncertainty or sampling irregularities (DeLong et al., 2013, 2014; Flannery et al., 2017; Grothe et al., 2020; Sayani et al., 2019). These compounding sources of error have been broadly characterized as red-noise processes (McPartland et al., 2024), implying that longer records inherently carry greater uncertainty.

While the block bootstrap cross-validation framework accounts for some of this temporal variability by incorporating serial autocorrelation and out-of-sample error, it remains tethered to the calibration period and does not fully reflect how calibration skill may evolve over longer timescales. In this light, the interrecord comparison offers a valuable complementary approach to directly testing for proxy calibration drift by assessing both spatial and temporal generalizability. Applying a model trained on one coral record to another tests calibration robustness under novel environmental, chemical, and biological conditions, paralleling the challenges faced when applying a model down-core. This conceptual symmetry, treating spatial heterogeneity as a stand-in for temporal change, provides a powerful, if indirect, lens through which to evaluate the long-term stability of SST calibration methods. Taken together, block-bootstrap cross-validation and the interrecord comparisons extend the evaluation of model skill beyond the bounds of the original calibration period.

As detailed in Section 4.3.2, I observe clear spatial patterns in the interrecord comparisons with respect to when certain methods succeed under certain conditions. SMITE generally outperforms Sr/Ca and Li/Mg across all cross-applications, except in cases where models trained on the Galápagos corals (GI1 or GI2) are applied to GBR coral datasets. Across the full matrix of comparisons, correlation differences are almost always statistically insignificant, but SMITE holds a slight edge in the total number of reconstructions where it achieves higher correlation values (57% versus Sr/Ca, 73% versus Li/Mg).

Differences become more pronounced when considering nRMSE. As discussed earlier, SMITE yields lower nRMSEs in most cases, and in more than half of those, the results are statistically significant. The exceptions primarily involve models trained on GI2, as well as applications to the less skillful GBR13-15 and Galápagos records. Exceptions also occur in the diagonal cases (where model and target coral records are the same) and a few clusters in the center of each panel indicating local proximity. Nonetheless, SMITE performs consistently well with respect to nRMSE across these datasets. Furthermore, SMITE produces lower RMSEs in every comparison conducted (Figure C.11).

Taken together, these results suggest that SMITE yields more reproducible regression coefficients for reconstructing SST than the univariate methods, making it a stronger candidate for fossil applications and less vulnerable to temporal regression instability. Its built-in variance suppression likely yields conservative but stable estimates of SST variability, resulting in slightly better correlation and substantially better RMSE and nRMSE performance in cross-application scenarios. When viewed alongside the intrarecord results, these findings suggest that Li/Mg and

Sr/Ca SST models may be overfit to individual records and are thus less generalizable than SMITE across space or time. That said, caution is warranted: GI-trained SMITE models and applications to lower-quality records (e.g., GBR13-15) demonstrate that intercoral transfer is not universally robust. A more prudent recommendation is that SMITE SST models are best applied between corals from the same region, and when similar analytical methods are used.

4.4.3 Corals and Climate Field Reconstructions

Rationale for Great Barrier Reef Field Reconstructions

While this study does not produce a practical field reconstruction from real coral data, it is the first application of a pseudo-proxy framework to evaluate PDA-enKF performance of coral-based proxy records within a region as spatially constrained as the GBR. This testbed is particularly well-suited for network scaling experiments, given the availability of a large database of analyzed coral records on the GBR (Arzey et al., 2024), as well as many additional cores in repository collections that have yet to be analyzed for paleoclimate studies. Despite these advantages, producing spatially explicit reconstructions of the GBR presents substantial challenges. The region is relatively small, spatially autocorrelated, and thus exhibits low spatial degrees of freedom, as evidenced by its broad coherence in SST anomalies (Lough, 1992, 2007). Yet, this coherence masks a complex underlying climate signal. The northern GBR is generally sensitive to ENSO, particularly Central Pacific events during the austral summer (Redondo-Rodriguez et al., 2012), and that sensitivity is modulated by PDO phase (Lough, 2007; Power et al., 1999). Additionally, some extreme SST and bleaching events have occurred in non-ENSO years and appear more closely linked to strong positive IOD phases (Smith et al., 2020; Smith, 2024).

Hydroclimate variability in southeastern Australia is strongly tied to IOD dynamics, via Indian Ocean SST anomalies that drive tropical moisture transport (King et al., 2020; Ummenhofer et al., 2009). Curiously, although IOD is rarely linked to SST variability in the southern GBR, the ESR maps suggest significant signal recoverability, raising the possibility that spatially resolved reconstructions may uncover underappreciated teleconnections. Zonal complexity also plays a role, driven in part by interactions with the East Australian Current and the anomalously cold North Queensland Current, which bisects the northern GBR (Ridgway et al., 2018). Taken together, these complexities underscore why spatially explicit coral-based CFRs of the GBR, while challenging, would be invaluable. They could clarify regional expressions of ENSO and IOD, improve interpretation of historical SST extremes, and support more informed reef management and monitoring efforts.

Synthetic Field Reconstructions: Implications for Future Work

I designed the synthetic CFR experiment used in this study to focus on the effects of proxy network size, motivated by the lack of significant results from the practical CFR. These earlier efforts suggested that insufficient spatiotemporal coverage was a primary limitation in recovering meaningful SST patterns across the GBR. The question of how many coral records are needed to resolve climate signals has clear precedent in both paleoclimatology (Comboul et al., 2015) as well as other disciplines. In paleontology, for example, rarefaction techniques are used to determine the number of samples required to characterize population diversity (Foote, 1992; Raup, 1975; Tipper, 1979). I approached the GBR in much the same way: how large must a coral network be to reliably reconstruct the spatial structure of dominant climate modes like ENSO and IOD on the GBR?

While the synthetic CFR experiment was unable to resolve fine-scale zonal variability associated with regional hydrography due to the coarse $1° \times 1°$ field resolution, they nonetheless captured a strong meridional gradient in SST variability. This gradient is broadly consistent with known spatial patterns of ENSO and IOD influence. This interpretation is reinforced by EOF analysis of SST variability from the CCI dataset across the GBR for the 1981-2016 calibration period (Figure 4.12 and C.14). The first EOF explains 80% of the variance in the field and reflects large-scale field coherence. However, EOF2, which explains 13% of variance, likely captures interannual variability, with statistically significant correlations to both the Niño3.4 index ($r = 0.39$, $p < 0.001$) and the HadISST IOD index ($r = 0.15$, $p = 0.03$). Spatially, this EOF mode features opposing loadings in the northernmost and southernmost GBR, precisely where the ESR maps indicate optimal signal recoverability for ENSO and IOD.

Interestingly, zonal differences in summary statistics (Figure C.13) appear to arise from the covariance structure of the CMIP6 ensemble used to generate the pseudo-proxy fields. Since coral locations were randomized in each ensemble iteration, and each method-specific CFR was derived from identical randomized locations, these biases must originate from structural differences in the ensemble of prior covariance matrices themselves. Thus, despite the GBR's low spatial degrees of freedom, these results suggest that both meridional and zonal skill patterns are discernible, even in randomized simulations. It is therefore likely that higher-resolution CFRs could help detect the colder zonal anomalies driven by regional hydrography, but even at coarse scale, systematic spatial biases were evident.

However, the randomized spatial sampling implemented in the synthetic CFR experiment differs markedly from the distribution of real coral records. According to a recently published GBR coral record database (Arzey et al., 2024), over 70% of analyzed coral records are clustered between 16° and 21°S, with only 5% coming from the northern GBR. Yet, the ESR maps show that ENSO sensitivity is strongest north of 16°S, while IOD sensitivity is strongest south of 21°S. Thus most of the existing coral network is missing the very regions where these dominant modes are best expressed. Taken together, these results suggest that producing skillful CFRs of the GBR will require

not just larger proxy networks, but strategically targeted sampling. Specifically, additional coral records are most needed in the northern and southern regions, depending on the dominant climate mode of interest.

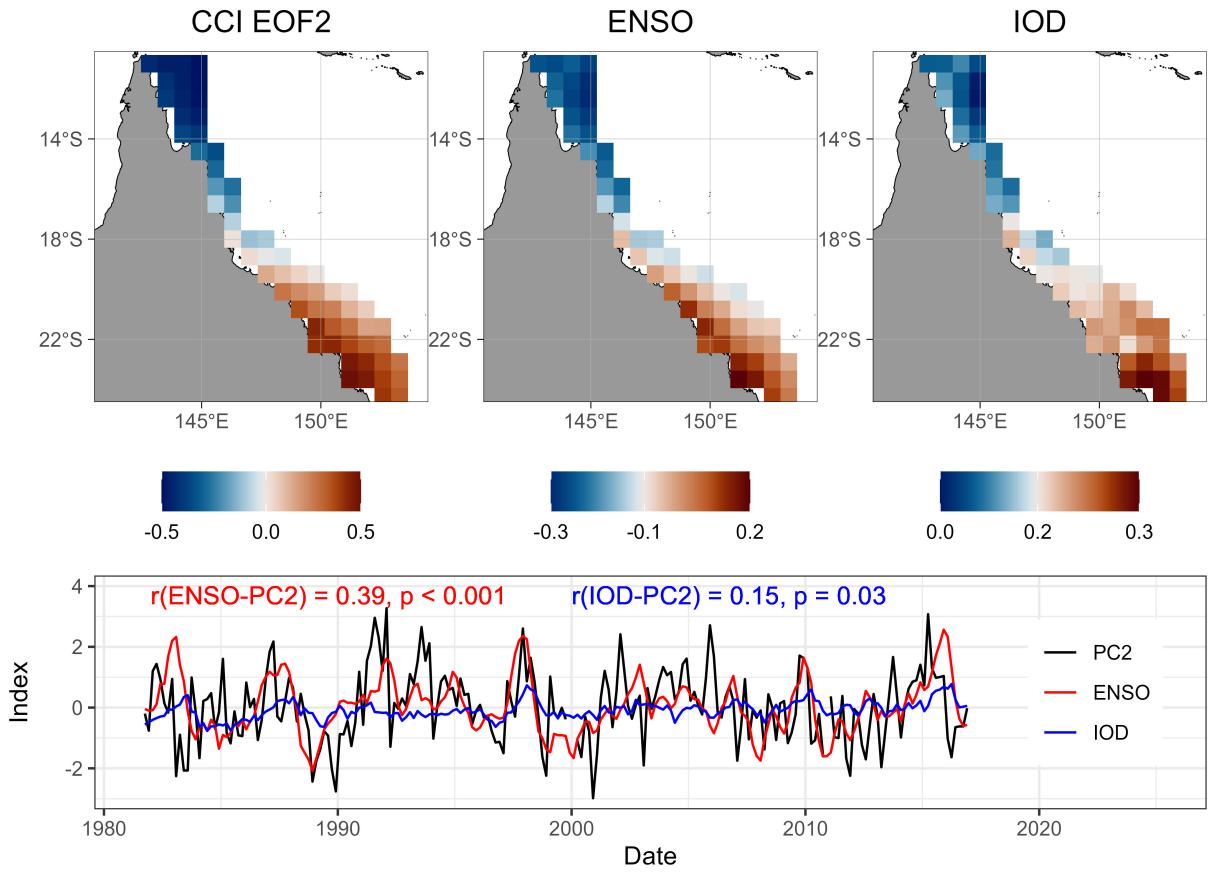

Figure 4.12: Spatial and temporal patterns of SST variability over the Great Barrier Reef (GBR) associated with the second Empirical Orthogonal Function (EOF2) of the European Space Agency Climate Change Initiative (CCI) sea surface temperature dataset (1981-2016), and its relationship to the El Niño Southern Oscillation (ENSO) and Indian Ocean Dipole (IOD). Top panels: Spatial loadings of CCI EOF2 (left), and regression maps showing the SST expression of ENSO (center) and IOD (right) over the GBR. The color scale of each map is centered on the mean value to highlight bilateral symmetry. Bottom panel: Time series of the second principal component (PC2) of CCI SST (black), Niño3.4 index for ENSO (red), and the Hadley Center's SST version 2 estimate for the IOD (Kumar et al., 2020, blue). PC2 is moderately correlated with ENSO (r = 0.39, p $<$ 0.001) and weakly but significantly correlated with the IOD (r = 0.15, p = 0.03).

Despite the clear need for expanded spatial coverage, producing new coral records, particularly from the northern and southern GBR, is logistically challenging. The Central GBR has historically been the focus of most sampling efforts, largely due to more continuous reef structures, better accessibility, and the presence of long-standing research infrastructure (Arzey et al., 2024; Lough and Barnes, 2000). In contrast, the regions with greatest interannual variability tend to have less continuous reef development, likely reflecting higher exposure to extreme events (Hughes et al., 2017). These conditions not only reduce the probability of finding suitable colonies, but also limit the growth and preservation of fast-growing corals that are ideal for subannual resolution.

Coral paleoclimate studies are typically restricted to massive, fast-growing boulder corals, especially when using solution-based methods that require sufficient amounts of sample for subannual reconstructions (e.g., D'Olivo et al., 2018). If LA-ICP-MS could reliably produce high-quality geochemical data for coral-based paleothermometry, it would significantly expand the pool of potential samples from climatically sensitive regions. However, the small sample of laser-ablated records included in this study (GBR13-15) shows that the reconstructions derived from these records still suffer from reduced skill, particularly in tracking interannual variability. This underscores the need for further methodological development if LA-ICP-MS is to play a larger role in expanding regional coverage.

Given these challenges, it becomes even more important that future efforts emphasize multiproxy geochemical datasets. As discussed earlier in this section, solution-based ICP-OES is the optimal technique for high-precision Sr/Ca measurements. However, it typically supports simultaneous analysis of only a few TE/Ca ratios (typically Mg/Ca and Ba/Ca; Olesik, 2020; Schrag, 1999). By contrast, ICP-MS allows for a broader suite of elemental ratios to be measured concurrently, enabling studies to better resolve the overlapping climatic, biological, and diagenetic signals that influence coral skeletal geochemistry (Thompson, 2021). This multiproxy approach can help diagnose and deconvolve reconstruction uncertainties, particularly in environmentally complex settings like the Galápagos Islands.

These results also highlight that different proxies and calibration methods offer distinct strengths depending on the study context. Within individual coral records, Li/Mg shows a slight but consistent advantage over SMITE and Sr/Ca in capturing interannual anomalies. In contrast, SMITE demonstrates greater reproducibility across records, making it potentially more appropriate for long-term studies or fossil coral applications. For future CFR efforts using PDA, univariate methods like Li/Mg and Sr/Ca appear to perform better with respect to spatial fidelity, though its performance under long-term, temporally unstable conditions remains an open question (see the following section for details).

Ultimately, collecting multiproxy datasets, especially from geographically targeted sites in the northern and southern GBR, will enable more flexible and robust reconstructions of regional climate variability. Importantly, these analyses can be performed on existing coral archives, reducing the ecological footprint associated with new coral core collection. Doing so will not only improve paleoclimatic insights but also support management and monitoring strategies for one of the world's most ecologically, economically, and culturally valuable marine ecosystems.

Limitations and Caveats

Despite encouraging results from the synthetic CFR experiment, particularly with respect to proxy network size, signal recoverability, and method-specific performance, it is important to acknowledge the key assumptions and limitations that shape these findings. An important limitation of the synthetic CFR experiment is its "inverse" approach to the PDA-enKF framework. In this approach, all observations and priors are treated directly in the end-

product units of SST. This contrasts with a standard PDA-enKF configuration, in which prior estimates are forward-modeled into the proxy observation space. The latter allows for more explicit treatment of proxy-specific errors, provided that reliable forward models exist. In this case, the inverse approach assumes that block-bootstrap cross-validated calibration errors are conservative enough to capture the diverse and potentially compounding processes that degrade proxy-climate relationships. As noted in Section 4.4.2, these errors are still fundamentally constrained by the short duration of the calibration period from which they were derived.

Each synthetic record in this experiment was generated using the cross-validated residuals from the GBR1-12 coral records. These records are relatively short: the longest spans approximately 13 years, and the shortest just over 4. However, the synthetic records themselves were assigned lengths based on an exponential, right-skewed distribution, ranging from 50 to 1327 months. This introduces a key structural mismatch: many of the synthetic records are much longer than the calibration data from which their error properties were drawn.

As a result, I have likely overestimated the stationarity of the proxy-climate relationship, effectively underestimating the extent of temporal regression instability that could accumulate in real long-term records. While I attempt to address this concern via the interrecord comparison (Section 4.3.1), and find method-specific patterns in stability across space and time, it remains likely that the ESR values for all methods are biased high. However, SMITE appears more robust to this kind of instability, as suggested by the distribution of autoregression coefficients from cross-validated residuals (Figure 4.8) as well as from the cross-application interrecord experiment. This implies that the signal recoverability of Sr/Ca and Li/Mg may be overestimated relative to that of SMITE in the synthetic CFR framework.

Another important limitation relates to how I define the threshold for ESR. In this framework, ESR is calculated as the ratio of effective signal variance to CFR uncertainty, approximated by RMSE squared (see Section 4.2.5 for details). This metric inherently assumes that teleconnections between SST and large-scale climate modes like ENSO and IOD are stationary along the GBR throughout the 20th century. At a minimum, it assumes that the modern calibration period (1981-2016) provides a reliable baseline for signal strength, and by extension, that signal variance has not degraded significantly in the earlier historical record.

However, it is generally thought that 20th century ENSO amplitude and variability increased after the 1960s (Cai et al., 2023; Cane, 2005; Cobb et al., 2003; D'Arrigo et al., 2006; Stevenson et al., 2019). The Niño3.4 index suggests that ENSO variance was approximately 35% lower in the early 20th century relative to the latter half. Conversely, all CMIP6 ensemble members used in this study required various degrees of variance suppression to match ORA-20C, due to large overestimations in modeled interannual variability. Despite the likelihood of a lower-amplitude ENSO in the early 20th century, there is no guarantee that this would result in different local regression slopes between SST and ENSO. Thus, I assume that the local regression slopes calculated during the calibration period of 1981-2016 are suitable for early 20th century signal detection of ENSO and, by proxy, IOD variability.

These ESR estimates also do not account for seasonal dependence in climate-proxy relationships. Grid-point ESRs were computed over the entire 20th century experimental period, effectively smoothing over seasonal dynamics. Yet prior work suggests that SST anomalies in the northern GBR are particularly responsive to Central Pacific El Niño events during the austral summer (Smith et al., 2020; Smith, 2024). As such, it is important to note that ESR, as implemented here, is a time-averaged, grid-based metric, potentially underestimating seasonally specific skill.

I previously noted that the 11 CMIP6 models used in the prior ensemble contribute to the wide uncertainty in ESR estimates for both ENSO and IOD. However, it is also likely that the CMIP6 ensemble is degrading the overall performance of the synthetic CFRs themselves. As discussed in Section 4.2.1, many CMIP6 models continue to struggle with reproducing realistic interannual tropical climate variability (Gu and Sun, 2025; Liao et al., 2021; Planton et al., 2021; Rashid et al., 2022). Because the synthetic CFR experiment is designed to target precisely this kind of variability, a prior ensemble that poorly represents these signals may reduce overall reconstruction skill, dampening ESRs and summary statistics across all network sizes. Future work should prioritize more targeted model selection, such as choosing ensemble members based on their ability to reproduce satellite-era covariance structures over the GBR. Incorporating this selection criterion will be a key focus in a forthcoming study.

As noted in Section 4.2.6, I attempted to construct a modern, observationally anchored CFR of the GBR using coral records GBR1-15. However, even under reasonable and well-justified design assumptions, the results varied too widely to be considered reliable. I attribute this to two primary limitations. First, although a grid resolution of $0.7° \times 0.7°$ yields 62 grid cells across the region, the actual spatial degrees of freedom are substantially lower due to high spatial autocorrelation in the SST field. This is evident in an EOF analysis of the CCI SST product (Figure C.14), where the first EOF alone explains 80% of the variance—highlighting the broad spatial coherence that undermines the ability to resolve finer-scale variability. Second, even when including the continuous but relatively lower-skill records of GBR13-15, the total spatiotemporal coverage of the proxy network remains extremely limited (less than 5%). Excluding those three records, that coverage drops below 2%. This is simply an insufficient dataset for producing a meaningful field reconstruction, particularly in a region with low spatial degrees of freedom.

Despite these constraints, the synthetic CFR experiment provides highly conservative skill estimates. This confidence stems from the combination of block-bootstrap cross-validation, standard error propagation in ESR, and ensemble spread within the CMIP6 priors. These features collectively bound signal recoverability estimates within a wide but defensible uncertainty envelope. As illustrated in Figure 4.9, at the final network increment ($N = 90$), uncertainty in IOD signal recoverability remains considerable across all methods. Thus, while the synthetic CFR methodology is empirical and limited by design, its strength lies in its conservatism. While the uncertainty remains large, particularly for IOD, these estimates provide a cautious but informative foundation for interpreting the spatial and temporal limits of coral-based CFRs on the GBR.

4.5 Conclusion

This study conducted a rigorous series of fidelity tests to evaluate the correlation (r), accuracy (RMSE), relative accuracy (nRMSE), and reproducibility of three coral-based paleothermometry methods: Sr/Ca, Li/Mg, and the multivariate SMITE method. Assessments were carried out across multiple temporal (seasonal vs. deseasonalized) and spatial scales, including within individual coral records (intrarecord comparisons), across multiple coral records (interrecord comparisons) from different regions, and within spatially explicit synthetic field reconstructions.

Intrarecord comparisons revealed few statistically significant differences among calibration methods, largely due to wide confidence intervals. Nonetheless, on seasonal timescales, SMITE consistently produced higher correlations and lower errors in the vast majority of comparisons. On deseasonalized datasets, SMITE continued to outperform in correlation and RMSE but performed worse than Sr/Ca and Li/Mg in terms of relative accuracy. Sr/Ca and Li/Mg yielded comparable performance to one another in this context. SMITE's poorer performance was most pronounced in the laser-ablated GBR13-15 corals, where high noise contributed to a substantial loss in SST variance. All three methods exhibited limited predictive skill when applied to the Galápagos coral datasets.

In the interrecord comparisons, SMITE generally achieved the highest correlations and the lowest RMSE and nRMSE values compared to Sr/Ca and Li/Mg. While most correlation differences were not statistically significant, SMITE often produced significant improvements in both RMSE and nRMSE. Exceptions occurred when models trained on Galápagos corals were applied to GBR datasets, where SMITE's performance declined. Additionally, GBR13-15 records often yielded inconclusive results due to high uncertainty.

In the synthetic CFR experiment, I found that with as little as $\sim$15% spatiotemporal coverage of the GBR, all methods were able to resolve substantial interannual variability associated with IOD. However, resolving ENSO-related variability required over three times as much coverage ($\sim$50%), and only for Sr/Ca and Li/Mg. Sensitivity to interannual signals was highest at the northern (ENSO) and southern (IOD) margins of the GBR, regions that remain underrepresented in current coral sampling. In contrast, SMITE exhibited notably poorer performance in detecting SST field variability associated with ENSO and IOD. Variance suppression in the reconstructed SST fields severely limited SMITE's ability to resolve interannual variability, despite its residual errors being smaller and less autocorrelated than those from either univariate method. These results, while promising for univariate methods like Sr/Ca and Li/Mg, are accompanied by large confidence intervals and important caveats. As such, they should be interpreted with caution given the empirical nature of this approach.

Taken together, these results highlight the strengths and limitations of each SST reconstruction method depending on the specific research objective. For individual coral records aimed at capturing interannual variability, where detecting anomalies is more important than preserving absolute SST variance, univariate methods such as Sr/Ca and Li/Mg are well-suited. These approaches tend to outperform the multivariate SMITE method in high-noise

calibrations, where SMITE's performance is hindered by variance suppression. In contrast, for fossil applications that require applying model parameters trained on different corals, SMITE demonstrates greater reproducibility in regression coefficients, particularly in terms of accuracy and relative accuracy. This suggests that SMITE calibrations may be more stable down-core, making them potentially better suited for long-term reconstructions that span multiple decades or more. For future CFRs using a paleoclimate data assimilation framework, univariate methods like Sr/Ca and Li/Mg perform robustly. They produce strong summary statistics and are effective at spatially resolving interannual variability on the GBR, particularly signals associated with IOD and, with sufficient data coverage, ENSO.

Based on these findings, I recommend that future coral paleothermometry efforts prioritize sampling in the northern and southern GBR, where sensitivity to ENSO and IOD is highest but existing records are sparse. I also encourage the collection of multiproxy datasets, which offer greater flexibility for addressing a broad range of research questions and support the continued development of multivariate approaches that can disentangle climatological, chemical, and biological signals preserved in coral skeletons. Altogether, these results offer a framework for selecting and applying coral-based SST reconstruction methods, emphasizing the importance of aligning calibration strategies with the spatial scale, temporal resolution, and climate targets of interest.

4.6 AI Acknowledgment Statement

This chapter benefited from the use of OpenAI's ChatGPT to assist with writing refinement, code debugging, and figure generation. All critical analyses, interpretation, and research design were performed by the author. AI-generated contributions were used with a commitment to ethical integrity and research transparency.

BIBLIOGRAPHY

N. Allison and A. A. Finch. Reproducibility of minor and trace element determinations in porites coral skeletons by secondary ion mass spectrometry. *Geochem. Geophys. Geosyst.*, 10(4), 2009. ISSN 1525-2027. doi: 10.1029/2008GC002239.

A. K. Arzey, H. V. McGregor, T. R. Clark, J. M. Webster, S. E. Lewis, J. Mallela, N. P. McKay, H. W. Fahey, S. Chakraborty, T. B. Razak, and M. J. Fischer. Coral skeletal proxy records database for the great barrier reef, australia. *Earth Syst. Sci. Data*, 16(10):4869–4930, 2024. ISSN 1866-3516. doi: 10.5194/essd-16-4869-2024.

V. Banzon, T. M. Smith, T. M. Chin, C. Liu, and W. Hankins. A long-term record of blended satellite and in situ sea-surface temperature for climate monitoring, modeling and environmental studies. *Earth Syst. Sci. Data*, 8(1): 165–176, 2016. ISSN 1866-3516. doi: 10.5194/essd-8-165-2016.

Y. Bao, Z. Song, and F. Qiao. Fio-esm version 2.0: Model description and evaluation. *J. Geophys. Res-Oceans*, 125 (6):e2019JC016036, 2020. ISSN 2169-9275. doi: 10.1029/2019JC016036.

J. Beck, R. L. Edwards, E. Ito, F. W. Taylor, J. Recy, F. Rougerie, P. Joannot, and C. Henin. Sea-surface temperature from coral skeletal strontium/calcium ratios. *Science*, 257:644–647, 1992. doi: 10.1126/science.257.5070.644.

D. Bi, M. Dix, S. Marsland, S. O'Farrell, A. Sullivan, R. Bodman, R. Law, I. Harman, J. Srbinovsky, H. A. Rashid, P. Dobrohotoff, C. Mackallah, H. Yan, A. Hirst, A. Savita, F. B. Dias, M. Woodhouse, R. Fiedler, and A. Heerdegen. Configuration and spin-up of access-cm2, the new generation australian community climate and earth system simulator coupled model. *J. Southern Hem. Earth Sys. Sci.*, 70(1):225–251, 2020. doi: 10.1071/ES19040.

O. Boucher, J. Servonnat, A. L. Albright, O. Aumont, Y. Balkanski, V. Bastrikov, S. Bekki, R. Bonnet, S. Bony, L. Bopp, P. Braconnot, P. Brockmann, P. Cadule, A. Caubel, F. Cheruy, F. Codron, A. Cozic, D. Cugnet, F. D'Andrea, P. Davini, C. de Lavergne, S. Denvil, J. Deshayes, M. Devilliers, A. Ducharne, J.-L. Dufresne, E. Dupont, C. Éthé, L. Fairhead, L. Falletti, S. Flavoni, M.-A. Foujols, S. Gardoll, G. Gastineau, J. Ghattas, J.-Y. Grandpeix, B. Guenet, E. Guez, Lionel, E. Guilyardi, M. Guimberteau, D. Hauglustaine, F. Hourdin, A. Idelkadi, S. Joussaume, M. Kageyama, M. Khodri, G. Krinner, N. Lebas, G. Levavasseur, C. Lévy, L. Li, F. Lott, T. Lurton, S. Luyssaert, G. Madec, J.-B. Madeleine, F. Maignan, M. Marchand, O. Marti, L. Mellul, Y. Meurdesoif, J. Mignot, I. Musat, C. Ottlé, P. Peylin, Y. Planton, J. Polcher, C. Rio, N. Rochetin, C. Rousset, P. Sepulchre, A. Sima, D. Swingedouw, R. Thiéblemont, A. K. Traore, M. Vancoppenolle, J. Vial, J. Vialard, N. Viovy, and N. Vuichard. Presentation and evaluation of the ipsl-cm6a-lr climate model. *J. Adv. Model. Earth. Syst.*, 12(7): e2019MS002010, 2020. doi: 10.1029/2019MS002010.

W. Cai, B. Ng, T. Geng, F. Jia, L. Wu, G. Wang, Y. Liu, B. Gan, K. Yang, A. Santoso, X. Lin, Z. Li, Y. Liu, Y. Yang, F.-F. Jin, M. Collins, and M. J. McPhaden. Anthropogenic impacts on twentieth-century enso variability changes. *Nat. Rev. Earth Environ.*, 4(6):407–418, 2023. ISSN 2662-138X. doi: 10.1038/s43017-023-00427-8.

M. A. Cane. The evolution of el niño, past and future. *Earth Planet. Sc. Lett.*, 230(3):227–240, 2005. ISSN 0012-821X. doi: 10.1016/j.epsl.2004.12.003.

M. Canesi, E. Douville, P. Montagna, L. Bordier, S. Caquineau, E. Pons-Branchu, G. Iwankow, J. Stolarski, D. Allemand, S. Planes, C. Moulin, F. Lombard, G. Bourdin, R. Troublé, S. Agostini, B. Banaigs, E. Boissin, E. Boss, C. Bowler, C. de Vargas, J. M. Flores, D. Forcioli, P. Furla, E. Gilson, P. E. Galand, S. Pesant, S. Sunagawa, O. P. Thomas, R. V. Thurber, C. R. Voolstra, P. Wincker, D. Zoccola, and S. Reynaud. Sea surface temperature reconstruction in the pacific ocean using multi-elemental proxy in porites and diploastrea corals: Application to palau archipelago. *Chem. Geol.*, 645:121884, 2024. ISSN 0009-2541. doi: 10.1016/j.chemgeo.2023.121884.

J. Cao, B. Wang, Y. M. Yang, L. Ma, J. Li, B. Sun, Y. Bao, J. He, X. Zhou, and L. Wu. The nuist earth system model (nesm) version 3: description and preliminary evaluation. *Geosci. Model Dev.*, 11(7):2975–2993, 2018. ISSN 1991-9603. doi: 10.5194/gmd-11-2975-2018. GMD.

D. Chan. Combining statistical, physical, and historical evidence to improve historical sea surface temperature records. *Harvard Data Science Review*, 3(1), 2021. doi: 10.1162/99608f92.edcee38f.

D. Chan and P. Huybers. Correcting observational biases in sea surface temperature observations removes anomalous warmth during world war ii. *J. Clim.*, 34(11):4585–4602, 2021. ISSN 0894-8755. doi: 10.1175/JCLI-D-20-0907.1.

X. Chen, J. P. D'Olivo, G. Wei, and M. McCulloch. Anthropogenic ocean warming and acidification recorded by sr/ca, li/mg, 11b and b/ca in porites coral from the kimberley region of northwestern australia. *Palaeogeogr. Palaeocl.*, 528:50–59, 2019. doi: 10.1016/j.palaeo.2019.04.033.

K. M. Cobb, C. D. Charles, H. Cheng, and R. L. Edwards. El niño/southern oscillation and tropical pacific climate during the last millennium. *Nature*, 424:271, 2003. doi: 10.1038/nature01779.

M. Comboul, J. Emile-Geay, G. J. Hakim, and M. N. Evans. Paleoclimate sampling as a sensor placement problem. *J. Clim.*, 28(19):7717–7740, 2015. ISSN 0894-8755. doi: 10.1175/JCLI-D-14-00802.1.

E. R. Cook, K. R. Briffa, and P. D. Jones. Spatial regression methods in dendroclimatology: A review and comparison of two techniques. *Int. J. Climatol.*, 14(4):379–402, 1994. ISSN 0899-8418. doi: 10.1002/joc.3370140404. Defines coefficient of efficiency (CE) and reduction of error (RE).

E. R. Cook, D. M. Meko, D. W. Stahle, and M. K. Cleaveland. Drought reconstructions for the continental united states. *J. Clim.*, 12(4):1145–1162, 1999. ISSN 0894-8755. doi: 10.1175/1520-0442(1999)012⟨1145:DRFTCU⟩2.0.CO;2.

T. Corrège. Sea surface temperature and salinity reconstruction from coral geochemical tracers. *Palaeogeogr. Palaeoclimatol. Palaeoecol.*, 232:408–428, 2006. ISSN 0031-0182. doi: 10.1016/j.palaeo.2005.10.014. - Main takeaway: - FARM FOR REFERENCES! THIS MOTHER FUCKER HAS EVERYTHING -REF: Corals can live up to 1000 years - Highlights need for tropical Atlantic reconstructions.

K. Cuny-Guirriec, E. Douville, S. Reynaud, D. Allemand, L. Bordier, M. Canesi, C. Mazzoli, M. Taviani, S. Canese, and M. McCulloch. Coral li/mg thermometry: Caveats and constraints. *Chem. Geol.*, 523:162–178, 2019. doi: 10.1016/j.chemgeo.2019.03.038.

R. D'Arrigo, R. Wilson, J. Palmer, P. Krusic, A. Curtis, J. Sakulich, S. Bijaksana, S. Zulaikah, L. O. Ngkoimani, and A. Tudhope. The reconstructed indonesian warm pool sea surface temperatures from tree rings and corals: Linkages to asian monsoon drought and el niño–southern oscillation. *Paleoceanography*, 21(3), 2006. ISSN 0883-8305. doi: 10.1029/2005PA001256.

L. L. B. Davis, D. W. J. Thompson, J. J. Kennedy, and E. C. Kent. The importance of unresolved biases in twentieth-century sea surface temperature observations. *Bull. Amer. Meteor. Soc.*, 100(4):621–629, 2019. ISSN 0003-0007. doi: 10.1175/BAMS-D-18-0104.1.

E. de Boisséson, M. A. Balmaseda, and M. Mayer. Ocean heat content variability in an ensemble of twentieth century ocean reanalyses. *Clim. Dynam.*, 50(9):3783–3798, 2018. ISSN 1432-0894. doi: 10.1007/s00382-017-3845-0.

S. de Villiers, G. T. Shen, and B. K. Nelson. The sr/ca-temperature relationship in coralline aragonite: Influence of variability in (sr/ca) seawater and skeletal growth parameters. *Geochim. Cosmochim. Acta*, 58:197–208, 1994. doi: 10.1016/0016-7037(94)90457-X.

T. M. DeCarlo, G. A. Gaetani, A. L. Cohen, G. L. Foster, A. E. Alpert, and J. A. Stewart. Coral sr-u thermometry. *Paleoceanogr. Paleoclimatol.*, 31:626–638, 2016. doi: 10.1002/2015PA002908.

K. L. DeLong, T. M. Quinn, C. Shen, and K. Lin. A snapshot of climate variability at tahiti at 9.5 ka using a fossil coral from iodp expedition 310. *Geochem. Geophys. Geosyst.*, 11:Q06005, 2010. ISSN 1525-2027. doi: 10.1029/2009GC002758.

K. L. DeLong, J. A. Flannery, C. R. Maupin, R. Z. Poore, and T. M. Quinn. A coral sr/ca calibration and replication study of two massive corals from the gulf of mexico. *Palaeogeogr. Palaeoclimatol. Palaeoecol.*, 307:117–128, 2011. doi: 10.1016/j.palaeo.2011.05.005. Cailbration study shows that SidSids are great for intra and inter colony replication. Buoys are better than satellite data for temperature calibration in the Dry Tortugas.

K. L. DeLong, T. M. Quinn, F. W. Taylor, C. C. Shen, and K. Lin. Improving coral-base paleoclimate reconstructions by replicating 350 years of coral sr/ca variations. *Palaeogeogr. Palaeoclimatol. Palaeoecol.*, 373:6–24, 2013. ISSN 0031-0182. doi: 10.1016/j.palaeo.2012.08.019. -Two cores from the same coral -Straightforwardness of reproducing temp with Sr/Ca -Problems of skeletal architecture when sampling Porites - creates bias of (+/-) 2K.

K. L. DeLong, J. A. Flannery, R. Z. Poore, T. M. Quinn, C. R. Maupin, K. Lin, and C. Shen. A reconstruction of sea surface temperature variability in the southeastern gulf of mexico from 1734 to 2008 ce using cross-dated sr/ca records from the coral siderastrea siderea. *Paleoceanogr. Paleoclimatol.*, 29:403–422, 2014. doi: 10.1002/2013PA002524.

K. L. DeLong, C. R. Maupin, J. A. Flannery, T. M. Quinn, and C.-C. Shen. Refining temperature reconstructions with the atlantic coral siderastrea siderea. *Palaeogeogr. Palaeoclimatol. Palaeoecol.*, 462:1–15, 2016. doi: 10.1016/j.palaeo.2016.08.028.

J. P. D'Olivo, D. J. Sinclair, K. Rankenburg, and M. T. McCulloch. A universal multi-trace element calibration for reconstructing sea surface temperatures from long-lived porites corals: Removing 'vital-effects'. *Geochim. Cosmochim. Acta*, 239:109–135, 2018. doi: 10.1016/j.gca.2018.07.035.

R. Döscher, M. Acosta, A. Alessandri, P. Anthoni, T. Arsouze, T. Bergman, R. Bernardello, S. Boussetta, L. P. Caron, G. Carver, M. Castrillo, F. Catalano, I. Cvijanovic, P. Davini, E. Dekker, F. J. Doblas-Reyes, D. Docquier, P. Echevarria, U. Fladrich, R. Fuentes-Franco, M. Gröger, J. v. Hardenberg, J. Hieronymus, M. P. Karami, J. P. Keskinen, T. Koenigk, R. Makkonen, F. Massonnet, M. Ménégoz, P. A. Miller, E. Moreno-Chamarro, L. Nieradzik, T. van Noije, P. Nolan, D. O'Donnell, P. Ollinaho, G. van den Oord, P. Ortega, O. T. Prims, A. Ramos, T. Reerink, C. Rousset, Y. Ruprich-Robert, P. Le Sager, T. Schmith, R. Schrödner, F. Serva, V. Sicardi, M. Sloth Madsen, B. Smith, T. Tian, E. Tourigny, P. Uotila, M. Vancoppenolle, S. Wang, D. Wårlind, U. Willén, K. Wyser, S. Yang, X. Yepes-Arbós, and Q. Zhang. The ec-earth3 earth system model for the coupled model intercomparison project 6. *Geosci. Model Dev.*, 15(7):2973–3020, 2022. ISSN 1991-9603. doi: 10.5194/gmd-15-2973-2022. GMD.

J. P. D'Olivo and M. T. McCulloch. Response of coral calcification and calcifying fluid composition to thermally induced bleaching stress. *Scientific reports*, 7:2207, 2017. doi: 10.1038/s41598-017-02306-x.

J. Emile-Geay, K. M. Cobb, M. E. Mann, and A. T. Wittenberg. Estimating central equatorial pacific sst variability over the past millennium. part ii: Reconstructions and implications. *J. Clim.*, 26(7):2329–2352, 2013. ISSN 0894-8755. doi: 10.1175/JCLI-D-11-00511.1.

M. N. Evans, A. Kaplan, and M. A. Cane. Intercomparison of coral oxygen isotope data and historical sea surface temperature (sst): Potential for coral-based sst field reconstructions. *Paleoceanography*, 15(5):551–563, 2000. ISSN 0883-8305. doi: 10.1029/2000PA000498.

M. N. Evans, A. Kaplan, and M. A. Cane. Pacific sea surface temperature field reconstruction from coral 18o data using reduced space objective analysis. *Paleoceanography*, 17:1–7, 2002. doi: 10.1029/2000PA000590.

J. A. Flannery, J. N. Richey, K. Thirumalai, R. Z. Poore, and K. L. DeLong. Multi-species coral sr/ca-based sea-surface temperature reconstruction using orbicella faveolata and siderastrea siderea from the florida straits. *Palaeogeogr. Palaeoclimatol. Palaeoecol.*, 466:100–109, 2017. doi: 10.1016/j.palaeo.2016.10.022.

M. Foote. Rarefaction analysis of morphological and taxonomic diversity. *Paleobiology*, 18(1):1–16, 1992. ISSN 0094-8373. doi: 10.1017/S0094837300012185.

M. K. Gagan, G. B. Dunbar, and A. Suzuki. The effect of skeletal mass accumulation in porites on coral sr/ca and 18o paleothermometry. *Paleoceanography*, 27, 2012. doi: 10.1029/2011PA002215.

N. F. Goodkin, K. A. Hughen, and A. L. Cohen. A multicoral calibration method to approximate a universal equation relating sr/ca and growth rate to sea surface temperature. *Paleoceanography*, 22, 2007. doi: 10.1029/2006PA001312.

P. R. Grothe, K. M. Cobb, G. Liguori, E. Di Lorenzo, A. Capotondi, Y. Lu, H. Cheng, R. L. Edwards, J. R. Southon, G. M. Santos, D. M. Deocampo, J. Lynch-Stieglitz, T. Chen, H. R. Sayani, D. M. Thompson, J. L. Conroy, A. L. Moore, K. Townsend, M. Hagos, G. O'Connor, and L. T. Toth. Enhanced el niño–southern oscillation

variability in recent decades. *Geophys. Res. Lett.*, 47(7):e2019GL083906, 2020. ISSN 0094-8276. doi: 10.1029/2019GL083906.

Z. Gu and D.-Z. Sun. El niño magnitude and western pacific warm pool displacement. part i: Historical insights from cmip6 models. *Atmosphere*, 16(6):680, 2025. ISSN 2073-4433.

G. J. Hakim, J. Emile-Geay, E. J. Steig, D. Noone, D. M. Anderson, R. Tardif, N. Steiger, and W. A. Perkins. The last millennium climate reanalysis project: Framework and first results. *J. Geophys. Res-Atmospheres*, 121:6745–6764, 2016. doi: 10.1002/2016JD024751.

J. C. Hargreaves and J. D. Annan. On the importance of paleoclimate modelling for improving predictions of future climate change. *Clim. Past*, 5(4):803–814, 2009. ISSN 1814-9332. doi: 10.5194/cp-5-803-2009. CP.

S. Hastenrath. *Climate dynamics of the tropics*, volume 8. Springer Science Business Media, 2012. ISBN 9401131562.

E. C. Hathorne, A. Gagnon, T. Felis, J. Adkins, R. Asami, W. Boer, N. Caillon, D. Case, K. M. Cobb, E. Douville, P. DeMenocal, A. Eisenhauer, D. Garbe-Schönberg, W. Geibert, S. Goldstein, K. Hughen, M. Inoue, H. Kawahata, M. Kölling, F. L. Cornec, B. K. Linsley, H. V. McGregor, P. Montagna, I. S. Nurhati, T. M. Quinn, J. Raddatz, H. Rebaubier, L. Robinson, A. Sadekov, R. Sherrell, D. Sinclair, A. W. Tudhope, G. Wei, H. Wong, H. C. Wu, and C.-F. You. Interlaboratory study for coral sr/ca and other element/ca ratio measurements. *Geochem. Geophys. Geosyst.*, 14:3730–3750, 2013. doi: 10.1002/ggge.20230.

S. F. Heron, G. Liu, C. M. Eakin, W. J. Skirving, F. E. Muller-Karger, M. Vega-Rodriguez, J. L. De La Cour, T. F. R. Burgess, A. E. Strong, E. F. Geiger, L. S. Guild, and S. Lynds. Climatology development for noaa coral reef watch's 5-km product suite. Technical report, NOAA, 2014. (U.S.) (Carlon Mark) (William John) (Alan Earl).

T. O. Hodson. Root-mean-square error (rmse) or mean absolute error (mae): when to use them or not. *Geosci. Model Dev.*, 15(14):5481–5487, 2022. ISSN 1991-9603. doi: 10.5194/gmd-15-5481-2022. GMD.

Y. Hu, H. Beggs, and X. H. Wang. Intercomparison of high-resolution sst climatologies over the australian region. *J. Geophys. Res-Oceans*, 126(12):e2021JC017221, 2021. ISSN 2169-9275. doi: 10.1029/2021JC017221.

H. P. Hughes, D. Thompson, G. L. Foster, J. Lees, D. Surge, and C. D. Standish. Synthetic and practical reconstructions of sst and seawater ph using the novel multiproxy smite method. *PLoS ONE*, 19(6):e0305607, 2024. doi: 10.1371/journal.pone.0305607.

T. P. Hughes, J. T. Kerry, M. Álvarez Noriega, J. G. Álvarez Romero, K. D. Anderson, A. H. Baird, R. C. Babcock, M. Beger, D. R. Bellwood, R. Berkelmans, T. C. Bridge, I. R. Butler, M. Byrne, N. E. Cantin, S. Comeau, S. R. Connolly, G. S. Cumming, S. J. Dalton, G. Diaz-Pulido, C. M. Eakin, W. F. Figueira, J. P. Gilmour, H. B. Harrison, S. F. Heron, A. S. Hoey, J.-P. A. Hobbs, M. O. Hoogenboom, E. V. Kennedy, C.-y. Kuo, J. M. Lough, R. J. Lowe, G. Liu, M. T. McCulloch, H. A. Malcolm, M. J. McWilliam, J. M. Pandolfi, R. J. Pears, M. S. Pratchett, V. Schoepf, T. Simpson, W. J. Skirving, B. Sommer, G. Torda, D. R. Wachenfeld, B. L. Willis, and S. K. Wilson. Global warming and recurrent mass bleaching of corals. *Nature*, 543(7645):373–377, 2017. ISSN 1476-4687. doi: 10.1038/nature21707.

C. Karamperidou. Extracting paleoweather from paleoclimate through a deep learning reconstruction of last millennium atmospheric blocking. *Commun. Earth Environ.*, 5(1):535, 2024. ISSN 2662-4435. doi: 10.1038/s43247-024-01687-y.

J. J. Kennedy, N. A. Rayner, R. O. Smith, D. E. Parker, and M. Saunby. Reassessing biases and other uncertainties in sea surface temperature observations measured in situ since 1850: 2. biases and homogenization. *J. Geophys. Res.*, 116:D14104, 2011. doi: 10.1029/2010JD015220.

A. D. King, A. J. Pitman, B. J. Henley, A. M. Ukkola, and J. R. Brown. The role of climate variability in australian drought. *Nat. Clim. Change*, 10(3):177–179, 2020. ISSN 1758-6798. doi: 10.1038/s41558-020-0718-z.

D. J. Kinsman and H. Holland. The co-precipitation of cations with caco3 – iv. the co-precipitation of sr2+ with aragonite between 16 and 96 c. *Geochim. Cosmochim. Acta*, 33:1–17, 1969. doi: 10.1016/0016-7037(69)90089-1. Calcite contains less Sr than aragonite "The solid-solution distribution coefficient for Sr in calcite is much lower than in aragonite." Constant Sr/Ca of seawater first developed K(T) = (Sr/Ca)aragonite (Sr/Ca)seawater.

I. B. Kuffner, P. L. Jokiel, K. S. Rodgers, A. J. Andersson, and F. T. Mackenzie. An apparent "vital effect" of calcification rate on the sr/ca temperature proxy in the reef coral montipora capitata. *Geochem. Geophys. Geosyst.*, 13: Q08004, 2012. doi: 10.1029/2012GC004128.

P. Kumar, B. Hamlington, S.-H. Cheon, W. Han, and P. Thompson. 20th century multivariate indian ocean regional sea level reconstruction. *J. Geophys. Res-Oceans*, 125(10):e2020JC016270, 2020. ISSN 2169-9275. doi: 10.1029/2020JC016270.

H. Liao, C. Wang, and Z. Song. Enso phase-locking biases from the cmip5 to cmip6 models and a possible explanation. *Deep Sea Research Part II: Topical Studies in Oceanography*, 189-190:104943, 2021. ISSN 0967-0645. doi: 10.1016/j.dsr2.2021.104943.

N. G. Loeb, J. M. Lyman, G. C. Johnson, R. P. Allan, D. R. Doelling, T. Wong, B. J. Soden, and G. L. Stephens. Observed changes in top-of-the-atmosphere radiation and upper-ocean heating consistent within uncertainty. *Nat. Geosci.*, 5(2):110–113, 2012. ISSN 1752-0908. doi: 10.1038/ngeo1375.

J. Lough. *Climate and climate change on the Great Barrier Reef*, book section 2. The Great Barrier Reef Marine Park Authority, 2007. ISBN 9781876945619.

J. M. Lough. Variations of sea-surface temperatures off north-eastern australia and associations with rainfall in queensland: 1956–1987. *Int. J. Climatol.*, 12(8):765–782, 1992. ISSN 0899-8418. doi: 10.1002/joc.3370120802.

J. M. Lough. Climate records from corals. *WIRES. Clim. Change*, 1:318–331, 2010. doi: 10.1002/wcc.39.

J. M. Lough and D. J. Barnes. Environmental controls on growth of the massive coral porites. *J. Exp. Mar. Biol. Ecol.*, 245(2):225–243, 2000. ISSN 0022-0981. doi: 10.1016/S0022-0981(99)00168-9.

G. Madec. Nemo ocean engine. Report, Institut Pierre-Simon Laplace (IPSL), 2008.

M. E. Mann, R. S. Bradley, and M. K. Hughes. Global-scale temperature patterns and climate forcing over the past six centuries. *Nature*, 392:779, 1998. doi: 10.1038/33859.

M. E. Mann, R. S. Bradley, and M. K. Hughes. Northern hemisphere temperatures during the past millennium: Inferences, uncertainties, and limitations. *Geophys. Res. Lett.*, 26:759–762, 1999. doi: 10.1029/1999GL900070.

D. Maraun. Bias correcting climate change simulations - a critical review. *Current Climate Change Reports*, 2(4): 211–220, 2016. ISSN 2198-6061. doi: 10.1007/s40641-016-0050-x.

G. Margaritis, E. C. Kent, and G. L. Foster. Intercomparison of satellite-derived sst with logger data in the caribbean—implications for coral reef monitoring. *PLOS Climate*, 4(1):e0000480, 2025. doi: 10.1371/journal.pclm.0000480.

M. Y. McPartland, T. Münch, A. M. Dolman, R. Hébert, and T. Laepple. The colors of proxy noise. *Clim. Past Discuss.*, 2024:1–20, 2024. ISSN 1814-9359. doi: 10.5194/cp-2024-73. CPD.

C. J. Merchant, O. Embury, C. E. Bulgin, T. Block, G. K. Corlett, E. Fiedler, S. A. Good, J. Mittaz, N. A. Rayner, D. Berry, S. Eastwood, M. Taylor, Y. Tsushima, A. Waterfall, R. Wilson, and C. Donlon. Satellite-based time-series of sea-surface temperature since 1981 for climate applications. *Scientific Data*, 6(1):223, 2019. ISSN 2052-4463. doi: 10.1038/s41597-019-0236-x.

P. Montagna, M. McCulloch, E. Douville, M. L. Correa, J. Trotter, R. Rodolfo-Metalpa, D. Dissard, C. Ferrier-Pages, N. Frank, and A. Freiwald. Li/mg systematics in scleractinian corals: Calibration of the thermometer. *Geochim. Cosmochim. Acta*, 132:288–310, 2014. doi: 10.1016/j.gca.2014.02.005.

E. Moore. On the reciprocal of the general algebraic matrix. *Bull. Amer. Math. Soc.*, 26:394–395, 1920.

N. K. Murray, A. R. Muñoz, and J. L. Conroy. Machine learning solutions to regional surface ocean 18o-salinity relationships for paleoclimatic reconstruction. *Paleoceanogr. Paleoclimatol.*, 38(9):e2023PA004612, 2023. doi: 10.1029/2023PA004612.

W. A. Müller, J. H. Jungclaus, T. Mauritsen, J. Baehr, M. Bittner, R. Budich, F. Bunzel, M. Esch, R. Ghosh, H. Haak, T. Ilyina, T. Kleine, L. Kornblueh, H. Li, K. Modali, D. Notz, H. Pohlmann, E. Roeckner, I. Stemmler, F. Tian, and J. Marotzke. A higher-resolution version of the max planck institute earth system model (mpi-esm1.2-hr). *J. Adv. Model. Earth. Syst.*, 10(7):1383–1413, 2018. doi: 10.1029/2017MS001217.

J. Olesik. Icp-oes capabilities, developments, limitations, and any potential challengers? *Spectroscopy*, 2020.

R. J. O'Loughlin, D. Li, R. Neale, and T. A. O'Brien. Moving beyond post hoc explainable artificial intelligence: a perspective paper on lessons learned from dynamical climate modeling. *Geosci. Model Dev.*, 18(3):787–802, 2025. ISSN 1991-9603. doi: 10.5194/gmd-18-787-2025. GMD.

R. Penrose. A generalized inverse for matrices. *Proc. Cambridge Phil. Soc.*, 51:406–413, 1955.

Y. Y. Planton, E. Guilyardi, A. T. Wittenberg, J. Lee, P. J. Gleckler, T. Bayr, S. McGregor, M. J. McPhaden, S. Power, R. Roehrig, J. Vialard, and A. Voldoire. Evaluating climate models with the clivar 2020 enso metrics package. *Bull. Amer. Meteor. Soc.*, 102(2):E193–E217, 2021. ISSN 0003-0007. doi: 10.1175/BAMS-D-19-0337.1.

D. N. Politis, , and H. White. Automatic block-length selection for the dependent bootstrap. *Econometric Reviews*, 23(1):53–70, 2004. ISSN 0747-4938. doi: 10.1081/ETC-120028836.

S. Power, T. Casey, C. Folland, A. Colman, and V. Mehta. Inter-decadal modulation of the impact of enso on australia. *Clim. Dynam.*, 15(5):319–324, 1999. ISSN 1432-0894. doi: 10.1007/s003820050284.

H. A. Rashid, A. Sullivan, M. Dix, D. Bi, C. Mackallah, T. Ziehn, P. Dobrohotoff, S. O'Farrell, I. N. Harman, R. Bodman, and S. Marsland. Evaluation of climate variability and change in access historical simulations for cmip6. *J. Southern Hem. Earth Sys. Sci.*, 72(2):73–92, 2022. doi: 10.1071/ES21028.

D. M. Raup. Taxonomic diversity estimation using rarefaction. *Paleobiology*, 1(4):333–342, 1975. ISSN 0094-8373. doi: 10.1017/S0094837300002633.

A. Redondo-Rodriguez, S. J. Weeks, R. Berkelmans, O. Hoegh-Guldberg, and J. M. Lough. Climate variability of the great barrier reef in relation to the tropical pacific and el niño-southern oscillation. *Mar. Freshwater Res.*, 63 (1):34–47, 2012. doi: 10.1071/MF11151.

R. W. Reynolds, T. M. Smith, C. Liu, D. B. Chelton, K. S. Casey, and M. G. Schlax. Daily high-resolution-blended analyses for sea surface temperature. *J. Clim.*, 20(22):5473–5496, 2007. ISSN 0894-8755. doi: 10.1175/2007JCLI1824.1.

K. R. Ridgway, J. A. Benthuysen, and C. Steinberg. Closing the gap between the coral sea and the equator: Direct observations of the north australian western boundary currents. *J. Geophys. Res-Oceans*, 123(12):9212–9231, 2018. ISSN 2169-9275. doi: 10.1029/2018JC014269.

W. T. Rogers and K. D. Hopkins. Power estimates in the presence of a covariate and measurement error. *Educ. Psychol. Meas.*, 48(3):647–656, 1988. doi: 10.1177/0013164488483008.

S. Rutherford, M. E. Mann, T. J. Osborn, K. R. Briffa, P. D. Jones, R. S. Bradley, and M. K. Hughes. Proxy-based northern hemisphere surface temperature reconstructions: Sensitivity to method, predictor network, target season, and target domain. *J. Clim.*, 18:2308–2329, 2005. doi: 10.1175/JCLI3351.1.

J. Sadler, G. E. Webb, L. D. Nothdurft, and B. Dechnik. Geochemistry-based coral palaeoclimate studies and the potential of 'non-traditional' (non-massive porites) corals: Recent developments and future progression. *Earth-Sci. Rev.*, 139:291–316, 2014. ISSN 0012-8252. doi: 10.1016/j.earscirev.2014.10.002. Unread.

S. C. Sanchez, N. Westphal, G. H. Haug, H. Cheng, R. L. Edwards, T. Schneider, K. M. Cobb, and C. D. Charles. A continuous record of central tropical pacific climate since the midnineteenth century reconstructed from fanning and palmyra island corals: A case study in coral data reanalysis. *Paleoceanogr. Paleoclimatol.*, 35(8): e2020PA003848, 2020. ISSN 2572-4517. doi: 10.1029/2020PA003848.

H. R. Sayani, K. M. Cobb, K. DeLong, N. T. Hitt, and E. R. M. Druffel. Intercolony 18o and sr/ca variability among porites spp. corals at palmyra atoll: Toward more robust coral-based estimates of climate. *Geochem. Geophys. Geosyst.*, 20(11):5270–5284, 2019. ISSN 1525-2027. doi: 10.1029/2019GC008420.

G. A. Schmidt, J. D. Annan, P. J. Bartlein, B. I. Cook, Guilyardi, J. C. Hargreaves, S. P. Harrison, M. Kageyama, A. N. LeGrande, and B. Konecky. Using palaeo-climate comparisons to constrain future projections in cmip5. *Clim. Past*, 10:221–250, 2013. doi: 10.5194/cp-10-221-2014.

D. P. Schrag. Rapid analysis of high-precision sr/ca ratios in corals and other marine carbonates. *Paleoceanography*, 14:97–102, 1999. doi: 10.1029/1998PA900025.

Seland, M. Bentsen, D. Olivié, T. Toniazzo, A. Gjermundsen, L. S. Graff, J. B. Debernard, A. K. Gupta, Y. C. He, A. Kirkevåg, J. Schwinger, J. Tjiputra, K. S. Aas, I. Bethke, Y. Fan, J. Griesfeller, A. Grini, C. Guo, M. Ilicak, I. H. H. Karset, O. Landgren, J. Liakka, K. O. Moseid, A. Nummelin, C. Spensberger, H. Tang, Z. Zhang, C. Heinze, T. Iversen, and M. Schulz. Overview of the norwegian earth system model (noresm2) and key climate response of cmip6 deck, historical, and scenario simulations. *Geosci. Model Dev.*, 13(12):6165–6200, 2020. ISSN 1991-9603. doi: 10.5194/gmd-13-6165-2020. GMD.

T. Semmler, S. Danilov, P. Gierz, H. F. Goessling, J. Hegewald, C. Hinrichs, N. Koldunov, N. Khosravi, L. Mu, T. Rackow, D. V. Sein, D. Sidorenko, Q. Wang, and T. Jung. Simulations for cmip6 with the awi climate model awi-cm-1-1. *J. Adv. Model. Earth. Syst.*, 12(9):e2019MS002009, 2020. doi: 10.1029/2019MS002009.

D. J. Sinclair. Rbme coral temperature reconstruction: An evaluation, modifications, and recommendations. *Geochim. Cosmochim. Acta*, 154:66–80, 2015. ISSN 0016-7037. doi: 10.1016/j.gca.2015.01.006.

D. J. Sinclair, B. Williams, and M. Risk. A biological origin for climate signals in corals—trace element "vital effects" are ubiquitous in scleractinian coral skeletons. *Geophys. Res. Lett.*, 33:L17707, 2006. doi: 10.1029/2006GL027183.

J. E. Smerdon, E. R. Cook, and N. J. Steiger. The historical development of large-scale paleoclimate field reconstructions over the common era. *Rev. Geophys.*, 61(4):e2022RG000782, 2023. ISSN 8755-1209. doi: 10.1029/2022RG000782.

D. M. Smith, A. A. Scaife, R. Eade, P. Athanasiadis, A. Bellucci, I. Bethke, R. Bilbao, L. F. Borchert, L.-P. Caron, F. Counillon, G. Danabasoglu, T. Delworth, F. J. Doblas-Reyes, N. J. Dunstone, V. Estella-Perez, S. Flavoni, L. Hermanson, N. Keenlyside, V. Kharin, M. Kimoto, W. J. Merryfield, J. Mignot, T. Mochizuki, K. Modali, P.-A. Monerie, W. A. Müller, D. Nicolí, P. Ortega, K. Pankatz, H. Pohlmann, J. Robson, P. Ruggieri, R. Sospedra-Alfonso, D. Swingedouw, Y. Wang, S. Wild, S. Yeager, X. Yang, and L. Zhang. North atlantic climate far more predictable than models imply. *Nature*, 583:796–800, 2020. doi: 10.1038/s41586-020-2525-0.

G. A. Smith. Seasonal climate summary southern hemisphere (autumn 2020): another coral bleaching event for the great barrier reef without an active el niño. *J. Southern Hem. Earth Sys. Sci.*, 74(3), 2024. doi: 10.1071/ES24014.

S. V. Smith, R. W. Buddemeier, R. C. Redalje, and J. E. Houck. Strontium-calcium thermometry in coral skeletons. *Science*, 204:404–407, 1979. doi: 10.1126/science.204.4391.404. K(T) = 1.30-0.0094T Like.. the textbook on this stuff. Dismissed Growth Rate as compounding factor, despite prior studies.

T. M. Smith and R. W. Reynolds. Bias corrections for historical sea surface temperatures based on marine air temperatures. *J. Clim.*, 15(1):73–87, 2002. ISSN 0894-8755. doi: 10.1175/1520-0442(2002)015⟨0073:BCFHSS⟩2.0.CO;2.

C. D. Standish, T. B. Chalk, M. Saeed, F. Lei, M. C. Buckingham, C. D'Angelo, J. Wiedenmann, and G. L. Foster. Geochemical responses of scleractinian corals to nutrient stress. *Geochim. Cosmochim. Acta*, 351:108–124, 2023. ISSN 0016-7037. doi: 10.1016/j.gca.2023.04.011.

N. J. Steiger, J. E. Smerdon, E. R. Cook, and B. I. Cook. A reconstruction of global hydroclimate and dynamical variables over the common era. *Nature Sci. Data*, 5(1):5:180086, 2018. doi: 10.1038/sdata.2018.86. - 180086.

C. L. Stephans, T. M. Quinn, F. W. Taylor, and T. Corrège. Assessing the reproducibility of coral-based climate records. *Geophys. Res. Lett.*, 31(18), 2004. ISSN 0094-8276. doi: 10.1029/2004GL020343.

S. Stevenson, A. Capotondi, J. Fasullo, and B. Otto-Bliesner. Forced changes to twentieth century enso diversity in a last millennium context. *Clim. Dynam.*, 52(12):7359–7374, 2019. ISSN 1432-0894. doi: 10.1007/s00382-017-3573-5.

J. A. Stewart, L. F. Robinson, R. D. Day, I. Strawson, A. Burke, J. W. B. Rae, P. T. Spooner, A. Samperiz, P. J. Etnoyer, B. Williams, A. Paytan, M. J. Leng, V. Häussermann, L. N. Wickes, R. Bratt, and H. Pryer. Refining trace metal temperature proxies in cold-water scleractinian and stylasterid corals. *Earth Planet. Sc. Lett.*, 545:116412, 2020. ISSN 0012-821X. doi: 10.1016/j.epsl.2020.116412.

N. C. Swart, J. N. S. Cole, V. V. Kharin, M. Lazare, J. F. Scinocca, N. P. Gillett, J. Anstey, V. Arora, J. R. Christian, S. Hanna, Y. Jiao, W. G. Lee, F. Majaess, O. A. Saenko, C. Seiler, C. Seinen, A. Shao, M. Sigmond, L. Solheim, K. von Salzen, D. Yang, and B. Winter. The canadian earth system model version 5 (canesm5.0.3). *Geosci. Model Dev.*, 12(11):4823–4873, 2019. ISSN 1991-9603. doi: 10.5194/gmd-12-4823-2019. GMD.

H. Tatebe, T. Ogura, T. Nitta, Y. Komuro, K. Ogochi, T. Takemura, K. Sudo, M. Sekiguchi, M. Abe, F. Saito, M. Chikira, S. Watanabe, M. Mori, N. Hirota, Y. Kawatani, T. Mochizuki, K. Yoshimura, K. Takata, R. O'Ishi, D. Yamazaki, T. Suzuki, M. Kurogi, T. Kataoka, M. Watanabe, and M. Kimoto. Description and basic evaluation of simulated mean state, internal variability, and climate sensitivity in miroc6. *Geosci. Model Dev.*, 12(7):2727–2765, 2019. ISSN 1991-9603. doi: 10.5194/gmd-12-2727-2019. GMD.

D. Thompson, M. McCulloch, J. E. Cole, E. V. Reed, J. P. D'Olivo, K. Dyez, M. Lofverstrom, J. Lough, N. Cantin, A. W. Tudhope, A. H. Cheung, L. Vetter, and R. L. Edwards. Marginal reefs under stress: Physiological limits render galápagos corals susceptible to ocean acidification and thermal stress. *AGU Advances*, 3(1):e2021AV000509, 2022. ISSN 2576-604X. doi: 10.1029/2021AV000509.

D. M. Thompson. Environmental records from coral skeletons: A decade of novel insights and innovation. *WIREs Clim. Change*, 13(1):e745, 2021. ISSN 1757-7780. doi: 10.1002/wcc.745.

J. E. Tierney, N. J. Abram, K. J. Anchukaitis, M. N. Evans, C. Giry, K. H. Kilbourne, C. P. Saenger, H. C. Wu, and J. Zinke. Tropical sea surface temperatures for the past four centuries reconstructed from coral archives. *Paleoceanography*, 30:226–252, 2015. ISSN 1944-9186. doi: 10.1002/2014PA002717. - Western Atlantic reconstruction is weak, due to insufficient data.

J. E. Tierney, C. J. Poulsen, I. P. Montañez, T. Bhattacharya, R. Feng, H. L. Ford, B. Hönisch, G. N. Inglis, S. V. Petersen, N. Sagoo, C. R. Tabor, K. Thirumalai, J. Zhu, N. J. Burls, G. L. Foster, Y. Goddéris, B. T. Huber, L. C. Ivany, S. Kirtland Turner, D. J. Lunt, J. C. McElwain, B. J. W. Mills, B. L. Otto-Bliesner, A. Ridgwell, and Y. G. Zhang. Past climates inform our future. *Science*, 370(6517):eaay3701, 2020. doi: 10.1126/science.aay3701.

J. C. Tipper. Rarefaction and rarefiction—the use and abuse of a method in paleoecology. *Paleobiology*, 5(4):423–434, 1979. ISSN 0094-8373. doi: 10.1017/S0094837300016924.

K. E. Trenberth and J. T. Fasullo. Tracking earth's energy: From el niño to global warming. *Surv. Geophys.*, 33(3):413–426, 2012. ISSN 1573-0956. doi: 10.1007/s10712-011-9150-2.

J. W. Tukey. *Exploratory Data Analysis*, volume 2. Addison-Wesley, Reading, MA, 1977.

C. C. Ummenhofer, M. H. England, P. C. McIntosh, G. A. Meyers, M. J. Pook, J. S. Risbey, A. S. Gupta, and A. S. Taschetto. What causes southeast australia's worst droughts? *Geophys. Res. Lett.*, 36(4), 2009. ISSN 0094-8276. doi: 10.1029/2008GL036801.

R. M. Walter, H. R. Sayani, T. Felis, K. M. Cobb, N. J. Abram, A. K. Arzey, A. R. Atwood, L. D. Brenner, P. Dassié, K. L. DeLong, B. Ellis, J. Emile-Geay, M. J. Fischer, N. F. Goodkin, J. A. Hargreaves, K. H. Kilbourne, H. Krawczyk, N. P. McKay, A. L. Moore, S. A. Murty, M. R. Ong, R. D. Ramos, E. V. Reed, D. Samanta, S. C. Sanchez, J. Zinke, and P. C. k. P. M. the. The coralhydro2k database: a global, actively curated compilation of coral 18o and srthinsp;thinsp;ca proxy records of tropical ocean hydrology and temperature for the common era. *Earth Syst. Sci. Data*, 15(5):2081–2116, 2023. ISSN 1866-3516. doi: 10.5194/essd-15-2081-2023. ESSD.

Y.-C. Wang, H.-H. Hsu, C.-A. Chen, W.-L. Tseng, P.-C. Hsu, C.-W. Lin, Y.-L. Chen, L.-C. Jiang, Y.-C. Lee, H.-C. Liang, W.-M. Chang, W.-L. Lee, and C.-J. Shiu. Performance of the taiwan earth system model in simulating climate variability compared with observations and cmip6 model simulations. *J. Adv. Model. Earth. Syst.*, 13(7): e2020MS002353, 2021. doi: 10.1029/2020MS002353.

A. Watkins. Using paleoclimate analogues to inform climate projections. *Perspectives on Science*, 32(4):415–459, 2024. ISSN 1063-6145. doi: 10.1162/posc_a_00622.

J. N. Weber and P. M. J. Woodhead. Temperature dependence of oxygen-18 concentration in reef coral carbonates. *J. Geophys. Res.*, 77:463–473, 1972. doi: 10.1029/jc077i003p00463. As far as I know, this is the first paper on oxygen isotopes in corals.

Y. Wei, W. Deng, X. Chen, and G. Wei. A comprehensive evaluation of machine learning on coral trace element paleothermometers for sea surface temperature reconstruction. *Paleoceanogr. Paleoclimatol.*, 39(10): e2024PA004885, 2024. doi: 10.1029/2024PA004885.

R. Wilson, A. Tudhope, P. Brohan, K. Briffa, T. Osborn, and S. Tett. Two-hundred-fifty years of reconstructed and modeled tropical temperatures. *J. Geophys. Res-Oceans*, 111, 2006. doi: 10.1029/2005JC003188.

Y. Wu, S. J. Fallon, N. E. Cantin, and J. M. Lough. Assessing multiproxy approaches (sr/ca, u/ca, li/mg, and b/mg) to reconstruct sea surface temperature from coral skeletons throughout the great barrier reef. *Sci. Total. Environ.*, 786:147393, 2021. ISSN 0048-9697. doi: 10.1016/j.scitotenv.2021.147393.

Y.-Y. Xu, S. Pearson, and K. H. Kilbourne. Assessing coral sr/ca–sst calibration techniques using the species diploria strigosa. *Palaeogeogr. Palaeoclimatol. Palaeoecol.*, 440:353–362, 2015. doi: 10.1016/j.palaeo.2015.09.016.

CHAPTER 5

Conclusion

This dissertation seeks establish and improve the resolution, reliability, and interpretability of paleoclimate reconstructions from two marine archives: the bivalve *Astarte borealis* and *Porites* corals. Through the development of novel analytical and statistical techniques, I aim to extract more robust environmental signals from these high-resolution climate proxies. Below, I summarize the primary research questions, methodological approaches, and key findings of each chapter, followed by a synthesis of the broader contributions of this work to the field of paleoclimatology.

5.1 Summary of Chapter 2

5.1.1 Research Questions

1. How do local environmental factors (temperature and salinity) influence SIMS $\delta^{18}O_{shell}$ values measured from an *A. borealis* bivalve specimen collected from the southern margin of the Baltic Sea?

2. To what extent do temperature and salinity at depth reflect broader (i.e., regional) patterns of climate variability in the Baltic Sea?

3. What is the feasibility of using SIMS $\delta^{18}O_{shell}$ values from *A. borealis* in the Baltic Sea as a proxy for regional-scale interannual hydroclimate variability throughout the Holocene?

5.1.2 Methods

I assess 451 SIMS $\delta^{18}O_{shell}$ measurements from an *A. borealis* specimen collected in May 2001, which exhibit a quasi-sinusoidal pattern spanning 24 annual growth increments. A minimally constrained age model is implemented by aligning SIMS $\delta^{18}O_{shell}$ maxima with the coldest winter months, with linear interpolation used to estimate the earliest growth interval as March 1977. To investigate the drivers of SIMS $\delta^{18}O_{shell}$ variability, I compare the record against *in situ* temperature and salinity, reanalysis-based sea surface temperature (SST), and the North Atlantic Oscillation (NAO) index.

5.1.3 Key Findings

I find that age-modeled SIMS $\delta^{18}O_{shell}$ values correlate significantly with both *in situ* temperature and regional reanalysis-based SST on seasonal timescales. On interannual timescales, SIMS $\delta^{18}O_{shell}$ values show the strongest correlation with salinity, along with a moderately strong correlation with the NAO. I suggest that the pronounced coherence between local and regional climate variability at this site is enhanced by the NAO's influence on SST–seawater $\delta^{18}O$ covariance at interannual and longer timescales in the Baltic Sea. Collectively, these results demonstrate the potential of *A. borealis* as a robust archive of regional hydroclimate variability.

5.2 Summary of Chapter 3

5.2.1 Research Questions

1. Does a multivariate calibration method I developed (SMITE) improve reconstruction of SST and seawater pH from coral skeletal geochemistry relative to traditional approaches with respect to correlation, accuracy, precision, and reproducibility?

2. How do SMITE-based SST and seawater pH estimates, along with their associated model parameters, respond to increasing levels of Gaussian noise, compared to estimates derived from Sr/Ca and boron isotopes ($\delta^{11}B$)?

3. What statistical advantages does SMITE offer in mitigating multicollinearity, noise, and non-climatic variability when applied to a small test dataset from a Bermudan *P. astreoides* coral?

5.2.2 Methods

I implement a synthetic "pseudo-reconstruction" experiment by modeling geochemical variables (Sr/Ca, $\delta^{18}O$, and $\delta^{11}B$) based on observational data. Using these modeled values, I generate SST estimates for both SMITE and Sr/Ca, as well as seawater pH estimates for SMITE and $\delta^{11}B$. I then evaluate the reconstruction skill of each method, specifically accuracy and precision, under increasing levels of Gaussian noise.

To compliment the synthetic experiment, I assess the performance of each calibration method (SMITE and Sr/Ca for SST, SMITE and $\delta^{11}B$ for seawater pH) using the top sections of two *Porites astreoides* coral records from Bermuda, measured via LA-ICP-MS. The analytical workflow involves converting two-dimensional geochemical maps into one-dimensional time series, providing a novel approach to constrain analytical noise from laser-ablated datasets.

Finally, I examine user-based strategies for improving SMITE reconstruction skill, including selective screening of geochemical variables and the implementation of a regularization procedure. This regularization mitigates collinearity and reduces overfitting, albeit with tradeoffs in reconstruction skill.

5.2.3 Key Findings

I find that SMITE SST estimates are robust to even extreme levels of Gaussian noise, maintaining high accuracy and precision, whereas Sr/Ca SST and δ^{11}B seawater pH errors increase linearly with noise. However, SMITE seawater pH estimates exhibit a substantial loss of variance after only moderate noise increases. Variance suppression is also observed in SMITE SST estimates, though it is minimal and mitigated by SMITE's ability to dynamically adjust its loadings in response to changing noise conditions.

Despite a short calibration and validation period ($<$3.5 years), SMITE SST and seawater pH estimates in the *P. astreoides* corals show significantly better accuracy, precision, and correlation with their target climate variables compared to Sr/Ca and δ^{11}B. Moreover, model performance is consistent across coral records, suggesting that the SMITE-derived parameters are reproducible across different datasets.

Finally, I find that including more geochemical variables as model inputs, regardless of their individual sensitivity to the climate target, tends to improve reconstruction skill across all metrics. Expanding the variable set also enhances flexibility with respect to regularization, enabling users to tune reconstructions for higher reproducibility (via stronger regularization) or for optimal performance during the calibration period (via weaker regularization).

5.3 Summary of Chapter 4

5.3.1 Research Questions

1. How do different coral-based geochemical calibration methods (Sr/Ca, Li/Mg, and SMITE) compare in their ability to reconstruct seasonal and deseasonalized SST variability across the Great Barrier Reef (GBR) and the Galápagos Archipelago, with respect to correlation, accuracy, and relative (variance-normalized) accuracy?

2. What can be inferred about the reproducibility of each calibration method when each unique SST calibration model is applied across all coral datasets?

3. What are the implications of individual calibration uncertainty for climate field reconstructions (CFRs) on the GBR, particularly in resolving interannual climate variability such as the El Niño Southern Oscillation and the Indian Ocean Dipole (IOD)?

5.3.2 Methods

I use 15 coral records from the GBR and 2 from the Galápagos, obtained from the literature, to conduct a rigorous intercomparison of three calibration methods: Sr/Ca, Li/Mg, and SMITE. Within each record (e.g., intrarecord comparisons), I assess method performance based on correlation, accuracy, and relative (variance-normalized)

accuracy. These comparisons are conducted on both the native seasonal datasets and their deseasonalized counterparts.

To evaluate reproducibility, I apply each of the 17 unique SST calibration models (one per coral record, per method) across all deseasonalized coral datasets. This cross-application allows for a systematic assessment of how well each calibration method generalizes across independent coral records.

Finally, I implement a paleoclimate data assimilation (PDA) framework to generate synthetic climate field reconstructions (CFRs) for the GBR. Synthetic coral records are produced by modeling the error structure of each calibration method and perturbing a known 'true' SST signal. This allows for direct evaluation of each method's ability to recover interannual climate signals, such as those associated with ENSO and the IOD.

5.3.3 Key Findings

For the intrarecord comparisons, I find few significant differences among calibration methods for both seasonal and deseasonalized datasets. While SMITE consistently yields the highest correlation and accuracy scores, it performs poorly in terms of relative accuracy for deseasonalized records. This suggests that Sr/Ca and Li/Mg may better capture interannual variability at the individual-core level than the multivariate SMITE approach.

For the interrecord comparisons, SMITE consistently outperforms Sr/Ca and Li/Mg in both accuracy and relative accuracy. Correlation differences are less pronounced, but SMITE more often achieves the highest correlations across records. However, SMITE often produces statistically significant improvements in relative accuracy over Sr/Ca and Li/Mg. These findings indicate that Sr/Ca and Li/Mg may be overfit to interannual variability within individual records, whereas SMITE yields more reproducible regression coefficients across diverse coral datasets.

Using a PDA framework to create synthetic CFRs, I show that Li/Mg is most effective at resolving spatial SST variability on the GBR associated with ENSO and the IOD. While SMITE delivers the best statistical performance (correlation, accuracy, efficiency), its tendency toward variance suppression limits signal recoverability. Finally, I find that ENSO and IOD signals primarily affect the northern and southern GBR, respectively—regions that are currently underrepresented in the coral network. These findings suggest future CFR efforts should prioritize multiproxy sampling from these geographic extremes to better resolve interannual variability across the GBR.

5.4 Overall Contributions of this Dissertation

Taken together, this dissertation advances analytical methods for extracting climate signals from slow-growing marine archives. Chapter 2 demonstrates the utility of SIMS $\delta^{18}O_{shell}$ values in *A. borealis*, establishing its potential as a high-latitude, high-resolution archive for Holocene hydroclimate variability. Chapter 3 introduces

a novel 2D-to-1D LA-ICP-MS sampling strategy for *Porites astreoides*, enabling the effective use of laser-ablation data in high-resolution reconstructions.

Chapters 3 and 4 present and evaluate the SMITE calibration framework, which leverages multivariate geochemical covariance to reconstruct SST and seawater pH. SMITE outperforms traditional univariate approaches in terms of accuracy, noise robustness, and cross-record reproducibility, though it also exhibits variance suppression under low signal-to-noise conditions.

Beyond its utility as a calibration method, SMITE represents a conceptual advance in modeling coral geochemistry. By capturing covariation across multiple tracers, it functions as a data-driven proxy system model, an increasingly critical tool for integrating paleoclimate data into assimilation-based reconstructions. This approach offers not only more robust climate estimates, but also mechanistic insight into coral biomineralization and how environmental signals are encoded as skeletal geochemistry. As such, SMITE provides a flexible and scalable foundation for future coral-based reconstructions in both empirical and modeling studies.

In its entirety, this dissertation offers a path forward for high-resolution paleoclimatology using corals and bivalves: expanding the proxy network through the inclusion of slow-growing species, providing a means of generating records from previously inaccessible specimens; and improving the extraction and interpretation of paleoclimate signals. As the field moves towards climate field reconstructions and data assimilation frameworks, this work lays a foundation for improving spatial coverage and calibration fidelity in marine systems. By enhancing both analytical access and statistical rigor, this dissertation provides a road map for building next-generation paleoclimate proxy networks.

APPENDIX A: CHAPTER 2 SUPPLEMENTAL FIGURES AND TABLES

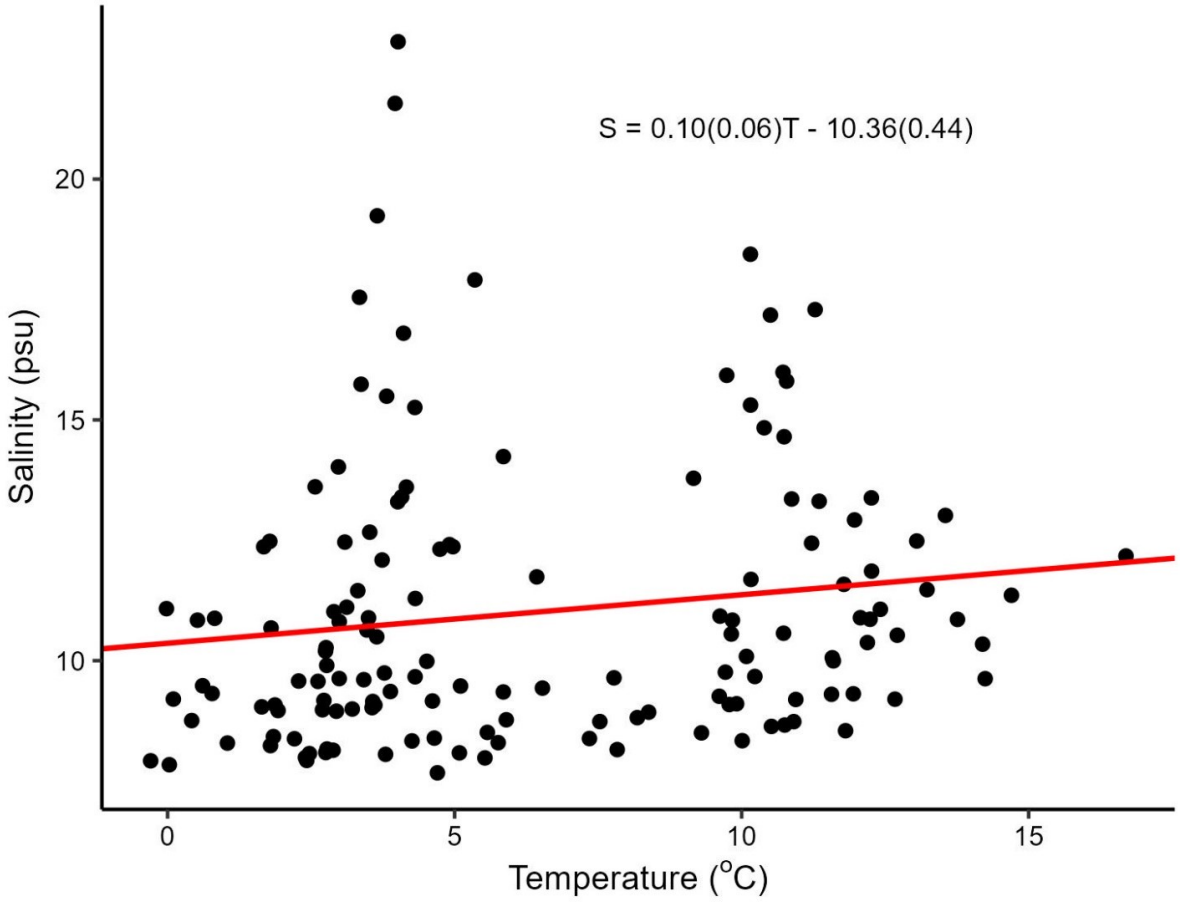

Figure A.1: Cross-plot of *in situ* temperature and salinity measured less than 2 km from where specimen RFP3S-47 was collected (54°47'30.1"N, 13°03'29.9"E). There is no significant relationship between temperature and salinity (n = 146, r^2 = 0.02, p = 0.08), indicating that there is no seasonal cycle of salinity at our study site.

Table A.1: Lagged correlation analysis between yearly-averaged SIMS $\delta^{18}O_{shell}$ values and *in situ* salinity. 'Cold' ('Warm') represents salinities where temperatures were below (above) the median temperature value. 'DJFM' represents salinities collected in December, January, February, and March. 'JJAS' represents salinities collected in June, July, August, and September. The sample size for each dataset is as follows: Cold = 73, Warm = 73, DJFM = 63, JJAS = 30.

	Cold	Warm	DJFM	JJAS
Cold	1.00	–	–	–
Warm	0.13	1.00	–	–
DJFM	0.56	0.43	1.00	–
JJAS	0.81	0.19	0.59	1.00

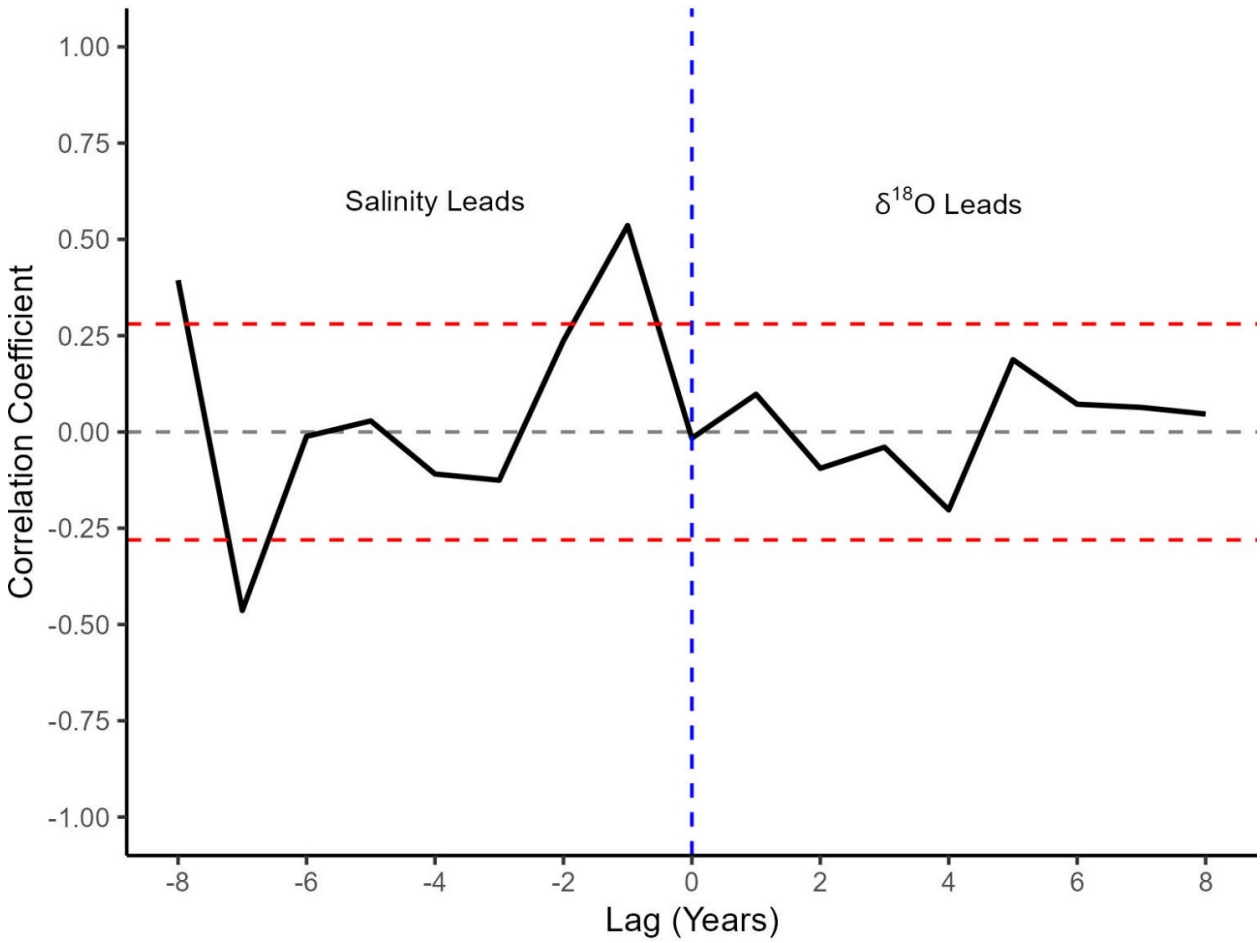

Figure A.2: Lagged correlation analysis between yearly-averaged SIMS $\delta^{18}O_{shell}$ values and *in situ* salinity. The x-axis values represent the number of years that salinity lags SIMS $\delta^{18}O_{shell}$ values. The red-dotted lines (r = $\pm$ 0.28) indicate the point at which the correlation becomes significant at the 95% confidence level (Hu et al., 2017).

APPENDIX B: CHAPTER 3 SUPPLEMENTAL FIGURES AND TABLES

Supporting information

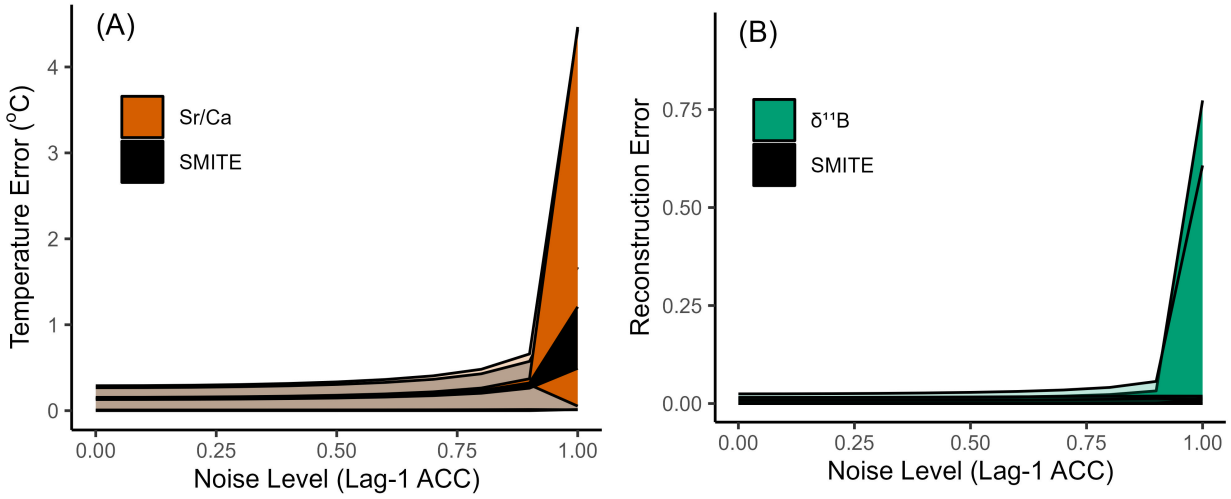

Figure B.1: Reconstruction statistics for SMITE SST, Sr/Ca SST (A), SMITE pH_{sw}, and $\delta^{11}B$ pH_{sw} (B) across various levels of autocorrelated noise. The RMSE (translucent shaded region) and SEP (opaque shaded region) for SST and pH_{sw} estimates derived from the SMITE method are black, while the colored regions represent the RMSE and SEP for Sr/Ca SST (orange) and $\delta^{11}B$ pH_{sw} (green). The x-axis represents the factor by which autocorrelated noise was increased in terms of RSD. The upper and lower bounds of each shaded region represent the maximum and minimum values for the RMSE and SEP at each noise increment.

Table B.1: Mean (μ), standard deviation (σ), analytical error (ε), and correlation coefficient (r) to SST and pH_{sw} for each coral variable measured in both Bermudan *P. astreoides* corals (1B and 3B).

Coral	**1B**				**3B**			
Statistic	(μ)	(σ)	(ε)	(r) - SST/pH_{sw}	(μ)	(σ)	(ε)	(r) - SST/ pH_{sw}
B/Ca (μmol/mol)	501.53	33.00	7.47	-0.75 / 0.63	501.97	25.48	8.52	-0.77 / 0.63
$\delta^{11}B$ (‰)	23.09	0.69	0.26	-0.41 / 0.33	23.17	0.57	0.23	-0.49 / 0.26
Li/Ca (μmol/mol)	5.54	0.26	0.10	-0.56 / 0.49	5.65	0.25	0.13	-0.47 / 0.37
Li/Mg (mmol/mol)	1.51	0.12	0.04	-0.83 / 0.81	1.44	0.11	0.04	-0.85 / 0.83
Mg/Ca (mmol/mol)	3.78	0.27	0.12	0.57 / -0.58	4.01	0.27	0.13	0.70 / -0.72
Sr/Ca (mmol/mol)	9.06	0.12	0.04	-0.85 / 0.80	9.03	0.11	0.04	-0.77 / 0.72
U/Ca (μmol/mol)	1199.87	73.39	25.26	-0.70 / 0.70	1108.87	69.95	28.13	-0.67 / 0.65

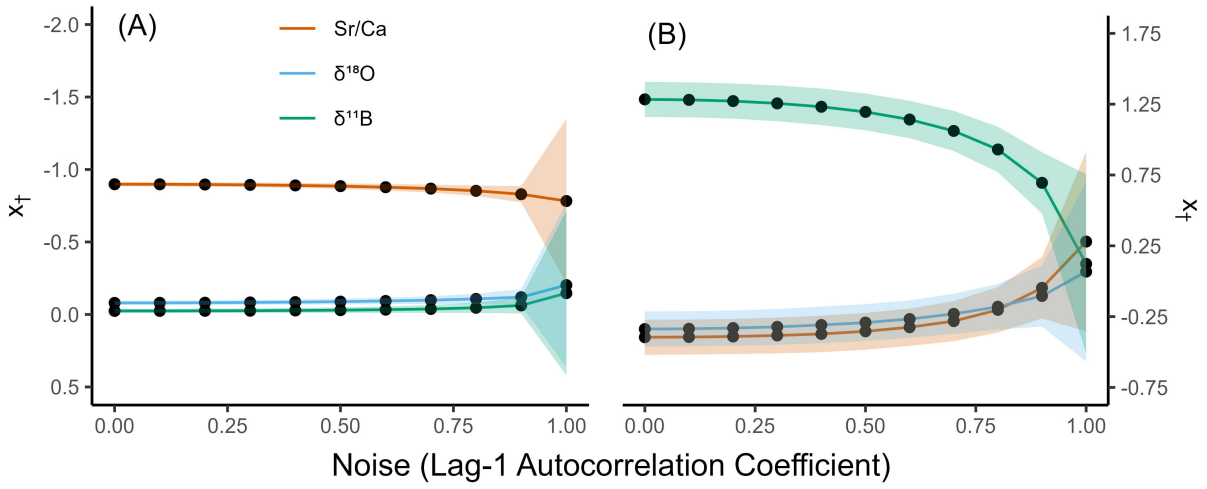

Figure B.2: Synthetic SMITE model parameters for SST (A) and pH_{sw} (B) as the lag-1 autocorrelation coefficient of the noise term is increased. The color of each line denotes the proxy associated with each model parameter (orange = Sr/Ca, blue = $\delta^{18}O$, green = $\delta^{11}B$). The shaded region around each line indicates the 95% confidence interval associated with that model parameter.

Table B.2: Reconstruction statistics for pH_{sw} reconstructions in Bermudan *P. astreoides* corals (1B and 3B).

Coral	1B			3B		
pH_{sw} Reconstruction	(r^2)	(SEP)	(RMSE)	(r^2)	(SEP)	(RMSE)
SMITE	0.68	0.01	0.02	0.68	0.01	0.02
$\delta^{11}B$	0.11	0.21	0.15	0.07	0.35	0.2
Li/Mg	0.66	0.05	0.04	0.69	0.05	0.03

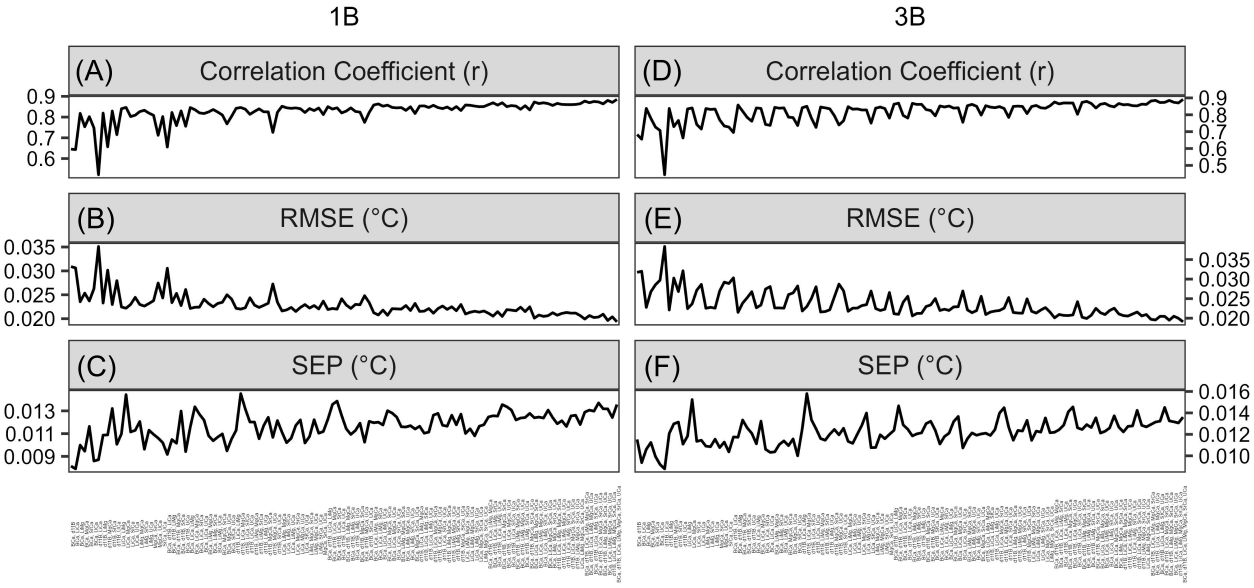

Figure B.3: The correlation coefficient (r; A and D), the root-mean-square-error (RMSE; B and E), and standard error of prediction (SEP; C and F) for each SMITE pH_{sw} reconstruction from the Bermudan *P. astreoides* corals through every combination of the seven coral geochemical variables (n = 120). The left side of each plot begins with only two coral variables (B/Ca and $\delta^{11}B$). Each line then tracks the corresponding reconstruction statistic as variables are systematically replaced and added to the SMITE pH_{sw} reconstruction. Each line thus ends on the final value of each reconstruction statistic when all seven coral variables are used.

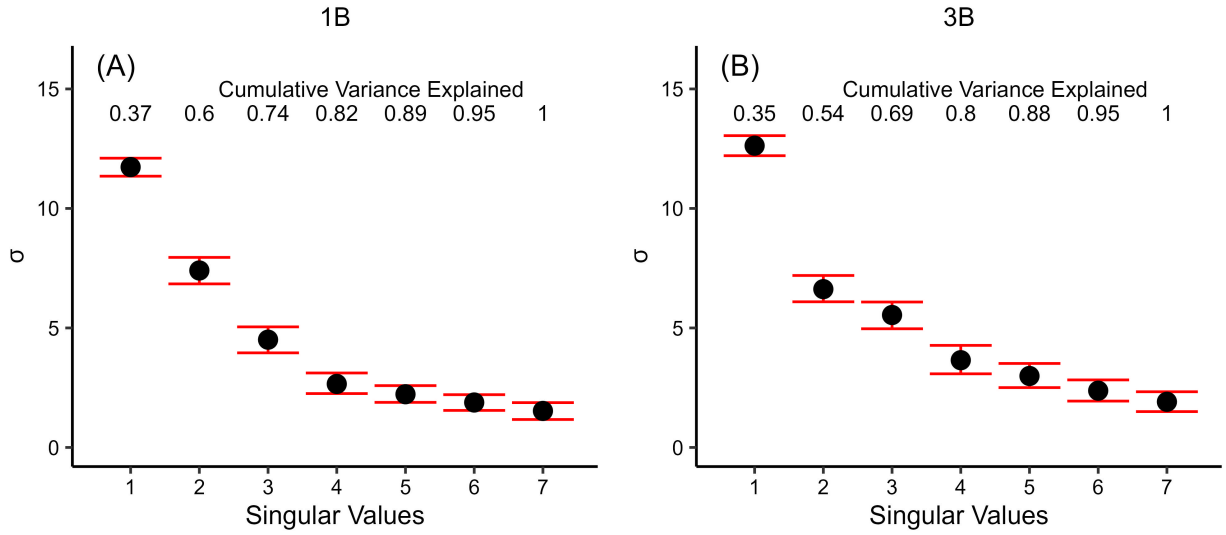

Figure B.4: The singular values from the two Bermudan *P. astreoides* corals. The red error bars around each point indicate the 95% confidence interval estimated using a bootstrap Monte Carlo approach.

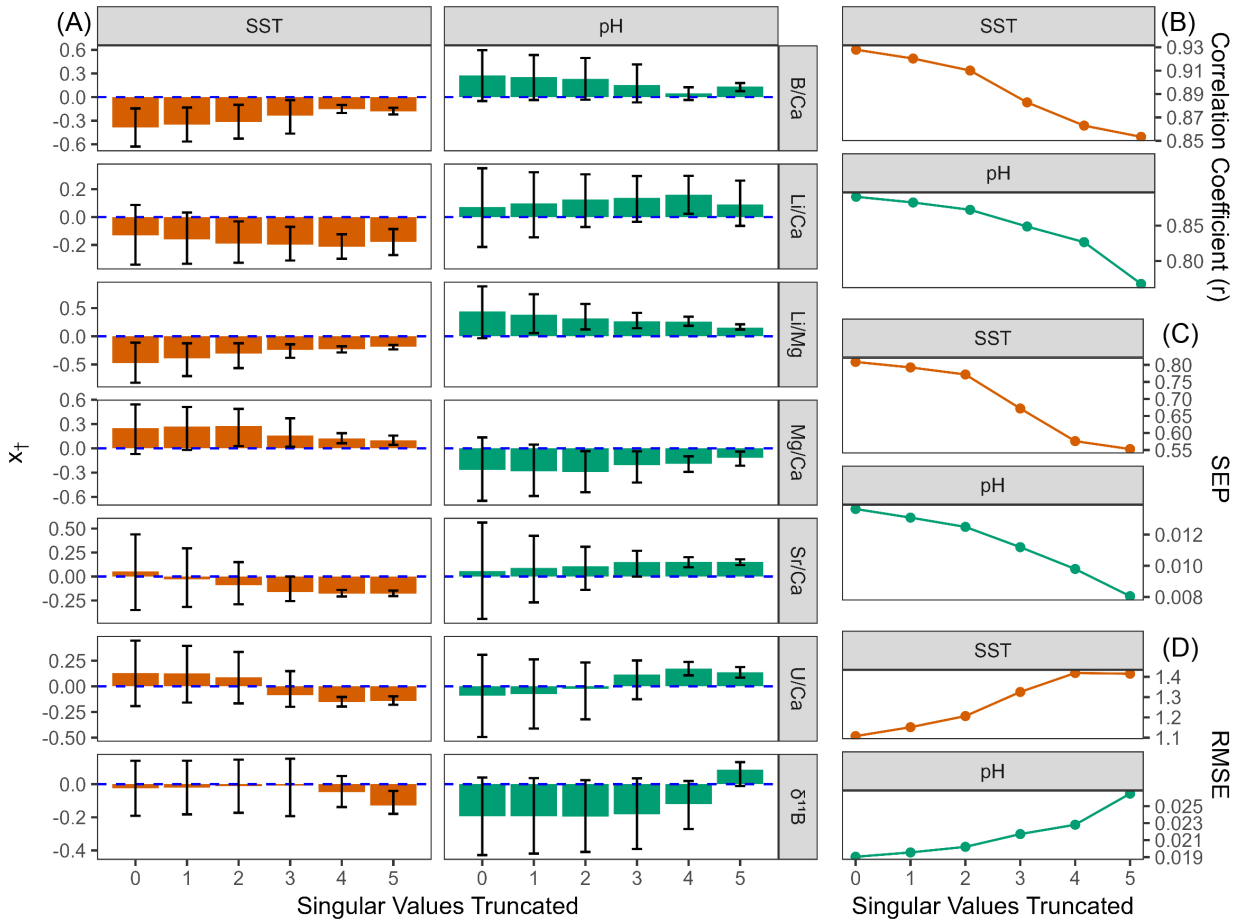

Figure B.5: The effects of truncating singular values from coral 3B on the SMITE SST reconstruction. The x-axis in each plot denotes the number of singular values truncated. Each plot thus shows the progressive effects from no truncation (left) to maximum truncation (right). Truncation occurs from the highest (least dominant) singular values to the lowest (most dominant) singular values. The first two singular values can never be truncated. Colors distinguish the results from the SST reconstructions (orange) versus the pH_{sw} reconstructions (green). (A) SMITE model parameters, or $x_\dagger$ values, at each successive level of truncation. Rows denote the SMITE model parameter. The colored bar within each plot indicates the $x_\dagger$ value of the corresponding SMITE model parameter at a given level of truncation. Error bars for each $x_\dagger$ value denote the 95% confidence interval based on a Monte Carlo approach. (B – D) The correlation coefficient (r; B), the standard error of prediction (SEP; C), and the root-mean-square-error (RMSE; D) at each successive level of truncation.

APPENDIX C: CHAPTER 4 SUPPLEMENTAL FIGURES AND TABLES

C.1 Supplemental Figures

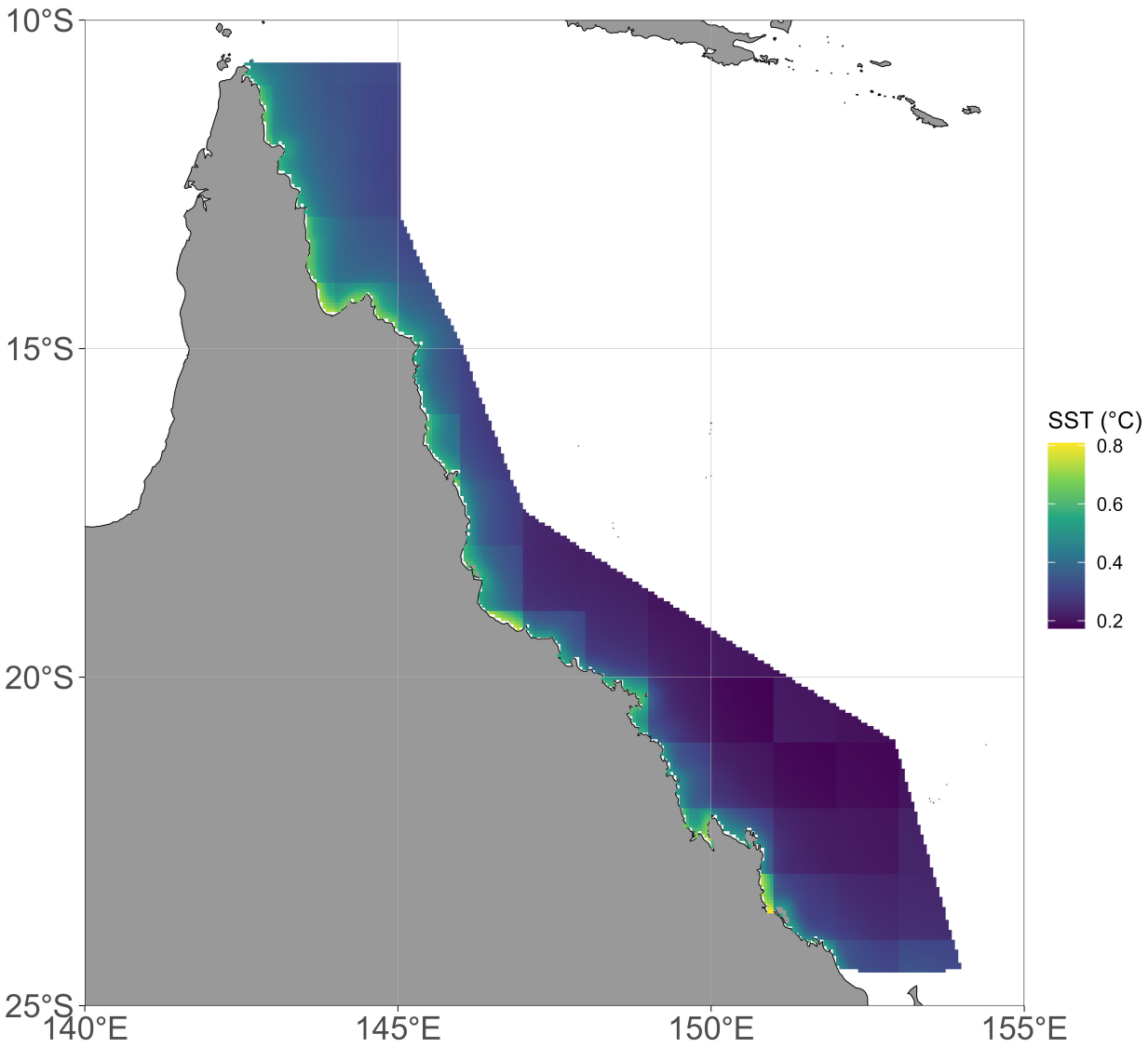

Figure C.1: Map of uncertainties on the Great Barrier Reef in the European Space Agency's Climate Change Intiative SST dataset (Merchant et al., 2019). Uncertainty is defined as the standard deviation of the error distributions from multiple satellite sensors.

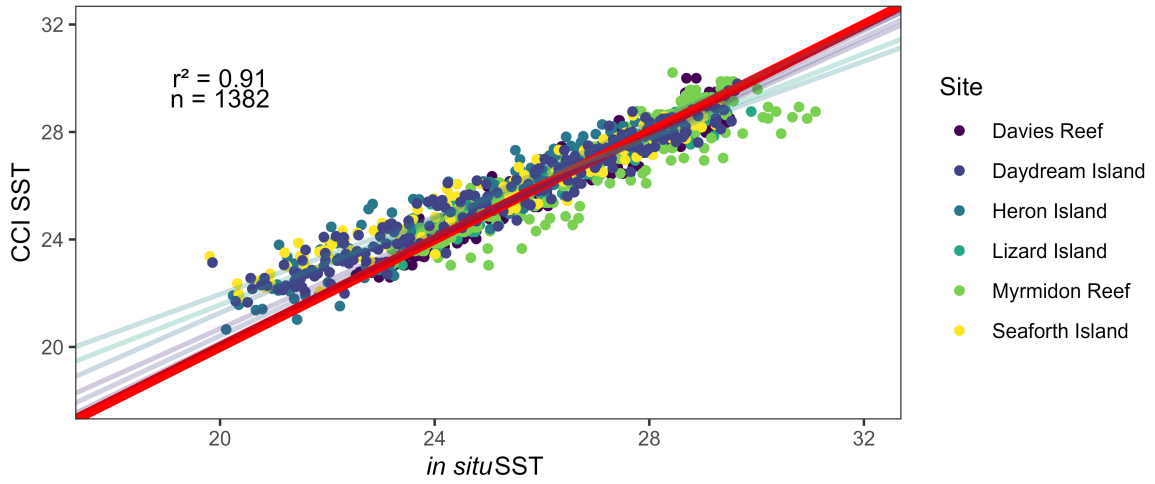

Figure C.2: Comparison between CCI SST and *in situ* logger SST across GBR sites. Sample size (n) and pearson correlation coefficient (r^2) are included. Data points are colored by site. The red bold line indicates the line of best fit, according to Weighted Least Squares regression.

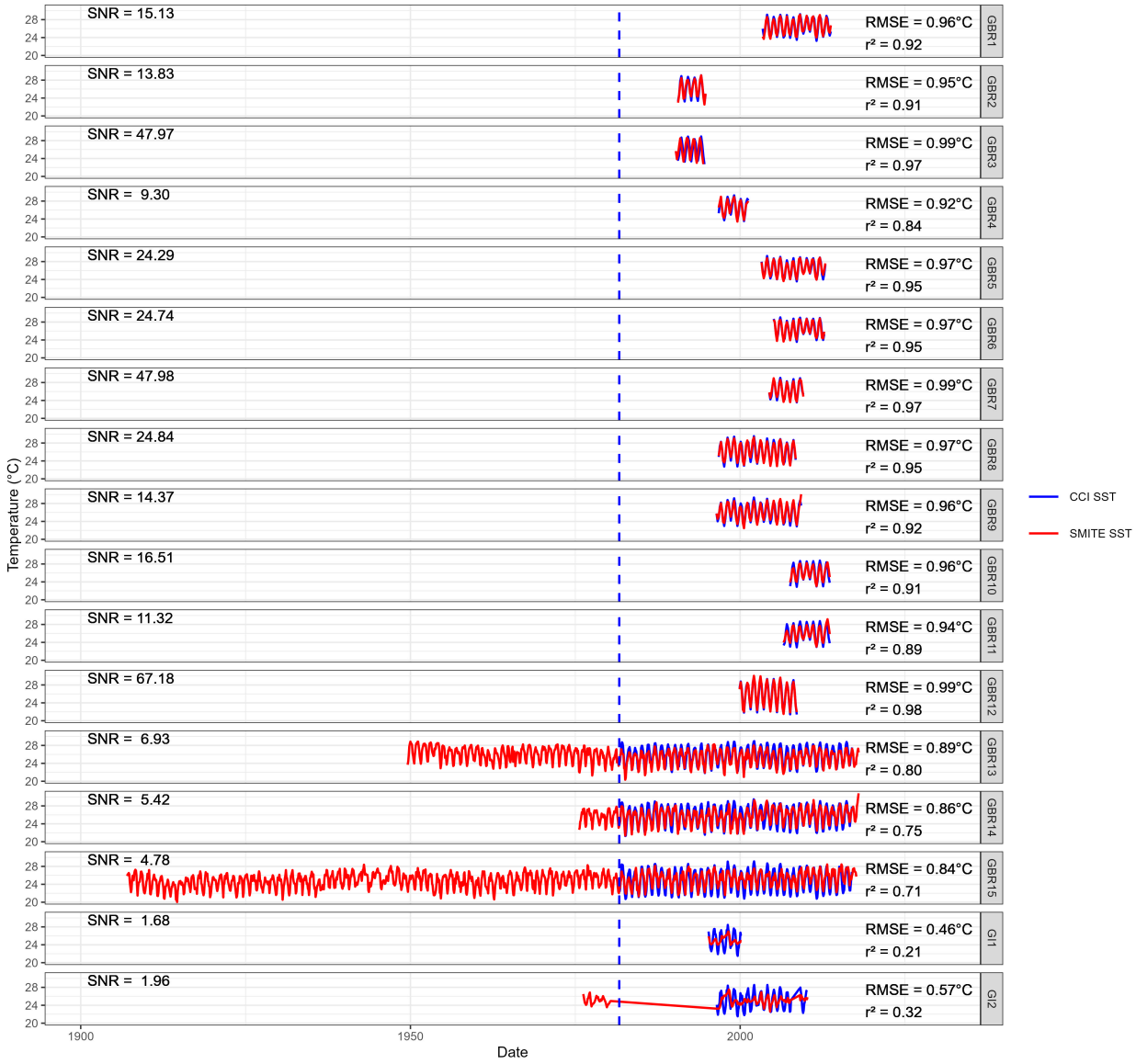

Figure C.3: Individual SMITE SST reconstructions across all seasonal coral records used in this study (GBR1-15, GI1-2). Each panel shows the reconstructed SST time series (red) along the satellite-derived CCI SST target (blue). The root mean square error (RMSE) and correlation coefficient (r^2) between SMITE SST and CCI SST for each reconstruction are reported in the upper-right corner of each panel. The signal-to-noise ratio (SNR) for each reconstruction, defined as the proportion of variance in CCI SST and the squared RMSE, are reported in the upper-left corner of each panel. The vertical dashed line represents the earliest date of the CCI SST dataset. These reconstructions reflect fully regularized SMITE models, designed to minimize overfitting and maximize reproducibility.

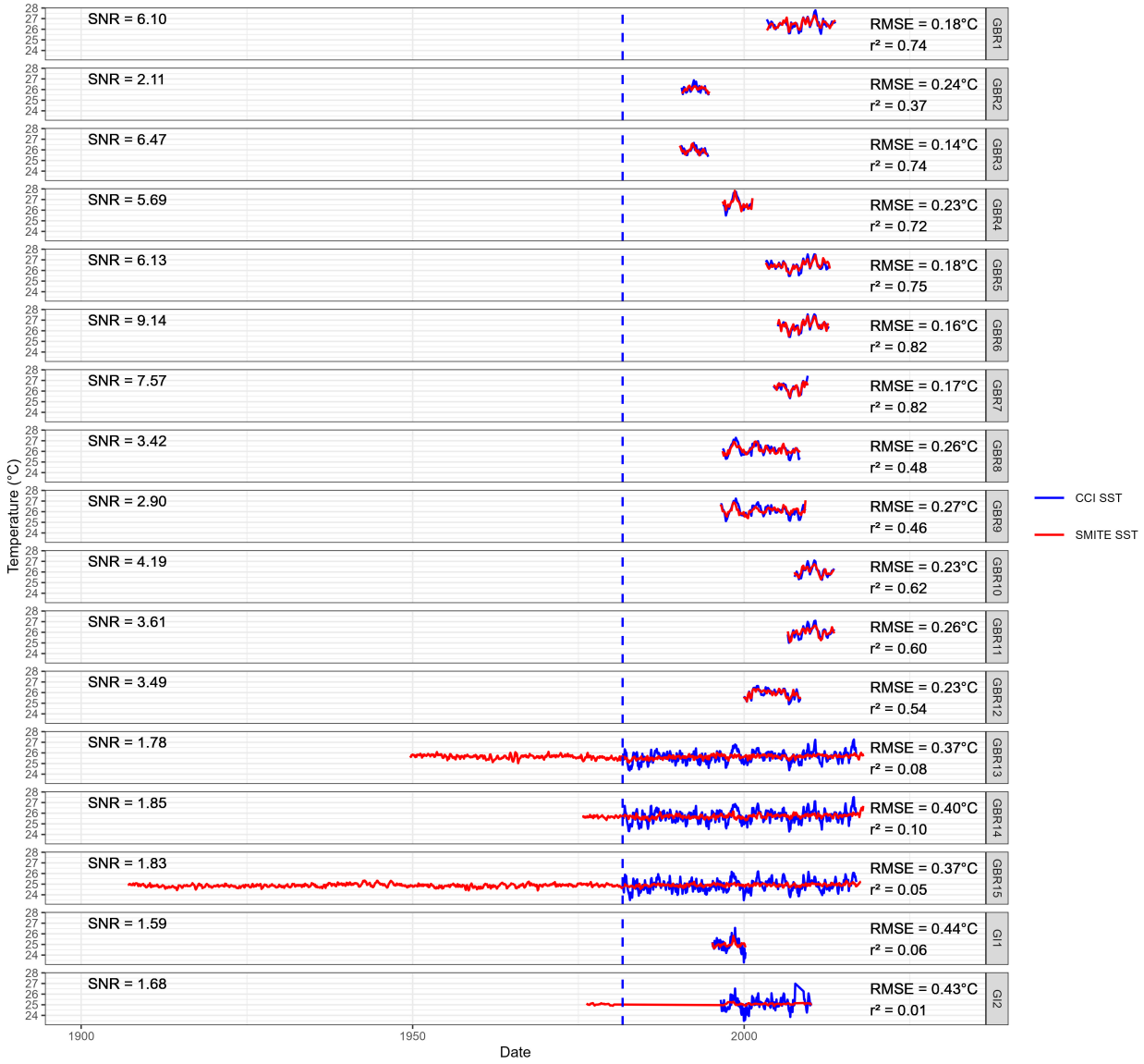

Figure C.4: Individual SMITE SST reconstructions across all deseasonalized coral records used in this study (GBR1-15, GI1-2). Each panel shows the reconstructed SST time series (red) along the satellite-derived CCI SST target (blue). The root mean square error (RMSE) and correlation coefficient (r^2) between SMITE SST and CCI SST for each reconstruction are reported in the upper-right corner of each panel. The signal-to-noise ratio (SNR) for each reconstruction, defined as the proportion of variance in CCI SST and the squared RMSE, are reported in the upper-left corner of each panel. The vertical dashed line represents the earliest date of the CCI SST dataset. These reconstructions reflect fully regularized SMITE models, designed to minimize overfitting and maximize reproducibility.

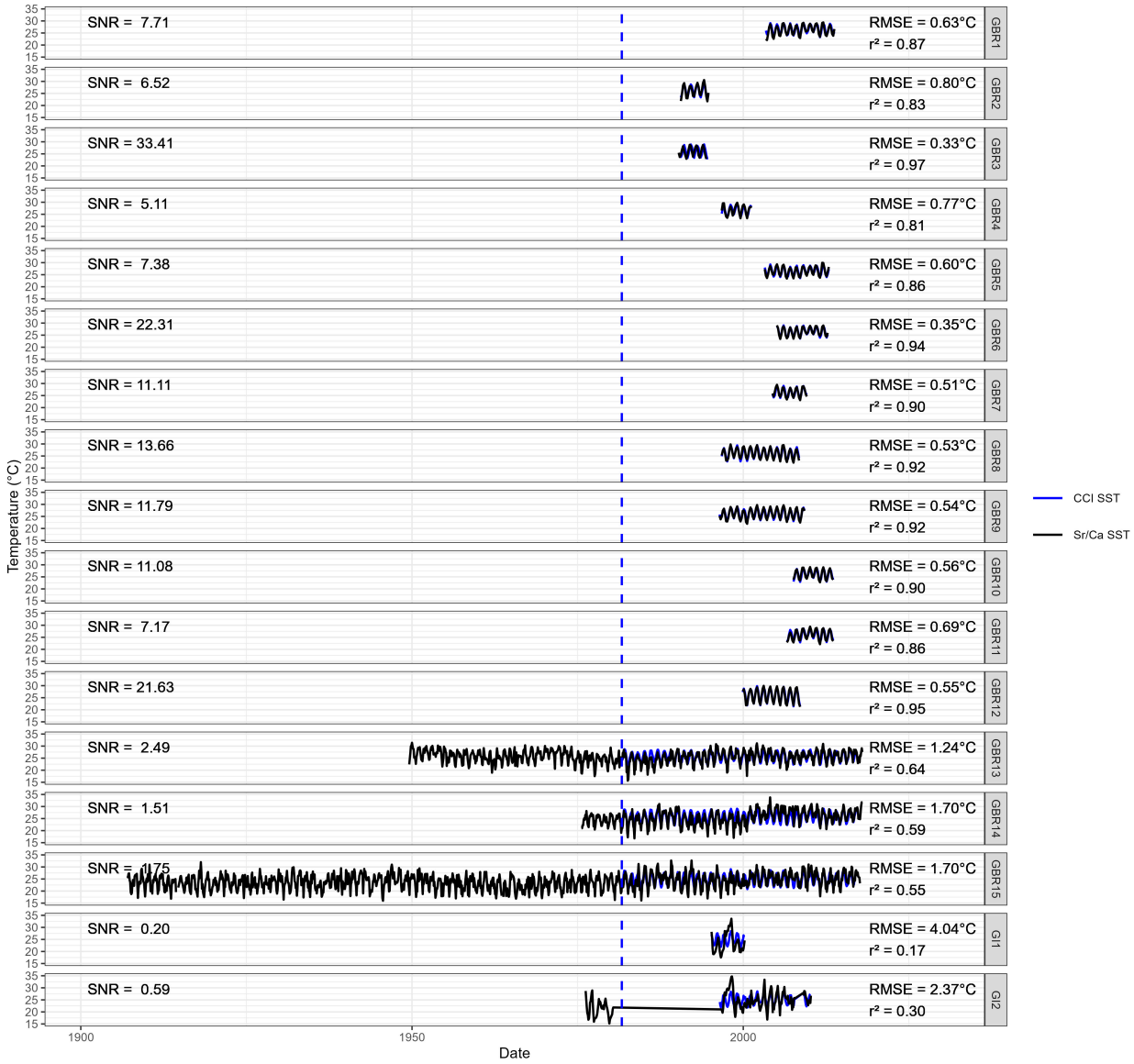

Figure C.5: Individual Sr/Ca SST reconstructions across all seasonal coral records used in this study (GBR1-15, GI1-2). Each panel shows the reconstructed SST time series (black) along the satellite-derived CCI SST target (blue). The root mean square error (RMSE) and correlation coefficient (r^2) between SMITE SST and CCI SST for each reconstruction are reported in the upper-right corner of each panel. The signal-to-noise ratio (SNR) for each reconstruction, defined as the proportion of variance in CCI SST and the squared RMSE, are reported in the upper-left corner of each panel. The vertical dashed line represents the earliest date of the CCI SST dataset.

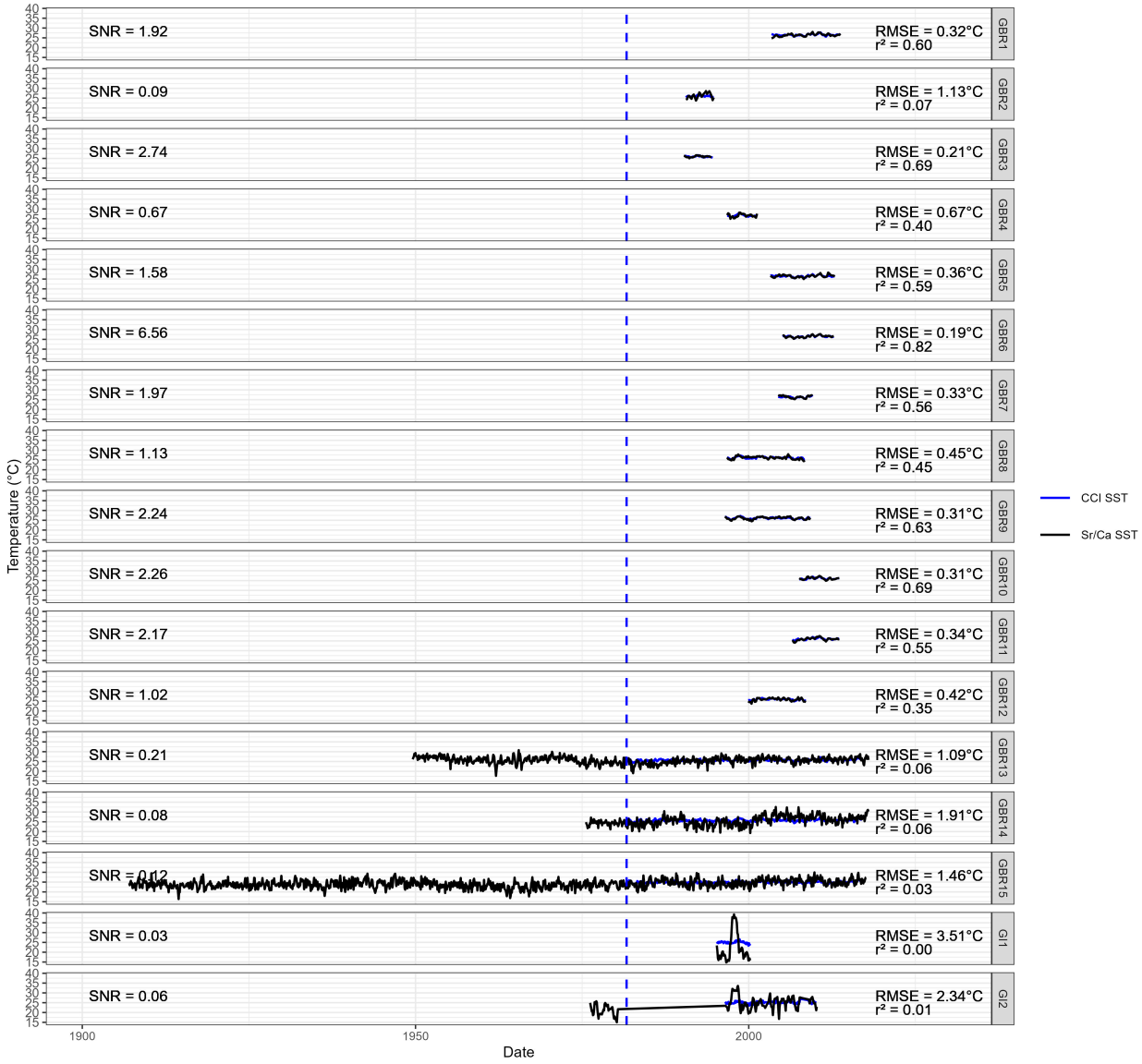

Figure C.6: Individual Sr/Ca SST reconstructions across all deseasonalized coral records used in this study (GBR1-15, GI1-2). Each panel shows the reconstructed SST time series (black) along the satellite-derived CCI SST target (blue). The root mean square error (RMSE) and correlation coefficient (r^2) between SMITE SST and CCI SST for each reconstruction are reported in the upper-right corner of each panel. The signal-to-noise ratio (SNR) for each reconstruction, defined as the proportion of variance in CCI SST and the squared RMSE, are reported in the upper-left corner of each panel. The vertical dashed line represents the earliest date of the CCI SST dataset.

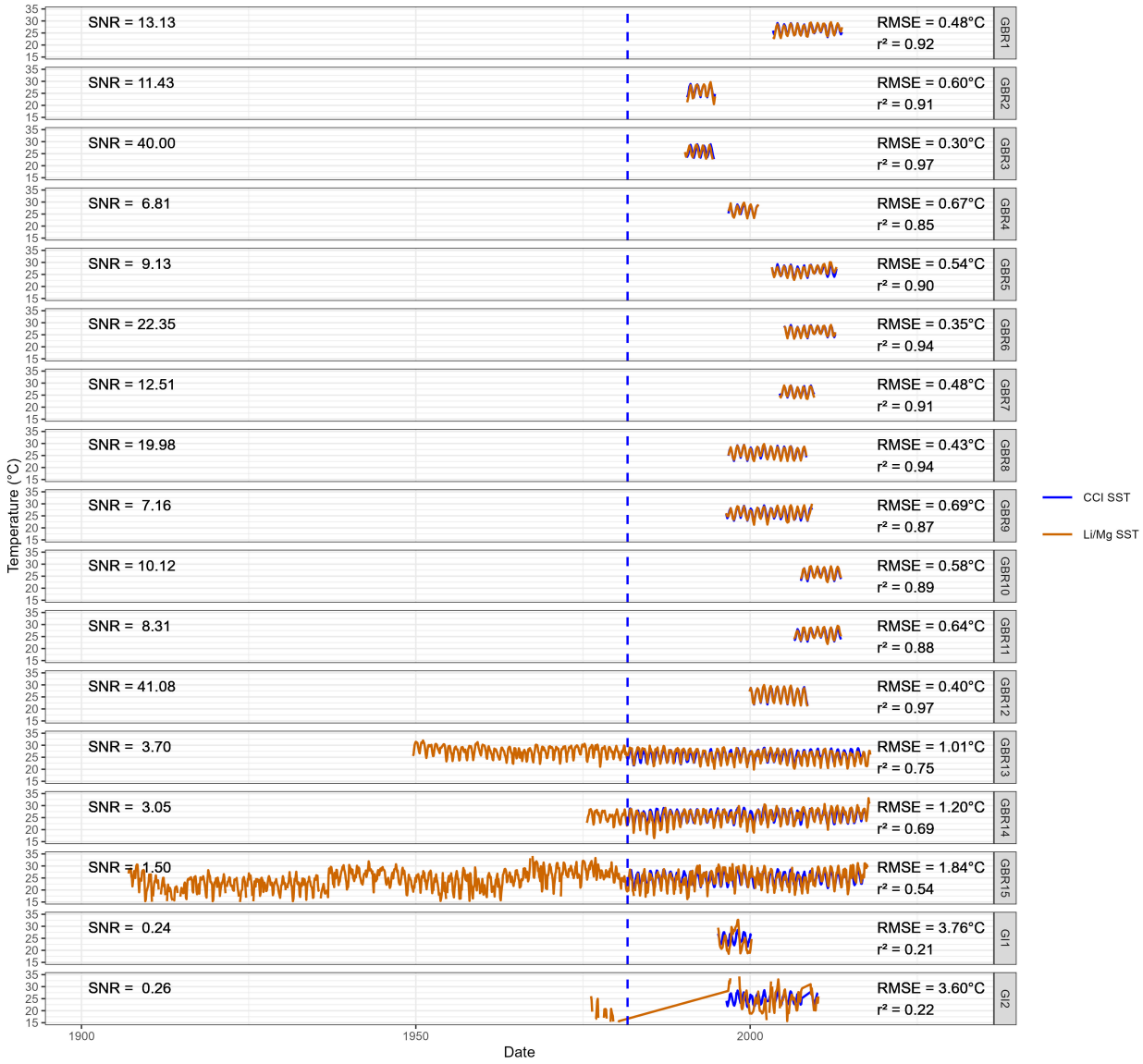

Figure C.7: Individual Li/Mg SST reconstructions across all seasonal coral records used in this study (GBR1-15, GI1-2). Each panel shows the reconstructed SST time series (orange) along the satellite-derived CCI SST target (blue). The root mean square error (RMSE) and correlation coefficient (r^2) between SMITE SST and CCI SST for each reconstruction are reported in the upper-right corner of each panel. The signal-to-noise ratio (SNR) for each reconstruction, defined as the proportion of variance in CCI SST and the squared RMSE, are reported in the upper-left corner of each panel. The vertical dashed line represents the earliest date of the CCI SST dataset.

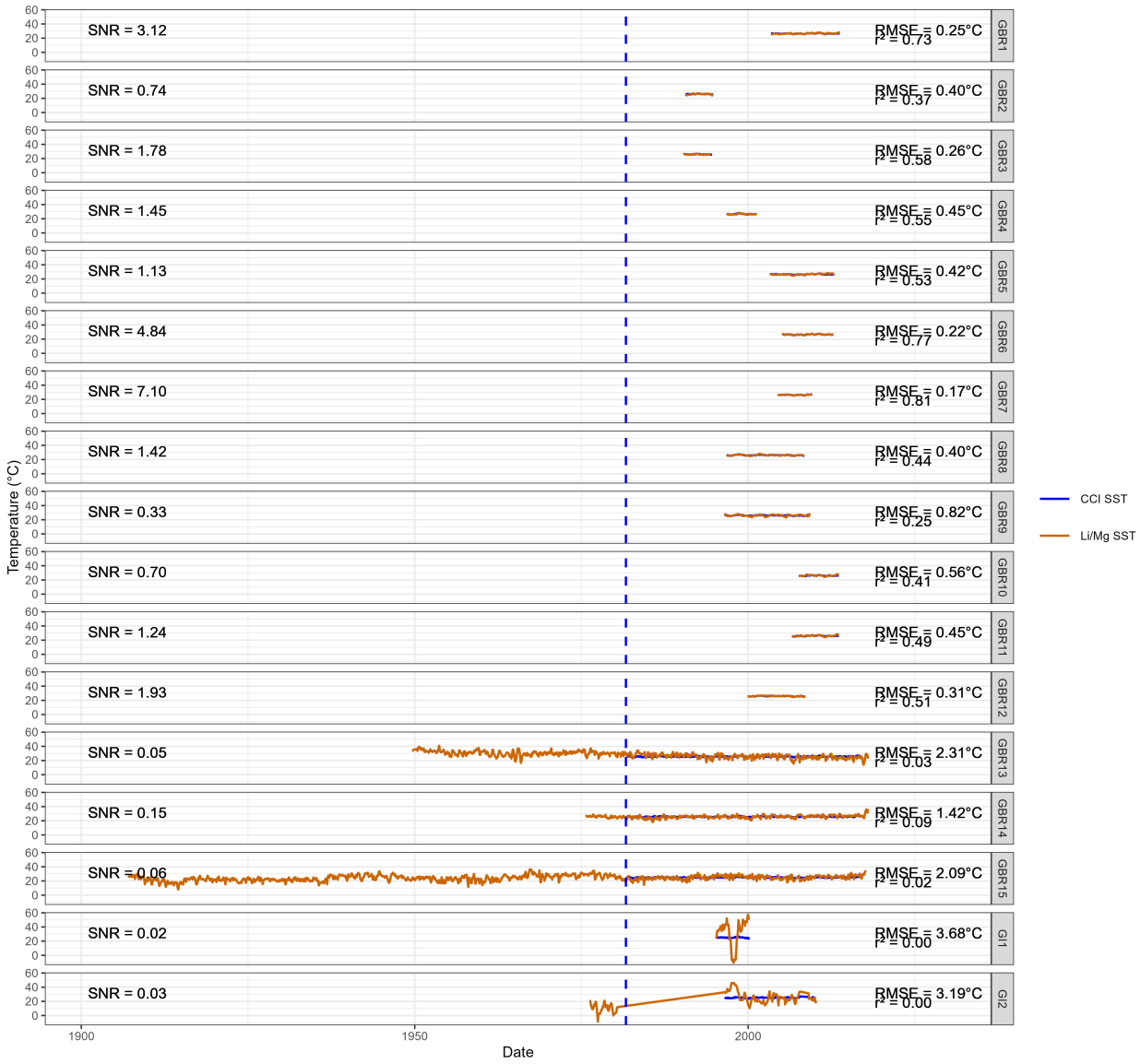

Figure C.8: Individual Li/Mg SST reconstructions across all deseasonalized coral records used in this study (GBR1-15, GI1-2). Each panel shows the reconstructed SST time series (orange) along the satellite-derived CCI SST target (blue). The root mean square error (RMSE) and correlation coefficient (r^2) between SMITE SST and CCI SST for each reconstruction are reported in the upper-right corner of each panel. The signal-to-noise ratio (SNR) for each reconstruction, defined as the proportion of variance in CCI SST and the squared RMSE, are reported in the upper-left corner of each panel. The vertical dashed line represents the earliest date of the CCI SST dataset.

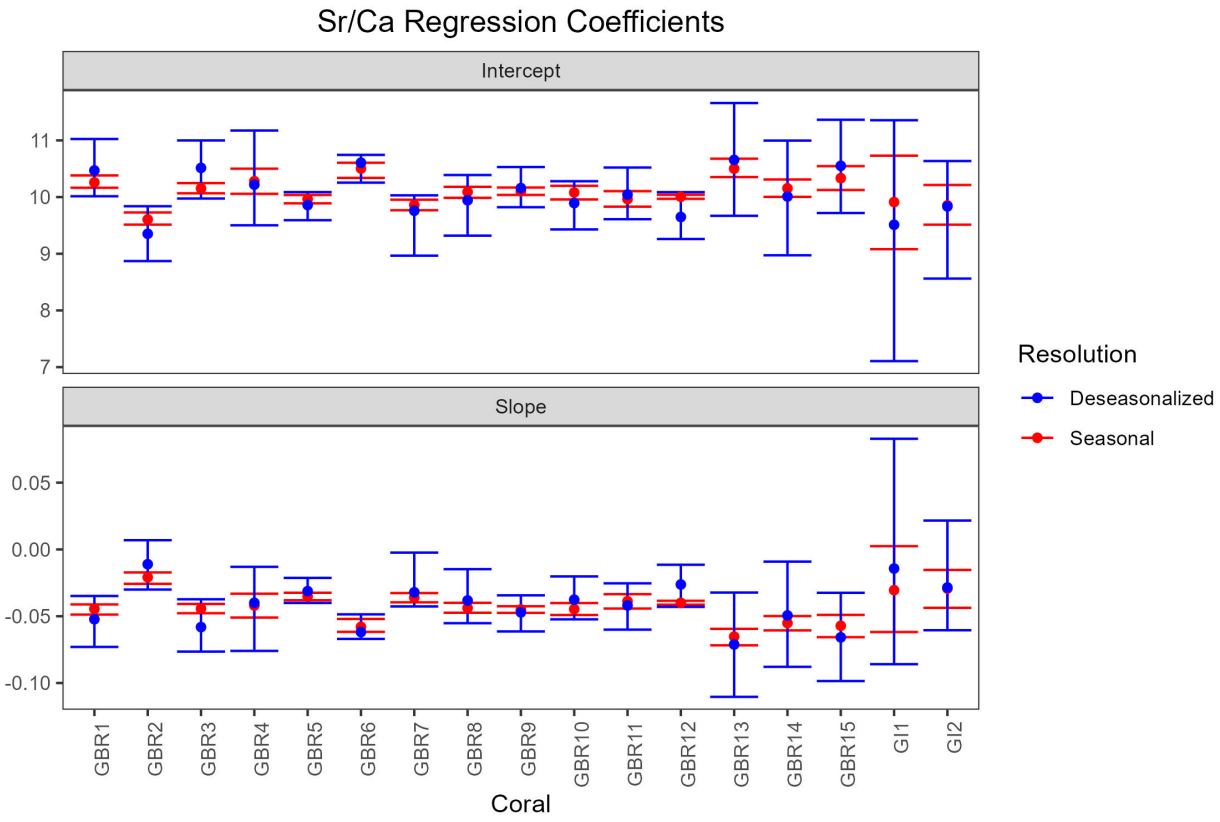

Figure C.9: Model parameters from the linear univariate Sr/Ca calibrations performed on all corals used in this study, inferred from block-bootstrap cross-validated Weighted Least Squares regression. GBR1-15 denote Great Barrier Reef corals, while GI1-2 denote Galapagos corals. Red error bars indicate the 95% confidence interval.

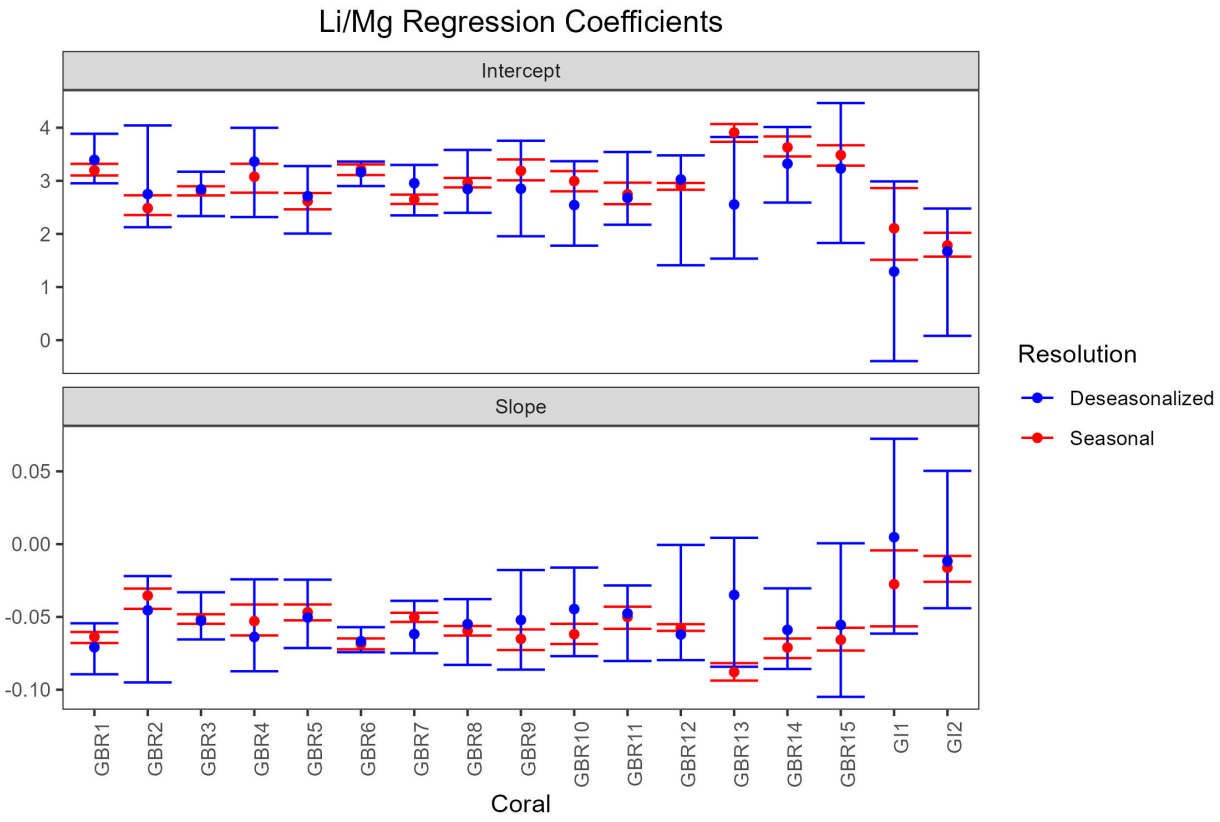

Figure C.10: Model parameters from the linear univariate Li/Mg calibrations performed on all corals used in this study, inferred from block-bootstrap Weighted Least Squares regression. GBR1-15 denote Great Barrier Reef corals, while GI1-2 denote Galapagos corals. Red error bars indicate the 95% confidence interval.

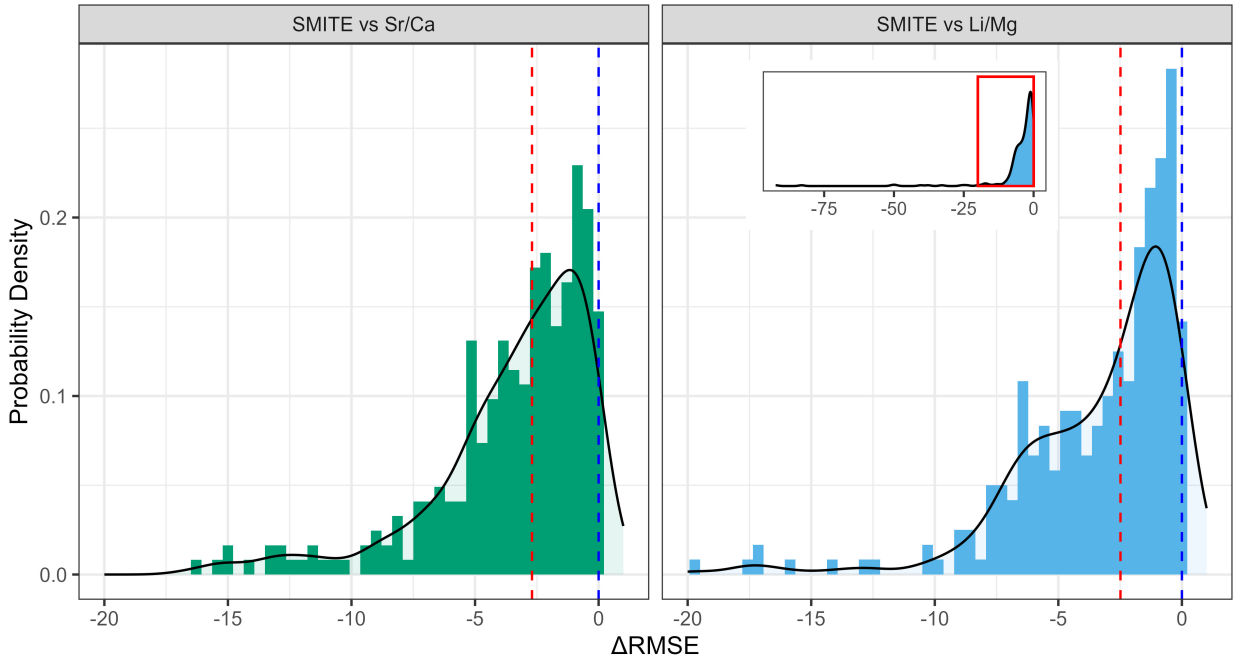

Figure C.11: Histograms showing the difference in root mean square error (RMSE) between SMITE and Sr/Ca (left column), and between SMITE and Li/Mg (right column), for all possible combinations of deseasonalized SST models and coral datasets. Black lines overlaying the histograms indicate probability density functions (PDFs). Blue dashed lines mark zero, indicating no difference between SMITE and the corresponding univariate method. Red dashed lines indicate the median of each distribution. The inset within the right panel shows the full range of ΔnRMSE values between SMITE and Li/Mg, with the red box indicating the domain of the larger panel.

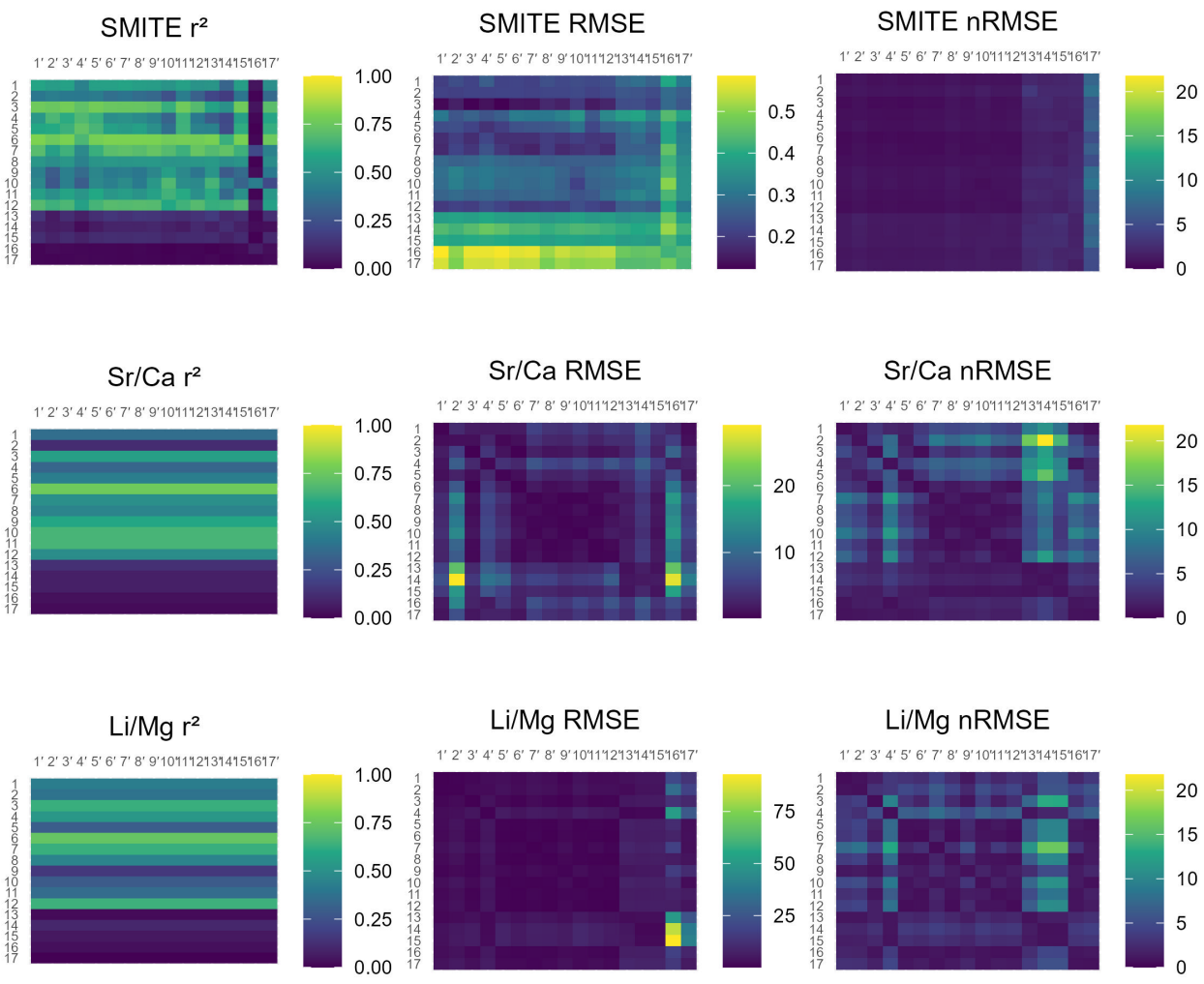

Figure C.12: Summary statistics for SMITE (top row), Sr/Ca (middle row), and Li/Mg (bottom row), for all possible combinations of deseasonalized SST models (x-axis) and coral datasets (y-axis). The diagonal represents where an SST model is applied to the same coral that it was generated from. Off-diagonal elements thus represent some combination of coral and model. Colors in each cell indicate the value of each summary statistics. Purple indicates lower values for either the squared correlation coefficient (r^2, left column), the root-mean-square-error (RMSE, middle column) or the normalized root mean square error (nRMSE, right column).

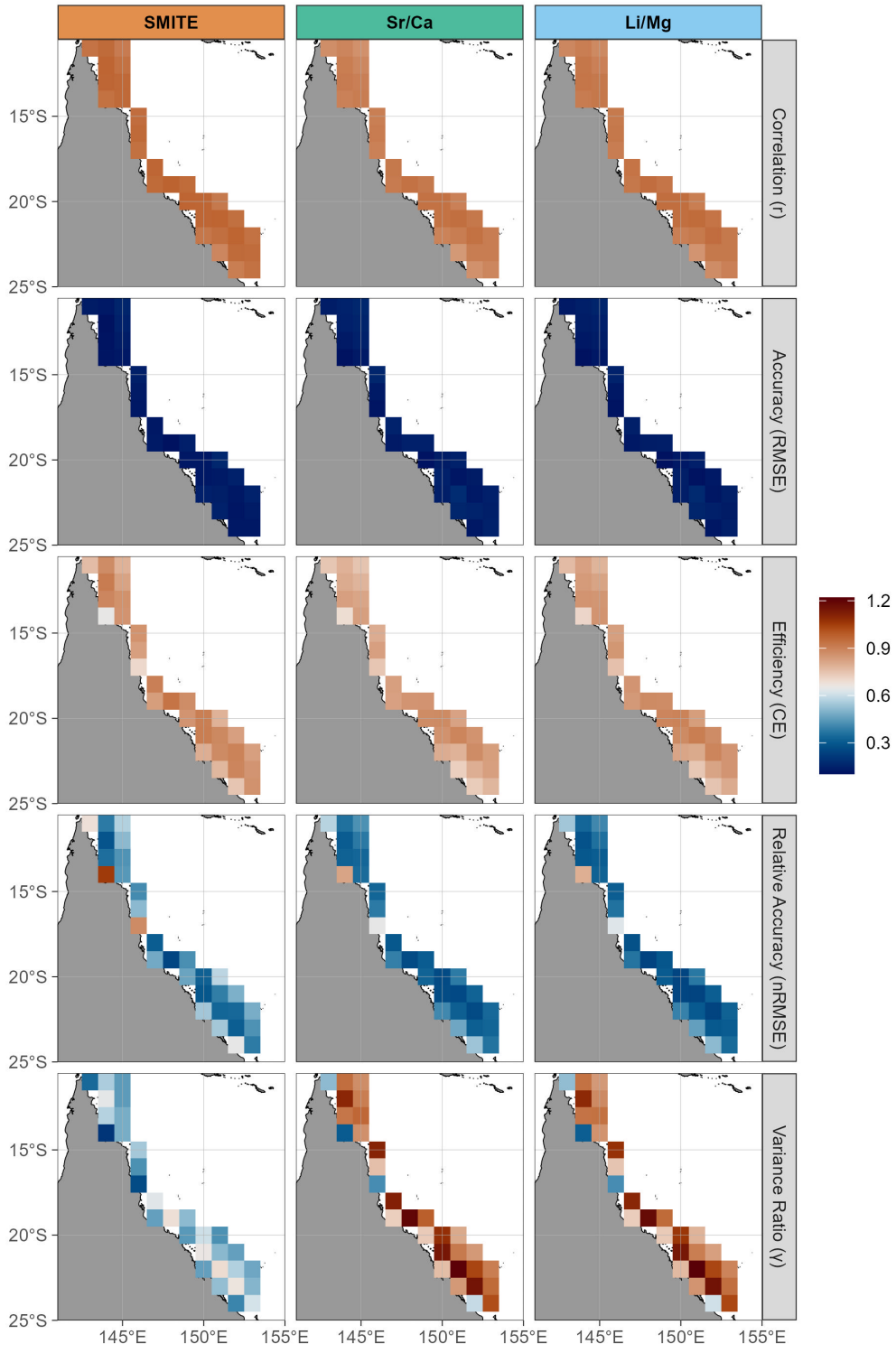

Figure C.13: Median summary statistics for each reconstruction method (columns) across the Great Barrier Reef at the final proxy network size (N=90). Rows represent correlation (r), accuracy (RMSE), coefficient of efficiency (CE), relative accuracy (nRMSE), and variance ratio (γ), respectively. Values are mapped onto each SST grid cell to highlight regional variation in reconstruction performance. Summary statistic definitions are provided in Sections 4.2.4 and 4.2.5.

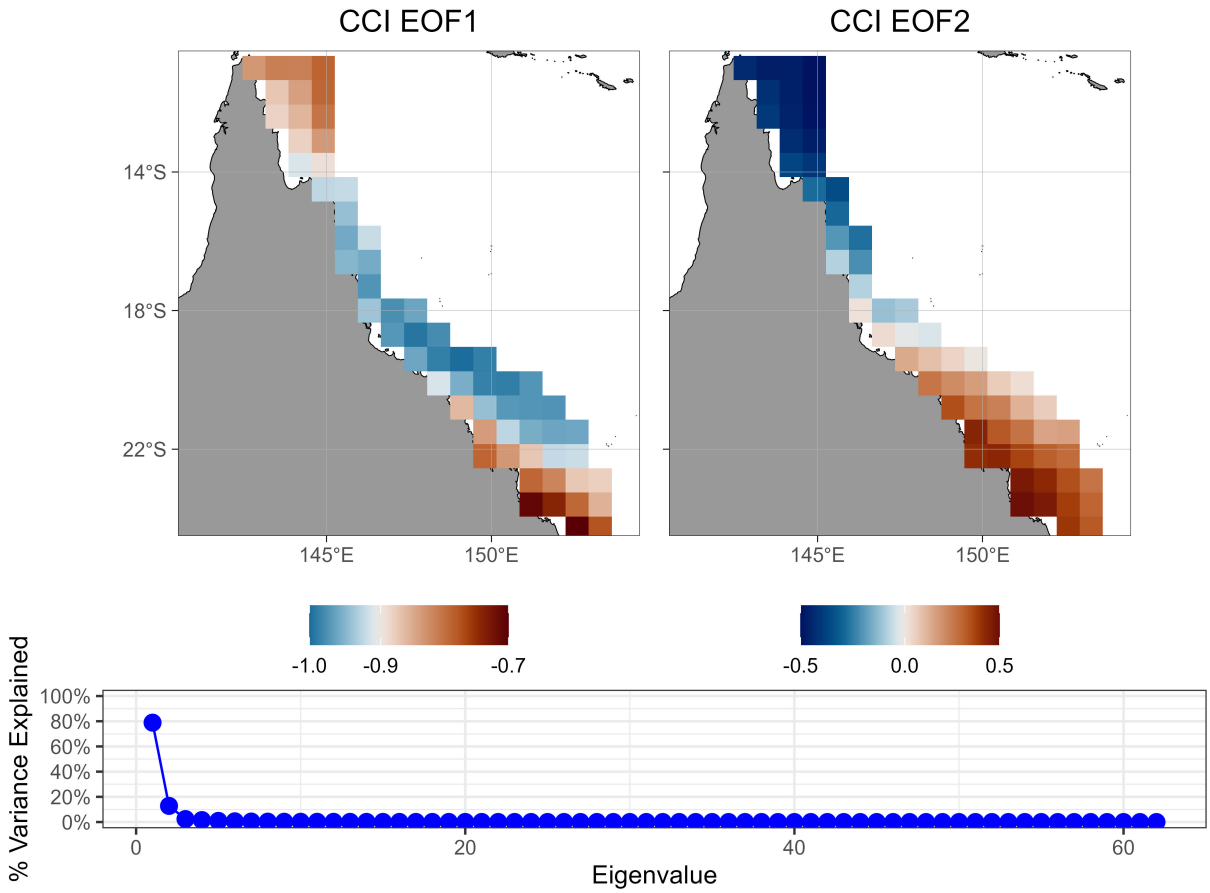

Figure C.14: Leading modes of SST variability over the Great Barrier Reef (GBR) associated with the first and second Empirical Orthogonal Function (EOF1 and EOF2) of the European Space Agency Climate Change Initiative sea surface temperature dataset (CCI; 1981-2016). Top panels: Spatial loadings of CCI EOF1 and EOF2 over the GBR. The color scale of each map is centered on the mean value to contrast loadings. Bottom panel: Eigenvalues derived from the CCI SST dataset against their respective total variance explained (%).

C.2 Individual Seasonal Reconstruction Summaries

The following pages contain individual reconstruction results from the seasonal calibrations of all Great Barrier Reef (GBR1-15) and Galapagos (GI1-2) corals. The following results are reported for each coral record:

1) The covariance matrix of the coral geochemical variables that were input into the SMITE calibration (B/Ca, Li/Ca, Li/Mg, Mg/Ca, Sr/Ca, U/Ca).

2) Normalized, age-modeled time-series of each coral geochemical variable (orange) plotted alongside normalized sea surface temperature (SST) estimates from the European Space Agency's Climate Change Initiative SST dataset (CCI SST; black).

3) SST reconstructions for SMITE (orange), Sr/Ca (green), and Li/Mg (blue), plotted alongside CCI SST (black). Error bars around each SST reconstruction are the cross-validated root mean square error (RMSE) from each calibration.

4) SMITE model parameters for the respective calibration (large red points) plotted over the SMITE model parameters for all calibrations. Error bars on the local SMITE model parameters are defined using a block-bootstrap cross-validation approach described in Section 4.2.4. The legend for the color and shape of the points is provided by Figure 4.5 in the main body of the manuscript.

5) A table of the summary statistics for each SST reconstruction method for each coral record (SEP = Standard Error of Prediction, RMSE = root-mean-square-error, R = Pearson Correlation Coefficient). Errors estimated using a block-bootstrap cross-validation approach for each summary statistic (except for SEP) can be seen in Figure 4.3.

GBR1

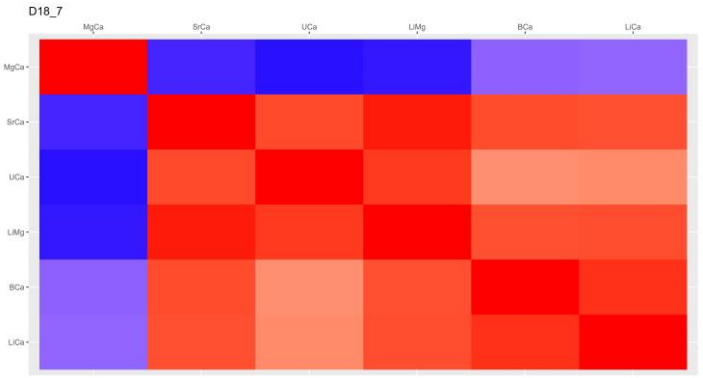

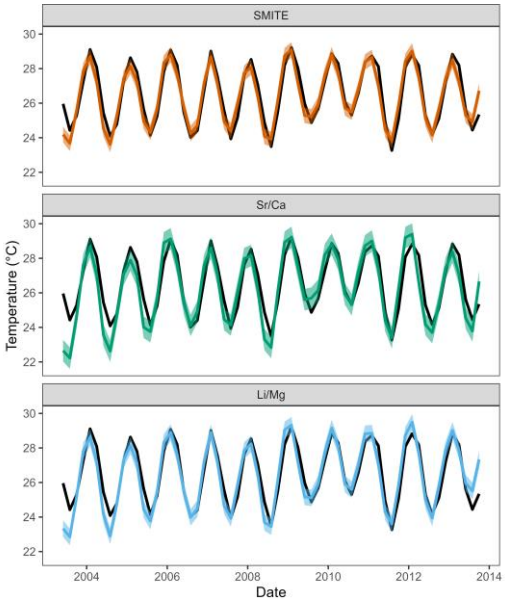

	RMSE	R
SMITE	0.28	0.99
Sr/Ca	0.33	0.98
Li/Mg	0.30	0.98

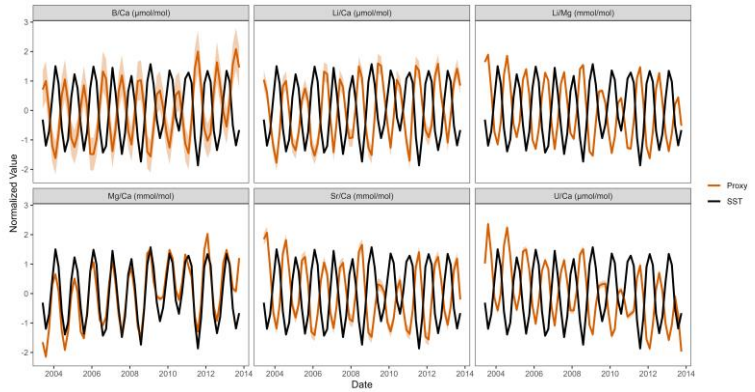

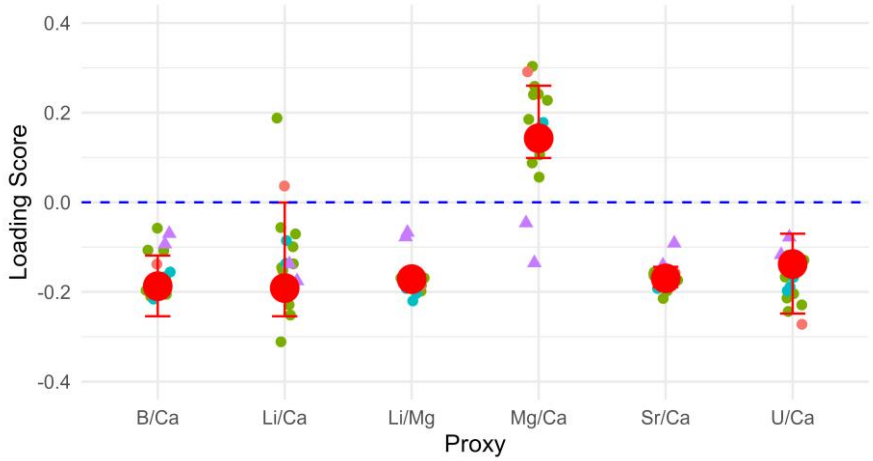

GBR2

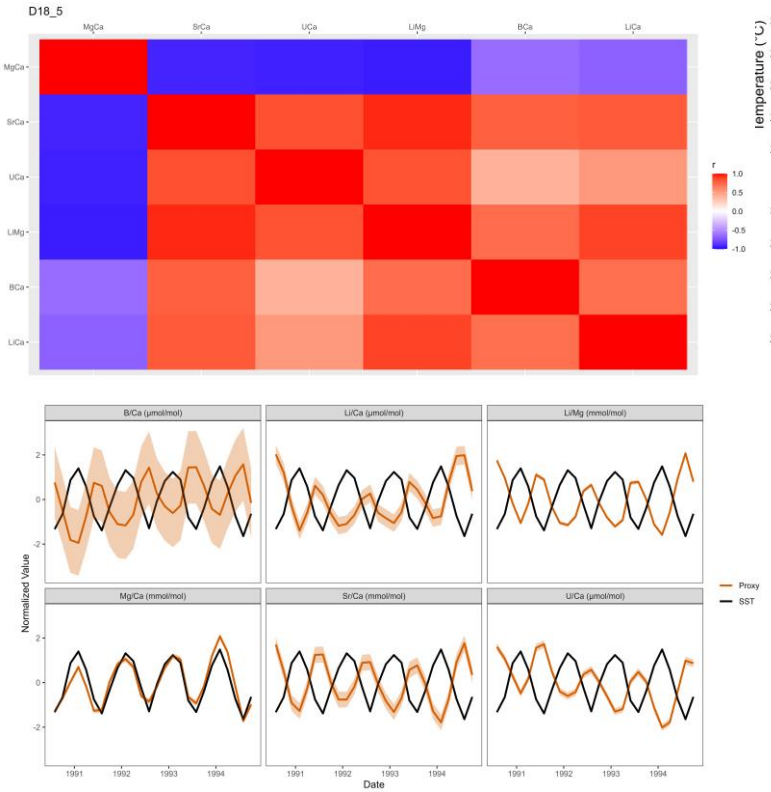

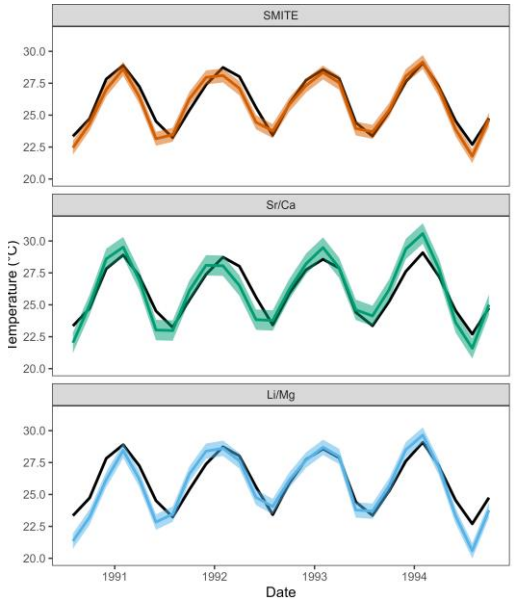

	RMSE	R
SMITE	0.49	0.96
Sr/Ca	0.54	0.96
Li/Mg	0.69	0.94

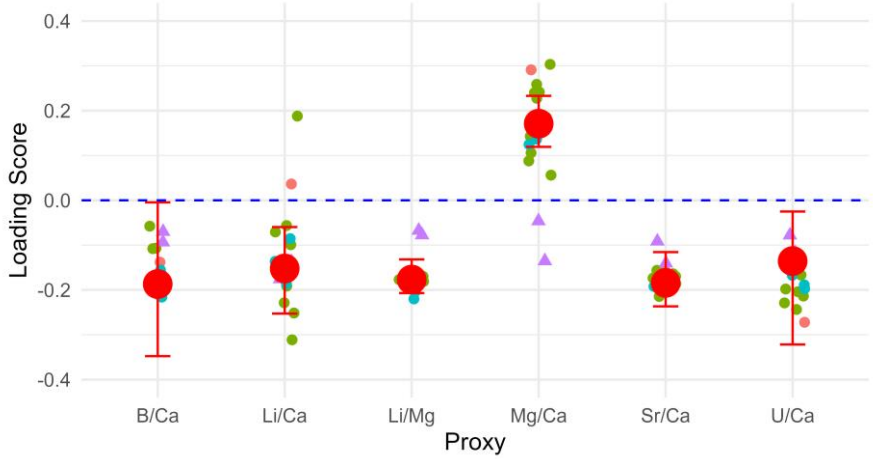

GBR3

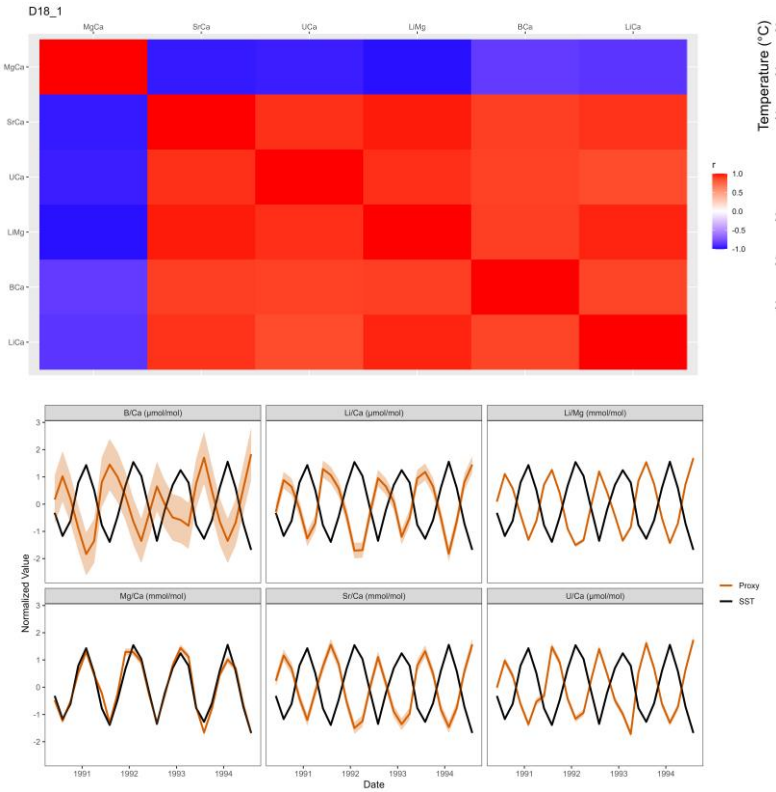

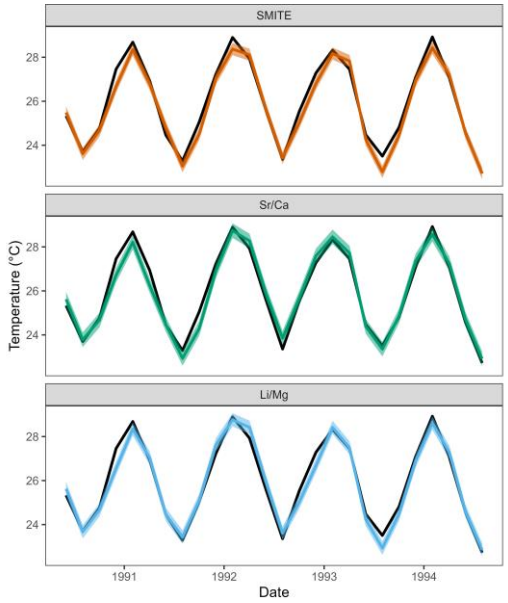

	RMSE	R
SMITE	0.46	0.96
Sr/Ca	0.56	0.95
Li/Mg	0.58	0.94

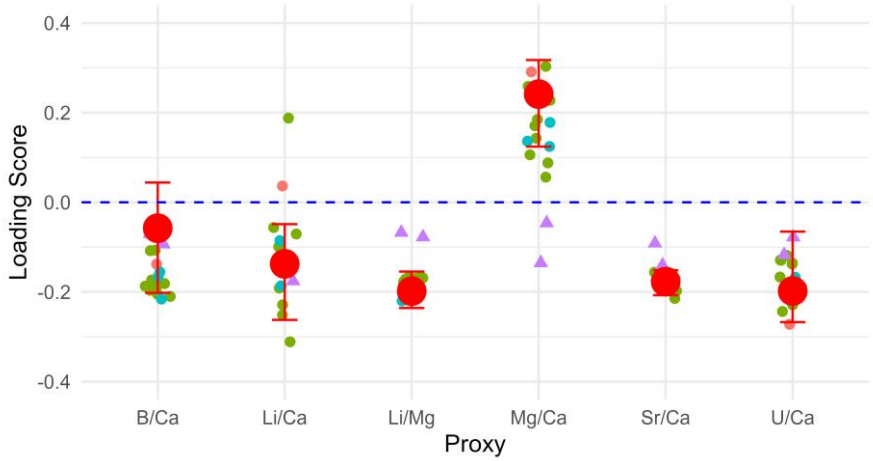

GBR4

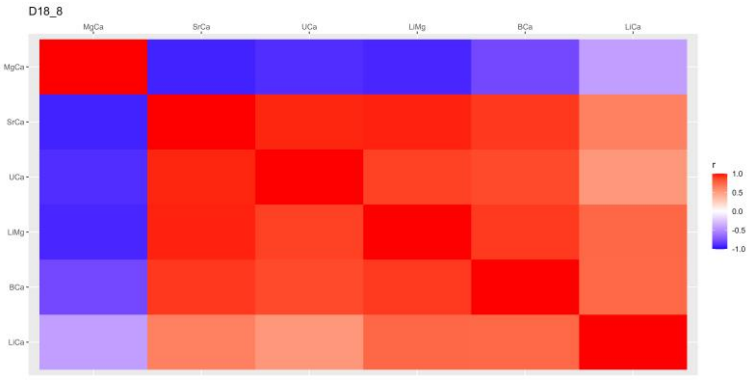

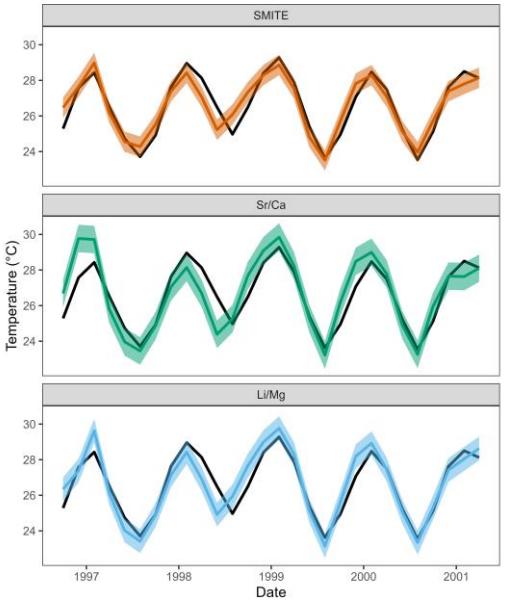

	RMSE	R
SMITE	0.55	0.94
Sr/Ca	0.69	0.93
Li/Mg	0.64	0.94

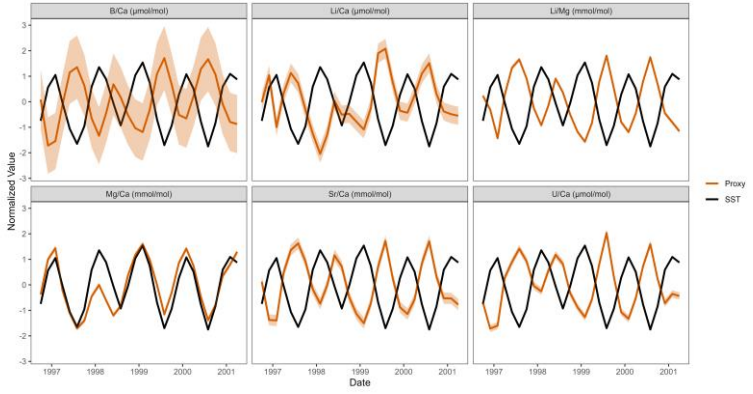

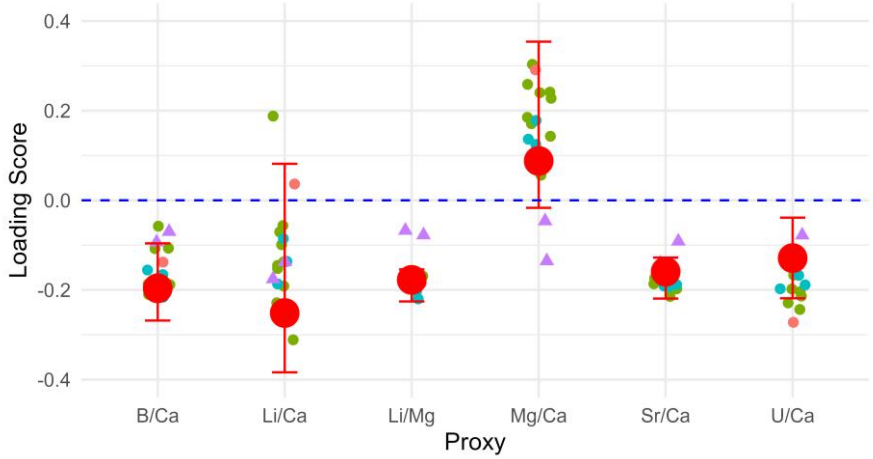

GBR5

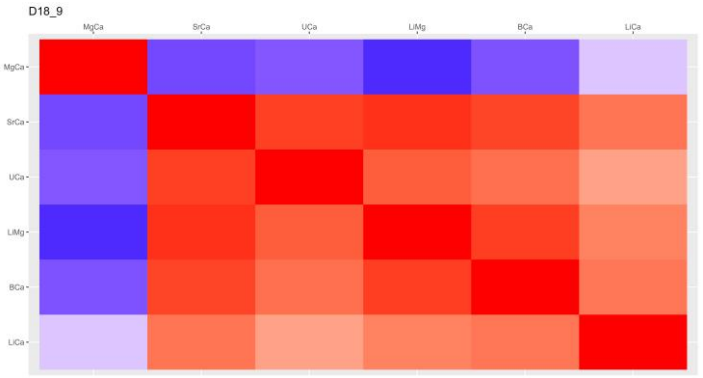

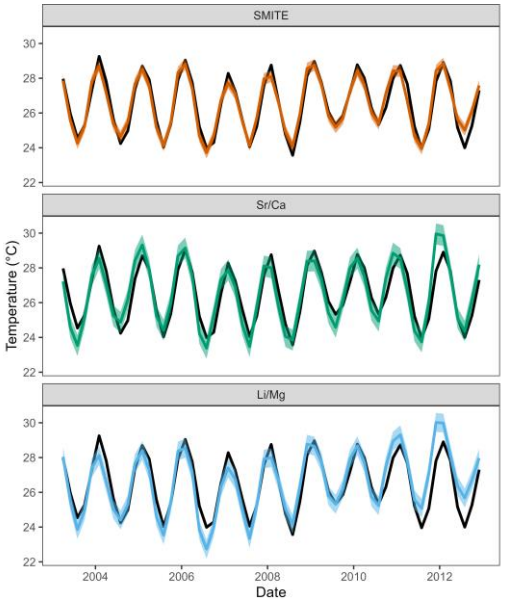

	RMSE	R
SMITE	0.54	0.95
Sr/Ca	0.80	0.91
Li/Mg	0.60	0.95

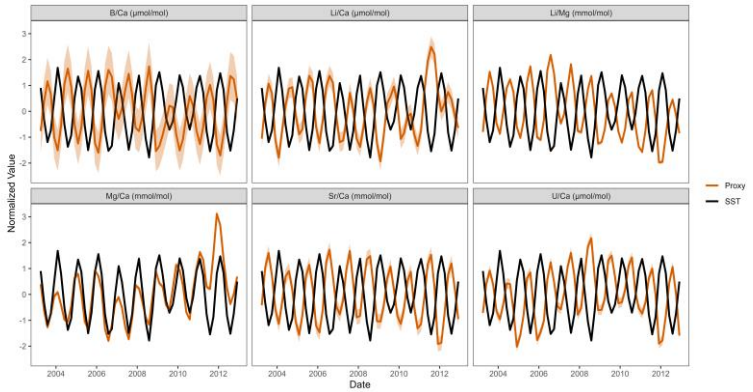

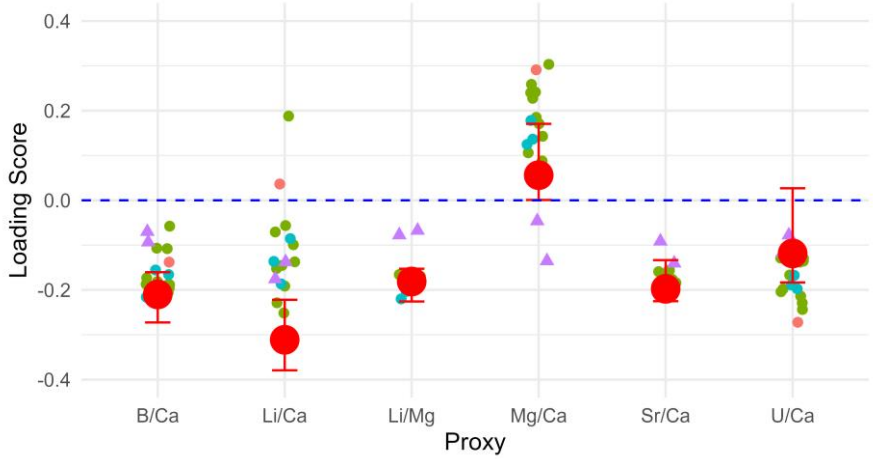

GBR6

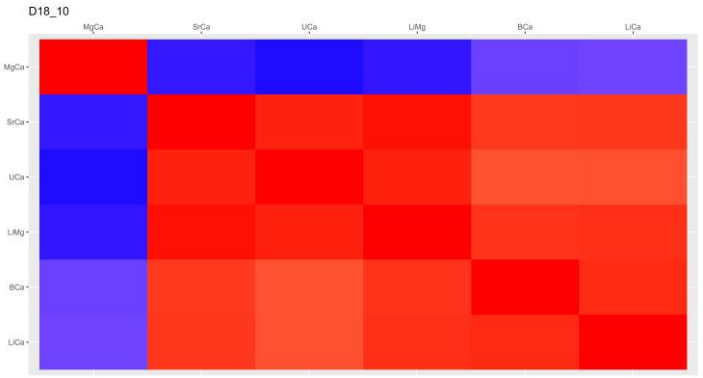

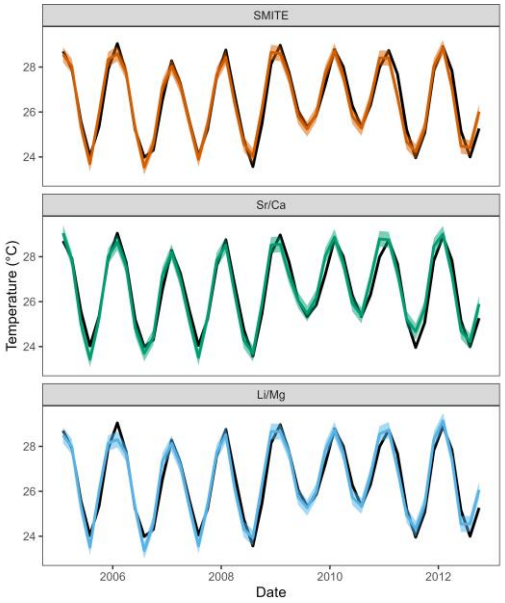

	RMSE	R
SMITE	0.31	0.99
Sr/Ca	0.55	0.97
Li/Mg	0.40	0.99

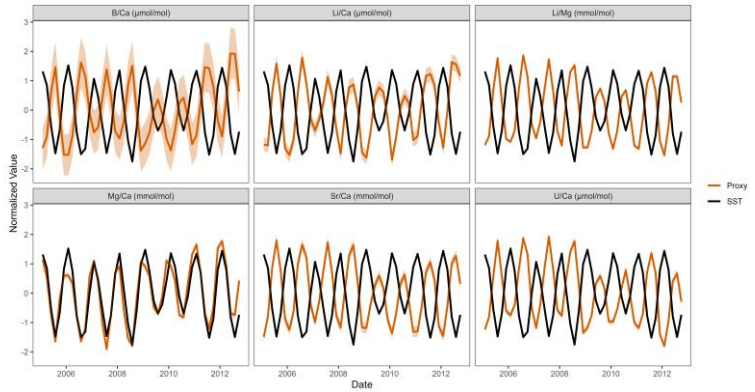

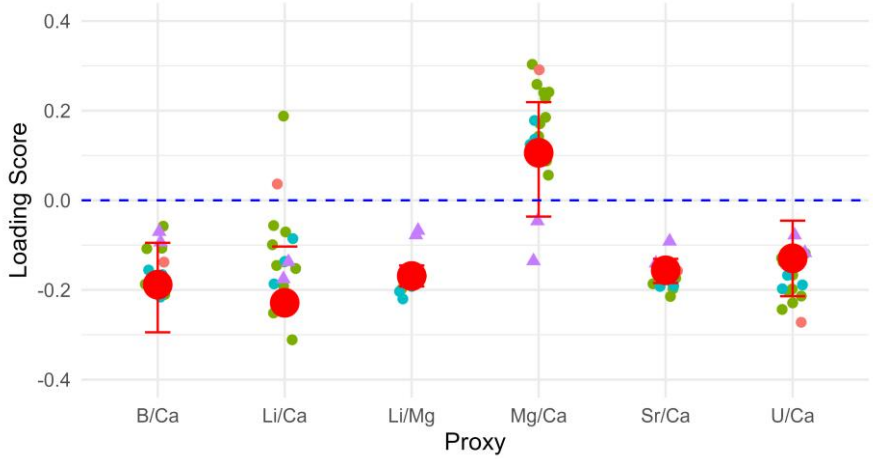

GBR7

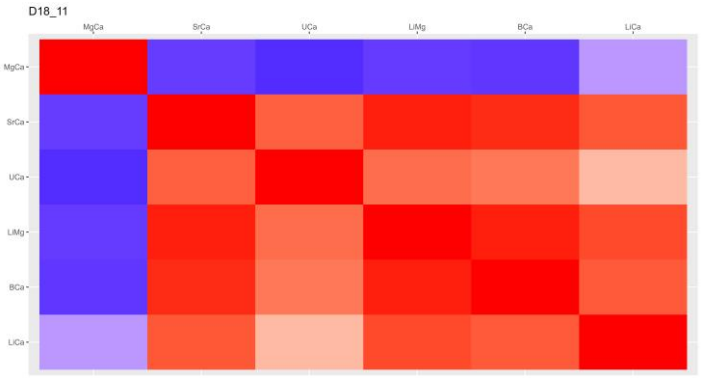

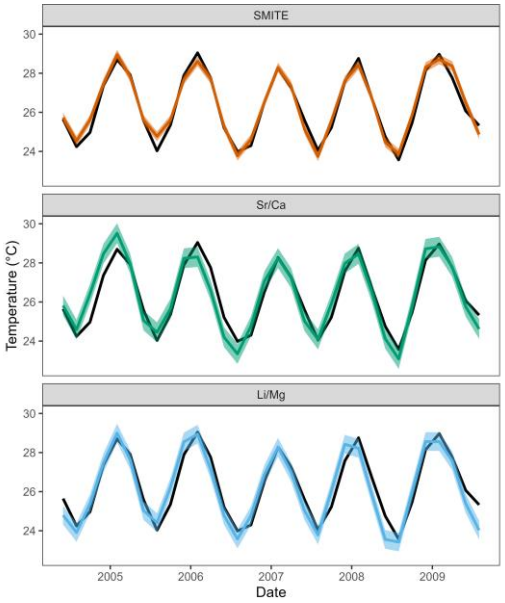

	RMSE	R
SMITE	0.45	0.96
Sr/Ca	0.63	0.93
Li/Mg	0.48	0.96

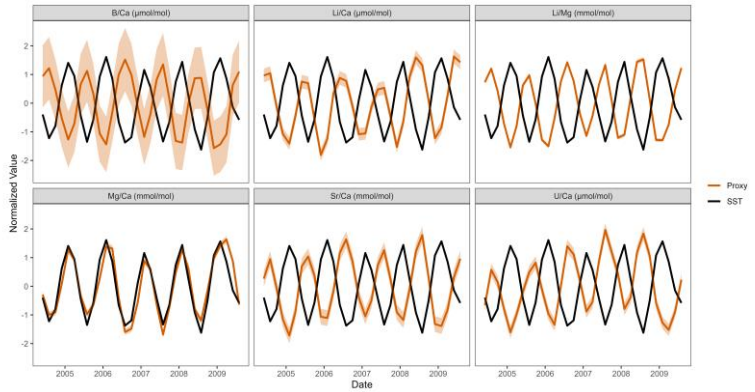

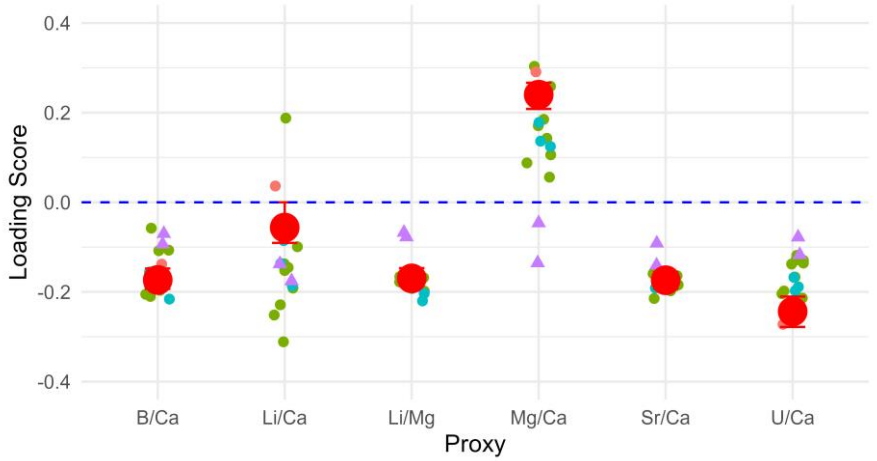

GBR8

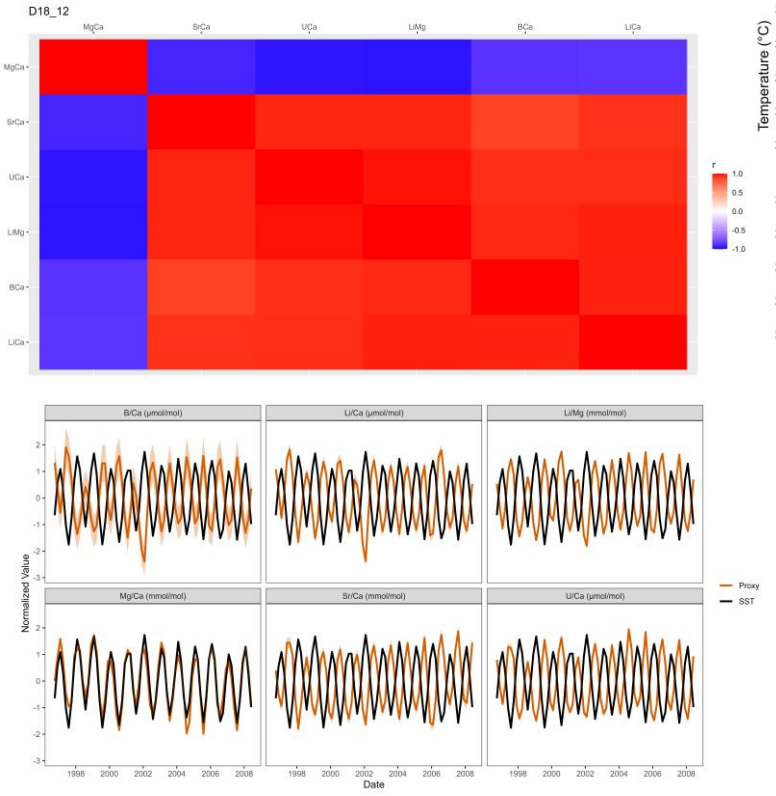

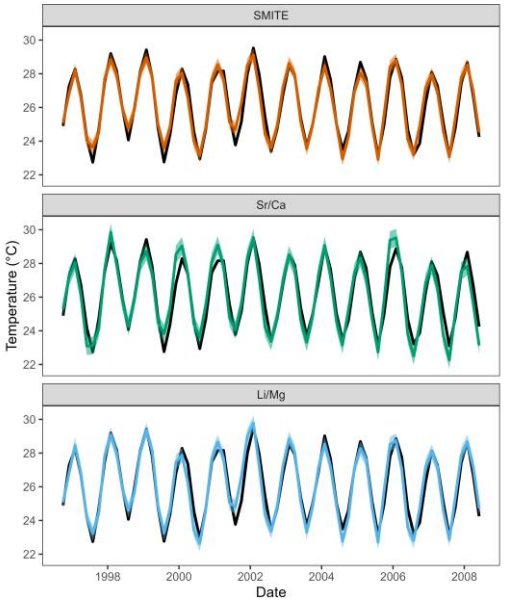

	RMSE	R
SMITE	0.57	0.92
Sr/Ca	0.77	0.90
Li/Mg	0.67	0.92

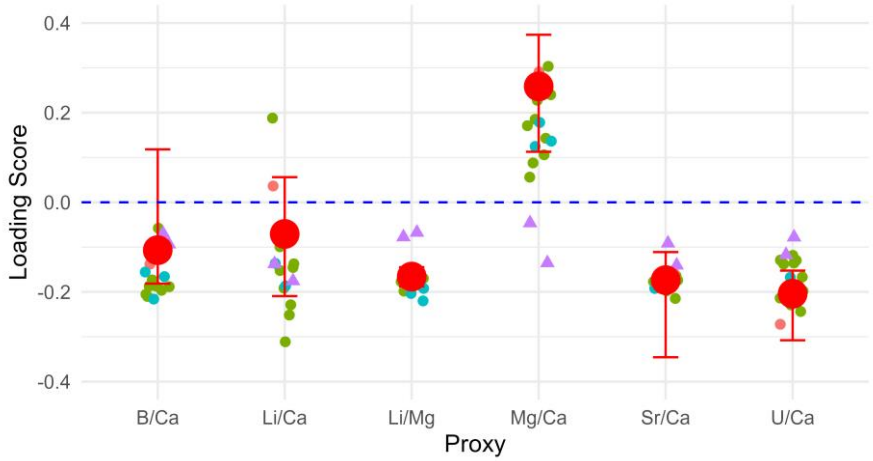

GBR9

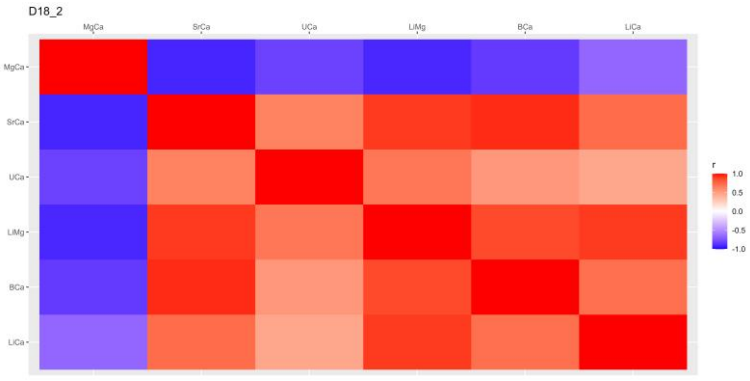

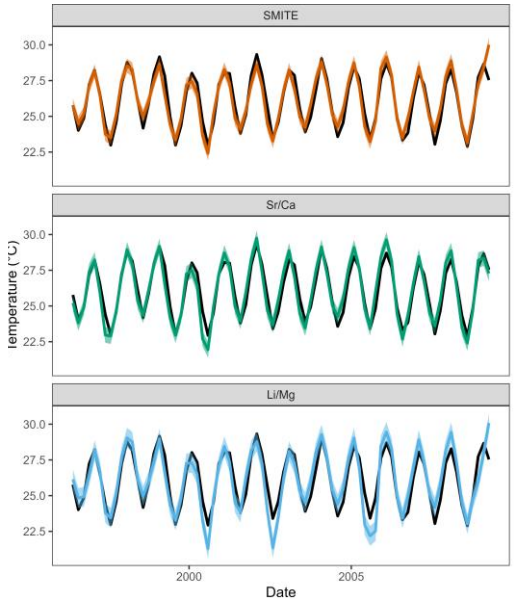

	RMSE	R
SMITE	0.33	0.97
Sr/Ca	0.60	0.93
Li/Mg	0.54	0.95

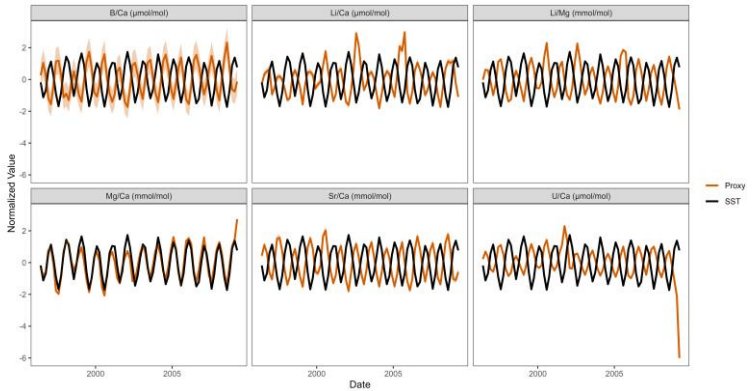

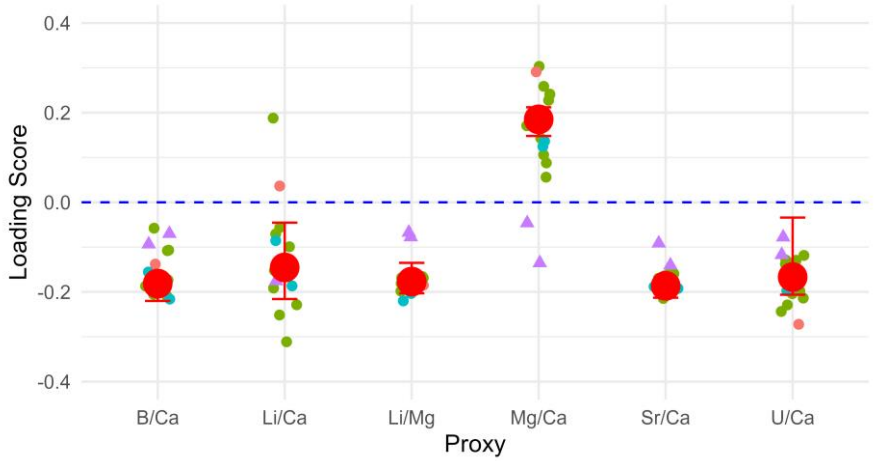

GBR10

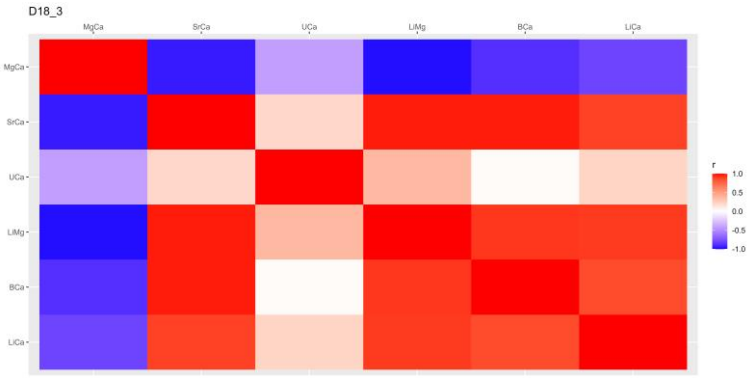

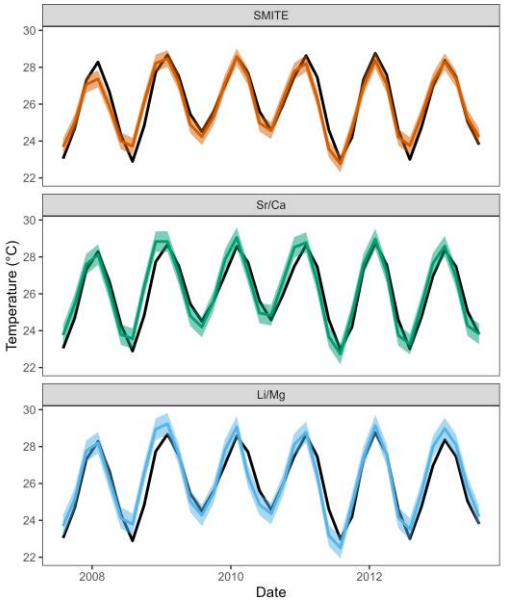

	RMSE	R
SMITE	0.34	0.97
Sr/Ca	0.35	0.97
Li/Mg	0.35	0.97

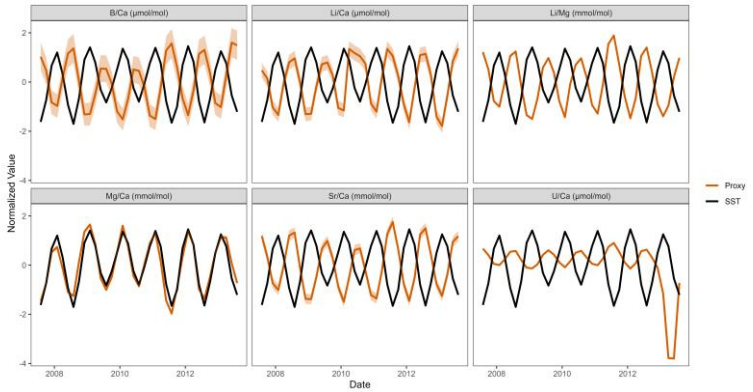

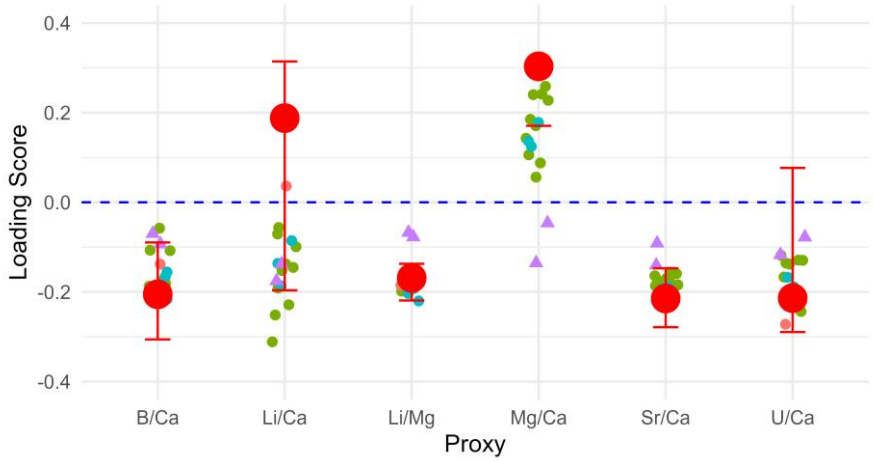

GBR11

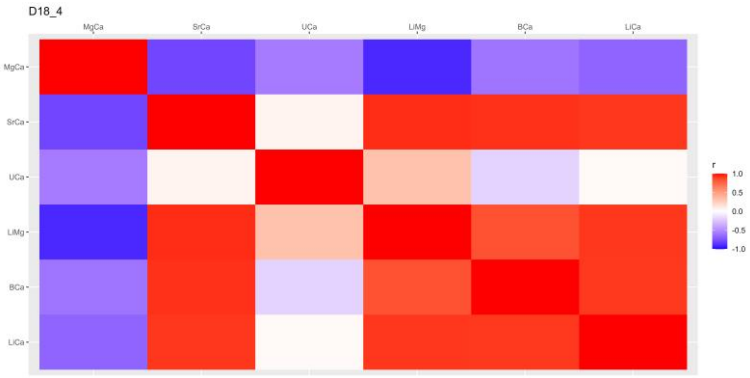

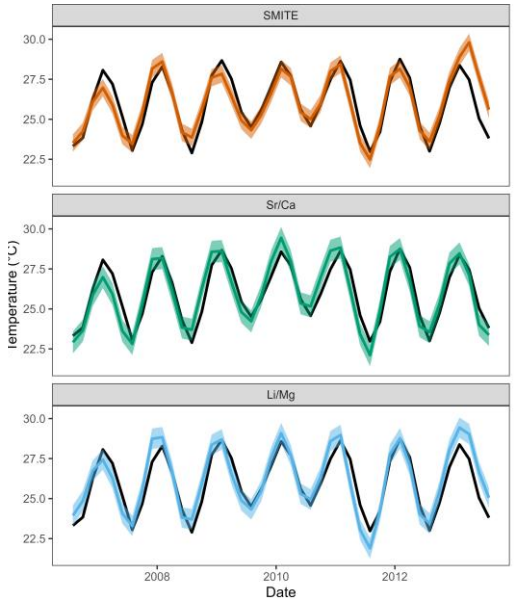

	RMSE	R
SMITE	0.24	0.99
Sr/Ca	0.51	0.95
Li/Mg	0.48	0.95

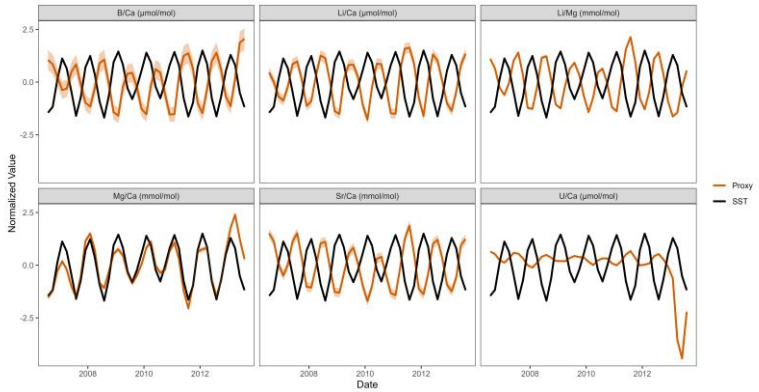

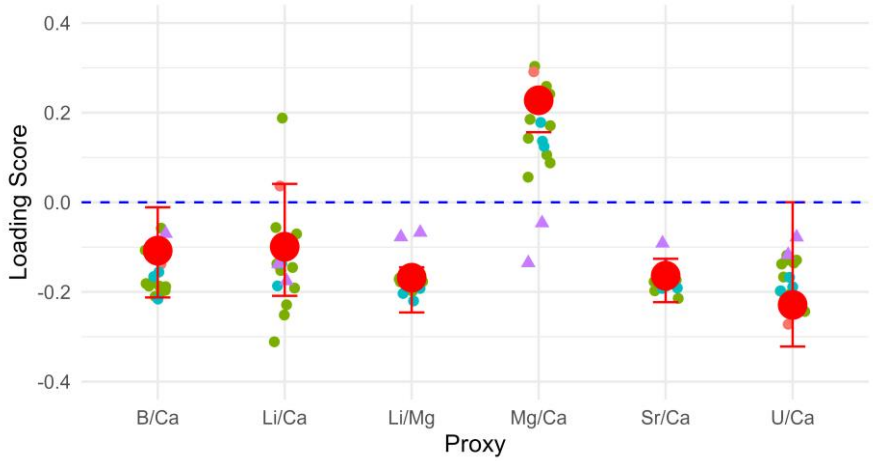

GBR12

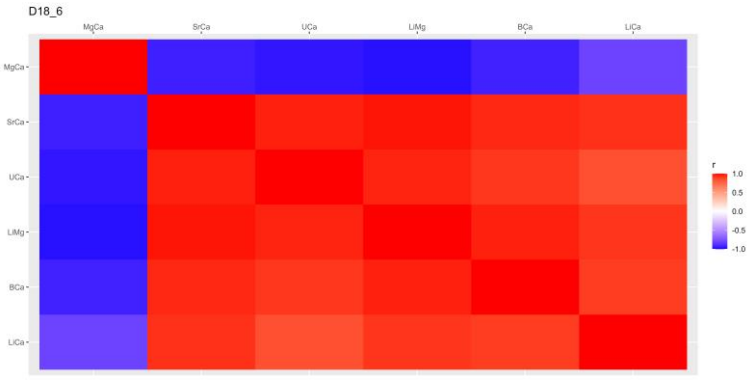

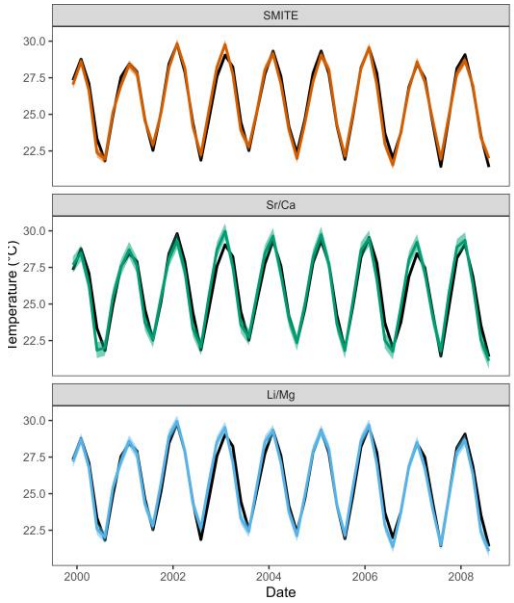

	RMSE	R
SMITE	0.39	0.97
Sr/Ca	0.53	0.96
Li/Mg	0.43	0.97

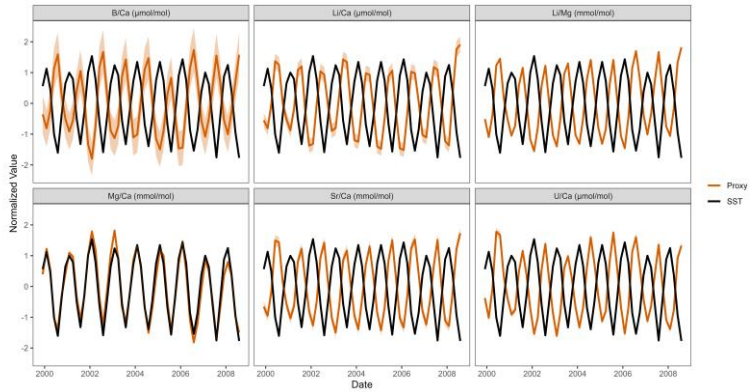

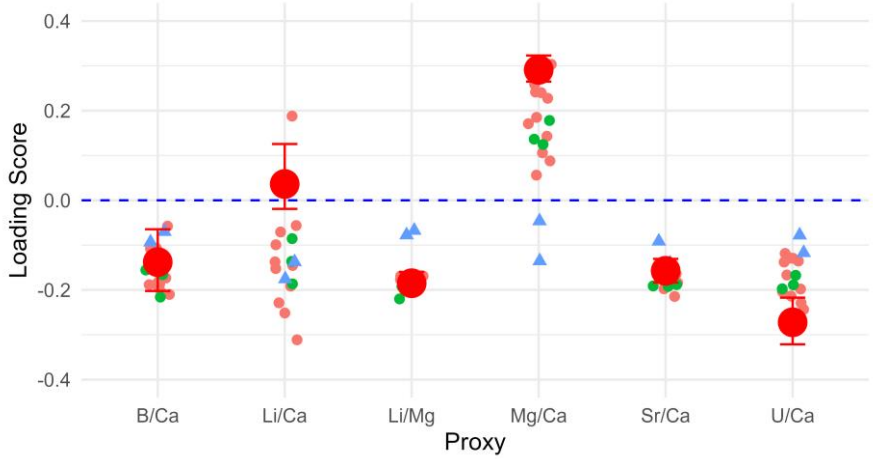

GBR13

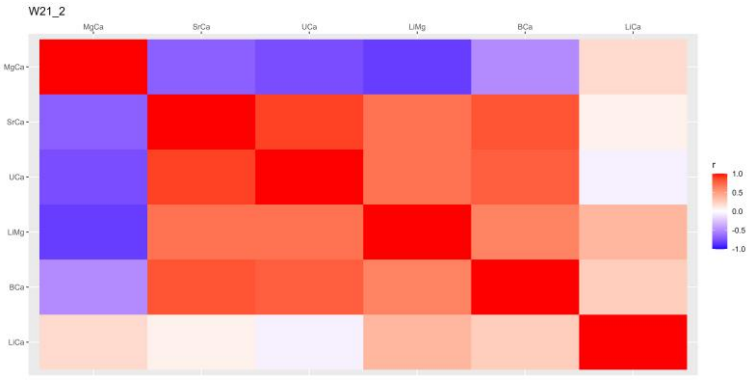

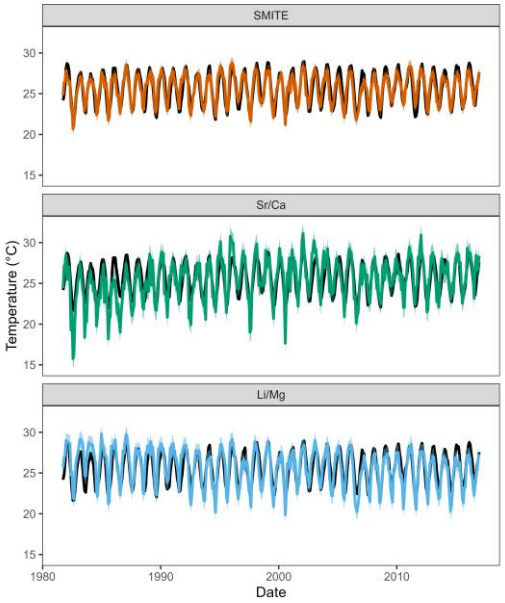

	RMSE	R
SMITE	1.03	0.84
Sr/Ca	1.70	0.74
Li/Mg	1.84	0.74

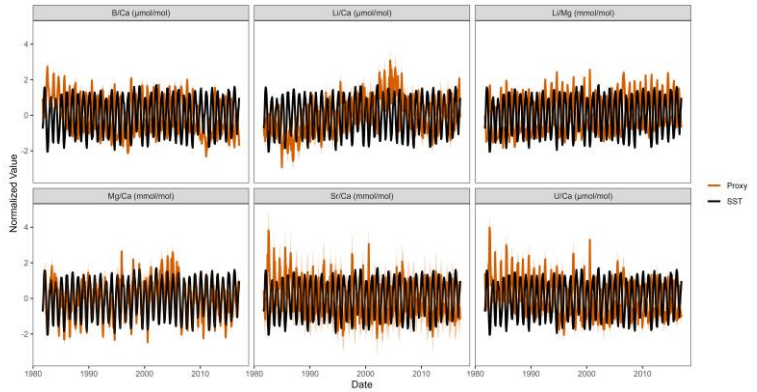

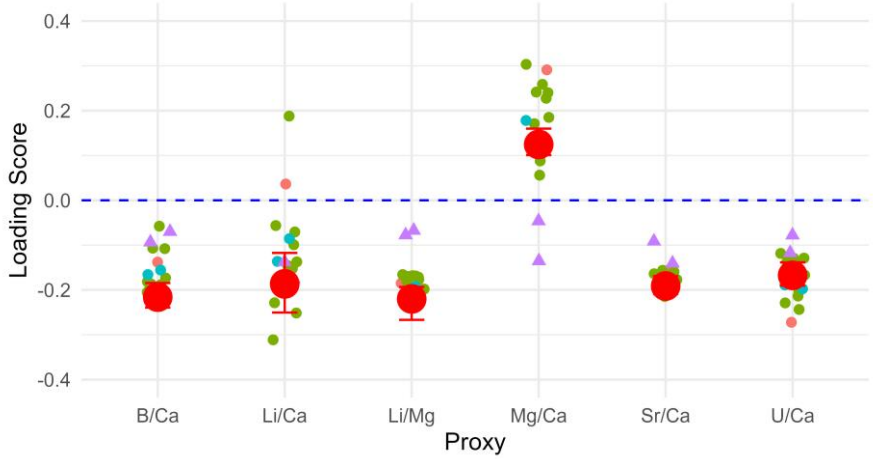

GBR14

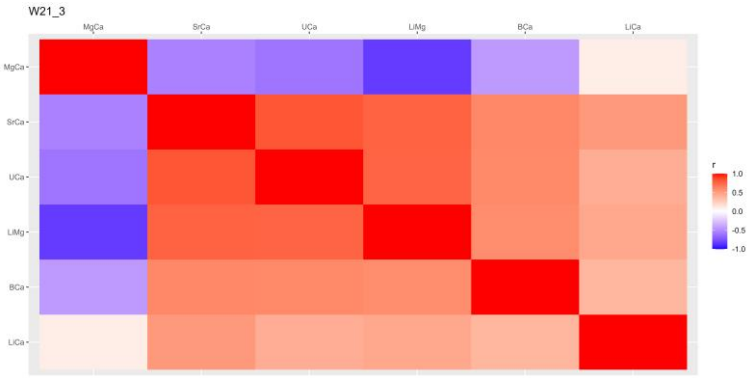

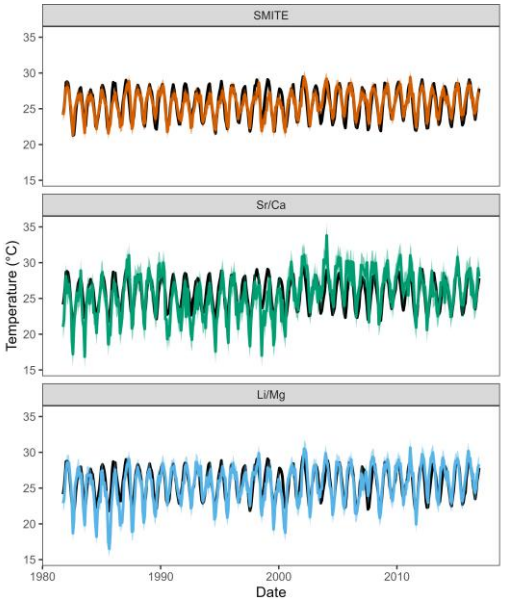

	RMSE	R
SMITE	0.74	0.89
Sr/Ca	1.24	0.80
Li/Mg	1.01	0.86

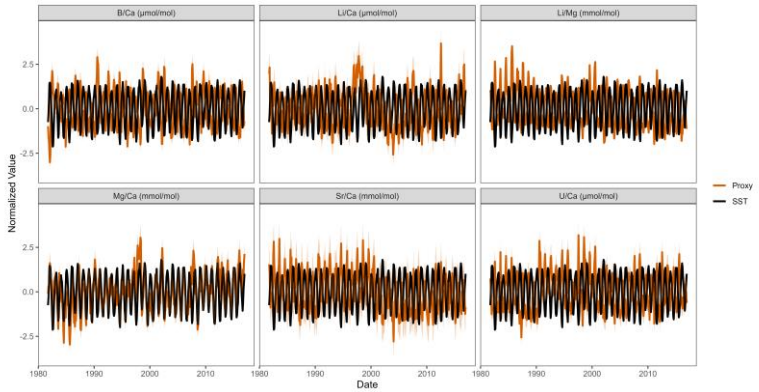

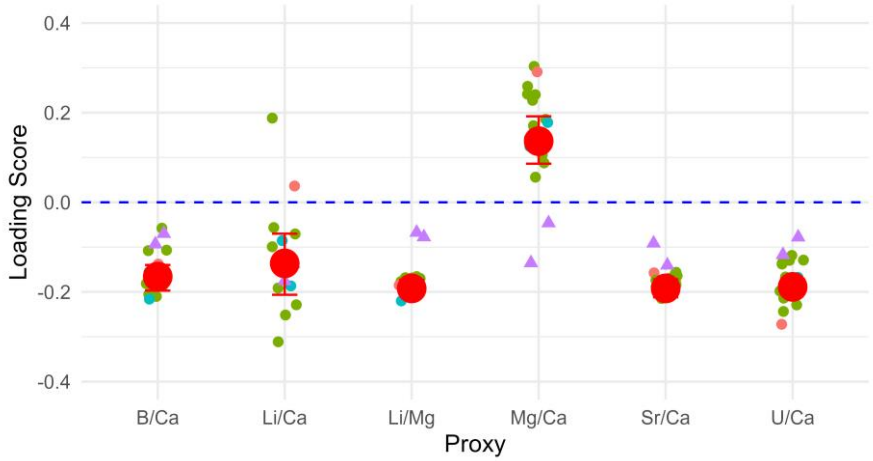

GBR15

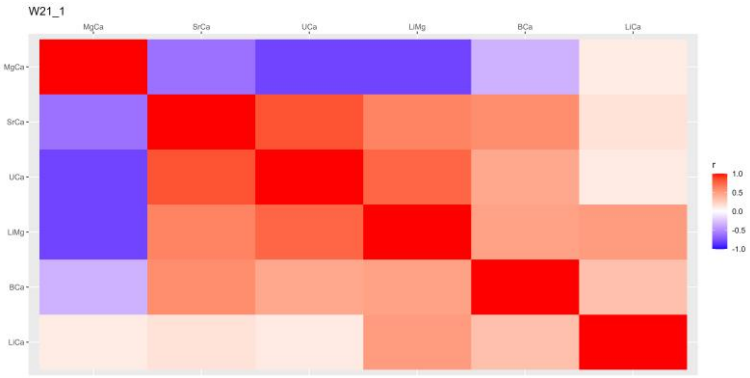

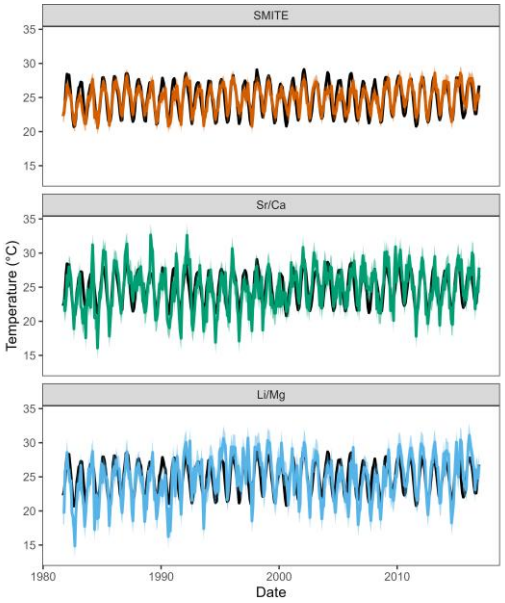

	RMSE	R
SMITE	0.90	0.86
Sr/Ca	1.70	0.77
Li/Mg	1.20	0.83

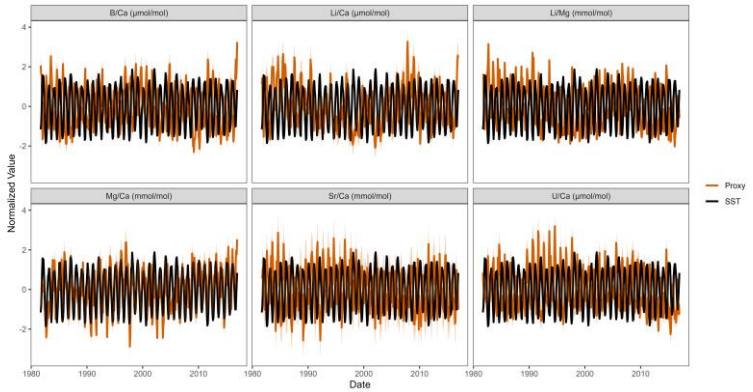

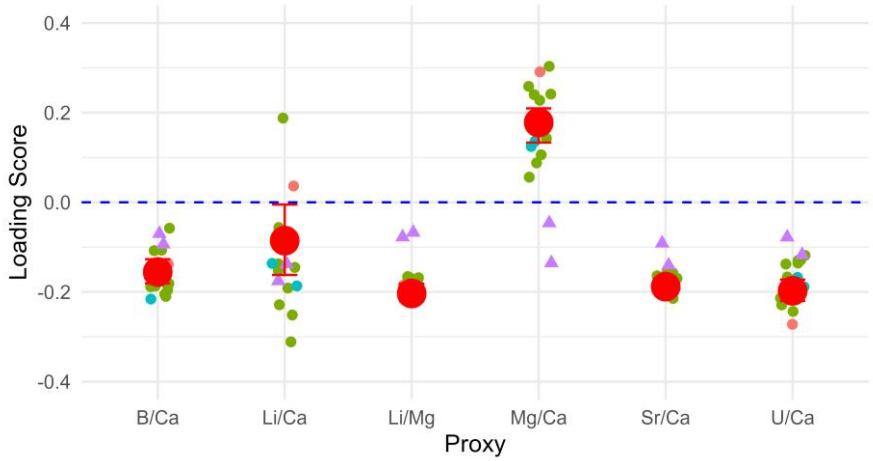

GI1

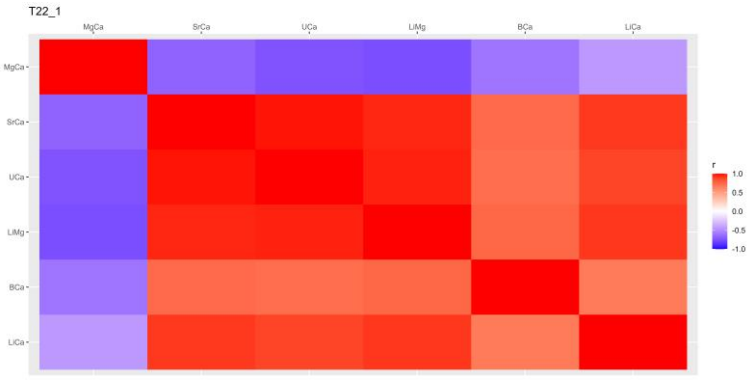

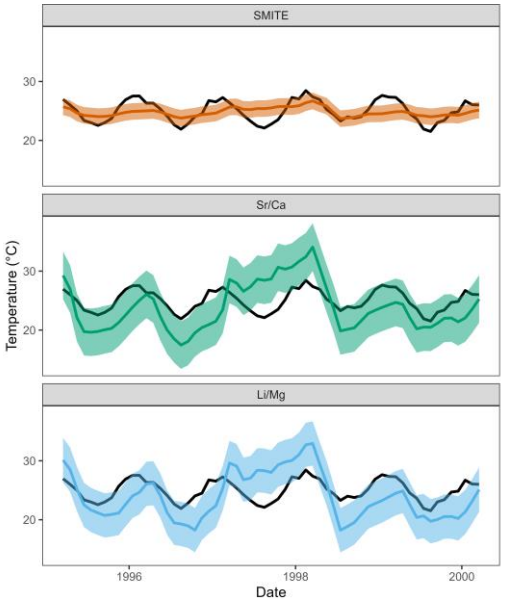

	RMSE	R
SMITE	1.41	0.46
Sr/Ca	4.04	0.42
Li/Mg	3.76	0.45

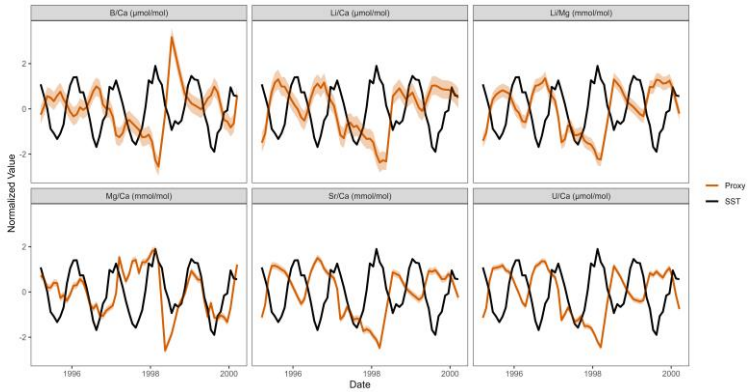

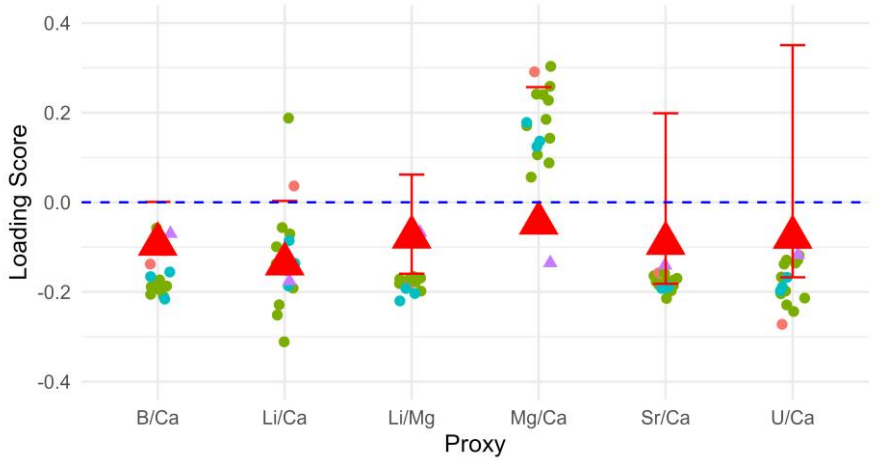

GI2

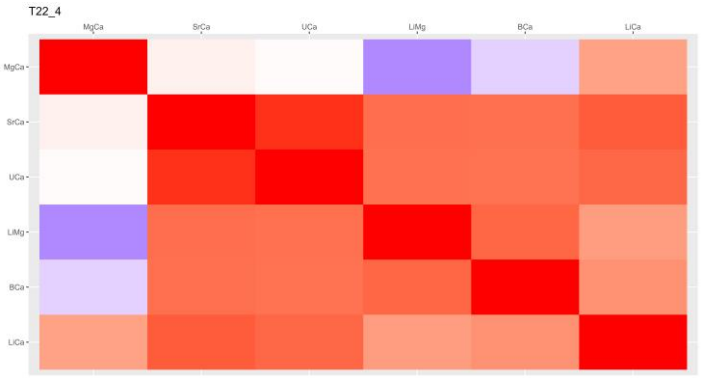

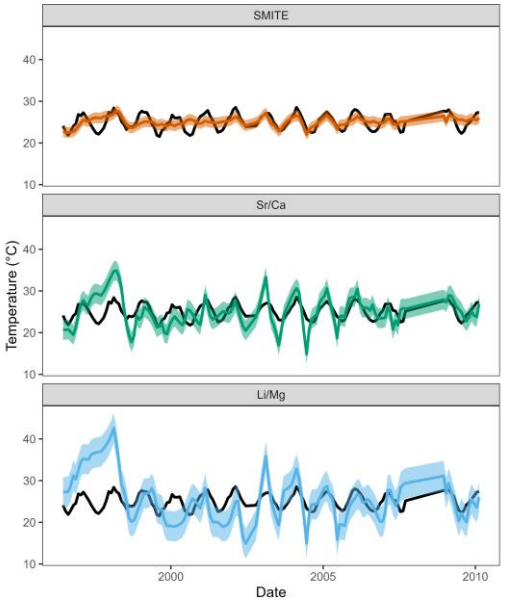

	RMSE	R
SMITE	1.30	0.57
Sr/Ca	2.37	0.55
Li/Mg	3.60	0.47

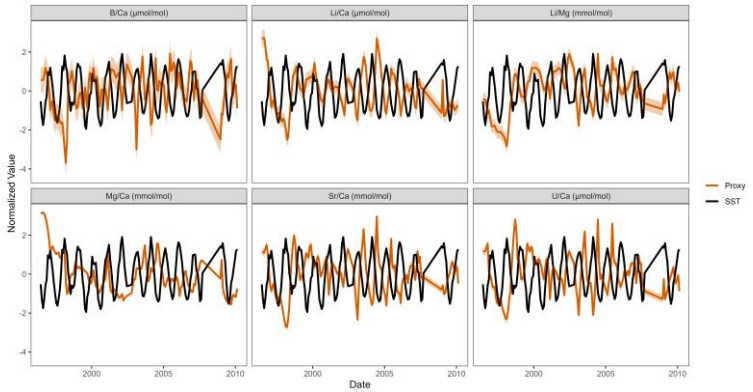

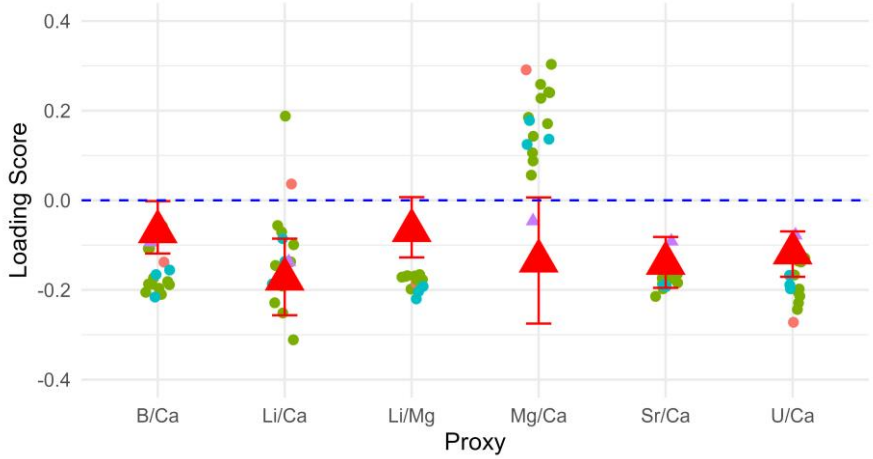

C.3 Individual Deseasonalized Reconstruction Summaries

The following pages contain individual reconstruction results from the deseasonalized calibrations of all Great Barrier Reef (GBR1-15) and Galapagos (GI1-2) corals. The following results are reported for each coral record:

1) The covariance matrix of the coral geochemical variables that were input into the SMITE calibration (B/Ca, Li/Ca, Li/Mg, Mg/Ca, Sr/Ca, U/Ca).

2) Normalized, age-modeled time-series of each coral geochemical variable (orange) plotted alongside normalized sea surface temperature (SST) estimates from the European Space Agency's Climate Change Initiative SST dataset (CCI SST; black).

3) SST reconstructions for SMITE (orange), Sr/Ca (green), and Li/Mg (blue), plotted alongside CCI SST (black). Error bars around each SST reconstruction are the cross-validated root mean square error (RMSE) from each calibration.

4) SMITE model parameters for the respective calibration (large red points) plotted over the SMITE model parameters for all calibrations. Error bars on the local SMITE model parameters are defined using a block-bootstrap cross-validation approach described in Section 4.2.4. The legend for the color and shape of the points is provided by Figure 4.5 in the main body of the manuscript.

5) A table of the summary statistics for each SST reconstruction method for each coral record (SEP = Standard Error of Prediction, RMSE = root-mean-square-error, R = Pearson Correlation Coefficient). Errors estimated using a block-bootstrap cross-validation approach for each summary statistic (except for SEP) can be seen in Figure 4.4.

GBR1

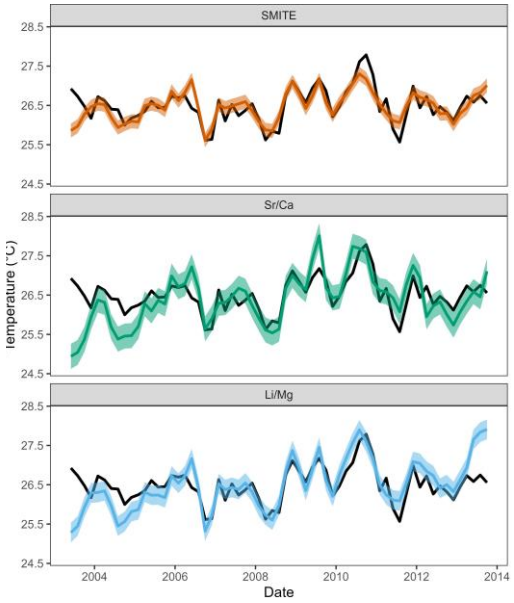

	RMSE	R
SMITE	0.14	0.86
Sr/Ca	0.21	0.83
Li/Mg	0.26	0.76

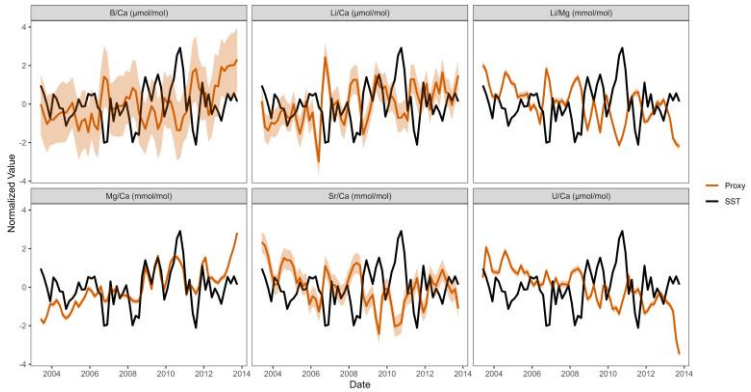

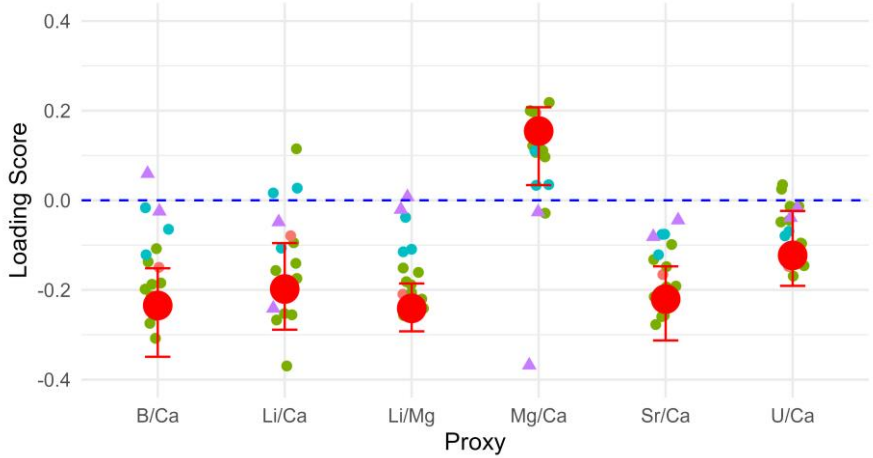

GBR2

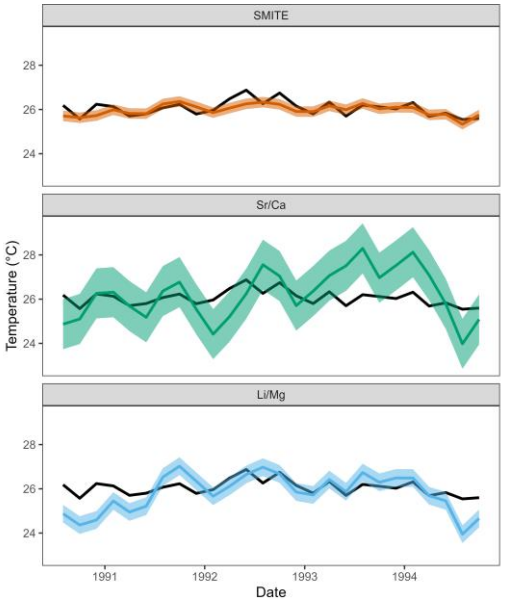

	RMSE	R
SMITE	0.27	0.68
Sr/Ca	0.31	0.79
Li/Mg	0.82	0.50

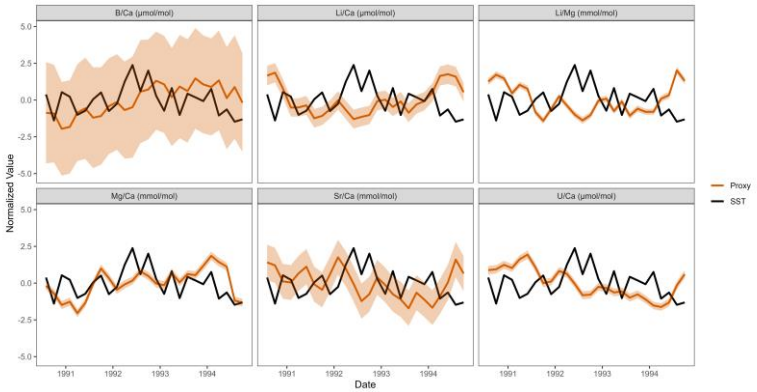

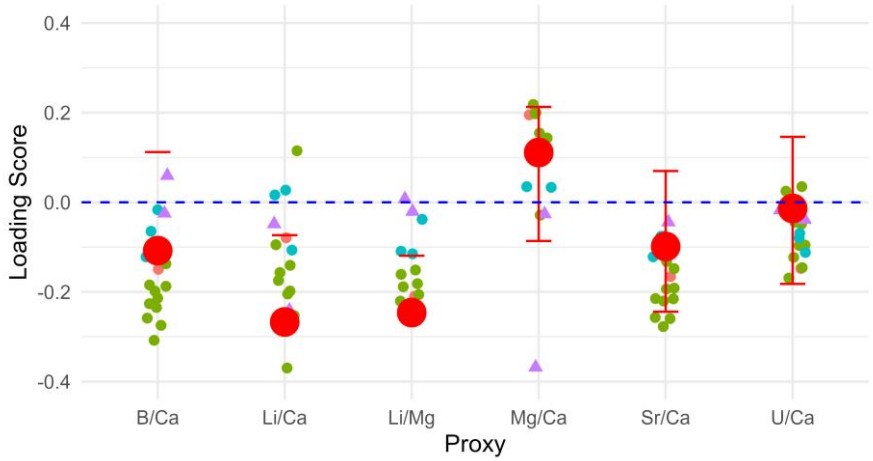

GBR3

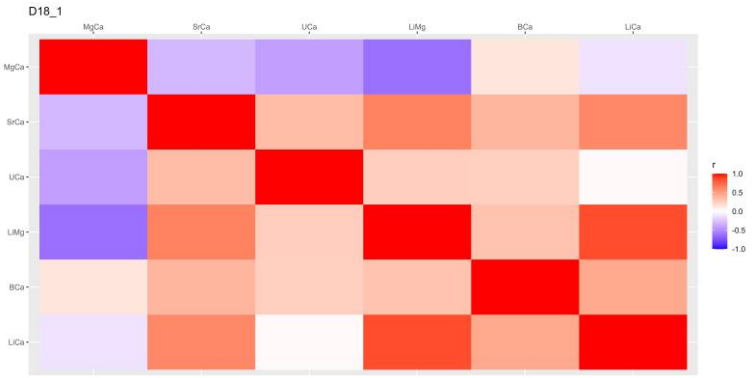

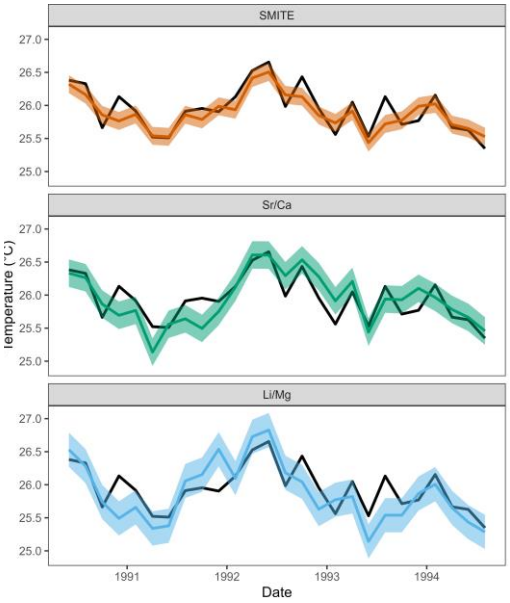

	RMSE	R
SMITE	0.23	0.79
Sr/Ca	0.31	0.83
Li/Mg	0.56	0.64

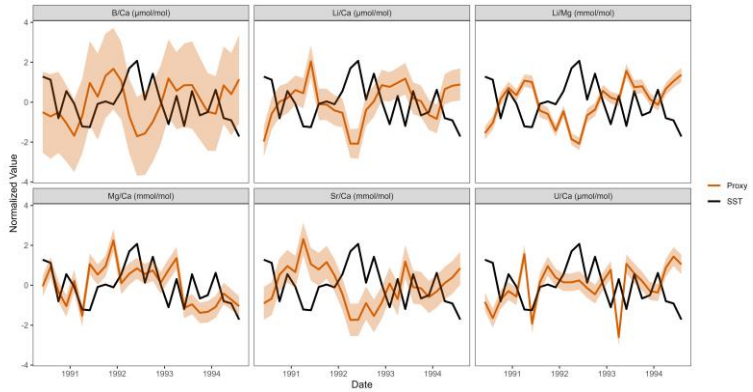

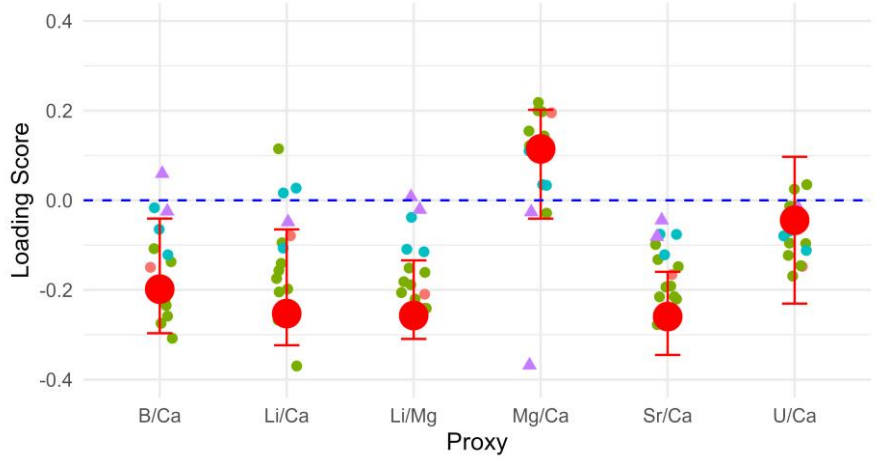

GBR4

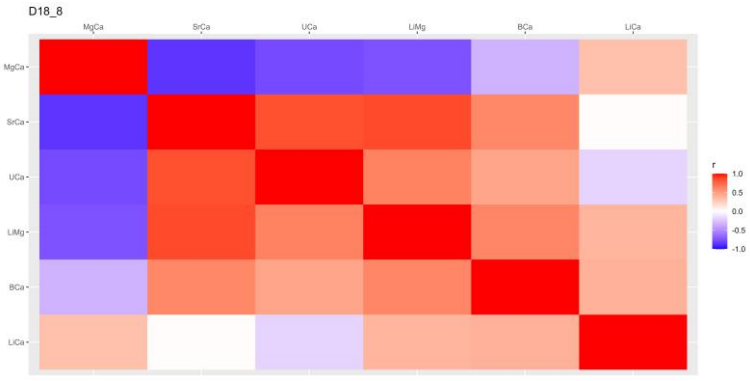

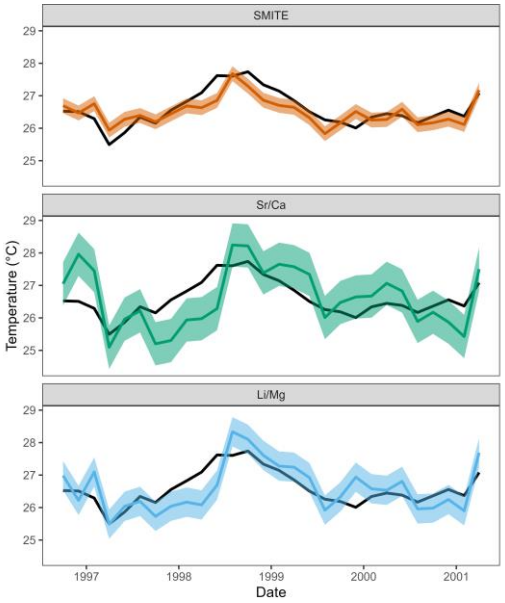

	RMSE	R
SMITE	0.26	0.78
Sr/Ca	0.34	0.74
Li/Mg	0.45	0.70

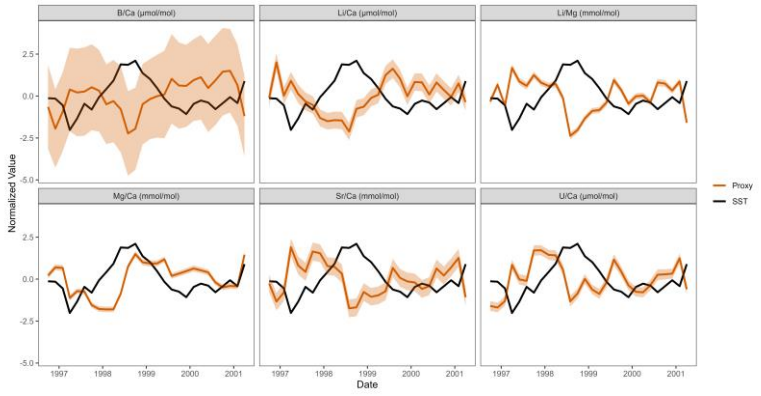

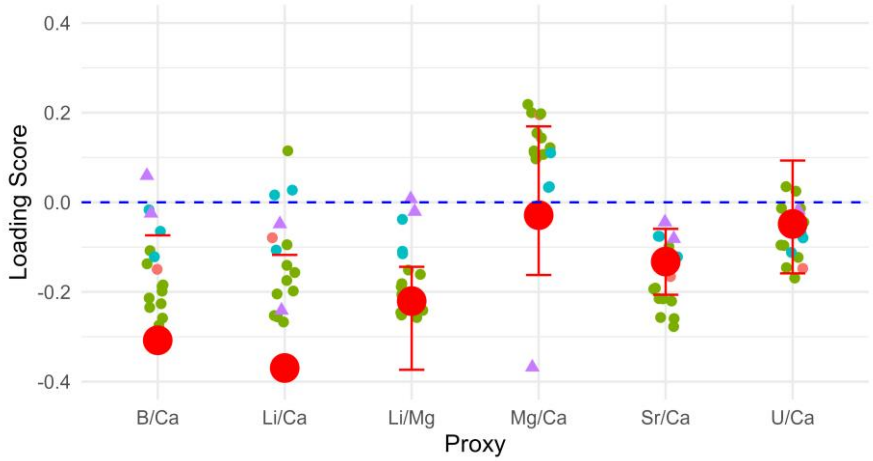

GBR5

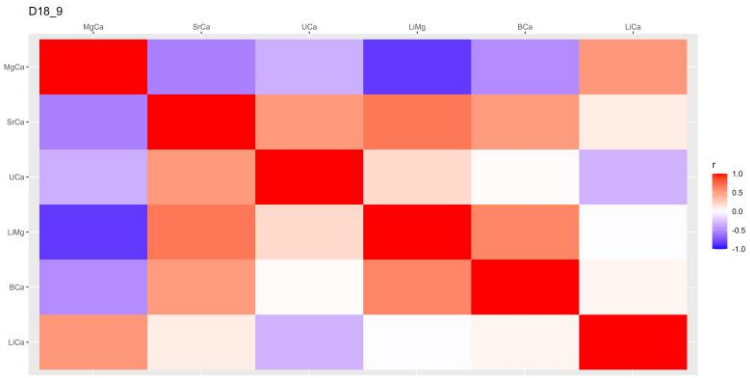

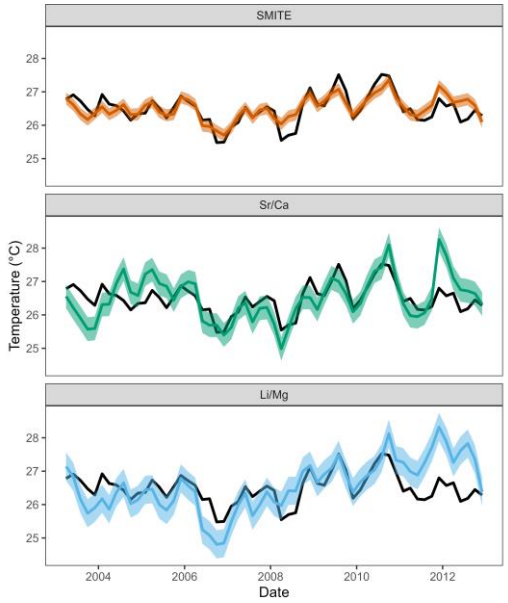

	RMSE	R
SMITE	0.24	0.61
Sr/Ca	1.13	0.26
Li/Mg	0.40	0.61

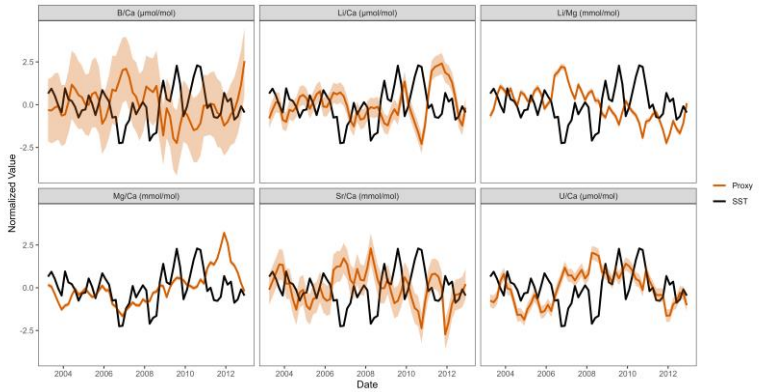

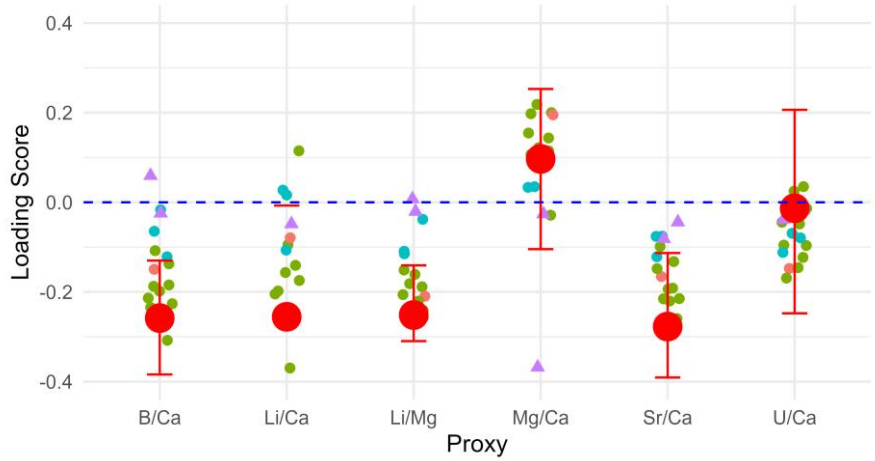

GBR6

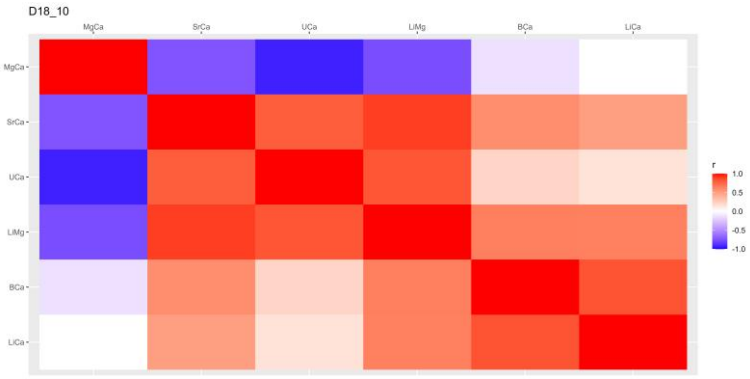

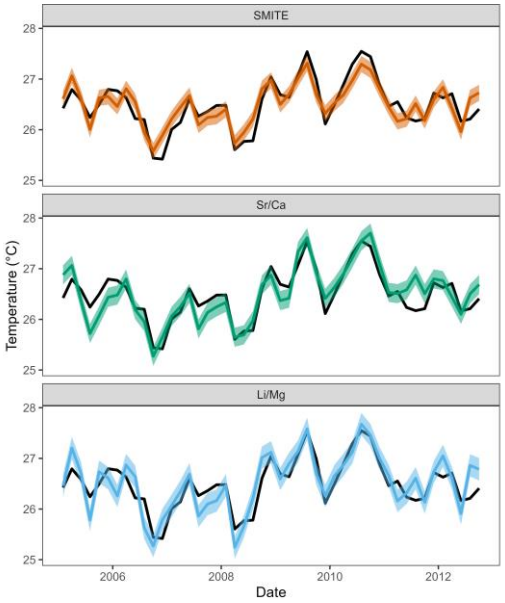

	RMSE	R
SMITE	0.23	0.74
Sr/Ca	0.42	0.59
Li/Mg	0.31	0.71

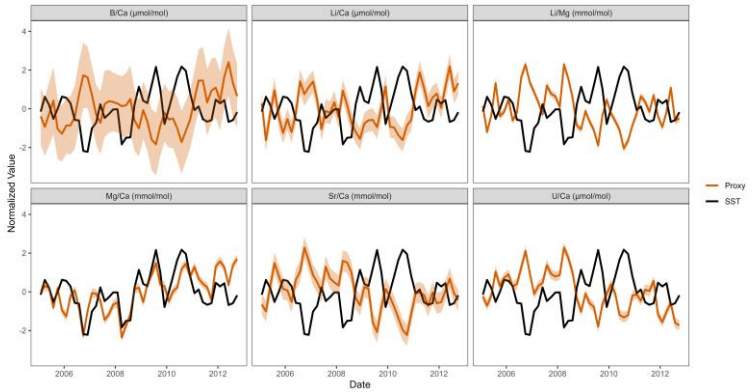

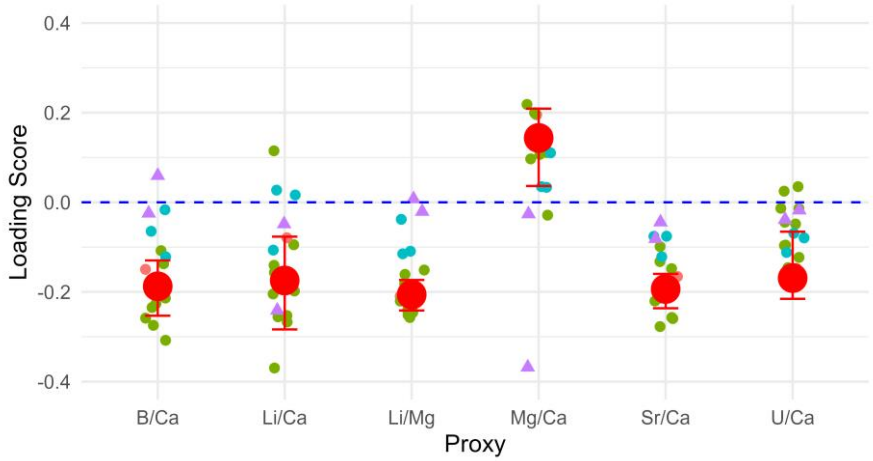

GBR7

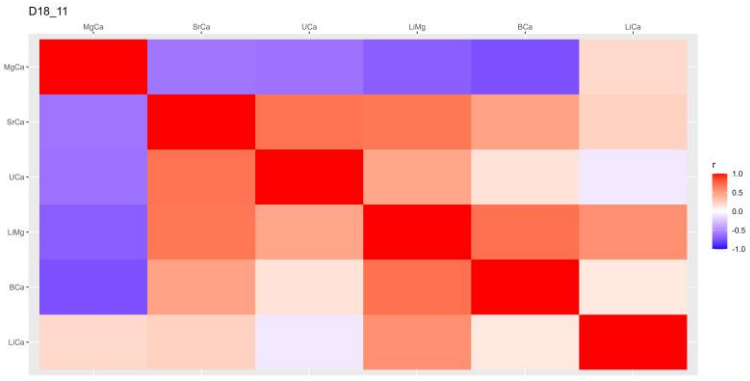

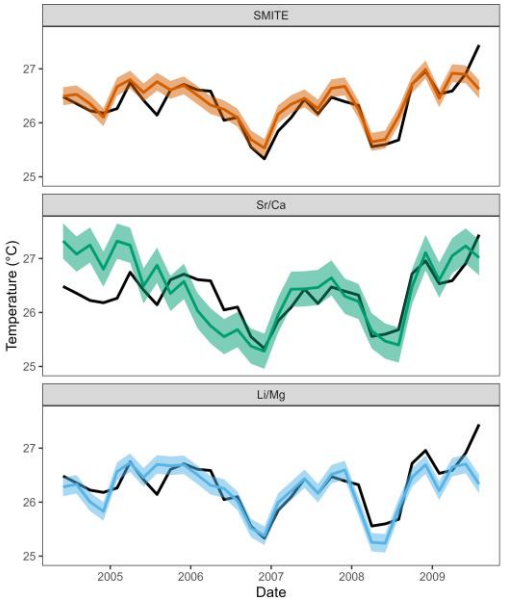

	RMSE	R
SMITE	0.18	0.86
Sr/Ca	0.32	0.78
Li/Mg	0.25	0.85

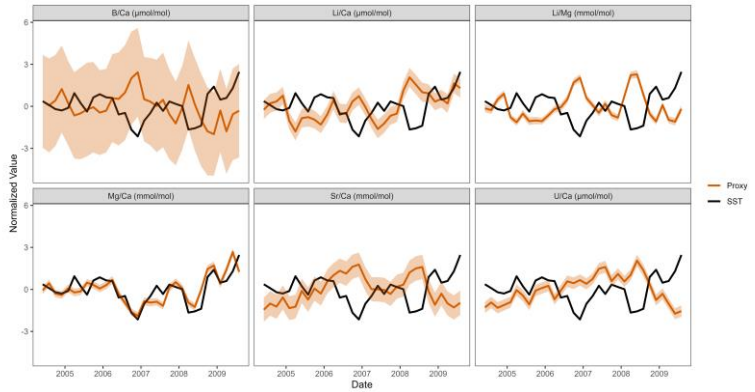

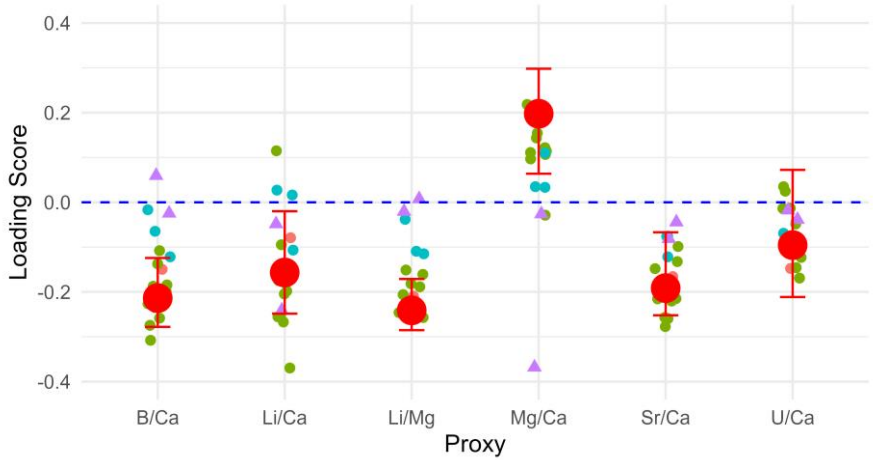

GBR8

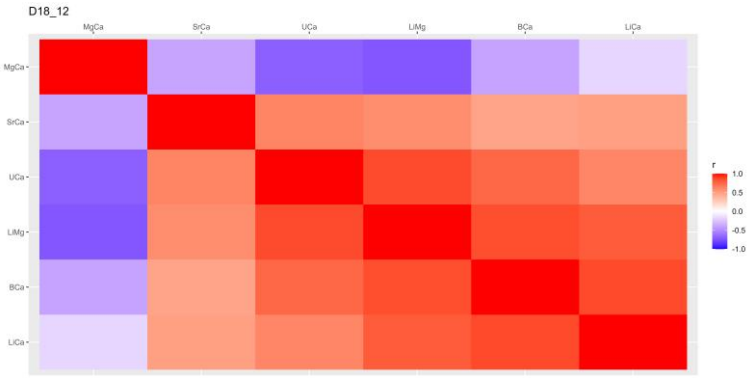

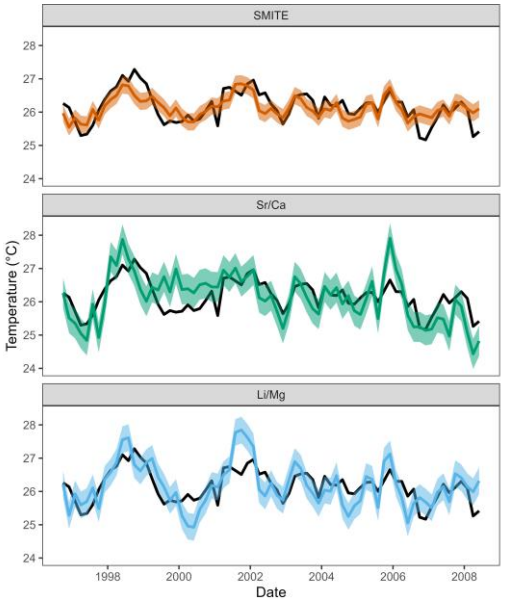

	RMSE	R
SMITE	0.23	0.85
Sr/Ca	0.67	0.63
Li/Mg	0.45	0.74

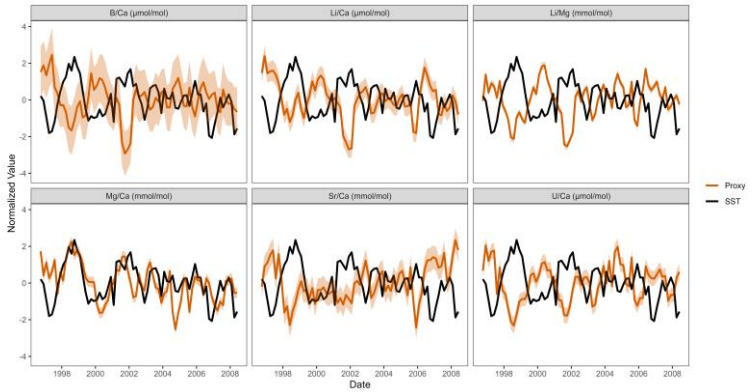

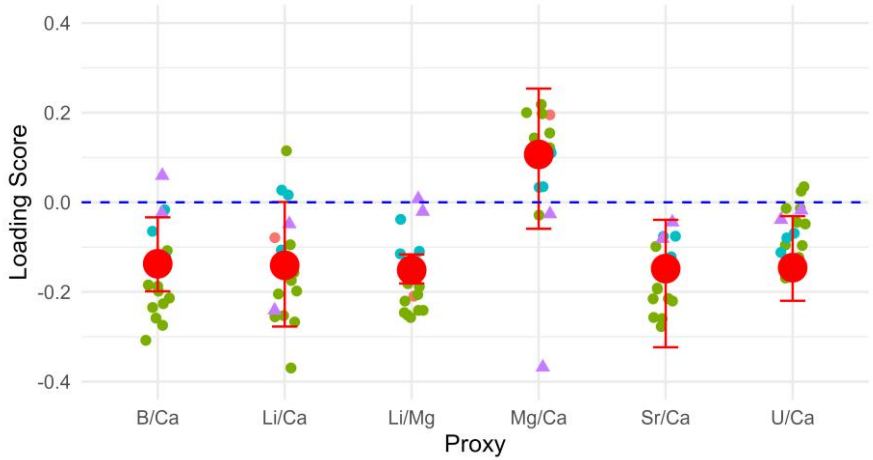

GBR9

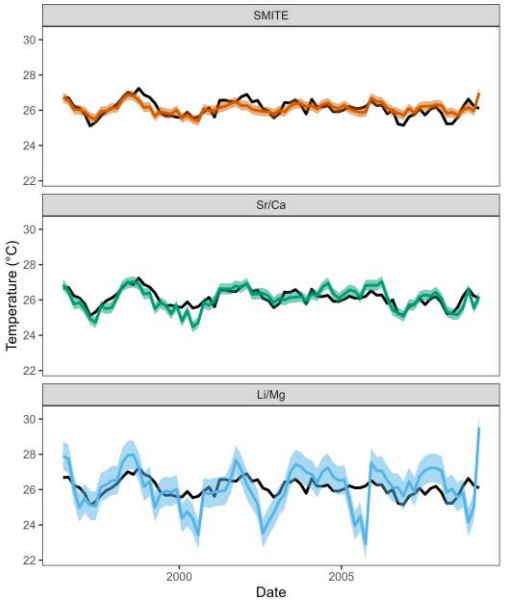

	RMSE	R
SMITE	0.18	0.87
Sr/Ca	0.36	0.77
Li/Mg	0.42	0.73

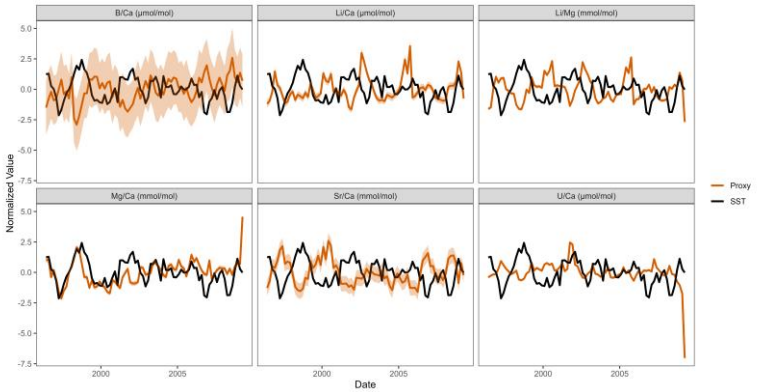

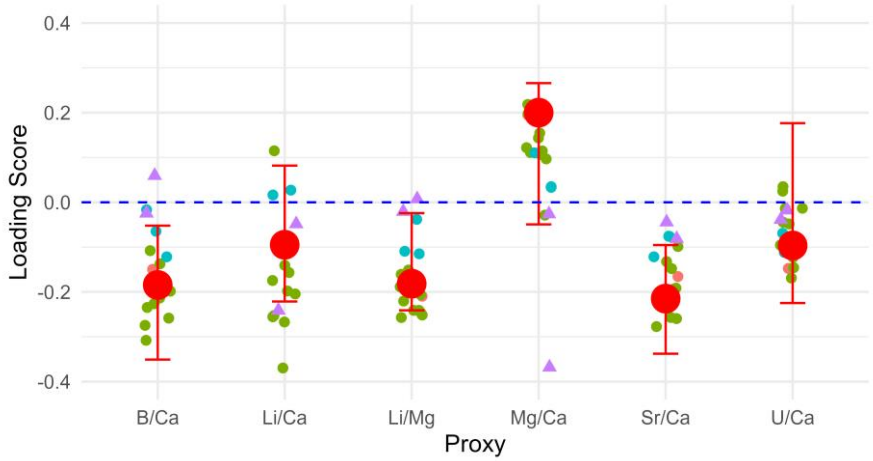

GBR10

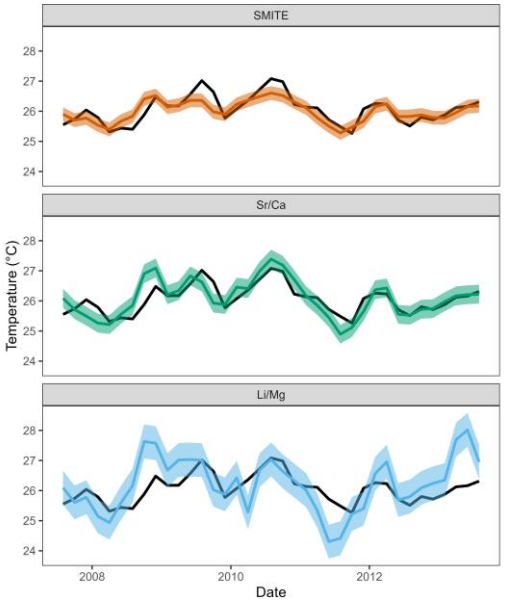

	RMSE	R
SMITE	0.16	0.90
Sr/Ca	0.19	0.91
Li/Mg	0.22	0.88

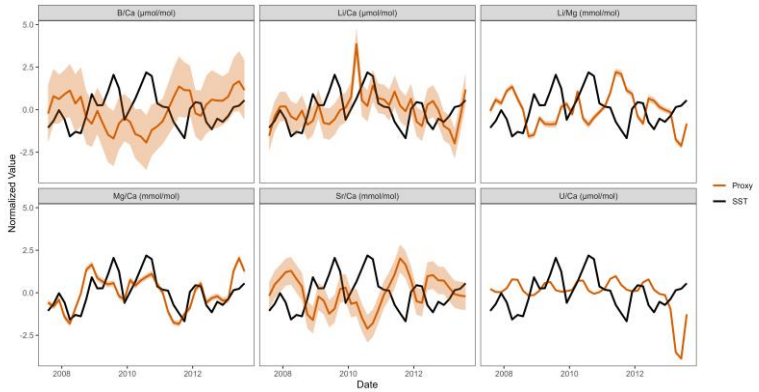

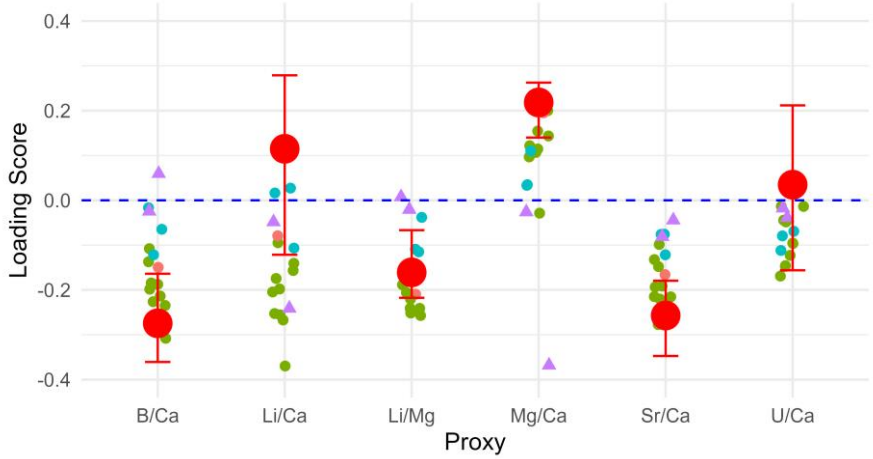

GBR11

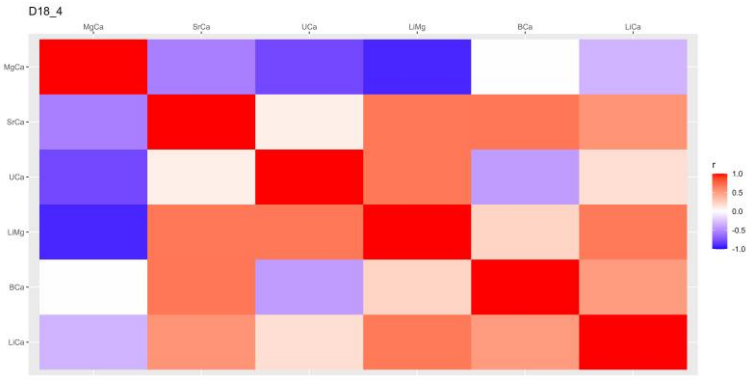

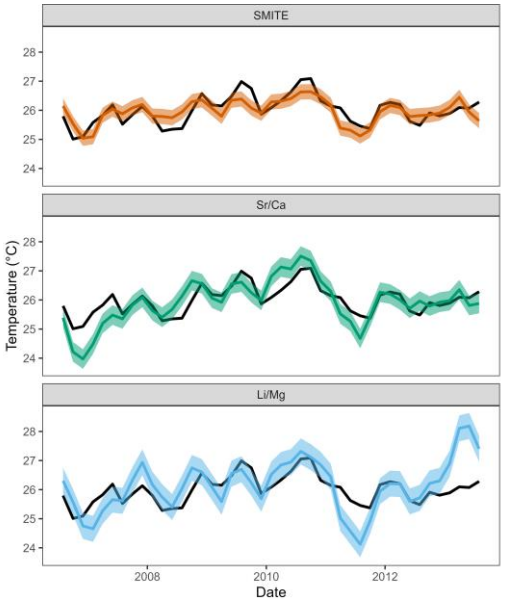

	RMSE	R
SMITE	0.17	0.90
Sr/Ca	0.33	0.75
Li/Mg	0.17	0.90

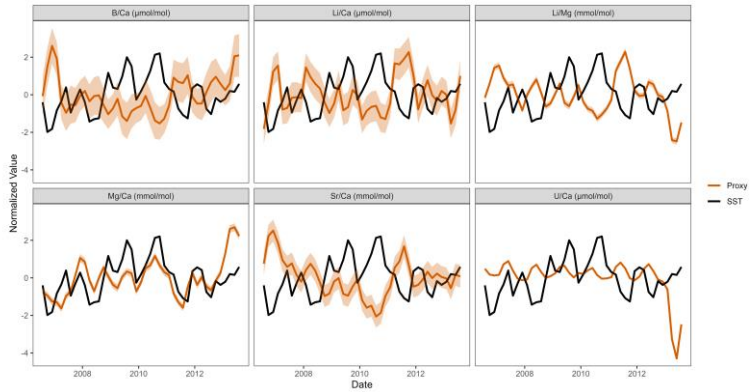

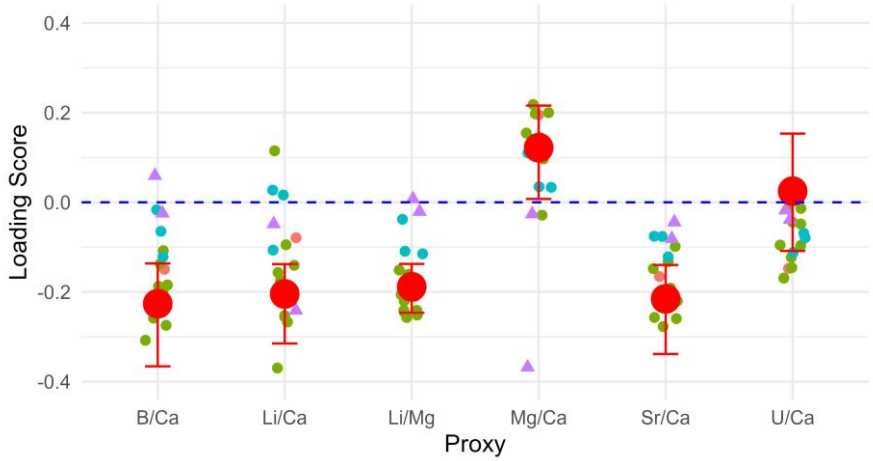

GBR12

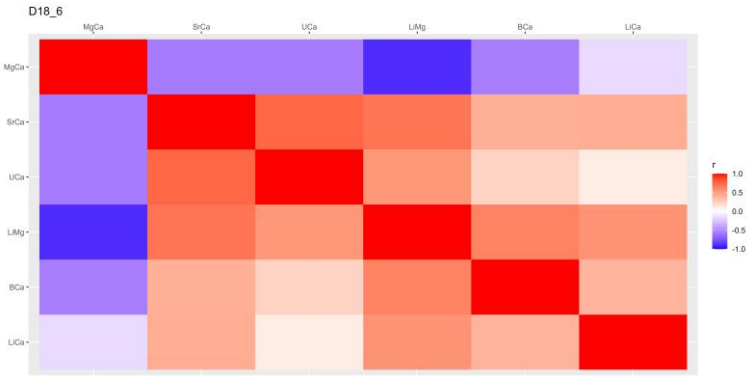

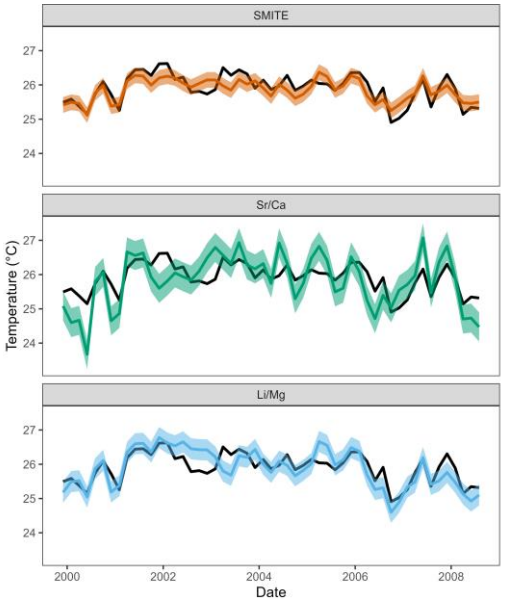

	RMSE	R
SMITE	0.26	0.69
Sr/Ca	0.45	0.67
Li/Mg	0.40	0.67

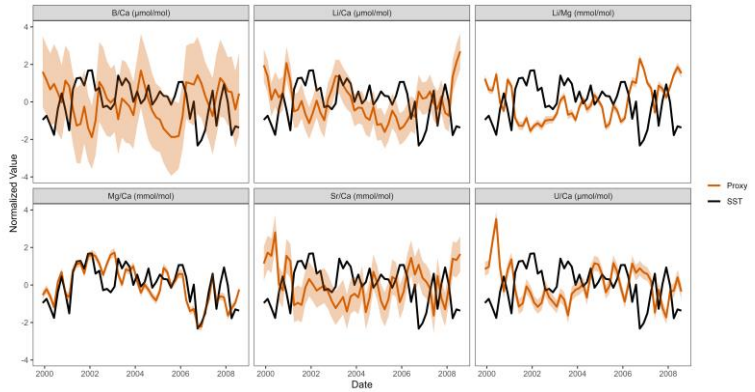

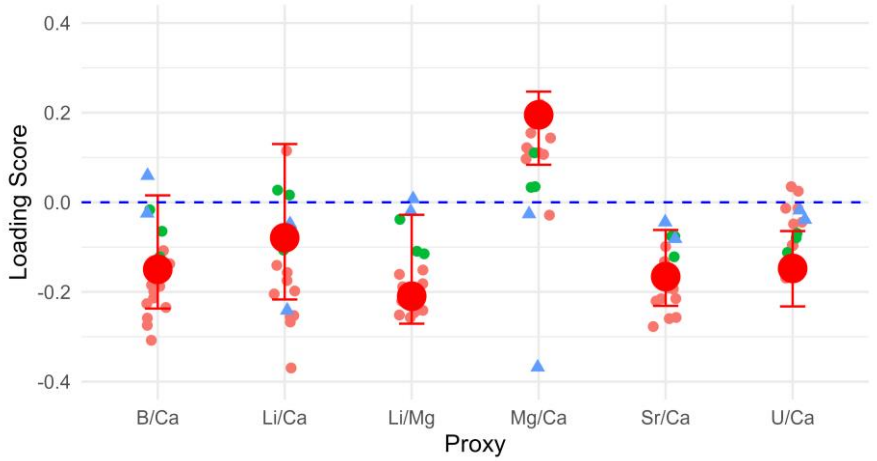

GBR13

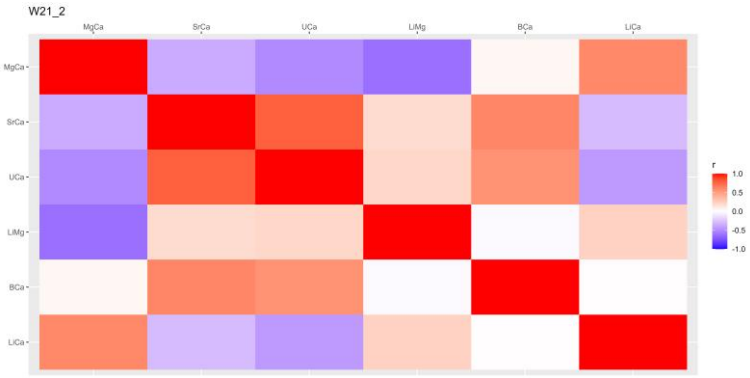

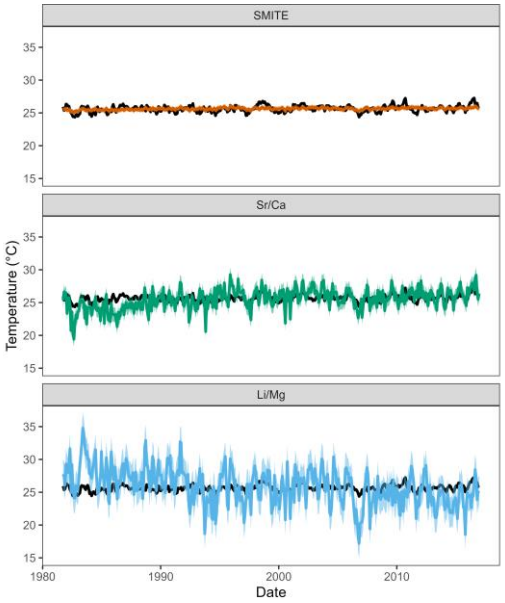

	RMSE	R
SMITE	0.37	0.23
Sr/Ca	1.46	0.19
Li/Mg	2.09	0.16

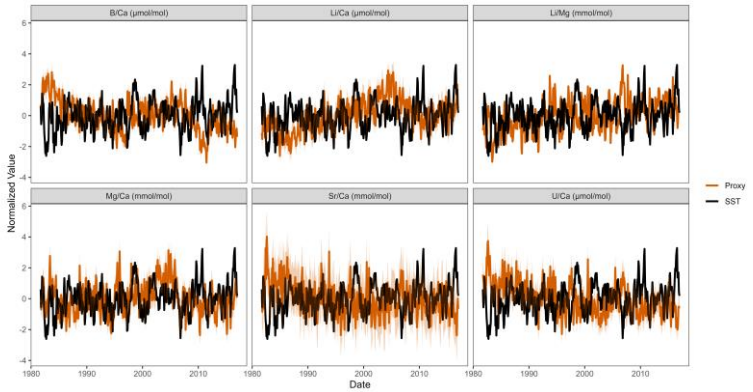

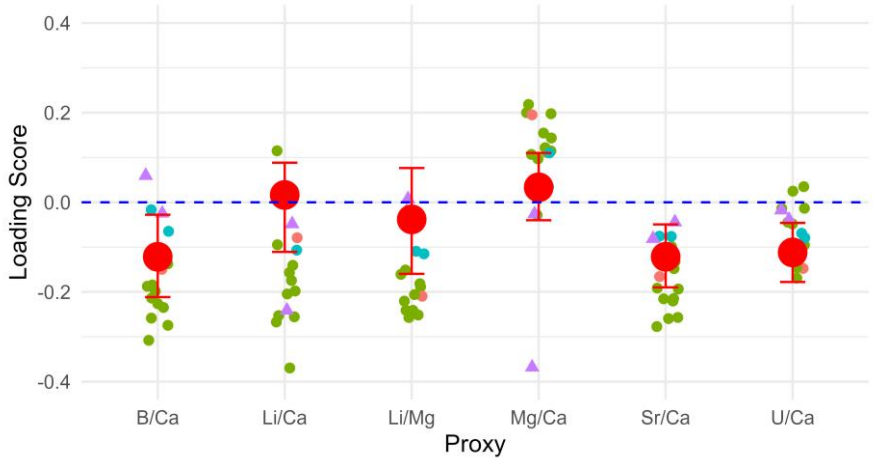

GBR14

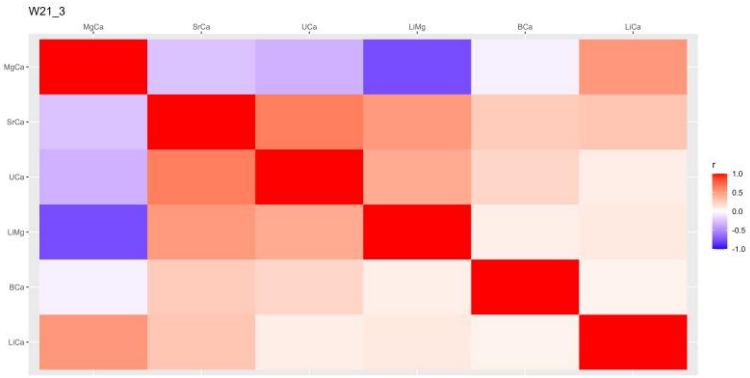

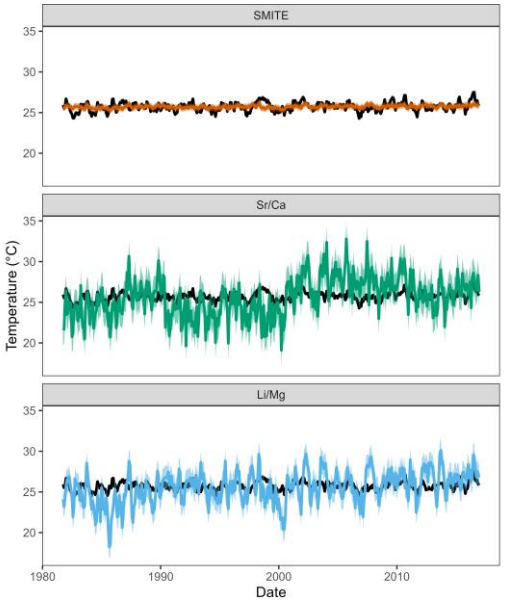

	RMSE	R
SMITE	0.37	0.29
Sr/Ca	1.09	0.24
Li/Mg	2.31	0.17

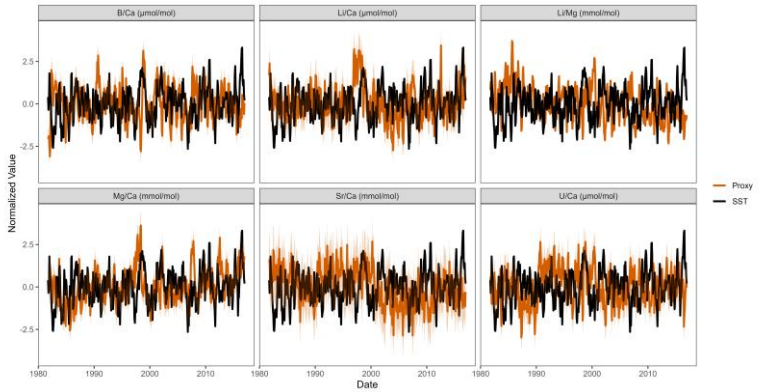

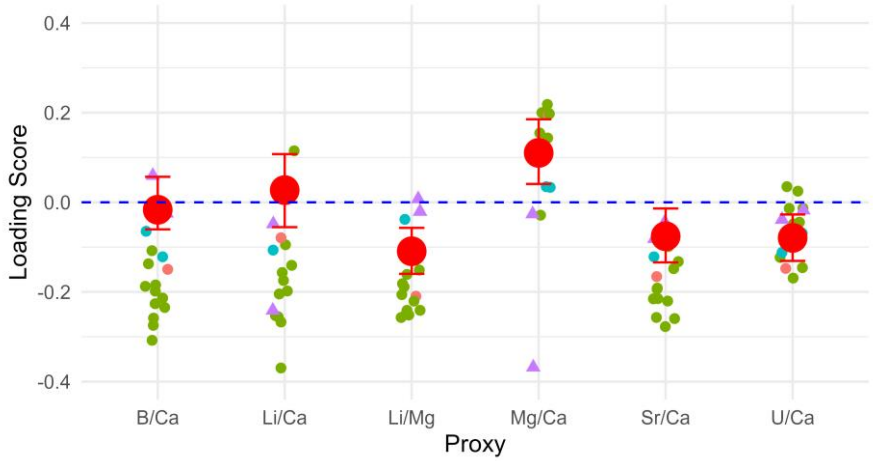

GBR15

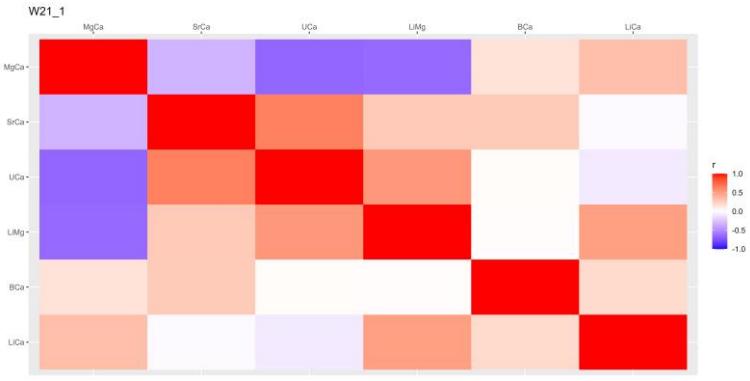

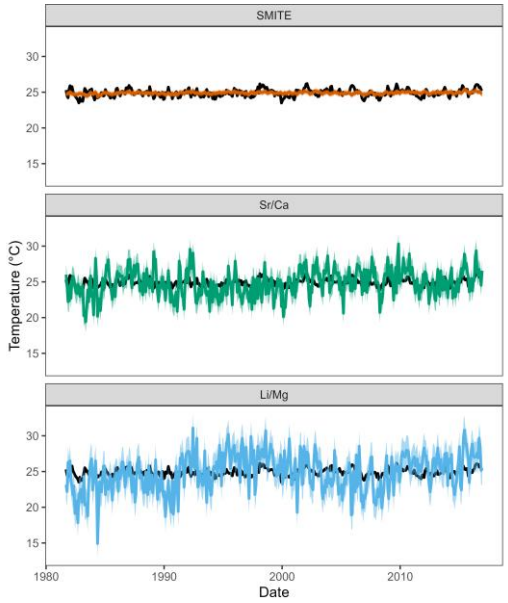

	RMSE	R
SMITE	0.40	0.32
Sr/Ca	1.91	0.24
Li/Mg	1.42	0.29

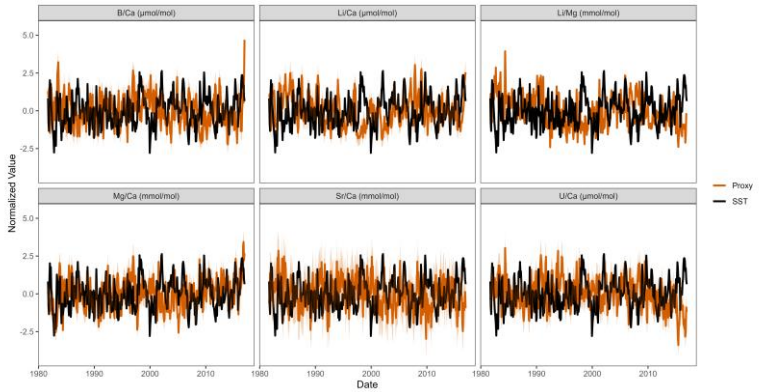

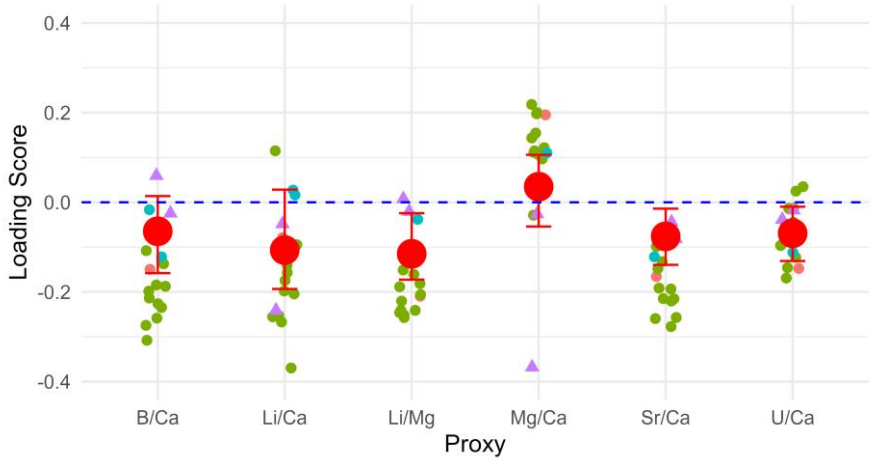

GI1

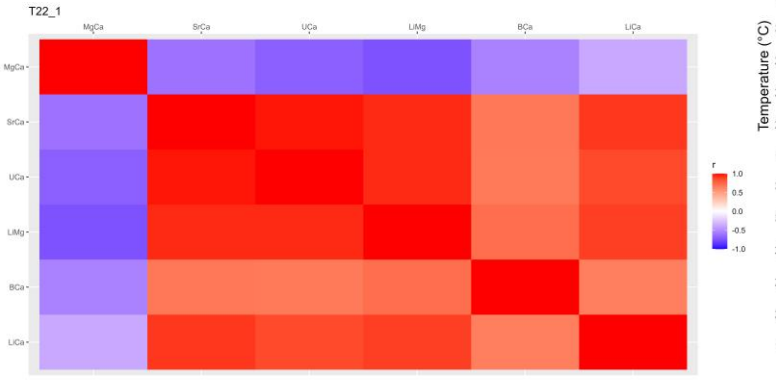

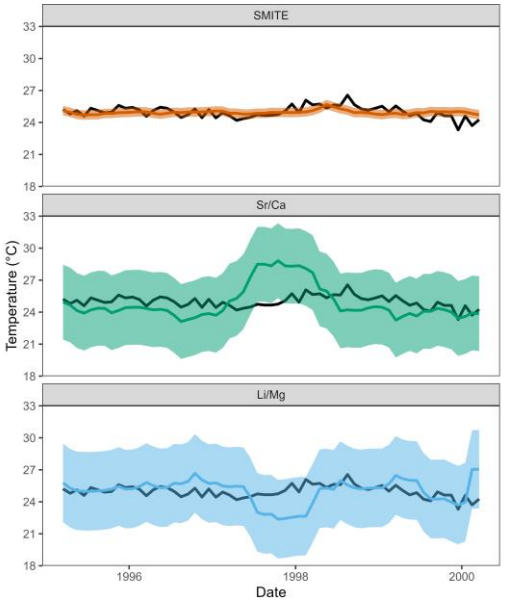

	RMSE	R
SMITE	0.44	0.24
Sr/Ca	3.51	0.05
Li/Mg	3.68	0.04

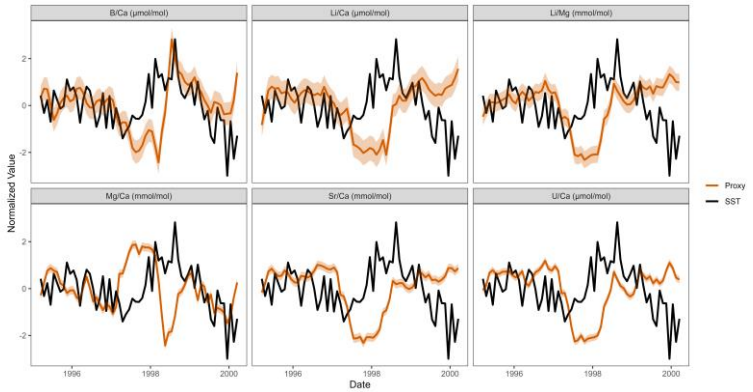

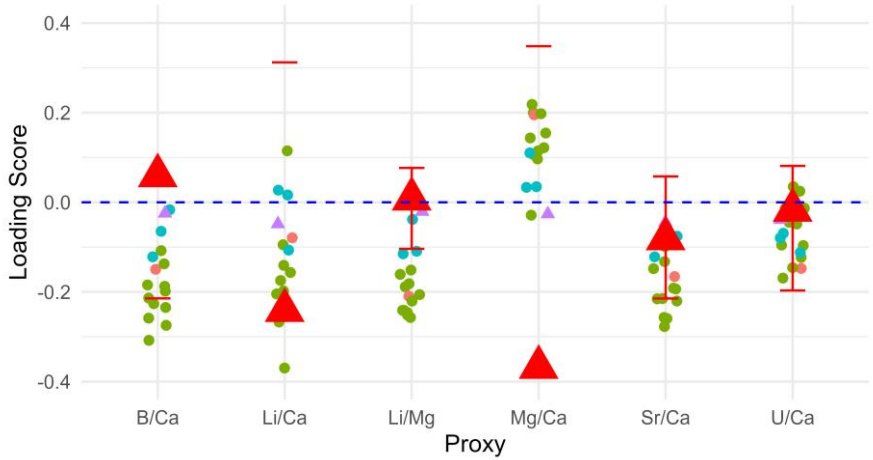

GI2

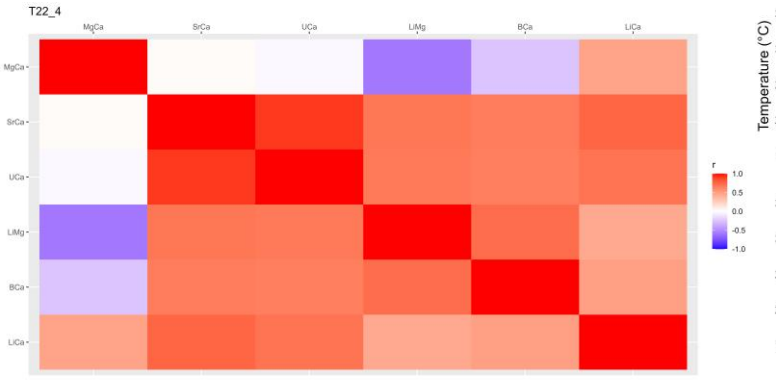

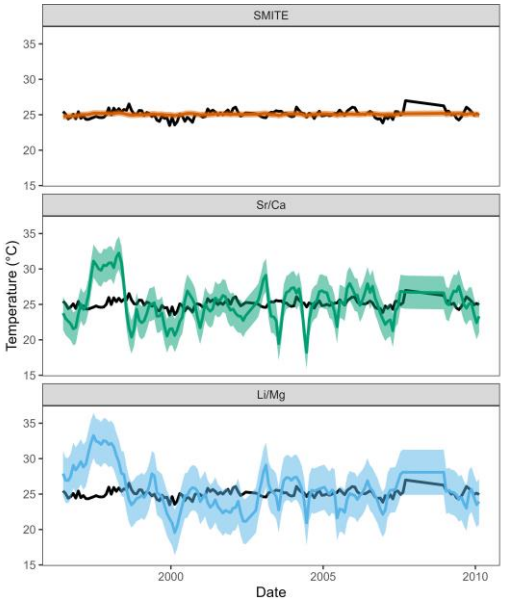

	RMSE	R
SMITE	0.43	0.07
Sr/Ca	2.34	0.12
Li/Mg	3.19	0.03